

© 2017 by Yi Ren. All rights reserved.

DEVELOPMENT OF MECHANO-ACTIVE ORGANIC MATERIALS
FOR SHOCK WAVE ENERGY DISSIPATION

BY
YI REN

DISSERTATION

Submitted in partial fulfillment of the requirements
for the degree of Doctor of Philosophy in Chemistry
in the Graduate College of the
University of Illinois at Urbana-Champaign, 2017

Urbana, Illinois

Doctoral Committee:

Professor Jeffrey S. Moore, Chair
Professor Nancy R. Sottos
Professor Steven C. Zimmerman
Professor Paul J. Hergenrother

Abstract

Materials capable of shock wave energy dissipation (SWED) are of interest for protecting personnel and machinery from explosions and ballistic impacts. Although current protective armors often prevent physical injuries by stopping shrapnel or bullets, the shock waves generated by explosions or ballistic impacts can still cause psychological and cognitive injuries as they pass through the armors, even in the absence of detectable physical injury. This leads to an urgent need for the development of effective energy-dissipative materials. Here, we hypothesize that chemical and physical transformations involving intra- or intermolecular volume collapse effectively dissipate shock wave energy and weaken shock propagation due to the generation of rarefaction waves. Several classes of organic materials capable of volume reductions upon exposure to external stimuli, such as mechanical force, temperature, and light, have been developed as potential candidates for SWED.

Chapter 2 explores the feasibility of shock-induced intramolecular volume collapse via the cyclization of molecular and polymeric arenediynes and cyclophanes. The steric and electronic effects of bulky, electron rich aryl substituents on the cyclization pathways of molecular arenediynes are also discussed. Since the kinetics/rate of volume collapse is crucial for SWED, chapter 3 focuses on the development of organic materials that undergo pressure-induced neutral-to-ionic transitions via ultrafast electron transfer reactions. Due to the enhanced ionic interactions, intermolecular volume decreases as electron transfers occur from electron donors to electron acceptors. Both hydrostatic pressure and transient shock waves are utilized to investigate the mechanoactivities and SWED properties of these materials. Analogous to the electron transfers, ultrafast proton transfers induced by high-speed shock waves are investigated in chapter 4. The effects of shock compression in a series of polymers, including blends composed of polymer Brønsted bases and molecular proton donors are probed with the emission of Nile Red, a polarity sensing dye possessing a fast response that is within the shock duration. In addition to these chemical approaches, a physical approach involving an amorphous-to-crystalline transition is also employed to achieve intermolecular volume collapse. In chapter 5, we describe a metastable supercooled liquid, i.e. 1,2-bis(phenylethynyl)benzene, that undergoes accelerated nucleation from its supercooled state when exposed to shock waves. Various analysis techniques are utilized to build an understanding of shock-induced nucleation and its role in energy dissipation.

Based on our studies, shock-induced densification via covalent bond rearrangements, e.g. cyclization reactions, is unlikely to occur due to the relatively high activation energy and long reaction time. In contrast, intermolecular volume reduction induced by electron/proton transfer and subsequent ionic interaction readily occurs on the nanosecond time scale when exposed to shock waves. These and other studies on the development of SWED materials provide design strategies for enhancing the energy-absorbing ability of protective armors and shed light on the mechanism of shock wave mitigation.

To family, friends, and my rock – Mianzhi

Acknowledgements

Graduate school has been an adventurous ride for me, filled with many ups and downs. I cannot picture myself crossing the finish line without the help and support from many people in my life. First and foremost, I would like to express my sincere gratitude to my advisor/mentor, Professor Jeffrey Scott Moore, for his continual support and guidance. He has been a constant inspiration and taught me many invaluable lessons about chemistry and life. What I appreciate most is the “incubator” that Jeff has provided for me to grow as an independent scientist. Although his hands-off management was somewhat unsettling during my first two years in graduate school, it allowed me to make mistakes, learn from failures, and eventually take control of my research project with a clear purpose and direction.

I would also like to thank my committee members: Professor Nancy Sottos, Professor Steven Zimmerman, and Professor Paul Hergenrother. Their constructive feedback and encouragement have been very helpful throughout my Ph.D. education at UIUC. Additionally, I want to thank Professor Sottos, Professor Dana Dlott, Professor Ken Suslick, and Professor Todd Martínez for providing insightful discussions and suggestions for the SWED project.

The work described here would not be possible without the efforts of my amazing collaborators including Dr. Nagarjuna Gavvalapalli, Dr. Semin Lee, Dr. Kristin Hutchins, Dr. Nikolay Plotnikov, Dr. Alexandr Banishev, Dr. William Shaw, James Christensen, Jaejun Lee, Mark Burgess, Jingshu Hui, Dr. David Moon, Dr. Taras Pogorelove, Dr. Jeffery Bertke, and Dr. Danielle Gray. It is a privilege to work with them and I am truly grateful for our interactions through the years. Financial support for this work was provided by the Department of the Navy, Office of Naval Research under MURI grant N00014-12-1-0828.

I've received countless help from the Moore group members since my visiting weekend in February 2012. First, I want to thank Dr. Nina Sekerak, my loyal friend, for encouraging me to join the group and helping with my transition to graduate school. I thank Dr. Olivia Lee for offering lots of positive thoughts on research, technical writing, and life in general. Thanks to Dr. Shawn Miller for editing my manuscripts and organizing lots of group activities. Dr. Ke Yang, my unscripted SWED collaborator, made my time in Beckman both productive and joyful. I am grateful for all of the helpful discussions and suggestions from Dr. Scott Sisco, Dr. James Herbison, Dr. Joshua Kaitz, Dr. Yang Song, Dr. Charles Diesendruck, Dr. Tomohiro Shiraki, Dr. Bora Inci, and Dr. Vivian Lau. I also thank Dr. Kristin Hutchins, Dr. Semin Lee, Dr. Lily

Robertson, Dr. Kenneth Schwieter, Anna Yang, and Kevin Cheng for their assistance in editing this dissertation.

I thank everyone from the Moore group, both current members and alumni, for providing an open and supportive environment. I sincerely enjoyed my time here and thank you all for your company: Dr. Xiaocun Lu, Dr. Max Robb, Dr. Gabe Rudebusch, Dr. Xing Jiang, Dr. Yu Cao, Dr. Se Hye Kim, Dr. Brian Wall, Dr. Etienne Chenard, Dr. Nagamani Chikkanagari, Dr. Pin-Nan Cheng, Dr. Michael Evans, Dr. Preston May, Dr. Hefei Dong, Dr. Windy Santa Cruz, Dr. Catherine Casey, Dr. Joshua Grolman, Dr. Jun Li, Ian Robertson, Shijia Tang, Marissa Giovino, Huiying Liu, Tim Moneypenny, Anderson Coates, Chengtian Shen, Abby Halmes, Jose Zavala, Hao Yu, Jordan Langston, Lijuan Zhu, and Masashi Arai. Lots of great memories were created in the past five years, which I will take with me. I would also like to acknowledge the entire AMS group for providing an incredible multidisciplinary environment.

Special thanks to Ashley Trimmell, who has been phenomenal in keeping the Moore group organized. I am also grateful to the administrative/supporting staff who helped me during graduate school: Erica Malloch, Stacy Olson, Becky Duffield, Lori Johnson, Gayle Adkisson, Jamison Lowe, Kara Metcalf, Connie Knight, Patricia Simpson, Gayle Nelsen, and Mike Hallock. They definitely made many processes at UIUC smooth for me.

I would be remiss not to mention Ms. Renae Allen at Union County High School in Lake Butler and Professor Mike Lewis at Saint Louis University. Ms. Allen, you are an awesome science teacher! Thank you for igniting and supporting my passion in chemistry. Mike, I was very fortunate to have you as my organic chemistry professor and thank you for letting me join your research group when I was a novice.

Finally, I want to acknowledge my friends and family, especially my parents for their unconditional love and encouragement throughout my life. I cannot even count how many pep talks they gave me during graduate school and I always feel much better after talking to them. Of course, I need to give a big shout-out to my husband, Dr. Mianzhi Wang, for his understanding, support, and love. There are many benefits of marrying a mechanical engineer including spontaneous one-to-one lessons on “Rankine-Hugoniot” and “Shell Script”, which turned out to be very useful for my Ph.D. research. Mianzhi, thank you for always being by my side. You are my best friend and I love you!

Table of Contents

Chapter 1: Introduction	1
1.1 Motivation: An Overview of Shock Waves and Associated Injuries	1
1.2 Recent Advances in Energy-Dissipative Materials.....	2
1.3 Design Principles of Mechano-Active Materials for Shock Wave Energy Dissipation	4
1.4 Overview of the Dissertation	5
1.5 Notes and References.....	8
Chapter 2: Endothermic Volume Collapse Reactions via π-Bond Rearrangements	9
2.1 Abstract.....	9
2.2 Introduction.....	9
2.3 Synthesis and Reactivity of Anthracenyl-Substituted Arenediynes	11
2.4 Incorporating Arenediynes into Polymeric Materials.....	17
2.5 Development of Molecular and Polymeric Cyclophanes	19
2.6 Conclusions.....	21
2.7 Experimental Details.....	22
2.7.1 Materials and General Methods.....	22
2.7.2 Experimental Procedures	22
2.7.3 TGA Data of 1-3	50
2.7.4 Absorption and Emission Spectra of 4 in Chloroform.....	51
2.7.5 Computational Methods.....	52
2.8 Notes and References.....	53
Chapter 3: Development of Redox-Active Organic Materials for Force-Induced Volume Collapse	55
3.1 Abstract.....	55
3.2 Introduction.....	55
3.3 Development of Crystalline Charge-Transfer Complexes that Undergo a Pressure-Induced Neutral-to-Ionic Transition (PINIT)	56

3.4 Improved TTF Functionalization of Polymers for Two-Dimensional Charge-Transfer Network.....	59
3.4.1 Introduction.....	59
3.4.2 Incorporating TTF Motifs into Polymeric Materials.....	60
3.4.3 Characterization of Polymers Bearing TTF Motifs.....	63
3.4.4 Conclusions.....	66
3.5 PINIT in an Amorphous Organic Material Bearing TCAQ Motifs.....	67
3.5.1 Introduction.....	67
3.5.2 Synthesis and Characterization of PTCAQ and its Blends with Molecular TTF	69
3.5.3 PINIT in TTF-(pTCAQ) ₂	71
3.5.4 Conclusions.....	74
3.6 Experimental Details.....	74
3.6.1 Experimental Details for Section 3.3.....	74
3.6.2 Experimental Details for Section 3.4.....	78
3.6.3 Experimental Details for Section 3.5.....	97
3.7 Notes and References.....	112

Chapter 4: Ultrafast Proton Transfer in Polymer Blends Triggered by Shock Waves 115

4.1 Abstract.....	115
4.2 Introduction.....	115
4.3 Shock-Induced Polarity Increase Probed with Nile Red.....	116
4.4 Shock-Induced Proton Transfer in Poly(4-Vinylpyridine)-Based Blends.....	119
4.5 Conclusions.....	121
4.6 Experimental Details.....	122
4.6.1 Materials and Sample Preparation Details.....	122
4.6.2 Laser-Launched Flyer Plates Apparatus.....	123
4.6.3 Absorption and Emission Results of Nile Red Embedded in Different Polymeric Matrices.....	124
4.6.4 Infrared Spectra of PVP and its Blends with Various Proton Donors under Ambient Conditions.....	125

4.6.5 Differential Scanning Calorimetry Curves of PVP and its Blends with Various Proton Donors	126
4.6.6 Results of the Varying Flyer Plate Velocity Experiments	126
4.7 Notes and References.....	127

Chapter 5: Crystal Structure, Thermal Properties, and Shock-Wave-Induced

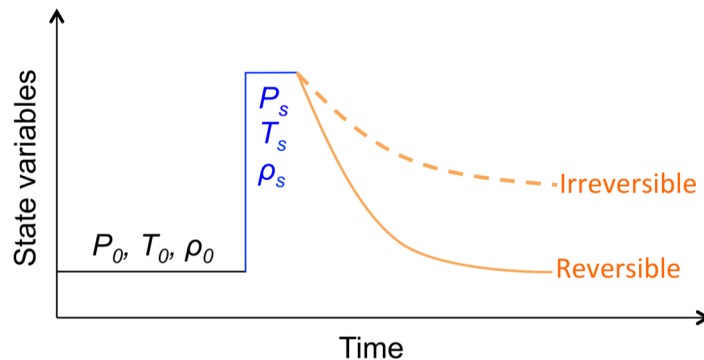
Nucleation of 1,2-Bis(phenylethynyl)benzene	129
5.1 Abstract.....	129
5.2 Introduction.....	129
5.3 Synthesis and Characterization of 1,2-Bis(Phenylethynyl)Benzene (PEB)	131
5.4 Shock-Induced Nucleation of Supercooled PEB	133
5.5 Scope and Generality of Shock-Induced Crystallization of Supercooled Liquids Bearing Phenyl Rings	135
5.6 Energy-Dissipative Properties of Supercooled Liquids Bearing Phenyl Rings.....	135
5.7 Conclusions.....	136
5.8 Experimental Details.....	137
5.8.1 General Experimental Details	137
5.8.2 Synthesis and Characterization of PEB	138
5.8.3 Speciment Preparation for Shock-Wave-Induced Nucleation	139
5.8.4 Experimental Procedures for Measreument of Shock Wave Pressure.....	140
5.8.5 Characterization of PEB Before and After Shock Wave Impact.....	142
5.8.6 Crystallization Experiments.....	142
5.8.7 Single Crystal X-Ray Diffraction Measurements	144
5.8.8 Other Properties of PEB, Salol, BP, DP, and PM.....	145
5.8.9 Theoretical Calculation of Tested Supercooled Liquids.....	146
5.9 Notes and References.....	147

Chapter 1: Introduction

1.1 Motivation: An Overview of Shock Waves and Associated Injuries

Generally caused by explosions and ballistic impacts, shock waves are high intensity stress waves that propagate through a medium at supersonic speeds.¹ Factors that heavily influence the magnitude and duration of a shock wave include the composition and amount of the explosives involved, the distance from the origin of the shock wave, and the surrounding environment. When a shock wave collides with a human target, a substantial amount of momentum and kinetic energy can be transferred inflicting physical, psychological, and cognitive injuries.²⁻³ Additionally, the passage of a shock wave often leads to near-discontinuous changes in material state variables such as density, temperature, and pressure (Scheme 1.1),⁴ which are detrimental for personnel, machinery, and infrastructure.

Scheme 1.1 A schematic depiction of shock-induced changes in material state variables. The black curve represents the conditions (P_0 , T_0 , and ρ_0) before a shock wave impact. During the shock wave impact, state variables, such as pressure, temperature, and density, rapidly increase (typically within $ps - \mu s$) to P_s , T_s , and ρ_s as illustrated by the blue curve. The orange curves represent the conditions after the shock wave impact as the state variables (partially) return to P_0 , T_0 , and ρ_0 . The kinetics of the relaxation process is material-dependent and shock-induced changes are frequently irreversible.



A RAND report published in 2008 estimated that ca. 20% of the deployed forces by the United States since 2001 suffer from blast-induced traumatic brain injury (TBI) even in the absence of detectable physical injury.⁵ In spite of the immense clinical and preclinical research on blast-induced injuries, current understanding of injury mechanisms, particularly for brain injuries, is limited. More importantly, the diagnostics and treatment of blast-induced brain injuries, such as TBI, remain controversial and relatively ineffective. Therefore, there exists an

urgent need for the development of novel energy-dissipative materials that could protect personnel, machinery, and infrastructure from explosions and ballistic impacts. This chapter provides an overview of recently developed energy-dissipative materials in the literature (section 1.2) as well as our efforts toward designing mechano-active materials as molecular sponges to effectively dissipate shock wave energy utilizing both chemical and physical approaches (section 1.3 & 1.4).

1.2 Recent Advances in Energy-Dissipative Materials

Protective gear (e.g. helmets and body armors) with proper mechanical strength and energy-dissipative properties is required to shield personnel and machinery from explosions and ballistic impacts. Figure 1.1 shows a basic summary of U.S. helmet designs and materials since World War I (WWI).⁶ With the invention of Kevlar® aramid fiber by DuPont in 1965,⁶ many polymer-based protective gears have been developed to reduce the risks associated with explosions and ballistic impacts. Compared to conventional steel, which was widely used during WWI and WWII, polymers have many advantages including tunable strength, toughness, elasticity, and processability, as well as being cost effective and lightweight. All of these features are ideal for fabricating protective gear.⁶⁻⁷

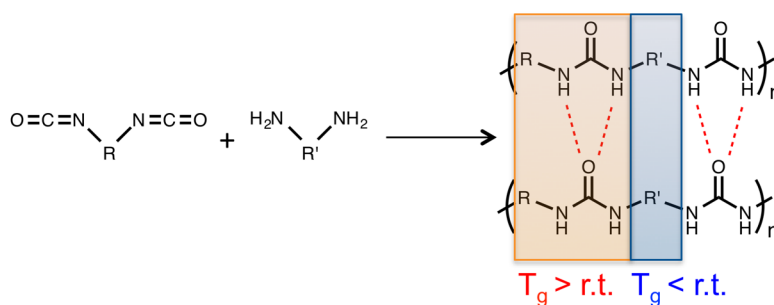


Figure 1.1 Historical perspective of U.S. Army helmet design and materials. PVB represents polyvinyl butyral. PASGT = Personal Armor System for Ground Troops. ACH = Advanced Combat Helmet. ECH = Enhanced Combat Helmet. Reproduced with permission from ref. 6. Copyright 2013 Elsevier.

Polyurea, an elastomeric polymer formed by rapid condensation reactions between polyamines and diisocyanates (Scheme 1.2), has recently been demonstrated as the benchmark material for shock wave energy dissipation (SWED).⁸⁻¹² Amini and coworkers illustrated that

coating steel structures with a layer of polyurea significantly improves their survivability under shock wave impacts.¹² Additionally, the peak pressure and the amount of energy transferred from a shock wave were drastically reduced when a thin layer of polyurea was applied.¹³ These experimental results suggest that polyurea is effective at mitigating shock wave impacts. As illustrated in Scheme 1.2, several mechanisms have been proposed to explain the shock-mitigating capability of polyurea including i) the breakage of hydrogen bonds between the urea repeating units in the hard domains,¹⁴ ii) the shock-induced rubbery-to-glassy phase transition in the soft domains,¹⁵⁻¹⁷ and iii) the high-frequency resonance of the hard domains.¹⁸ However, additional experimental and theoretical studies with systematic variations are required to establish a consistent and definitive understanding of the mechanism responsible for the energy-dissipative properties of polyurea.

Scheme 1.2 Synthesis of polyurea, an elastomer comprising both soft and hard domains, via condensation polymerization. The segment highlighted in orange represents the hard domain, which possesses a glass transition temperature (T_g) value above room temperature (r.t.). The R groups usually contain rigid aromatic motifs. The combination of the hydrogen bonds between the urea units (as shown by the dotted red lines) and the rigid and bulky R groups contributes to the high T_g value of the hard domain. The segment highlighted in blue represents the soft domain, which has a T_g value below room temperature. The R' groups are usually composed of flexible long alkyl or alkoxy chains, which leads to the low T_g value of the soft domains.



In addition to polyurea (a single-component system), multi-component systems such as polymer composites and shear thickening fluids (STFs) have been utilized for ballistic protection and shock wave mitigation.¹⁹⁻²³ STFs are non-Newtonian fluids, which are typically composed of condensed polymers, metals, or oxides suspended in a liquid. Tan and coworkers showed that both the peak pressure and the rate of pressure increase caused by a shock wave impact are drastically reduced after treating an aramid-based fabric, Twaron, with an STF (i.e. fumed silica

nanoparticles dispersed in liquid polyethylene glycol polymer).²¹ For both STFs and polymer composites, the shock-induced deformations and densifications have been proposed as the primary mechanism for energy dissipation.¹⁹⁻²²

1.3 Design Principles for Mechano-Active Materials Capable of Shock Wave Energy Dissipation

Despite the recently developed energy-dissipative materials mentioned in section 1.2, military personnel still frequently suffer from TBI along with other psychological and cognitive injuries when exposed to explosions and ballistic impacts. One thing to be noted is that materials equipped with potent ballistic-resistance do not always possess shock-mitigating capability. For example, when steel armor stops the bullet or shrapnel, the shock wave passing through the armor can still cause injuries. These types of injuries are problematic since they are not necessarily localized at the point of impact and also may result in chronic effects.

So, what are the key parameters to consider when designing materials for shock mitigation? To approach this question, we propose that as a target's volume collapses upon shock wave impacts, it will launch rarefaction waves in all directions with negative pressure, overtaking the shock front and alleviating shock pressure (Figure 1.2). Endothermic reactions are also ideal for shock mitigation because the energy released by an exothermic reaction, which generally occurs on the picosecond time scale,²⁴ may generate compression waves. Similar to the rarefaction waves, the compression waves can catch up with the shock front and amplify its pressure.

Based on the discussion above, volume collapse and endothermicity are the two design principles to follow when developing suitable materials for shock wave energy dissipation. Volume collapse is our primary focus, since it is the proposed energy-dissipative mechanism for polyurea, polymer composites, and STFs. In addition, simulation studies have demonstrated that enthalpy only plays a minor role for SWED when shock-induced volume collapse is feasible.²⁵

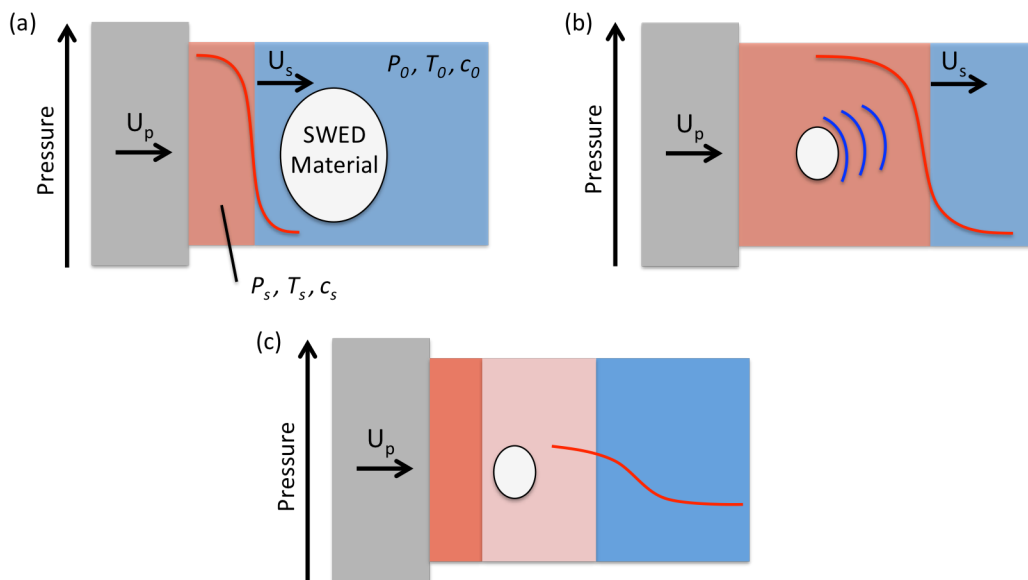
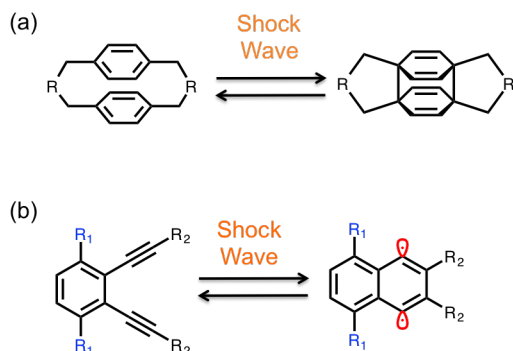


Figure 1.2 SWED by volume collapse. (a) A planar shock as shown in the red curve moving at U_s is created by pushing a medium with a plate moving at U_p . The shock speed $U_s \approx U_p + c_0$, where c_0 is the speed of sound in the unshocked material. (b) The volume of SWED material reduces behind the shock front, launching rarefaction waves as shown in the blue curves moving at ca. $U_p + c_s$, where c_s is the speed of sound behind shock front. (c) Since these rarefaction waves are faster than the shock wave ($U_p + c_s > U_p + c_0$), they overtake and attenuate the shock wave. Both the peak pressure and the rate of pressure increase caused by a shock wave are reduced.

1.4 Overview of the Dissertation

Volume collapse implies a change in density, which occurs in two essentially separable parts: the change in intramolecular volume and the change in intermolecular volume. In the case of intramolecular volume collapse, a chemical reaction must be involved. As shown in Figure 1.3a & b, two strategies utilizing the rearrangements of covalent bonds have been developed to achieve both endothermicity and volume collapse. Compared to a strong hydrogen bond, which has a bond dissociation energy (BDE) of ca. 15 kcal/mol, a typical C=C π bond has a BDE of ca. 80 kcal/mol.²⁶ Since the breakage of hydrogen bonds between the urea repeating units has been proposed as one of the main energy-dissipative mechanisms for polyurea,¹⁴ we hypothesize that the breakage of covalent bonds absorb more shock energy than that of hydrogen bonds, leading to superior energy-dissipative performance.

Intramolecular volume collapse



Intermolecular volume collapse

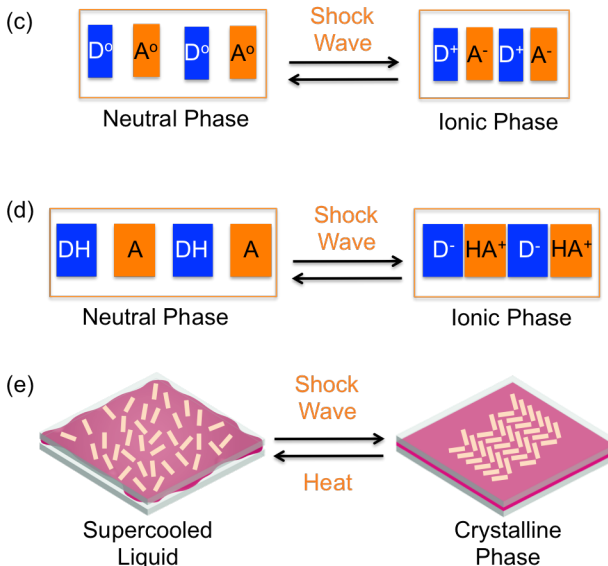


Figure 1.3 SWED via shock-induced intra- and intermolecular volume collapse. The intramolecular volume can be reduced when a chemical transformation occurs. Both (a) permanent and (b) transient π bond rearrangements have been proposed to achieve endothermic reactions with volume collapse. As to the intermolecular volume, it can be reduced via enhanced non-covalent interactions, i.e. ionic interactions, as (c) electrons or (d) protons transfer from the donors (D or DH) to the acceptors (A). (e) The transformation from an amorphous state to a crystalline state also yields reduced intermolecular volume, due to more efficient intermolecular packing.

The first approach involves the shock-induced cleavage of π bonds and subsequent formation of σ bonds (Figure 1.3a). Due to the increased proximity and lost aromaticity of the central ring motifs, the resulting structure would be physically denser and higher in energy than the starting cyclophane structure. In the second approach (Figure 1.3b), the metastable diradical intermediate in the Bergman cyclization also meets the desired qualities for SWED. In chapter 2, we explore the feasibility of intramolecular cyclization reactions of molecular and polymeric arenediynes and cyclophanes. Shock waves along with other external stimuli are utilized to induce the proposed endothermic volume collapse reactions. The steric and electronic effects of bulky and electron rich aryl substituents on the cyclization pathways of molecular arenediynes are also discussed. Although the proposed endothermic volume collapse reactions are feasible for cyclophanes and arenediynes, limitations of using such covalent bonds rearrangements for SWED include their relatively high activation energies and slow kinetics (i.e. the duration of a shock wave is not long enough to induce such transformations.)

Since a shock wave typically has a very brief transition time varying from ps to ms, ultrafast chemical and physical transitions with volume collapse are desired for SWED. Our investigation starts with organic materials that undergo pressure-induced neutral-to-ionic transitions (PINITs) via electron transfer reactions (chapter 3).²⁷ Compared to the cyclization reactions (Figure 1.3a & b), electron transfers occur much faster. Due to the closer packing between electron donors and acceptors via ionic interactions, intermolecular volume decreases after the electron transfers are induced by a shock wave (Figure 1.3c). In chapter 3, we discuss our efforts on developing crystalline and amorphous materials that undergo PINITs. We also address how to achieve larger volume reduction by replacing the planar redox-active motifs with saddle-shaped motifs in such materials. Similar to electron transfer, proton transfer can also reduce the intermolecular volume via ionic interactions (Figure 1.3d). In chapter 4, we utilize the emission of Nile Red, a polarity sensing dye with a fast response that can be used for shock sensing, to investigate shock-induced polarization and proton transfer in a series of solid-state polymer blends.

In addition to using chemical interactions to reduce intermolecular volume, we also investigate the feasibility of shock-induced crystallization of amorphous supercooled liquids, which is a physical approach to yield dense materials (Figure 1.3e). In chapter 5, we describe a metastable supercooled liquid (1,2-bis(phenylethynyl)benzene) that undergoes accelerated nucleation from its supercooled state when exposed to shock waves. Various analysis techniques are utilized to build an understanding of shock-induced nucleation and its role in energy dissipation.

In summary, this dissertation primarily focuses on the design, synthesis, and characterization of various materials that are potential candidates for SWED. Preliminary assessment of their energy dissipating properties by laser-induced shock wave experiments is also addressed, which potentially can be used to elucidate the energy-dissipative mechanisms of these materials.

1.5 Notes and References

1. Grujicic, M.; Yavari, R.; Snipes, J. S.; Ramaswami, S.; Runt, J.; Tarter, J.; Dillon, G., *J. Mater. Sci.* **2012**, *47*, 8197.
2. Nakagawa, A.; Manley, G. T.; Gean, A. D.; Ohtani, K.; Armonda, R.; Tsukamoto, A.; Yamamoto, H.; Takayama, K.; Tominaga, T., *J. Neurotrauma* **2011**, *28*, 1101.
3. Clemedson, C. J.; Hellstrom, G.; Lindgren, S., *Ann. N.Y. Acad. Sci.* **1968**, *152*, 187.
4. Greene, E. F., *J. Am. Chem. Soc.* **1954**, *76*, 2127.
5. Tanielian, T. L.; Jaycox, L. H., *Invisible Wounds of War: Psychological and Cognitive Injuries, Their Consequences, and Services to Assist Recovery*. RAND Corporation: Santa Monica, 2008.
6. Kulkarni, S. G.; Gao, X. L.; Horner, S. E.; Zheng, J. Q.; David, N. V., *Compos. Struct.* **2013**, *101*, 313.
7. Grujicic, A.; LaBerge, M.; Grujicic, M.; Pandurangan, B.; Runt, J.; Tarter, J.; Dillon, G., *J. Mater. Eng. Perform.* **2012**, *21*, 1562.
8. Grujicic, M.; Bell, W. C.; Pandurangan, B.; He, T., *Materials & Design* **2010**, *31*, 4050.
9. Arman, B.; Reddy, A. S.; Arya, G., *Macromolecules* **2012**, *45*, 3247.
10. Grujicic, M.; d'Entremont, B. P.; Pandurangan, B.; Runt, J.; Tarter, J.; Dillon, G., *J. Mater. Eng. Perform.* **2012**, *21*, 2024.
11. Grujicic, M.; Pandurangan, B., *J. Mater. Sci.* **2012**, *47*, 3876.
12. Amini, M. R.; Isaacs, J.; Nemat-Nasser, S., *Mech. Mater.* **2010**, *42*, 628.
13. Yang, K.; Lee, J.; Sottos, N. R.; Moore, J. S., *J. Am. Chem. Soc.* **2015**, *137*, 16000.
14. Grujicic, M.; Pandurangan, B.; Bell, W. C.; Cheeseman, B. A.; Yen, C. F.; Randow, C. L., *Mater. Sci. Eng. A* **2011**, *528*, 3799.
15. Bogoslovov, R. B.; Roland, C. M.; Gamache, R. M., *Appl. Phys. Lett.* **2007**, *90*.
16. Grujicic, M.; Snipes, J. S.; Ramaswami, S.; Yavari, R.; Runt, J.; Tarter, J.; Dillon, G., *J. Mater. Eng. Perform.* **2013**, *22*, 1964.
17. Grujicic, M.; Pandurangan, B.; He, T.; Cheeseman, B. A.; Yen, C. F.; Randow, C. L., *Mater. Sci. Eng. A* **2010**, *527*, 7741.
18. Qiao, J.; Amirkhizi, A. V.; Schaaf, K.; Nemat-Nasser, S.; Wu, G., *Mech. Mater.* **2011**, *43*, 598.
19. Di Landro, L.; Sala, G.; Olivieri, D., *Polym. Test.* **2002**, *21*, 217.
20. Morye, S. S.; Hine, P. J.; Duckett, R. A.; Carr, D. J.; Ward, I. M., *Compos. Sci. Technol.* **2000**, *60*, 2631.
21. Haris, A.; Lee, H. P.; Tay, T. E.; Tan, V. B. C., *Int. J. Impact Eng.* **2015**, *80*, 143.
22. Wagner, N. J.; Brady, J. F., *Physics Today* **2009**, *62*, 27.
23. Wang, Y.; Wang, F.; Yu, X.; Ma, Z.; Gao, J.; Kang, X., *Compos. Sci. Technol.* **2010**, *70*, 1669.
24. Seilmeier, A.; Kaiser, W., *Top. Appl. Phys.* **1988**, *60*, 279.
25. Antillon, E.; Strachan, A., *J. Chem. Phys.* **2015**, *142*.
26. Anslyn, E.; Dougherty, D. A., *Modern Physical Organic Chemistry*. University Science Books: Sausalito, CA, 2006.
27. Torrance, J. B.; Vazquez, J. E.; Mayerle, J. J.; Lee, V. Y., *Phys. Rev. Lett.* **1981**, *46*, 253.

Chapter 2: Endothermic Volume Collapse Reactions via π -Bond Rearrangements

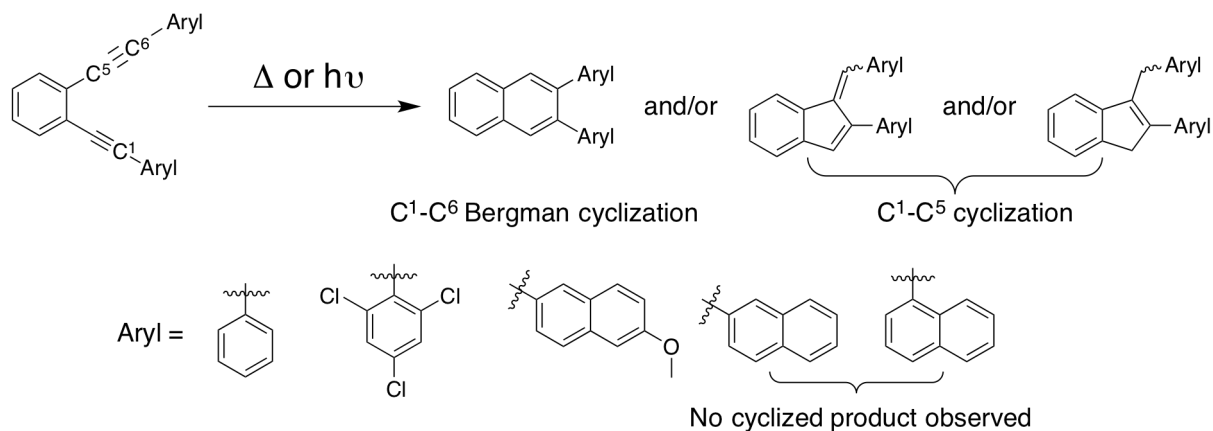
2.1 Abstract

Cyclization reaction pathways of aryl-substituted arenediynes depend on the interplay between the steric interactions and electronic properties of the aryl substituents. Herein, to probe the impact of bulky and electron rich aryl substituents on the cyclization of arenediynes, anthracenyl-substituted arenediynes with different *ortho* substituents were synthesized and their thermal, photo, radical, and shock-initiated cyclization reactions were studied. Since arenediynes that undergo cyclization via diradical intermediates are suitable for energy dissipation, we incorporated arenediyne motifs into polymeric materials to probe their shock-reactivity and energy-dissipative properties. Molecular and polymeric cyclophane derivatives were also developed as potential candidates for shock wave energy dissipation, due to their capability to undergo endothermic volume collapse reactions.

2.2 Introduction

Cyclization reactions of enediynes with aliphatic groups at the alkyne terminus are well studied compared to their aryl-substituted counterparts.³⁻⁶ As shown in Scheme 2.1, cyclization of aryl-substituted arenediynes yields a 6-membered ring (via C¹-C⁶ Bergman cyclization) or 5-membered ring (via C¹-C⁵ cyclization). Thus, the reaction is a useful synthetic method to generate polycyclic aromatic hydrocarbons and fulvenes.^{1-2, 5, 7-15} Polycyclic aromatic hydrocarbons with extended π -conjugation exhibit useful optical and charge transport properties for applications in photovoltaics and organic transistors.^{13, 15-17} Moreover, the photophysical properties of polycyclic aromatic hydrocarbons containing 5-membered rings are unique when compared to analogous molecules with 6-membered rings.^{2, 5, 7-14, 16} It is, thus, of interest to develop a better understanding of the structure-property relationships of 5-membered ring containing polycyclic aromatic hydrocarbons.

Scheme 2.1 Previously reported products from cyclization reactions of aryl-substituted arenediynes.



Cyclization of aryl-substituted arenediynes that proceeds via the C¹-C⁵ cyclization (5-membered cyclic product) or Bergman cyclization (6-membered cyclic product) pathway can be modulated by the sterics and electronics of the aryl substituents. For example, phenyl-substituted arenediyne generates both Bergman and C¹-C⁵ cyclized products, whereas the bulky trichlorobenzene substituted arenediyne yields only C¹-C⁵ cyclized products upon thermal induced cyclization (Scheme 2.1).⁹ Electronic effects on the cyclization pathway are more apparent in the case of naphthalenyl-substituted arenediynes.² Photoreaction of electron rich naphthalenyl-substituted arenediyne (6-methoxy naphthalen-2-yl derivative) yields a Bergman cyclized product whereas the bare naphthalenyl-substituted arenediynes (naphthalen-1-yl and naphthalen-2-yl) do not generate the expected cyclized products.² Photoreaction of dianthracene-*homo*-enediyne, in which only one of the anthracenylacetylene is in π -conjugation with the aryl moiety, generates a cyclized product with the benzene solvent used in the reaction.¹⁸

In this work, to further probe the interplay between steric and electronic effects of the aryl substituents on arenediyne cyclization reactions, 9-anthracenylethynyl arenediynes **1-3** in which both the anthracenylacetylenes are in π -conjugation with the aryl moiety are synthesized (Figure 2.1). Their thermal, photo, radical, and shock-initiated cyclization reactions are studied. We expect the cyclization of compounds **1-3** to proceed via C¹-C⁵ cyclization pathway given that anthracene is more sterically demanding than naphthalene. In addition, anthracene is also electron rich compared to naphthalene due to the extended π -conjugation. In arenediynes, it is known that the *ortho* substituents on the phenyl ring impact the kinetics of the cyclization

reaction.¹⁹⁻²⁰ Thus, we have varied the size of the *ortho* substituents (-H, -CH₃, and -TMS) on the phenyl ring and studied its impact on the conformation of anthracenyl groups and the cyclization reaction.

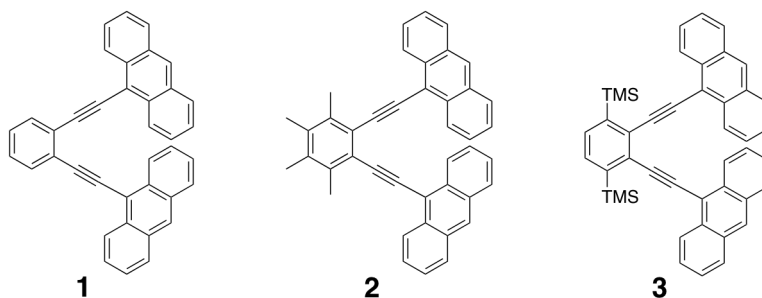
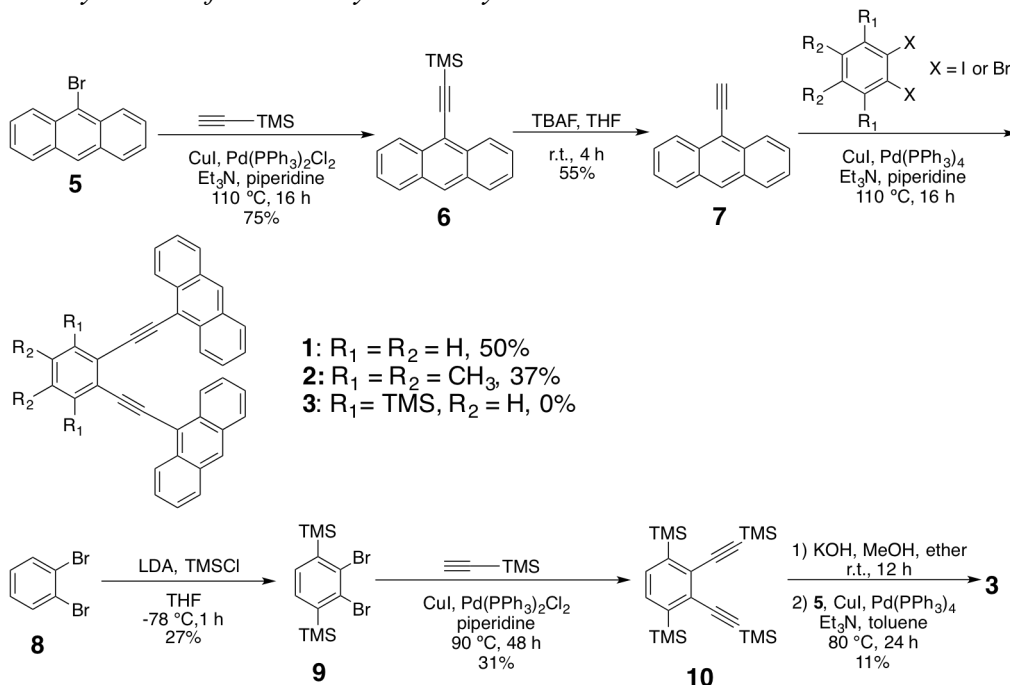


Figure 2.1 Chemical structures of anthracenyl-substituted arenediynes synthesized and studied in this work.

2.3 Synthesis and Reactivity of Anthracenyl-Substituted Arenediynes

9-anthracenylethynyl arenediynes **1-3**, possessing *ortho* substituents of increasing steric demand -H (**1**), -CH₃ (**2**), and -TMS (**3**) were synthesized (Scheme 2.2). Compounds **1** and **2** were prepared from 9-bromoanthracene (**5**). Sonogashira coupling of **5** with

Scheme 2.2 Synthesis of anthracenyl arenediynes **1-3**.



TMS acetylene followed by TMS deprotection yielded anthracenylacetylene (**7**). Sonogashira coupling of **7** with 1,2-diiodobenzene or 3,4,5,6-tetramethyl-1,2-diiodobenzene yielded **1** and **2**, respectively.² Unfortunately, in the case of **3**, Sonogashira coupling of **7** with (2,3-dibromo-1,4-phenylene)bis(trimethylsilane) afforded only the mono-substituted product due to the influence of the bulky -TMS groups. Thus, **3** was synthesized following an alternative route via Sonogashira coupling of 9-bromoanthracene with **10** ((2,3-diethynyl-1,4-phenylene)bis(trimethylsilane)).²¹ Compound **10** was prepared in three steps from dibromobenzene (**8**).

Cyclization reactions of arenediynes depend on the distance between the alkyne groups and the nature of the aryl substituents.³⁻⁶ To determine the distance between alkyne groups and the preferred intramolecular orientation of anthracenyl moieties, single crystals of molecules **1-3** were grown from slow evaporation of chloroform, tetrahydrofuran, and benzene, respectively (Figure 2.2). From the crystal structures, it is evident that the intramolecular distance between the alkynes and anthracene groups as well as their orientations with respect to each other change as the *ortho* substituents are varied. The distance between the C¹-C⁶ carbons in **1**, **2**, and **3** are 4.27, 4.02, and 4.18 Å, respectively, and the distance between C¹-C⁵ carbons in **1**, **2**, and **3** are 3.75, 3.52, and 3.61 Å, respectively. Furthermore, the anthracene moieties in **1** and **2** are interacting in an edge-to-face fashion whereas the anthracene moieties in **3** are interacting in face-to-face fashion.

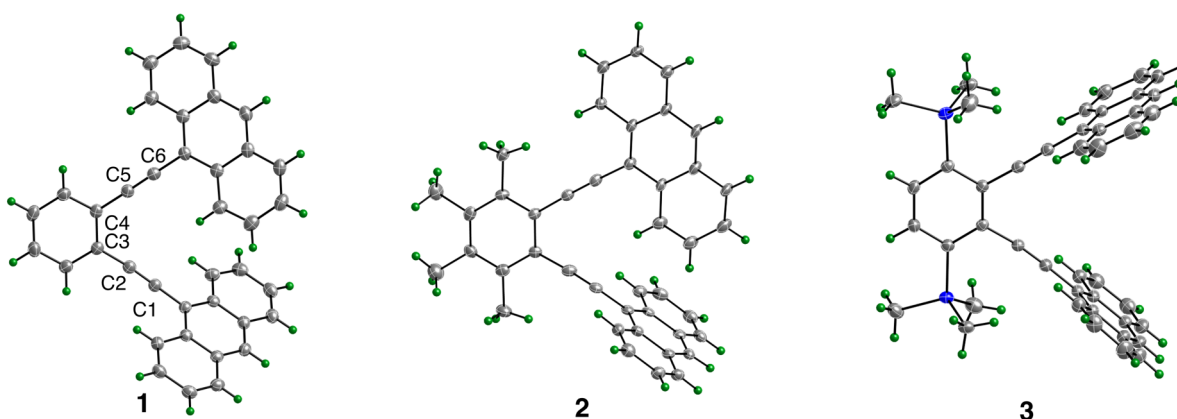


Figure 2.2 ORTEP view of crystal structures of **1-3**.

Absorption and fluorescence spectra were recorded to gain further insight into the intramolecular interaction between anthracene groups in molecules **1-3** (Figure 2.3). The absorption spectra of **1-3** are red shifted compared to phenyl and naphthalenyl-enediynes due to enhanced π -conjugation.² The absorption spectra of **1-3** are similar, except that the peaks in **1** and **2** are slightly broader than those for **3**. This could be because of the restricted rotational freedom of the anthracene moieties in **3** due to the bulky trimethyl silyl groups. The emission spectra of **1-3** (Figure 2.3) are also similar. The absorption and emission spectra of **1-3** indicate that there are no significant differences in the intramolecular interactions between the anthracene moieties in all three compounds.

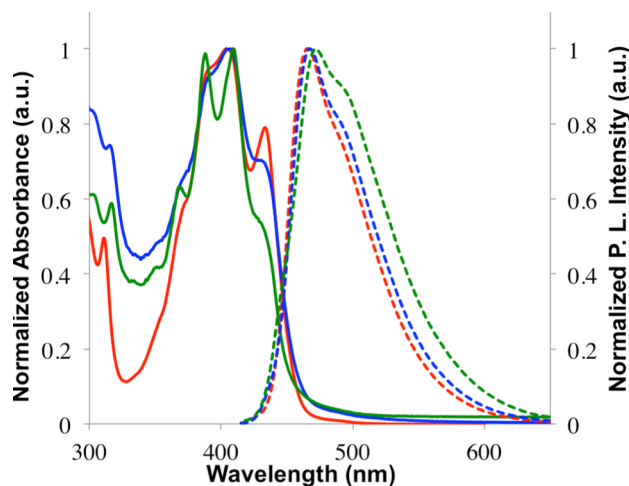


Figure 2.3 Normalized absorption (solid line) and emission (dotted line) spectra of **1** (red), **2** (blue), and **3** (green) in chloroform.

Bulky aryl groups are known to increase the activation energy for the cyclization reaction and favor C^1-C^5 cyclized products over Bergman cyclized products. In order to predict the preferred cyclization pathways in **1-3**, activation energies (ΔG^\ddagger) for the formation of both C^1-C^5 and Bergman cyclized products in **1-3** were calculated at the B3LYP/6-31G(d) level of theory (Table 2.1).¹⁶ The activation energy for both C^1-C^5 and Bergman cyclization decreases as the size of the *ortho* substituents increases in **1-3**. The decrease in intramolecular distance between the alkyne carbons in **1-3** as a result of the increased steric repulsion between the *ortho* substituents and the anthracenyl substituents could be the reason for the observed trend. Additionally, the activation energy for C^1-C^5 cyclization is *ca.* 5-7 kcal/mol lower than that for

the Bergman cyclization pathway, indicating that the bulky, electron-rich anthracenyl substituents direct the cyclization toward the C¹-C⁵ cyclization pathway as expected.

Table 2.1 Activation energies for cyclization reactions of **1-3**.^a

molecule	ΔG^\ddagger C ¹ -C ⁵ (kcal/mol) ^b	ΔG^\ddagger C ¹ -C ⁶ (kcal/mol) ^c	$\Delta\Delta G^\ddagger^{(5-6)}$ (kcal/mol) ^d
1	42.73	49.72	-6.99
2	41.70	48.84	-7.14
3	39.01	44.24	-5.23

^acalculations are performed using B3LYP/6-31G(d) level of theory; ^bactivation energy for 5-membered ring cyclization; ^cactivation energy for 6-membered ring cyclization; ^ddifference in activation energies for 5-membered and 6-membered cyclization.

Compounds **1-3** were subjected to thermal, photo, radical, and shock-induced cyclization reaction conditions. To determine the thermal reactivity, differential scanning calorimetry (DSC) of compounds **1-3** were recorded. It has been shown that the cyclization reaction in enediynes is associated with an exothermic peak in DSC.^{8, 22-25} Thermogravimetric analyses (TGA) (see section 4.7.3) and DSC (Figure 2.4) of **1-3** were recorded to determine the decomposition temperature and the onset temperature for the cyclization reaction. The decomposition temperatures of **1**, **2**, and **3** were found to be 384, 192, and 187 °C, respectively. The DSC of **1** shows both endothermic (maximum: 215 °C) and exothermic (maximum: 265 °C) peaks, while **2** and **3** do not show any peaks below their decomposition temperature. The endothermic peak at 215 °C matches with the experimentally determined melting point of **1**, while the exothermic peak at 265 °C might be associated with the cyclization reaction. The absence of exothermic

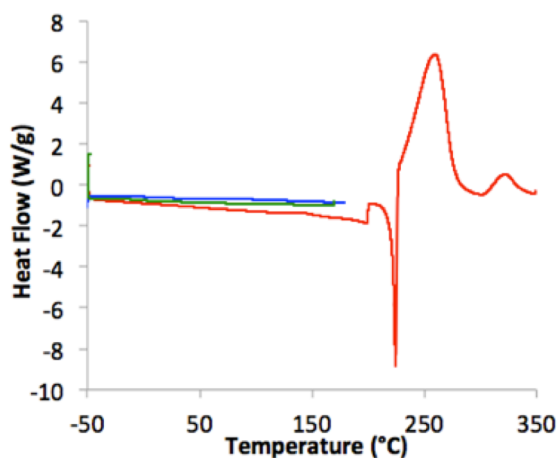


Figure 2.4 DSC curves of **1** (red), **2** (blue), and **3** (green) (heating rate: 10 °C/min).

peaks in **2** and **3** below their decomposition temperatures indicate that the cyclization reaction in these compounds is adversely affected by the geometrically constrained environment created by the bulky *ortho* (-CH₃ and -TMS in **2** and **3**) and/or anthracenyl substituents.

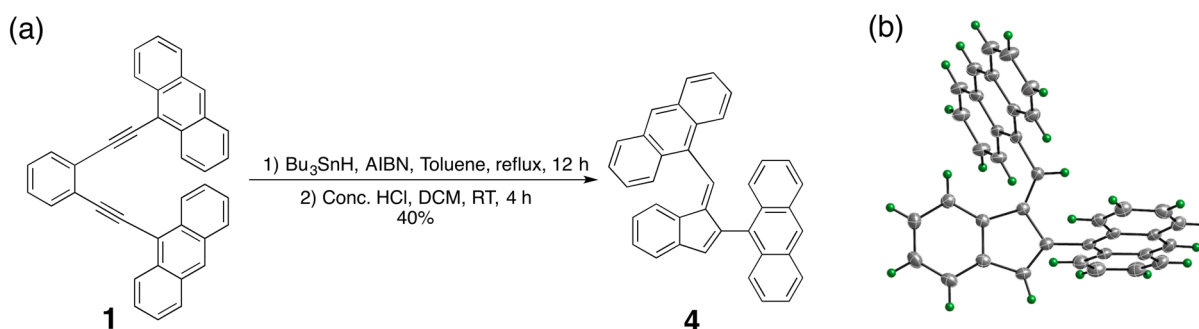
Since **1** showed an exothermic peak in DSC corresponding to a thermal induced reaction, a cyclization reaction of **1** was carried out in a sealed tube with 1,4-cyclohexadiene at 250 °C,¹⁹ the onset temperature determined from the DSC analysis. The thermal induced cyclization reaction of **1** resulted in a mixture of products. The ¹H NMR spectra of the isolated products were complex and could not be assigned to the expected cyclized product, thus making it difficult to deduce the actual chemical structures. Subsequent reactions that were carried out at lower temperature (200 °C) in toluene with proton sources such as 1,4-cyclohexadiene and phenol were also unsuccessful. Cyclization reactions of **2** and **3** in a mixture of toluene and 1,4-cyclohexadiene at 150 °C, which is below their respective decomposition temperatures, were unsuccessful. Although the calculated thermal activation energy barriers for cyclization of the phenyl (42.3 kcal/mol via C¹-C⁵ pathway) and anthracenyl-substituted arenediynes (42.7 kcal/mol via C¹-C⁵ pathway) are very close, only the phenyl derivative yielded the expected cyclized products.¹ A thermal induced cyclization reaction of the naphthalenyl-substituted arenediyne is not reported. Failure to observe the expected cyclized products in the case of anthracenyl-substituted arenediynes could be due to the underestimation of the steric effects imparted by the anthracenyl group in calculations.

After thermal conditions failed to initiate cyclization, compounds **1-3** were subjected to photoinitiated cyclization conditions. The reactions were performed in benzene as a solvent and 1,4-cyclohexadiene as a proton source over 24 h using a 150 W light source. All three samples yielded a mixture of products. ¹H NMR spectra of the isolated products were complex, making it difficult to deduce structural information for the products. Efforts to grow single crystals of the isolated products, as well as the use of different hydrogen sources (methanol and isopropanol) were also unsuccessful. We hypothesize that undesired intramolecular [4+4] cycloaddition (between the anthracenyl groups) and intermolecular [4+2] cycloaddition (between the anthracenyl and the alkyne groups), as well the intended cyclization reaction is responsible for the observed complex mixture of products.²⁶⁻²⁷ Failure to observe cyclized products in **1-3** under thermal and photo-mediated conditions compared to other aryl-substituted arenediynes (phenyl,

trichlorophenyl and naphthalenyl) is likely due to the increased steric demand of the anthracene groups. In the case of naphthalenyl arenediynes (naphthalen-1-yl, naphthalen-2-yl, and 6-methoxy naphthalen-2-yl), only the 6-methoxy naphthalen-2-yl derivative resulted in the expected Bergman cyclized product.² For arenediynes with simple aryl substituents of varying bulkiness (phenyl, naphthalen-1-yl, naphthalen-2-yl, and anthracen-9-yl), only the phenyl derivative yielded the expected cyclized product. Thus, the aryl substituents on the arenediynes play a key role in the photoreactivity of the arenediynes.

As attempts using thermal or photoreaction conditions to initiate the cyclization reaction were unsuccessful, compounds **1-3** were subjected to radical initiated cyclization reaction conditions. Radical initiated reactions of phenyl-substituted arenediynes are known to preferentially result in the formation of C¹-C⁵ cyclized products known as fulvenes.^{6, 10} Radical initiated cyclization of compounds **1-3** were performed by addition of tributyltin hydride/azobisisobutyronitrile (Bu₃SnH/AIBN) (Scheme 2.3). The reaction mixture was quenched with HCl after 12 h. Compound **1** with no *ortho* substituents yielded the expected fulvene product **4** with an isolated yield of 40% (Scheme 2.3). The molecular structure of **4** was confirmed by NMR spectroscopy, mass spectrometry, and single crystal X-ray diffraction. Radical initiated cyclization reactions of **2** and **3** gave a complex mixture of products, which could not be analyzed. In the cases of **2** and **3**, the bulky *ortho* substituents (-CH₃ and -TMS) might have prevented the tributyl tin radical from attacking the alkynyl carbon attached to phenyl. The *ortho* substituents on the phenyl ring seem to play a major role on the external radical initiated cyclization reaction pathway in anthracenyl-substituted arenediynes. Bulky anthracenyl substituents on the alkyne terminus seem to have less of an effect on the radical-mediated cyclization pathway, since **1** yielded the expected fulvene product with an external radical

Scheme 2.3 a) External radical initiated cyclization of **1**; b) ORTEP view of fulvene product.

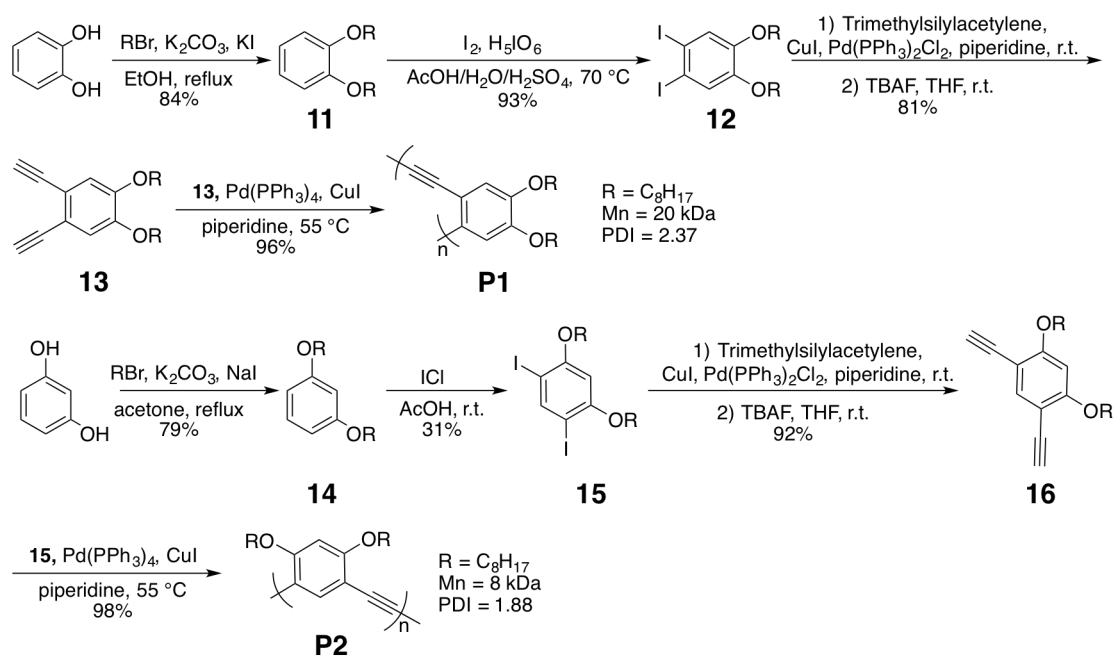


initiator but did not yield the expected cyclized products under thermal- or photo-mediated conditions. In their solid forms, compounds **1-3** were further subjected to shock waves. However, no chemical change was observed.

2.4 Incorporating Arenediynes into Polymeric Materials

To investigate shock-reactivity and SWED properties of materials bearing arenediyne motifs without the problem associated with loose packing of arenediyne small molecules, *ortho* poly(phenyl acetylene) (PPE), **P1**, was synthesized through Sonogashira coupling (Scheme 2.4). **P1** is expected to be active toward cyclization with the C≡C triple bond, whereas the control *meta* PPE, **P2**, is expected to be inactive. Upon heating under inert atmosphere, the triple bond in **P1** became reactive, while the triple bond signal in **P2** persisted as evidenced by the corresponding Raman spectra (Figure 2.5).

Scheme 2.4 Synthesis of polymer **P1** and **P2**.



SWED properties of **P1** and **P2** were investigated using a laser-induced stress wave.²⁸ Polyurea and **P1** showed comparable energy dissipation properties, which are more efficient at shock energy dissipation than **P2** (Table 2.2). However, the alkyne peak of **P1** was detected by

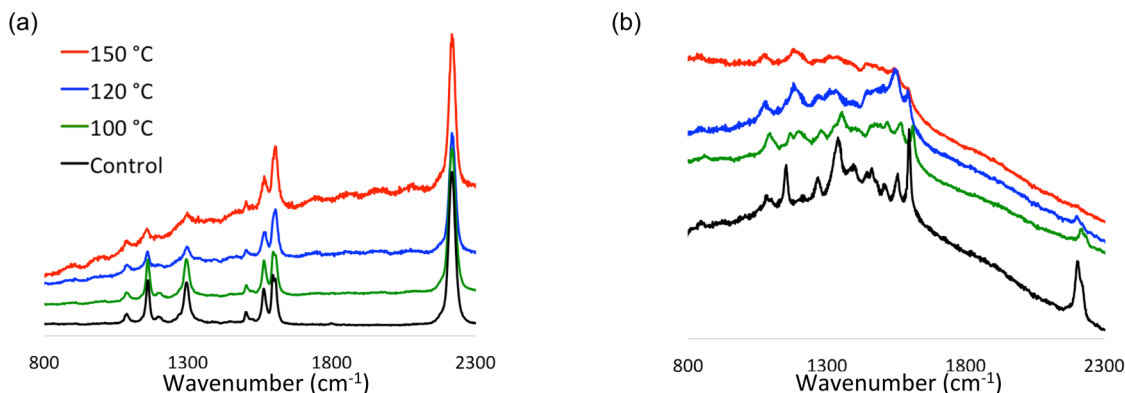


Figure 2.5 Raman spectra of (a) **P2** and (b) **P1** at different temperatures. The $C\equiv C$ stretching peak at ca. 2100 cm^{-1} of **P2** persists upon heating, indicating $C\equiv C$ bond remains inactive. In contrast, the peak at ca. 2100 cm^{-1} of **P1** disappears upon heating, which is strongly suggestive of chemical transformations.

Table 2.2 SWED properties of **P1** and **P2** with polyurea as a reference assessed by laser-induced stress wave.

Substrate	Fluence (kJ/m^2)
P1	0.90
P2	1.01
Polyurea	0.91
Glass (no substrate)	4.83

confocal Raman after treatment with the laser-induced stress wave and the ^1H NMR of the impacted **P1** was identical to the unshocked sample. These results suggest that cyclization cannot be induced at this level of stress wave. Optical micrographs of **P1** display clear differences between the film morphology before and after the direct stress wave tests, suggesting that a physical change may assist energy dissipation (Figure 2.6). Shock wave dissipation due to a morphology change is more likely to occur than our original hypothesis because a cyclization reaction with breakage of π bond and formation of σ bond may not be sufficiently facile at nanosecond timescale.

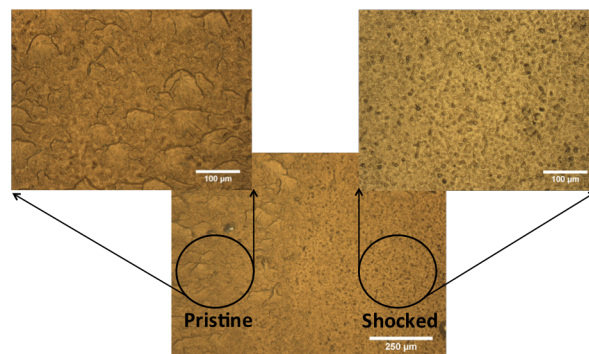


Figure 2.6 Comparison of optical microscope images between shocked and unshocked **P1**.

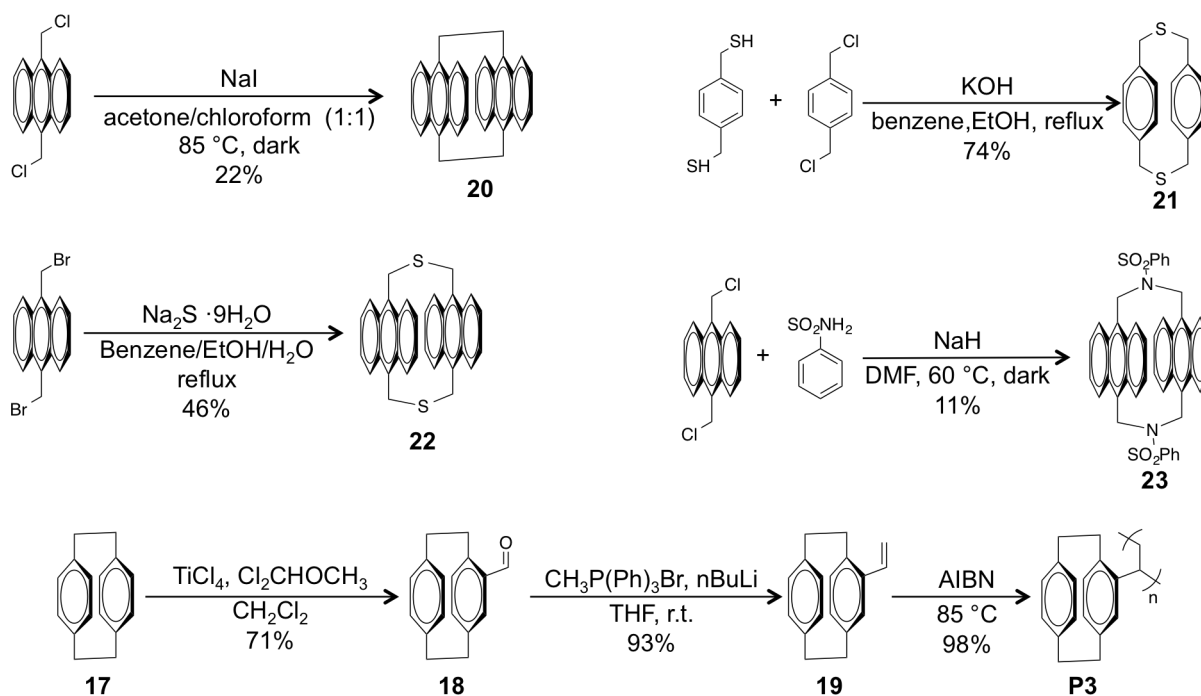
2.5 Development of Molecular and Polymeric Cyclophanes

Considerable experimental evidence has demonstrated the covalent dimerization of aromatic compounds occurring under shock conditions.²⁹⁻³⁰ Since these dimerization processes are endothermic, the aromatic compounds can potentially absorb energy generated by shock waves.³¹ We started our investigation with [2,2]paracyclophane (**17**), since the two aromatic rings connected with ethylene tethers may direct the compound toward dimerization reaction.³²⁻³³ In addition to **17**, we designed a series of cyclophanes (Scheme 2.5) to investigate how the aromaticity of the π -system, bridging linkers, and bridge strain affect the reactivity and energy absorption under shock wave impact. Based on density functional theory calculations at the B3LYP level with 6-31G(d) basis set (Table 2.5), endothermic cyclization reactions of various cyclophanes provide 7-10% intramolecular volume contraction.

The reaction of 9,10-di(chloromethyl)anthracene with sodium iodide in acetone yielded bi(anthracene-9,10-dimethylene), **20**. The synthesis of **21** involves nucleophilic substitution of benzylic dithiols, which thiolate in the presence of stoichiometric amounts of KOH in the reaction mixture, on benzylic dichlorides. **22** was obtained through the coupling reaction of 9,10-di(bromomethyl)anthracene with Na₂S in benzene-ethanol-water (44:9:1) solution. The reaction between 9,10-di(chloromethyl)anthracene and benzenesulfonamide with sodium hydride in DMF afforded **23**. The polymer analog of [2,2]paracyclophane, **P3**, was synthesized through free radical polymerization using azobisisobutyronitrile (AIBN) as the initiator at 85 °C.

Compared to cyclophanes **17** and **21** bearing phenyl rings, **20** and **22** are functionalized

Scheme 2.5 Synthesis of molecular and polymeric cyclophane derivatives.



with anthracene moieties, which exhibit a higher HOMO energy level and are more reactive than benzene. Since a C-N bond is much shorter than that a C-S bond, the distance between the two anthracene moieties of **23** is expected to be shorter than that of **22** leading to higher reactivity. Cyclization of **17**, which requires a higher activation energy than that of **21**, is expected to yield a 4-membered ring product with large strain.

Due to the poor processability of these crystalline materials, only cyclophanes **17** and **20** have been subjected to shock wave impacts generated by laser-launched Al flyer plates (Table 2.3).³⁴ At low-impact velocity, polyurea dissipated greater shock energy than **17** and **20**. As the impact velocity increased from 0.75 km/s to 1.6 km/s, cyclophane **17** dissipated more energy than polyurea. With an impact velocity of 1.6 km/s, the average fluence of **17** is ~ 10.8 kJ/m² less

Table 2.3 SWED properties of **17** and **20** with polyurea as a reference assessed by laser-launched 75 μ m thick Al flyer plates moving at different velocities.

Entry	Thickness (μ m)	Fluence (kJ/m ²)		
		0.75 km/s	1.3 km/s	1.6 km/s
Glass (input)	0	16.5 \pm 0.3	58.3 \pm 0.5	106.7 \pm 0.5
17	\sim 30	12.3 \pm 1.8	41.6 \pm 5.1	74.6 \pm 5.6
Polyurea	\sim 30	10.7 \pm 0.4	44.3 \pm 1.1	85.4 \pm 7.9
20	\sim 50	11.0 \pm 2.2	53.5 \pm 3.4	78.7 \pm 7.6

than that of polyurea. Since polyurea absorbs shock energy through hydrogen-bond disruption, the energy input at impact velocity above 1.3 km/s may exceed its energy dissipation threshold.³⁵ A direct comparison of energy dissipation performance between **17** and **20** cannot be made, since these samples have different thicknesses. Nevertheless, it is clear that **17** dissipates more energy than **20** as suggested by the SWED properties upon the shock wave impact moving at 1.6 km/s.

We hypothesized that cyclophanes absorb more shock energy than polyurea due to covalent dimerization. However, in attempts to characterize the products formed upon flyer impacts, we observed no significant optical changes (UV-Vis, IR, Raman, and fluorescence) in either cyclophane material. It is possible that the materials used for optical characterizations contain only a trace amount of dimerized product due to the high activation energy of dimerization. This outcome may also suggest that the applied shock pressure was insufficient to initiate chemical change. The dissipative properties of **17** can also be a result of a phase transition, which has been observed under a load of 3.9 GPa by a diamond anvil cell.³⁶ Another potential cause for the dissipative properties of **17** is the relatively loose packing of small molecules compared to that of polymers. In order to eliminate powder-packing problem, polymer **3** has been synthesized and will be subjected to shock wave impacts generated by flyer plates.

2.6 Conclusions

To summarize, 9-ethynylanthracenyl arenediynes with different *ortho* substituents were synthesized. Thermal, photo, radical, and shock-initiated cyclization reactions were investigated to elucidate the effects of the size of the *ortho* as well as the anthracenyl substituents on the cyclization reactions. Optical absorption spectra of **1-3** are red shifted compared to phenyl and naphthalenyl-substituted enediynes due to enhanced π -conjugation. Even though the simulated activation energies for 5-membered cyclization reactions of **1-3** are close to the other reported arenediynes, no cyclization products are observed in **1-3** upon thermal, photo-, and shock-initiation. This could be due to the underestimation of the steric effects imparted by the anthracenyl group in simulations. External radical activated reaction of **1** resulted in the corresponding fulvene product (**4**) whereas the cyclization reactions of **2** and **3** were not successful due to the bulky *ortho* substituents. In the case of external radical initiated reactions, *ortho* substituents played a major role compared to the aryl substituent at the alkyne terminus.

Although **P1** showed comparable energy dissipation properties as polyurea when subjected to the laser-induced stress waves, no chemical change was observed. Similar results were observed for a series of cyclophane derivatives that undergo intramolecular dimerization upon exposure to light. Based on these results, we conclude that the intramolecular densification and subsequent cyclization reaction require high activation energy and long reaction time leading to limited SWED utility.

2.7 Experimental Details

2.7.1 Materials and General Methods

Unless otherwise stated, all starting materials were obtained from commercial suppliers (Acros, Aldrich, TCI, and Strem) and used without purification. Flash column chromatography was conducted with silica gel 60 (230-400 mesh) from Silicycle.

Mass spectra were obtained through the SCS Mass Spectrometry Facility at University of Illinois at Urbana-Champaign (UIUC). ^1H and ^{13}C NMR spectra were obtained using either a Varian 400 or 500 MHz spectrometer in the VOICE NMR laboratory at UIUC. The residual solvent protons were used to reference the chemical shift. Coupling constants (J) are reported in Hertz (Hz), and splitting patterns are designated as s (singlet), d (doublet), t (triplet), q (quartet), and m (multiplet). UV-Vis spectra were recorded using a PerkinElmer Lambda 35 UV/Vis Spectrometer unless stated otherwise. Quartz cells with a path length of 1 cm or 2 mm from Starna Cells, Inc. were used. Fluorescence spectra were recorded using a Horiba FluoroMax-3. All samples were dissolved in chloroform unless stated otherwise. Crystal structures of **1-4** were obtained through the George L. Clark X-Ray Facility at UIUC by Dr. Danielle Gray. Thermogravimetric analysis (TGA) and differential scanning calorimetry (DSC) data were obtained using a TGA TA instruments Q50 and a DSC TA instruments Q20, respectively.

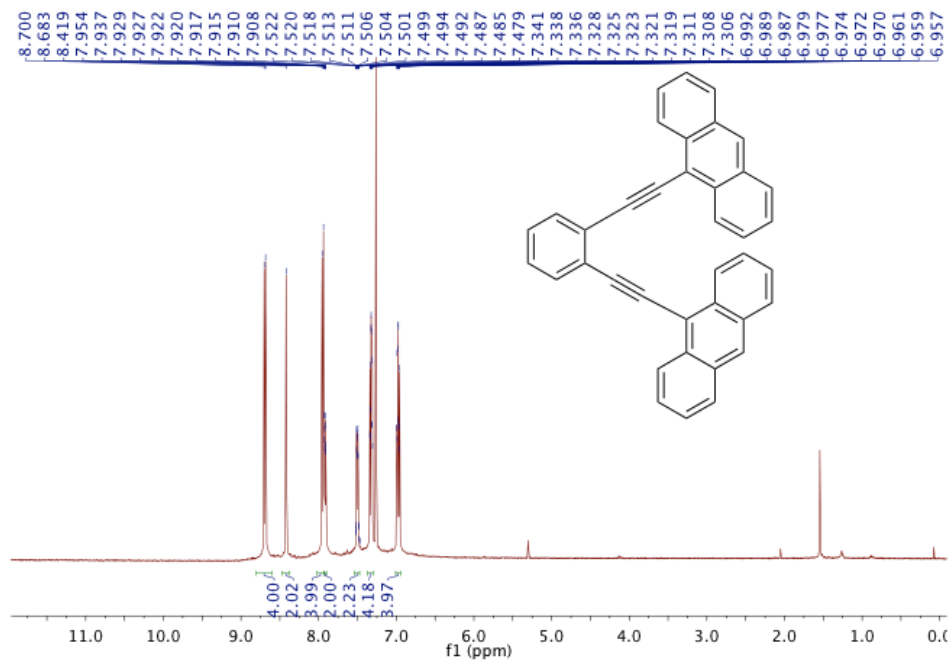
2.7.2 Experimental Procedures

Synthesis of 1,2-bis(anthracen-9-ylethynyl)benzene (1**)**

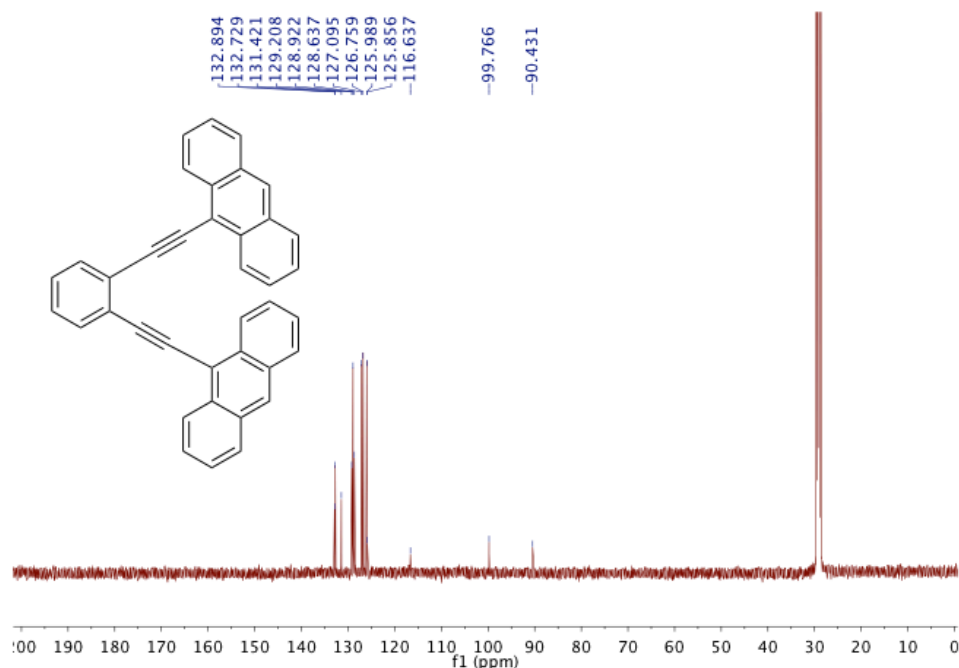
9-ethynylanthracene (0.213 g, 1.4 mmol), 1,2-diiodobenzene (0.200 g, 0.61 mmol), CuI (0.026 g, 0.14 mmol), and Pd(PPh₃)₄ (0.157 g, 0.14 mmol) were dissolved in deoxygenated piperidine (35

mL) under N₂. The solution was heated at 110 °C for 16 h. 40 mL of water was added and the aqueous layer was extracted with dichloromethane (4 x 50 mL). The combined organic phase was dried over MgSO₄. After filtration, the mixture was concentrated *in vacuo*. The purification of the residue by flash column (SiO₂, dichloromethane: hexanes = 1:9) afforded pure product as orange solid. Yield: 0.33 g (50%). Melting point: 216-220 °C. ¹H NMR (500 MHz, CDCl₃): δ 8.69 (d, *J* = 8.5 Hz, 4H), 8.42 (s, 2H), 7.95(d, *J* = 8.5 Hz, 4H), 7.93-7.90 (m, 2H), 7.53-7.48 (m, 2H), 7.36-7.30 (m, 4H), 7.00-6.94 (m, 4H); ¹³C NMR (125 MHz, (CD₃)₂CO): 132.89, 132.73, 131.42, 129.21, 128.92, 128.64, 127.09, 126.76, 125.99, 125.86, 116.64, 99.77, 90.43; HRMS (EI) calcd for C₃₈H₂₂ 478.17215, found 478.17270

¹H NMR of 1



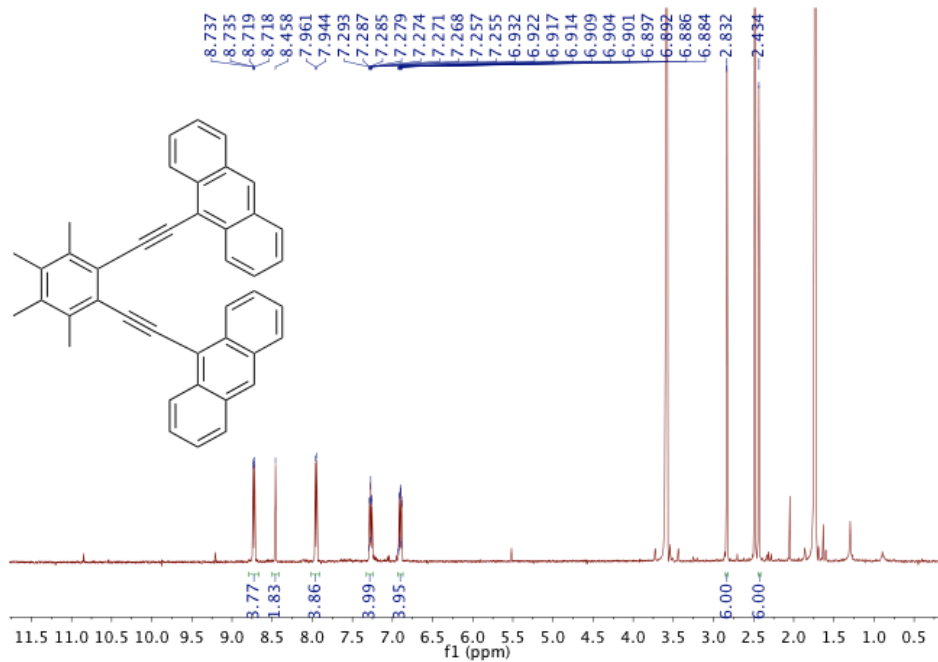
¹³C NMR of 1



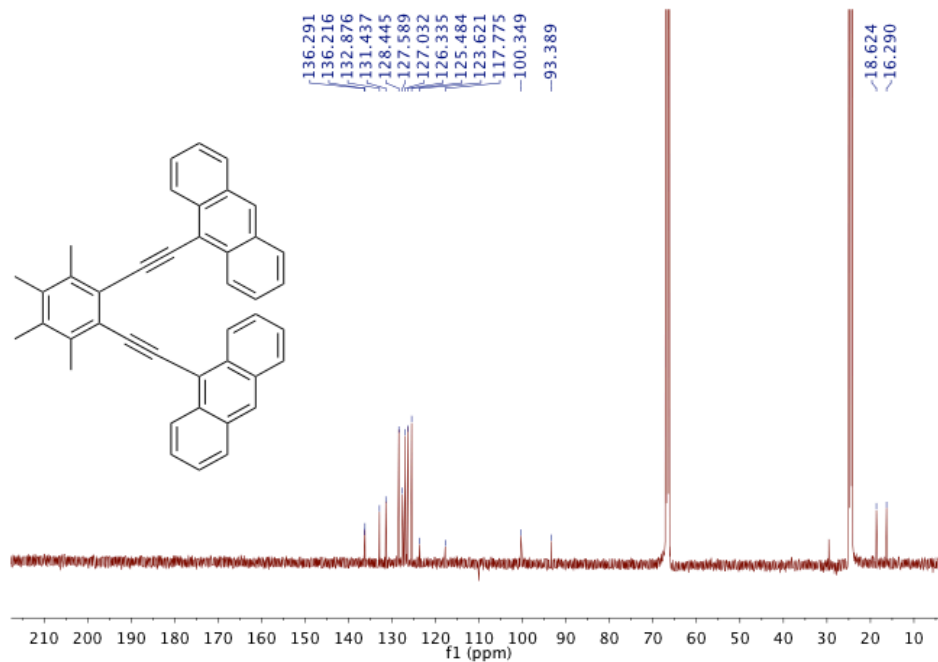
Synthesis of 9,9'-((3,4,5,6-tetramethyl-1,2-phenylene)bis(ethyne-2,1-diyl)dianthracene (2)

9-ethynylantracene (0.213 g, 1.4 mmol), 1,2-diiodo-3,4,5,6-tetramethylbenzene (0.236 g, 0.61 mmol), CuI (0.026 g, 0.14 mmol), and Pd(PPh₃)₄ (0.157 g, 0.14 mmol) were dissolved in deoxygenated piperidine (35 mL) under N₂. The solution was heated at 110 °C for 16 h. 40 mL of water was added and the aqueous layer was extracted with dichloromethane (4 x 50 mL). The combined organic phase was dried over MgSO₄. After filtration, the mixture was concentrated *in vacuo*. The purification of the residue by flash column (SiO₂, dichloromethane: hexanes = 1:9) afforded pure product as yellow solid. Yield: 0.28 g (37%). ¹H NMR (500 MHz, THF-d⁸): δ 8.73(dd, *J* = 9.5 Hz, 1 Hz, 4H), 8.45(s, 2H), 7.95(d, 8.5 Hz, 4H), 7.30-7.25 (m, 4H), 6.92-6.88 (m, 4H), 2.84(s, 6H), 2.45-2.41 (s, 6H); ¹³C NMR (125 MHz, THF-d⁸): δ 136.29, 136.22, 132.88, 131.44, 128.45, 127.59, 127.03, 126.34, 125.48, 123.62, 117.77, 100.35, 93.39, 18.62, 16.29; HRMS (EI) calcd for C₄₂H₃₀ 534.23475, found 534.23555.

¹H NMR of 2



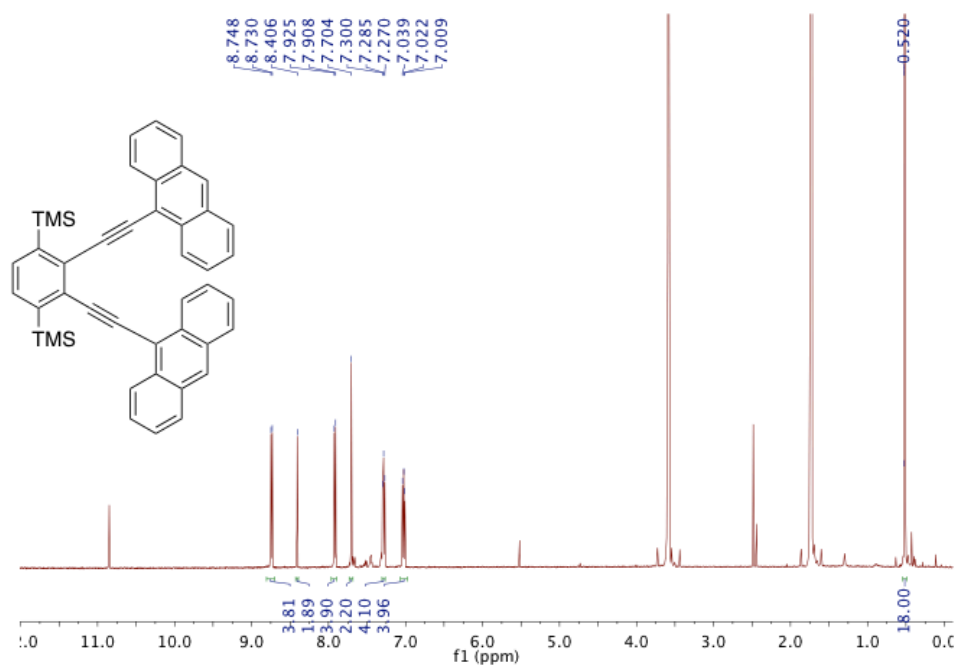
¹³C NMR of 2



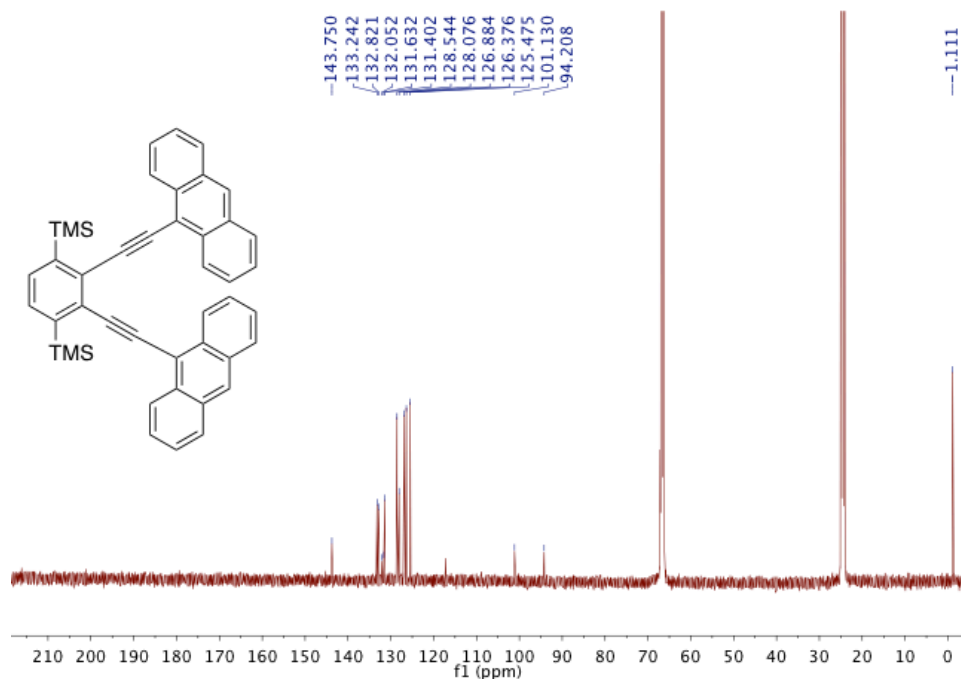
Synthesis of (2,3-bis(anthracen-9-ylethynyl)-1,4-phenylene)bis(trimethylsilane) (3)

9-bromoanthracene (0.8766 g, 3.4 mmol), (2,3-diethynyl-1,4-phenylene)bis(trimethylsilane) (0.4150 g, 1.53 mmol), CuI (0.0649 g, 0.34 mmol), and Pd(PPh₃)₄ (0.3939 g, 0.34 mmol) were dissolved in a deoxygenated liquid mixture of toluene (40 mL) and triethylamine (35 mL) under N₂. The solution was heated at 80 °C for 1 day. 100 mL of water was added and the aqueous layer was extracted with dichloromethane (4 X 100 mL). The combined organic phase was dried over MgSO₄. After filtration, the mixture was concentrated *in vacuo*. The purification of the residue by flash column (SiO₂, dichloromethane: hexanes = 5:95) afforded pure product as orange solid. Yield: 0.23 g (11%). ¹H NMR (500 MHz, THF-d⁸): δ 8.74 (d, *J* = 9 Hz, 4H), 8.36 (s, 2H), 7.92 (d, *J* = 8.5 Hz, 4H), 7.70 (s, 2H), 7.31-7.26 (m, 4H), 7.06-7.00 (m, 4H), 0.52 (s, 18H); ¹³C NMR (125 MHz, THF-d⁸): δ 143.75, 133.24, 132.82, 132.05, 131.63, 131.40, 128.54, 128.08, 126.88, 126.38, 125.47, 101.13, 94.21, -1.11; HRMS(EI) calcd for C₄₄H₃₈Si₂ 622.25121, found 622.25155.

¹H NMR of 3



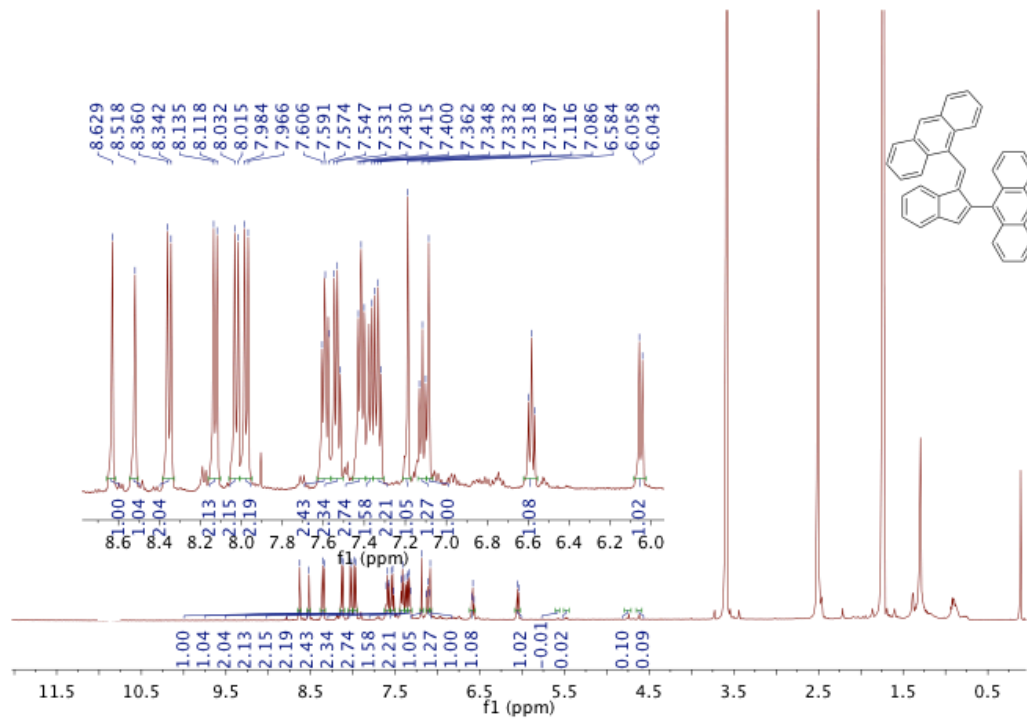
¹³C NMR of 3



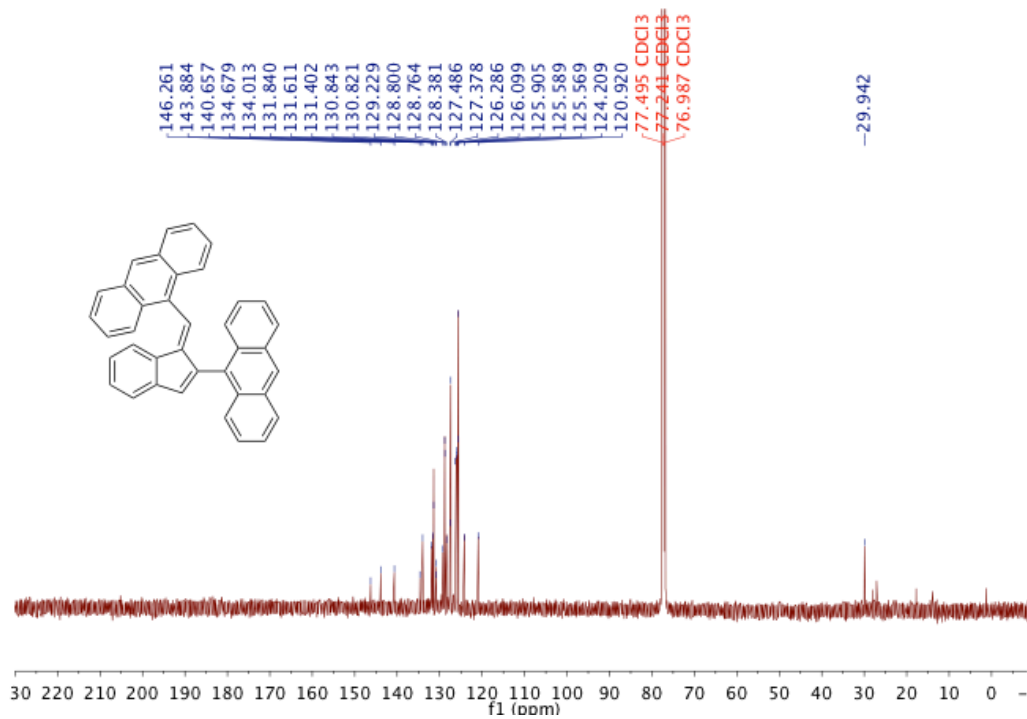
Synthesis of (*E*)-9-((2-(anthracen-9-yl)-1*H*-inden-1-ylidene)methyl)anthracene (4)

1,2-Bis(anthracen-9-ylethynyl)benzene (100 mg, 0.21 mmol) and Bu₃SnH (79 mg, 0.27 mmol) were dissolved in degassed anhydrous toluene (3.5 mL). AIBN (7.3 μL, 0.03 mmol) was mixed with another 3.5 mL of degassed toluene before adding the mixture dropwise. The reaction was refluxed overnight. To the reaction mixture, conc. HCl (1.0 mL) and CH₂Cl₂ (1.0 mL) were added and stirred for 4 hours at room temperature. 20 mL of water was added and the aqueous layer was extracted with dichloromethane (4 x 20 mL). The combined organic phase was dried over MgSO₄. After filtration, the mixture was concentrated *in vacuo*. The purification of the residue by flash column (SiO₂, dichloromethane: hexanes = 10:90) afforded product as orange solid. Yield: 40 mg (40%). ¹H NMR (500 MHz, THF-d⁸): δ 8.63 (s, 1H), 8.53(s, 1H), 8.35(d, *J* = 9 Hz, 2H), 8.13 (d, *J* = 8.5 Hz, 2H), 8.03 (d, *J* = 8.5 Hz, 2H), 7.98 (d, *J* = 8.5 Hz, 2H), 7.62-7.56 (m, 2H), 7.56-7.50 (m, 2H), 7.45-7.31 (m, 6H), 7.19 (s, 1H), 7.12 (t, *J* = 7.5 Hz, 1H), 7.09 (s, 1H), 6.59 (t, *J* = 7.5Hz, 1H), 6.05 (d, *J* = 7.5 Hz, 1H); ¹³C NMR (125 MHz, CDCl₃): δ 146.26, 143.88, 140.66, 134.68, 134.01, 131.84, 131.61, 131.40, 130.84, 130.82, 129.23, 128.80, 128.76, 128.38, 127.49, 127.38, 126.29, 126.10, 125.91, 125.59, 125.57, 124.21, 120.92.

¹H NMR of 4



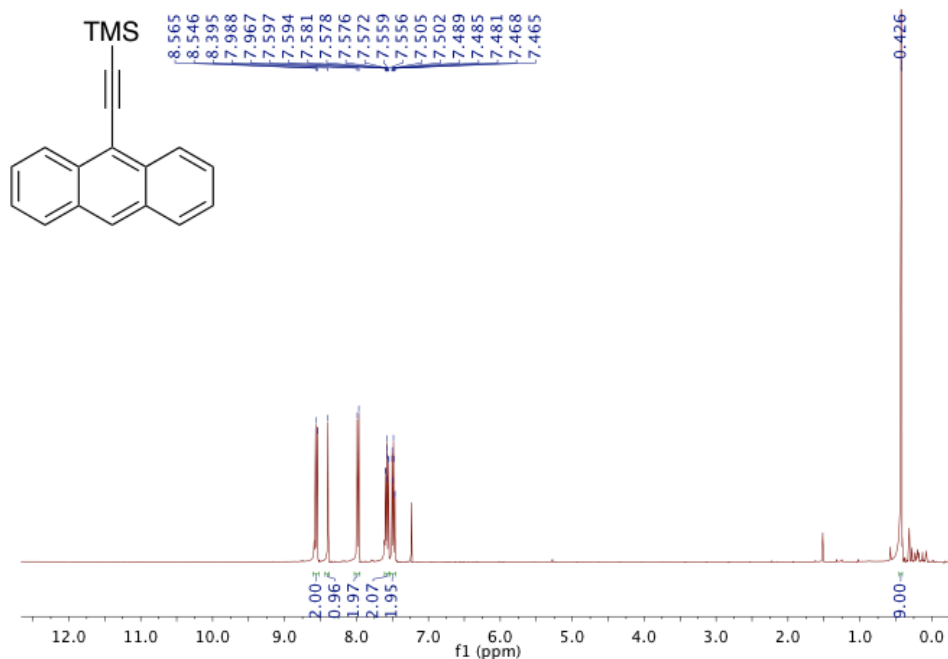
¹³C NMR of 4



Synthesis of (anthracen-9-ylethynyl)trimethylsilane (6)

9-Bromoanthracene (5.00 g, 19.45 mmol), CuI (0.3723 g, 1.94 mmol), and Pd(PPh₃)₂Cl₂ (1.3649 g, 1.94 mmol) were placed in a Schlenk flask under vacuum. A deoxygenated solution of triethylamine (100 mL) and piperidine (20 mL) was added before addition of ethynyltrimethylsilane (8.4 mL, 58.33 mmol). The solution was heated to 110 °C in the dark for 16 h and then concentrated *in vacuo*. 150 mL of water was added and the aqueous layer was extracted with chloroform (4 x 100 mL). The combined organic phase was dried over MgSO₄. After filtration, the mixture was concentrated *in vacuo*. The purification of the residue by flash column (SiO₂, hexanes) afforded pure product as yellow solid. Yield: 4.01 g (75%). ¹H NMR (400 MHz, CDCl₃): δ 8.55 (dq, *J* = 8.7 Hz, 1.0 Hz, 2H), 8.40(s, 1H), 8.03-7.97 (m, 2H), 7.62-7.57 (m, 2H), 7.55-7.48 (m, 2H), 0.43 (s, 9H).

¹H NMR of 6

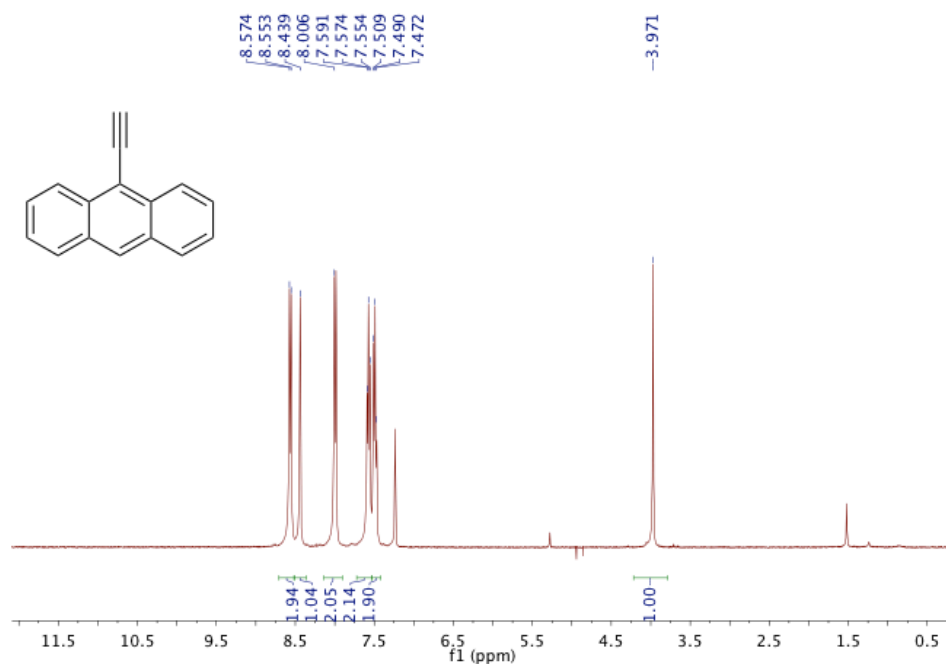


Synthesis of 9-ethynylanthracene (7)

(Anthracen-9-ylethynyl)trimethylsilane (4.0121 g, 14.62 mmol) was dissolved in THF (100 mL) and 1M TBAF in THF (29.24 mL, 29.24 mmol) was added. The mixture was stirred for 4 h and then concentrated *in vacuo*. 150 mL of water was added and the aqueous layer was extracted with dichloromethane (4 X 100 mL). The combined organic phase was dried over MgSO₄. After

filtration, the mixture was concentrated *in vacuo*. The purification of the residue by flash column (SiO₂, hexanes) afforded pure product as a dark red/brown solid. Yield: 1.60 g (54%). ¹H NMR (400 MHz, CDCl₃): δ 8.56 (d, *J* = 10.5 Hz, 2H), 8.44 (s, 1H), 8.00 (d, *J* = 10.5 Hz, 2H), 7.60 (t, *J* = 9.5 Hz, 2H), 7.50 (t, *J* = 9.5 Hz, 2H), 3.97 (s, 1H).

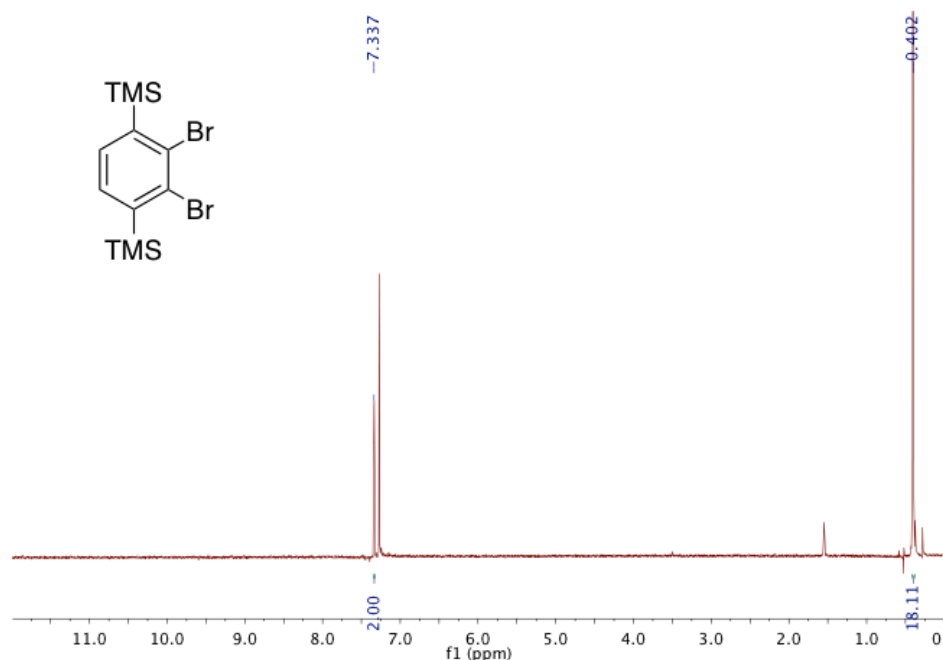
¹H NMR of 7



Synthesis of (2,3-dibromo-1,4-phenylene)bis(trimethylsilane) (9)²¹

1,2-Dibromobenzene (12 g, 58 mmol) was dissolved in THF (70 mL) under nitrogen. TMSCl (14 mL, 127.6 mmol) was added to the solution. The mixture was stirred for 5 minutes before cooling to -78 °C. 2M LDA in THF (55 mL, 110 mmol) was added to the solution dropwise and the mixture was left to stir for 1 h at -78 °C. The solution was hydrolyzed with 1.0 M sulfuric acid (10 mL) and extracted with ether. The organic layer was concentrated *in vacuo*. The crude product was purified by recrystallization with methanol:acetone = 1:1 (20 mL). Yield: 5.83 g (26.6%), white solid. ¹H NMR (500 MHz, CDCl₃): δ 7.33 (s, 2H), 0.40 (s, 18H).

¹H NMR of 9

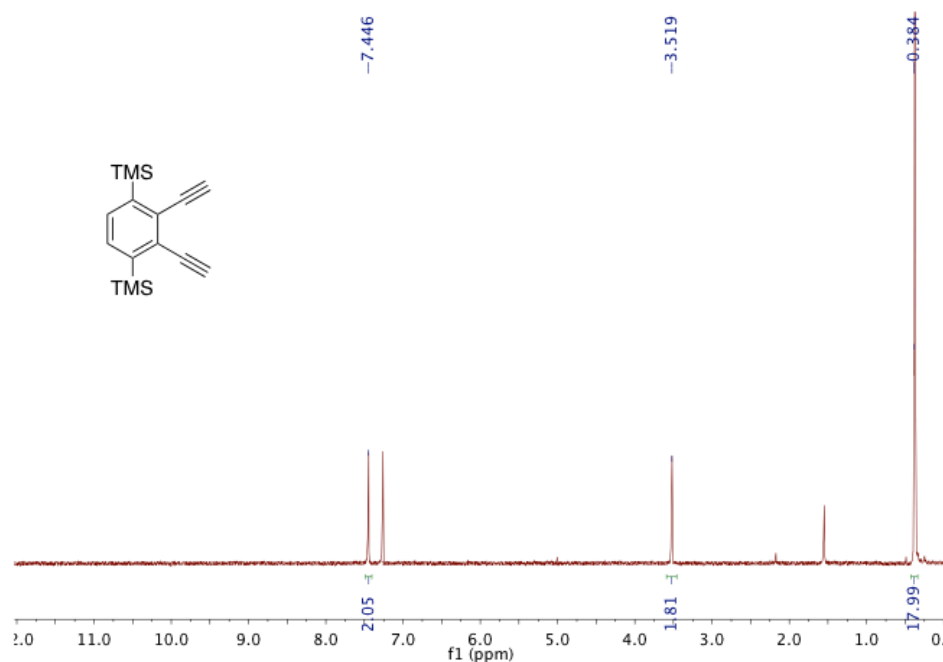


Synthesis of (2,3-diethynyl-1,4-phenylene)bis(trimethylsilane) (10)²¹

A mixture of (2,3-dibromo-1,4-phenylene)bis(trimethylsilane) (1.0100 g, 2.656 mmol), CuI (0.0090 g, 0.0473 mmol), and Pd(PPh₃)₂Cl₂ (0.7260 g, 0.682 mmol) was placed in a Schlenk flask under vacuum. A deoxygenated solution of piperidine (10 mL) was added before addition of ethynyltrimethylsilane (1.3 mL, 9.163 mmol). The solution was stirred at room temperature for 2h and then heated to 90 °C in the dark for 2 d. Hexanes was added to remove salts followed by filtration. The organic solution was concentrated *in vacuo*. The purification of the residue by flash column (SiO₂, hexanes) afforded pure (2,3-bis((trimethylsilyl)ethynyl)-1,4-phenylene)bis(trimethylsilane) as white solid. Yield: 0.34 g (31%). ¹H NMR (500 MHz, CDCl₃): δ 7.38 (s, 2H), 0.37 (s, 18H), 0.28 (s, 18H).

(2,3-bis((trimethylsilyl)ethynyl)-1,4-phenylene)bis(trimethylsilane) (0.5544 g, 1.3 mmol) and 1 pellet of KOH were dissolved in a mixture of MeOH (20 mL) and diethyl ether (25 mL). The solution was stirred overnight at room temperature. Dilute HCl was used to neutralize the solution and then the mixture was concentrated *in vacuo*. Extraction with dichloromethane and flash column (SiO₂, hexanes) were used to obtain 0.12 g (80%) of pure product: ¹H NMR (500 MHz, CDCl₃) δ 7.45 (s, 2H), 3.52 (s, 2H), 0.38 (s, 18H).

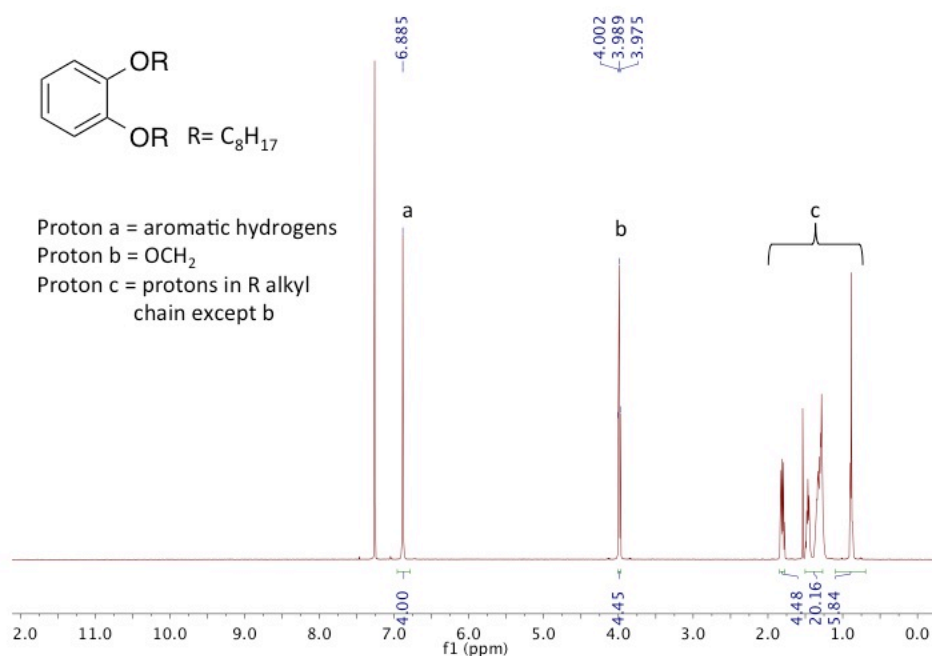
¹H NMR of 10



Synthesis of 1,2-bis(octyloxy)benzene (11)

Catechol (10.00 g, 90.8 mmol) was dissolved in EtOH (200 mL) before addition of K₂CO₃ (50.2 g, 363.3 mmol), KI (1.51 g, 9.08 mmol), and 1-bromooctane (39.2 mL, 227.0 mmol). The reaction was refluxed overnight under nitrogen. The solution was cooled to room temperature and dichloromethane (100 mL) was added. The salts were filtered and the organic solution was concentrated *in vacuo* before flash column (SiO₂, dichloromethane: hexanes/ 1:9) was used to obtain 25.5 g (84%) of pure product: ¹H NMR (500 MHz, CDCl₂) δ 6.92-6.86 (s, 4H), 4.01-3.97 (t, *J* = 6.6 Hz, 4H), 1.85-1.78 (m, 4H), 1.52-1.25 (m, 20H), 1.10-0.75 (t, *J* = 8 Hz, 6H).

^1H NMR of 11



Synthesis of 1,2-diiodo-4,5-bis(octyloxy)benzene (12)

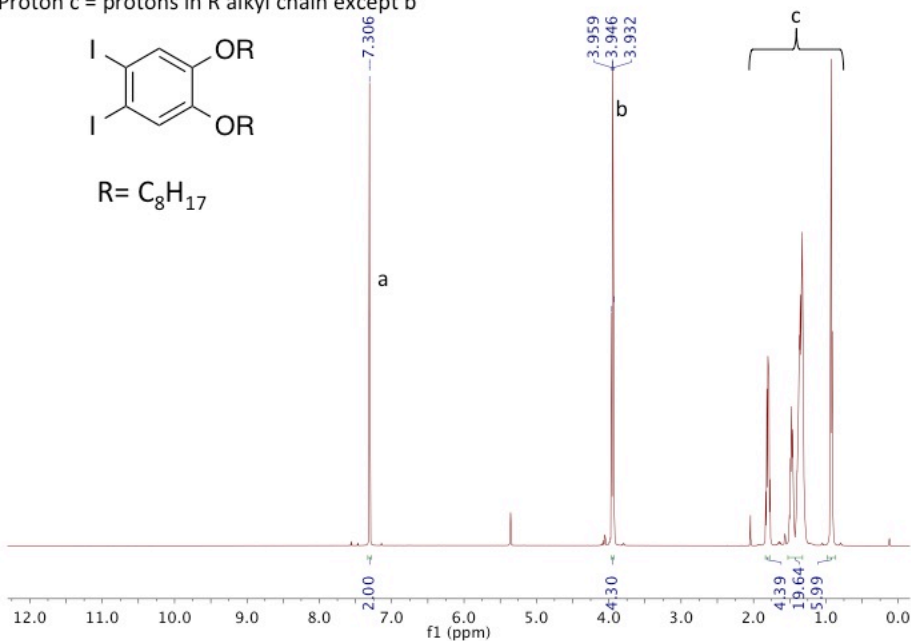
A mixture of 1,2-bis(octyloxy)benzene (10.00 g, 29.9 mmol), iodine (6.82 g, 26.9 mmol), and periodic acid (2.72 g, 11.9 mmol) was dissolved in liquid mixture of AcOH:H₂O:H₂SO₄/100:20:3 (120 mL). The solution was heated to 70 °C and left to react overnight. Na₂SO₃ aq. was added to the solution to remove I₂. The brown solids were filtered off, dissolved in chloroform, and washed with water and brine. The organic phase was dried over MgSO₄, and the solvent was evaporated under vacuum. Flash column (SiO₂, hexanes) was used to obtain 16.3 g (93%) of pure product: ^1H NMR (500 MHz, CDCl₃) δ 7.32-7.29 (s, 2H), 3.97-3.92 (t, J = 6.7 Hz, 4H), 1.84-1.76 (quintet, J = 7 Hz, 4H), 1.52-1.32 (m, 20H), 0.96-0.89 (t, J = 7 Hz, 6H); ^{13}C NMR (500 MHz, CD₂Cl₂) δ 150.06, 123.94, 95.97, 69.68, 32.06, 29.54, 29.50, 29.34, 26.16, 22.92, 14.15; LRMS (ESI) m/z 609.1 (M+Na).

^1H NMR of 12

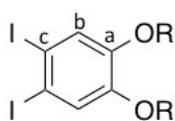
Proton a = aromatic hydrogens

Proton b = OCH_2

Proton c = protons in R alkyl chain except b



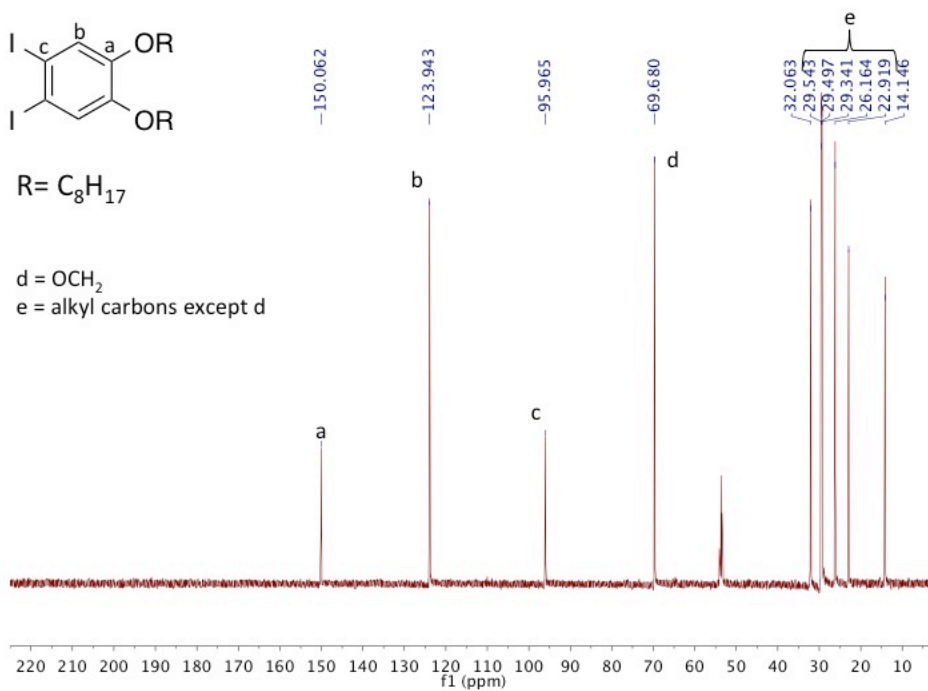
^{13}C NMR of 12



R = C_8H_{17}

d = OCH_2

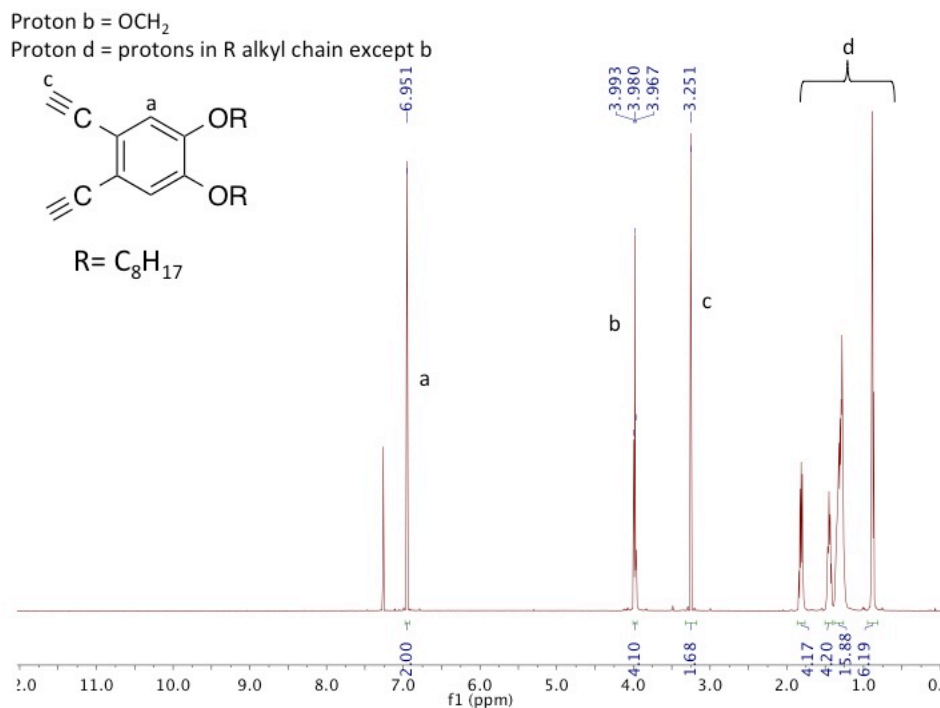
e = alkyl carbons except d



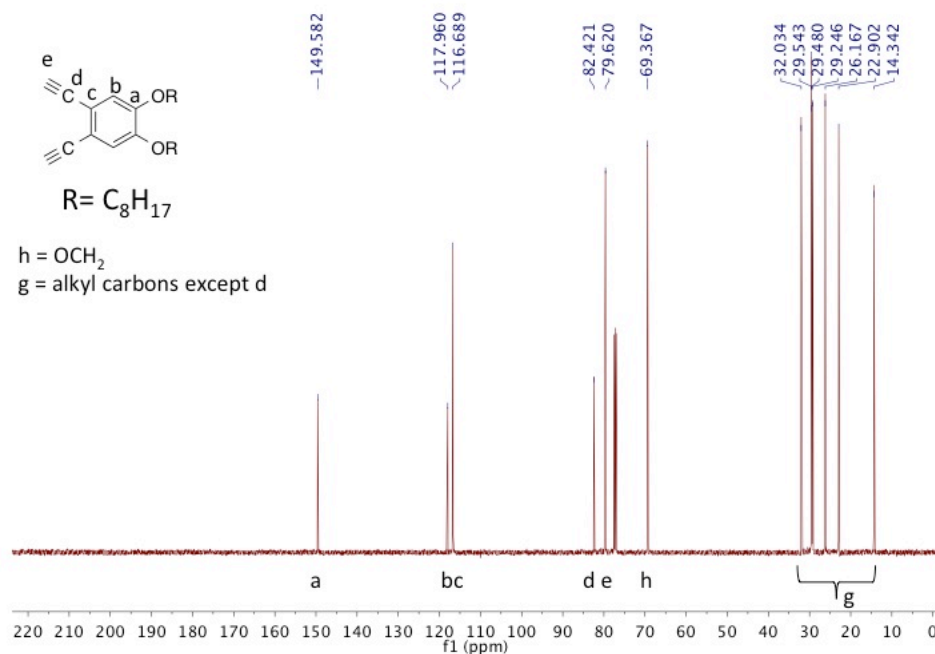
Synthesis of 1,2-diethynyl-4,5-bis(octyloxy)benzene (13)

A mixture of 1,2-diiodo-4,5-bis(octyloxy)benzene (6.97 g, 11.89 mmol), Pd(PPh₃)₂Cl₂ (0.8344 g, 1.19 mmol), and CuI (0.2264 g, 1.19 mmol) was dissolved in piperidine (54 mL) under N₂. Ethynyltrimethylsilane (4.18 mL, 29.7 mmol) was added dropwise to the solution. The mixture was left to react overnight at room temperature. The solvent was evaporated under vacuum and the solid was dissolved in THF and 1M TBAF in THF was added to deprotect the alkyne group. Extraction with dichloromethane and flash column (SiO₂, EtOAc: hexanes/ 5:95) were used to obtain 3.95 g (81%) of pure product: ¹H NMR (500 MHz, CDCl₃) δ 6.97-6.92 (s, 2H), 4.01-3.95 (t, *J* = 6.1 Hz, 4H), 3.32-3.20 (s, 2H), 1.87-1.76 (quintet, *J* = 6.9 Hz, 4H), 1.50-1.25 (m, 20H), 0.93-0.83 (t, 6H); ¹³C NMR (500 MHz, CDCl₃) δ 149.58, 117.96, 116.69, 82.42, 79.62, 69.37, 32.03, 29.54, 29.48, 29.25, 26.17, 22.90, 14.34; HRMS (EI) calcd for C₂₆H₃₈O₂ 382.28718, found 382.28764.

¹H NMR of 13



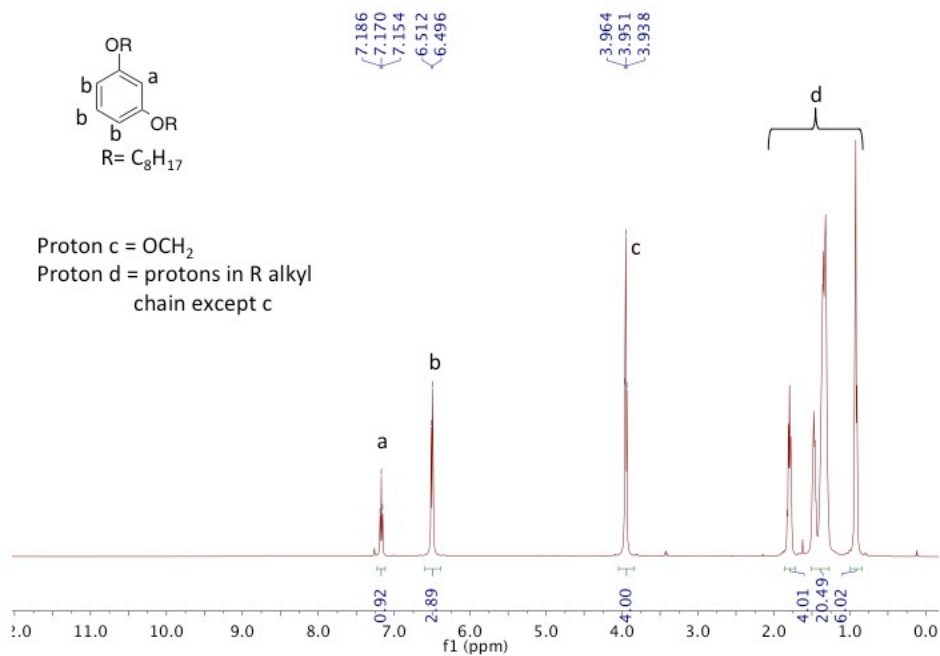
^{13}C NMR of 13



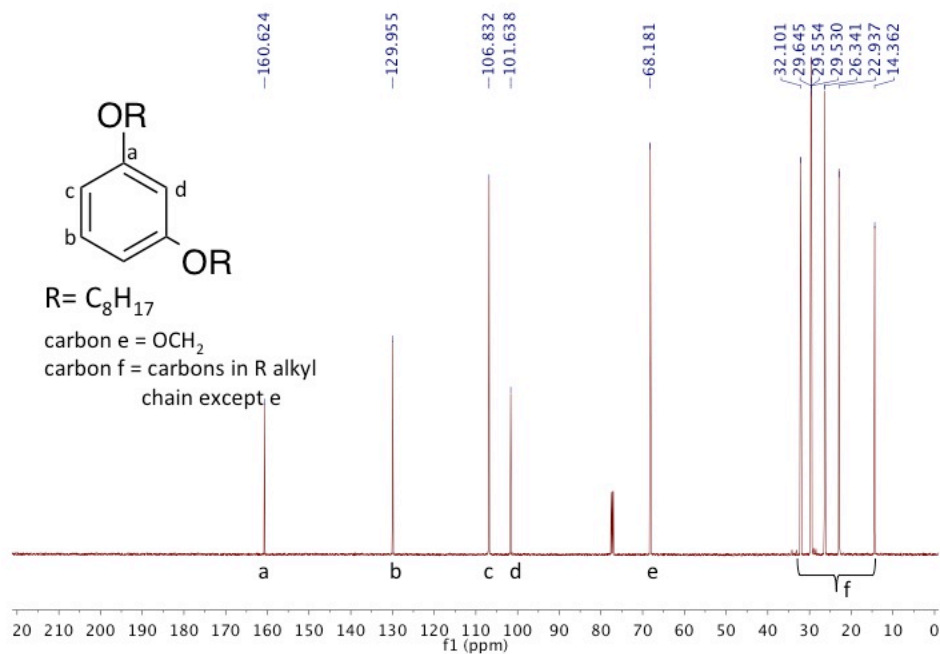
Synthesis of 1,3-bis(octyloxy)benzene (14)

Resorcinol (10.00 g, 90.8 mmol) was dissolved in acetone (90 mL) before addition of K_2CO_3 (50.2 g, 363.3 mmol), NaI (1.36 g, 9.08 mmol), and 1-bromooctane (39.2 mL, 227.0 mmol). The reaction was refluxed for 48 h under nitrogen. The solution was cooled to room temperature and dichloromethane (3 x 100 mL) was added to it. The salts were filtered and the organic solution was concentrated *in vacuo* before flash column (SiO_2 Et₂O: hexanes/ 5:95) was used to obtain 24.0 g (79%) of product: ^1H NMR (500 MHz, CDCl_3) δ 7.20-7.12 (d, $J = 8.1$ Hz, 1H), 6.56-6.44 (m, 3H), 4.01-3.91 (t, $J = 6.7$ Hz, 4H), 1.84-1.75 (quintet, $J = 7.5$ Hz, 4H), 1.52-1.28 (m, 20H), 0.98-0.85 (t, $J = 7.5$ Hz, 6H); ^{13}C NMR (500 MHz, CDCl_3) δ 160.62, 129.95, 106.83, 101.64, 68.18, 32.10, 29.65, 29.55, 29.53, 26.34, 22.94, 14.36.

¹H NMR of 14



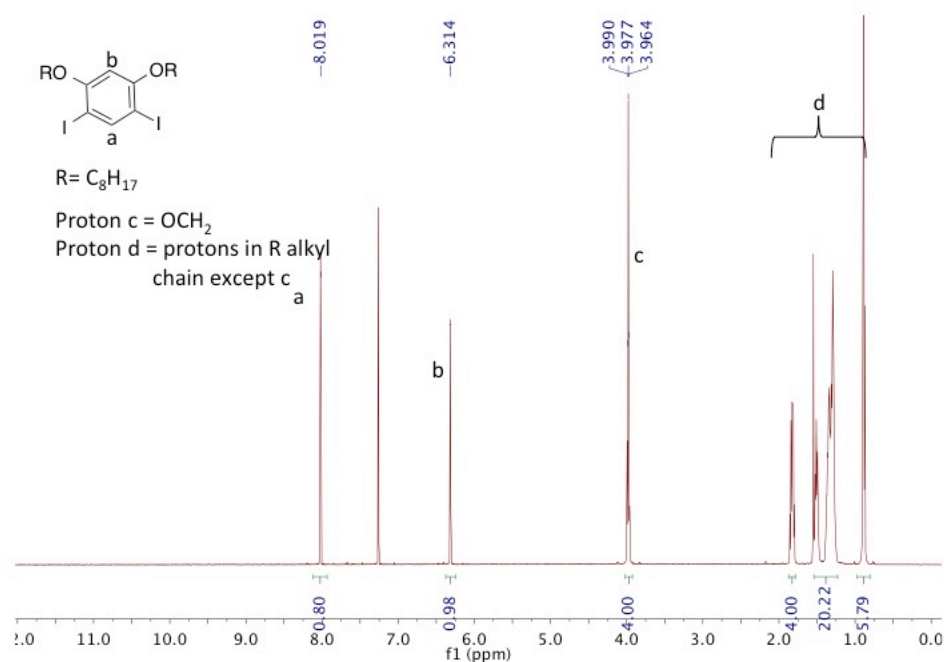
¹³C NMR of 14



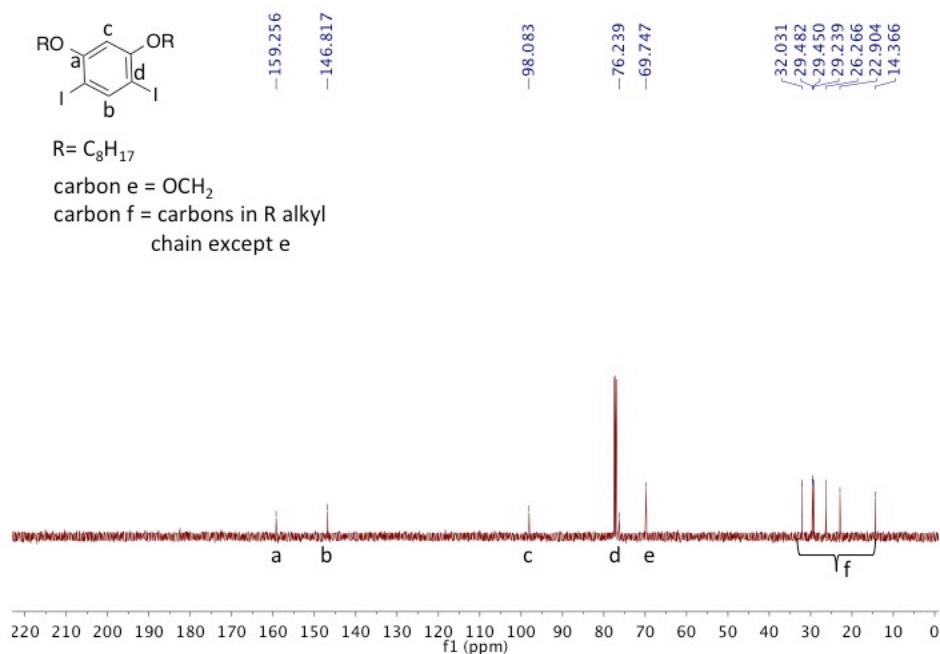
Synthesis of 1,5-diiodo-2,4-bis(octyloxy)benzene (15)

1,3-Bis(octyloxy)benzene (22.10 g, 66.1 mmol) was dissolved in AcOH (350 mL) before addition of ICl (7.0 mL, 139.5 mmol). The reaction was stirred at r.t. for 3 h. The reaction mixture was poured into water and extracted with chloroform. The combined organic layer was washed with Na₂S₂O₃, NaHCO₃, and dried over anhydrous MgSO₄. The organic solvents were removed *in vacuo* before purification with flash column (SiO₂, hexanes). The product was further purified by recrystallization with hexanes, which gives 12 g (31%) of pure product as a white solid: ¹H NMR (500 MHz, CDCl₃) δ 8.03-8.00 (s, 1H), 6.35-6.29 (s, 1H), 4.02-3.93 (t, *J* = 6.3 Hz, 4H), 1.87-1.78 (quintet, *J* = 6.3 Hz, 4H), 1.54-1.22 (m, 20H), 0.92-0.85 (t, *J* = 7.0 Hz, 6H); ¹³C NMR (500 MHz, CDCl₃) δ 159.26, 146.82, 98.09, 76.24, 69.75, 32.03, 29.48, 29.45, 29.24, 26.27, 22.90, 14.37; HRMS (EI) calcd for C₂₂H₃₆O₂I₂ 586.08053, found 586.08101.

¹H NMR of 15



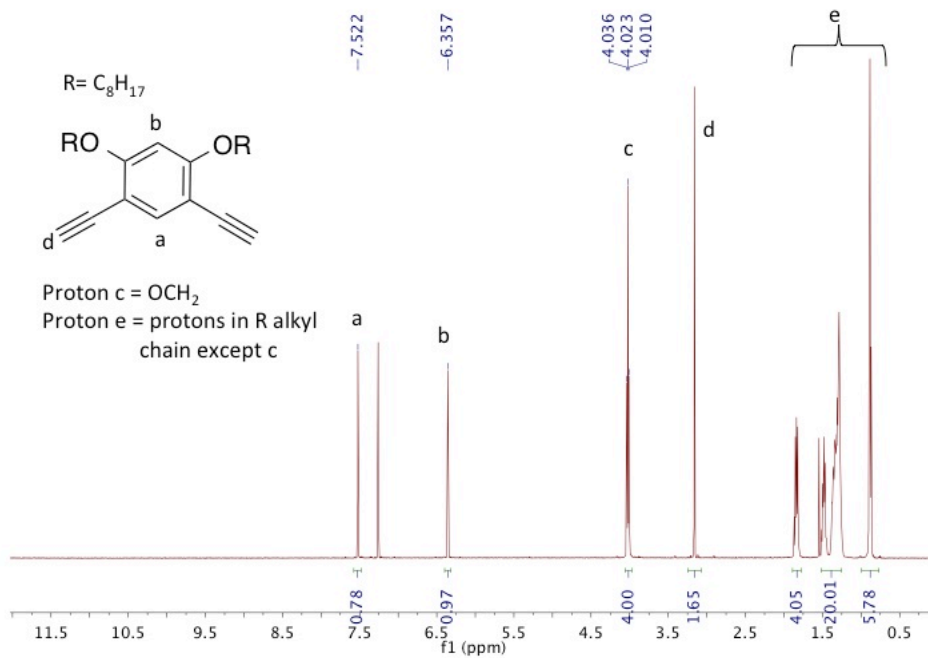
^{13}C NMR of 15



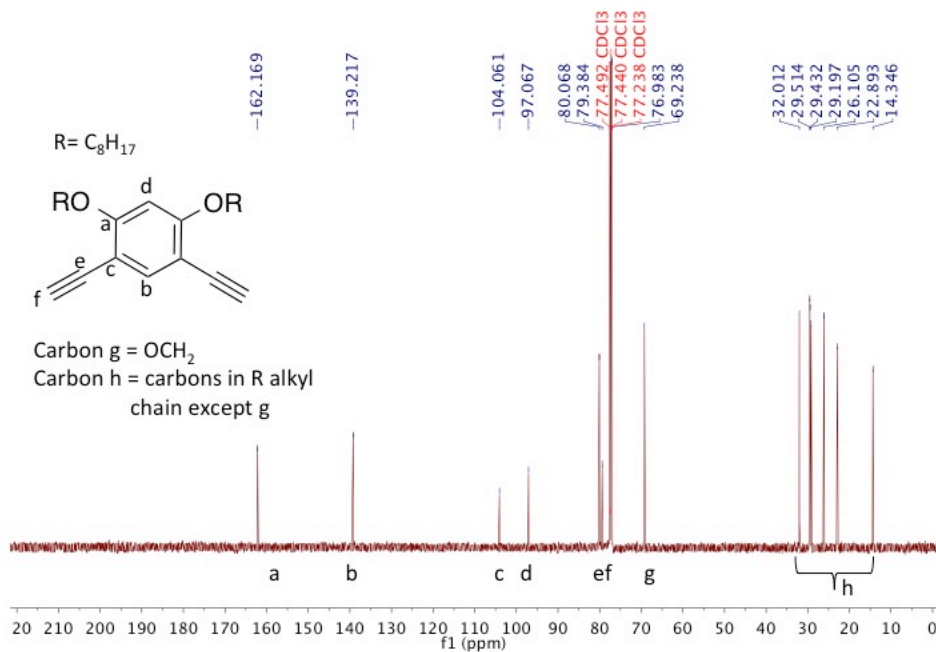
Synthesis of 1,5-diethynyl-2,4-bis(octyloxy)benzene (16)

A mixture of 1,5-diiodo-2,4-bis(octyloxy)benzene (5.0 g, 8.5 mmol), $\text{Pd}(\text{PPh}_3)_2\text{Cl}_2$ (0.2993 g, 0.43 mmol), and CuI (0.0812 g, 0.43 mmol) was dissolved in piperidine (40 mL) under N_2 . Ethynyltrimethylsilane (3.05 mL, 21.4 mmol) was added dropwise to the solution. The mixture was heated at 60 °C for 5 h. The solvent was evaporated under vacuum and the residual solid was dissolved in THF and 1M TBAF in THF was added to deprotect the alkyne group. Extraction with dichloromethane and flash column (SiO_2 , EtOAc: hexanes/ 5:95) were used to obtain 3.0 g (92%) of pure product: ^1H NMR (500 MHz, CDCl_3) δ 7.54-7.48 (s, 1H), 6.40-6.32 (s, 1H), 4.05-4.00 (t, $J = 6.7$ Hz, 4H), 3.24-3.08 (s, 2H), 1.87-1.78 (quintet, $J = 6.7$ Hz, 4H), 1.53-1.25 (m, 20H), 0.92-0.85 (t, $J = 7.0$ Hz, 6H); ^{13}C NMR (500 MHz, CDCl_3) 162.17, 139.22, 104.04, 97.07, 80.07, 79.38, 69.24, 32.01, 29.51, 29.43, 29.30, 26.10, 22.89, 14.35; HRMS (EI) calcd for $\text{C}_{22}\text{H}_{38}\text{O}_2$ 382.28718, found 382.28791.

^1H NMR of 16



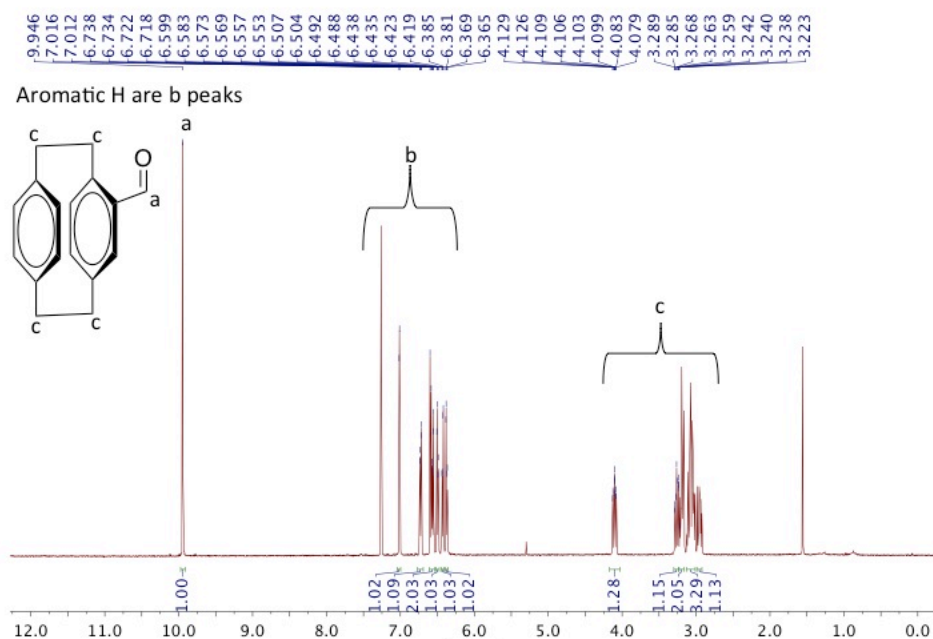
^{13}C NMR of 16



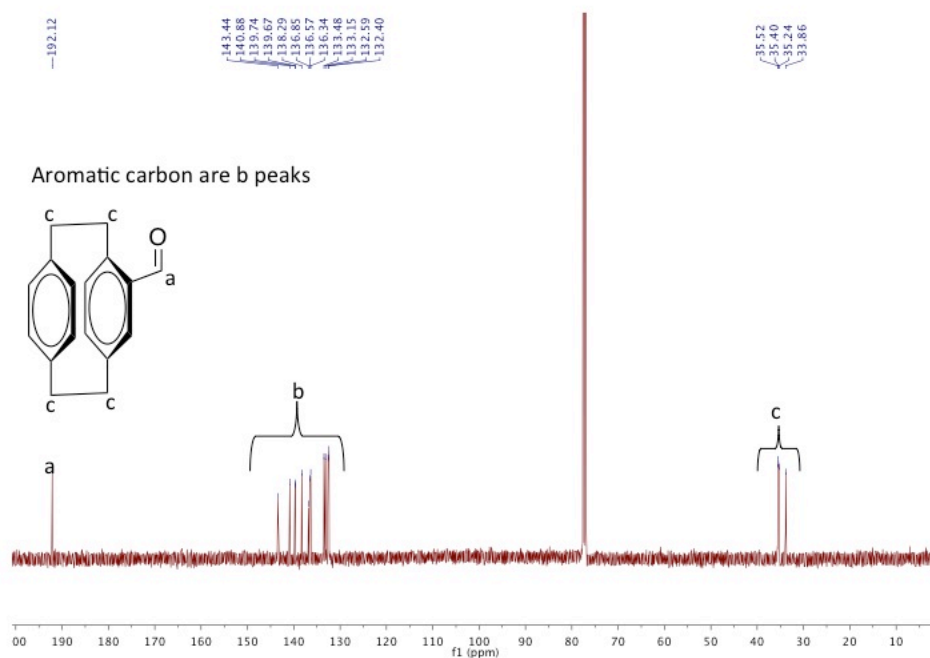
Synthesis of 4-formyl[2,2]paracyclophane (**18**)³⁷

[2,2]Paracyclophane (1.00 g, 4.8 mmol) was dissolved in dichloromethane (40 mL) and the solution was cooled to 0 °C before adding 1M TiCl₄ in DCM (10 mL) dropwise to the solution. The mixture was stirred for 20 minutes followed by dropwise addition of α,α -dichloromethyl methyl ether (0.51 mL, 5.6 mmol). The reaction mixture was stirred at room temperature for 6 h and subsequently poured into ice water (50 mL) and stirred for 2 h. The organic layer was washed with 3M HCl (2 x 37.5 mL), H₂O (2 x 37.5 mL), and dried over anhydrous MgSO₄. Flash column chromatography (SiO₂, EtOAc: Hexanes/ 5:95) was used to yield 0.80 g (71%) of pure product: ¹H NMR (500 MHz, CDCl₃) δ 9.96-9.91 (s, 1H), 7.02-6.98 (d, *J* = 5 Hz, 1H), 6.75-6.70 (dd, *J* = 5 Hz, 10 Hz, 1H), 6.61- 6.58 (d, *J* = 10 Hz, 1H), 6.58-6.54 (dd, *J* = 5 Hz, 5 Hz, 1H), 6.52-6.47 (dd, *J* = 5 Hz, 5 Hz, 1H), 6.45-6.41 (dd, *J* = 10 Hz, 5 Hz, 1H), 6.39-6.35 (dd, *J* = 10 Hz, 5 Hz, 1H), 4.15-4.06 (m, 1H), 3.30-3.23 (m, 1H), 3.23-3.16 (m, 2H), 3.13-3.01 (m, 3H), 2.99-2.91 (m, 1H); ¹³C NMR (500 MHz, CDCl₃) δ 192.12, 143.44, 140.88, 139.74, 139.67, 138.29, 136.85, 136.34, 133.48, 133.15, 132.59, 132.40, 35.52, 35.40, 35.24, 33.86; HRMS (EI) calcd for C₁₇H₁₆O 236.12012, found 236.12023.

¹H NMR of **18**



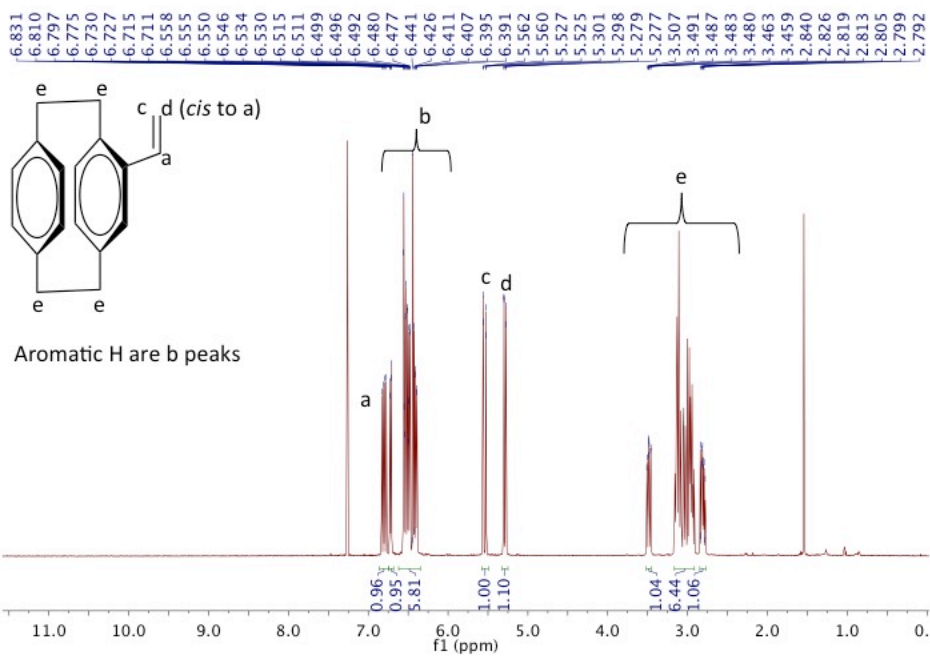
^{13}C NMR of 18



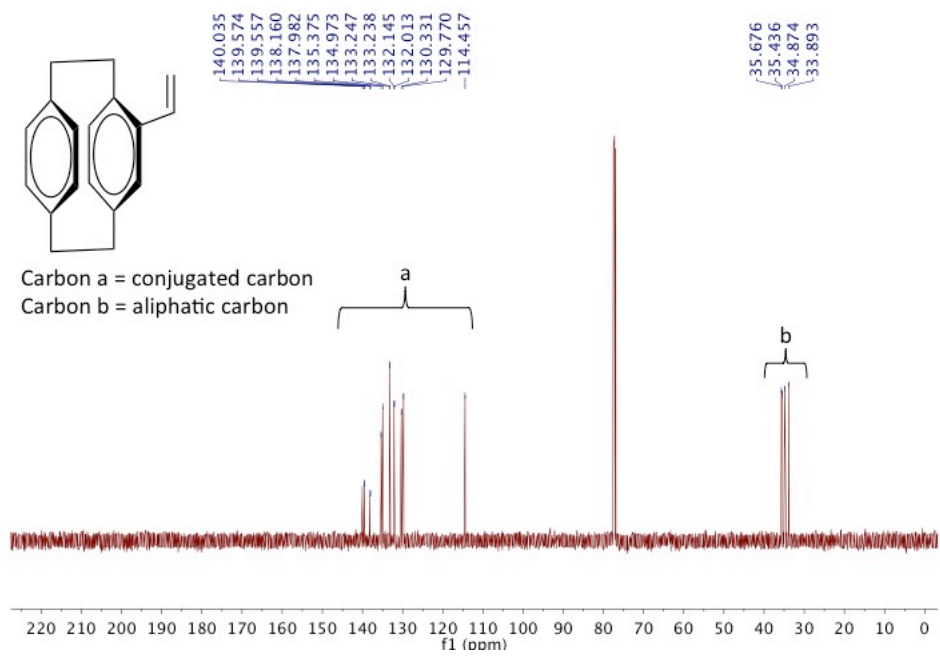
Synthesis of 4-vinyl[2,2]paracyclophane (19)

Methyl(triphenyl)phosphonium bromide (0.4535 g, 1.2695 mmol) was completely dissolved in anhydrous THF (4.2 mL) under nitrogen before cooling the solution to 0 °C. 1.6 M nBuLi in hexanes (0.8 mL) was added to the solution dropwise. The mixture was stirred at room temperature for 2 h to form the ylide. 4-formyl[2,2]paracyclophane (0.2000 g, 0.8463 mmol) was dissolved in anhydrous THF (5 mL) and then added dropwise to the ylide solution. The reaction was stirred overnight at room temperature. Water was used to hydrolyze the reaction. Extraction with dichloromethane and flash column (SiO_2 , dichloromethane) were used to obtain 0.18 g (93%) of pure product: ^1H NMR (500 MHz, CDCl_3) δ 6.85-6.76 (dd, $J = 15$ Hz, 10 Hz, 1H), 6.75-6.68 (dd, $J = 10$ Hz, 1.5 Hz, 1H), 6.58-6.36 (m, 6H), 5.58-5.50 (dd, $J = 15$ Hz, 1.5 Hz, 1H), 5.32-5.25 (dd, $J = 10$ Hz, 1.5 Hz, 1H), 3.515-3.45 (m, 1H), 3.17-2.91(m, 6H), 2.85-2.77(m, 1H); ^{13}C NMR (500 MHz, CDCl_3) δ 140.04, 139.57, 139.56, 138.16, 137.98, 135.37, 134.97, 133.25, 133.24, 132.14, 132.01, 130.33, 129.77, 114.46, 35.68, 35.44, 34.87, 33.89; HRMS (EI) calcd for $\text{C}_{18}\text{H}_{18}$ 234.14085, found 234.14046.

¹H NMR of 19



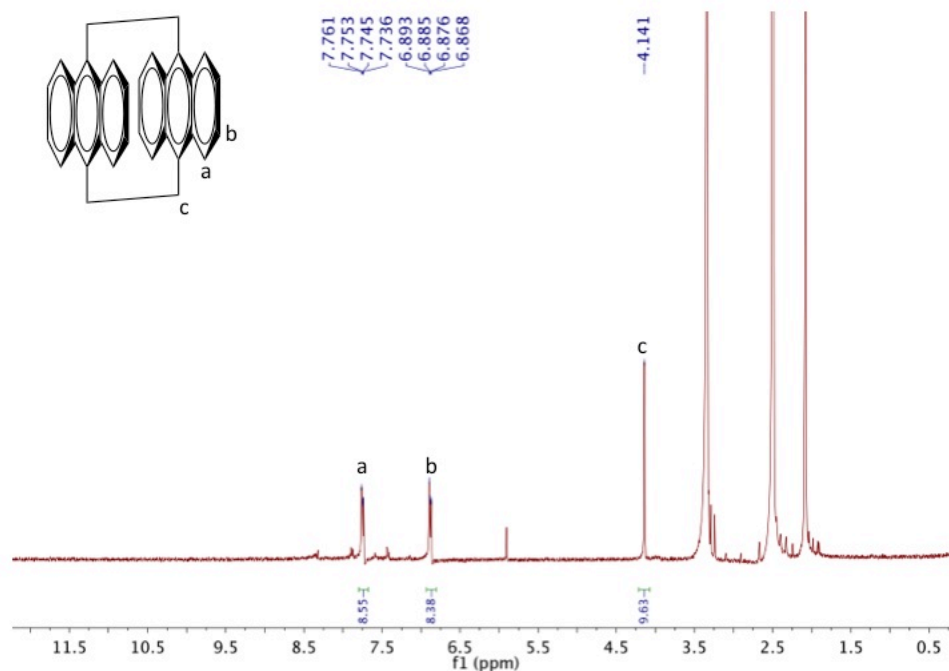
¹³C NMR of 19



Synthesis of anthracenophane (20)³⁸

9,10-Bis(chloromethyl)anthracene (5.12 g, 18.61 mmol) was extracted (Soxhlet) into a refluxing solution of NaI (15.00 g, 100.27 mmol) in deoxygenated acetone (250 mL) for 60 h in the dark. The red-brown solution was filtered hot and the residue was washed thoroughly with acetone and water and dried. The orange precipitate was extracted (Soxhlet) with chloroform (250 mL) for 72 h or until the extract became colorless. The solution was filtered hot and yielded 0.76 g (10%) of orange crystals: ¹H NMR (400 MHz, (CD₃)₂SO) δ 7.80-7.70 (dd, *J* = 3.2 Hz, 6.6 Hz, 8H), 6.93-6.82 (dd, *J* = 3.2 Hz, 6.6 Hz, 8H), 4.20-4.05 (s, 8H); LRMS (EI) *m/z* 204.1, 408.1.

¹H NMR of 20

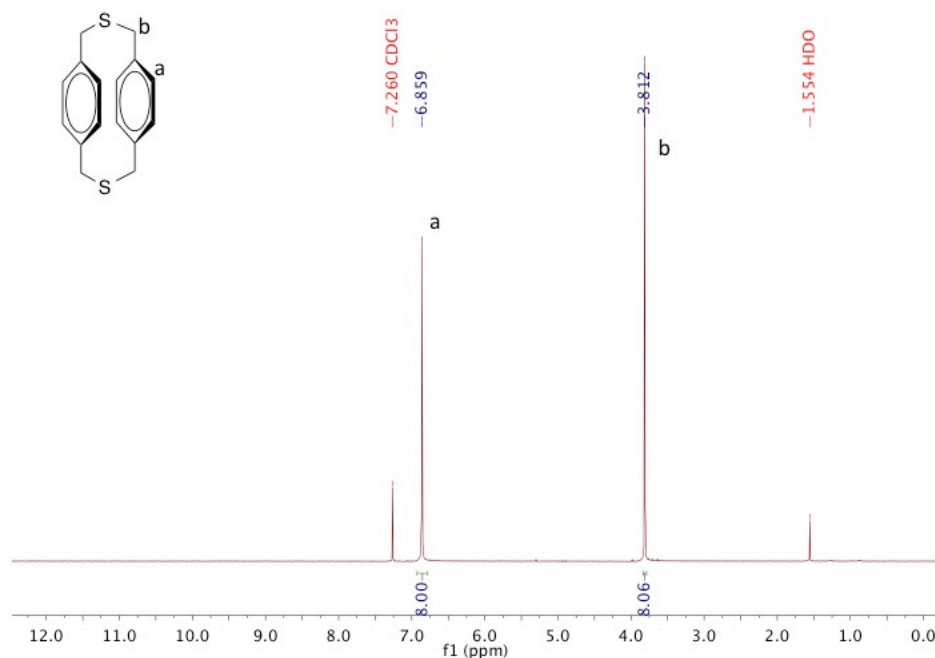


Synthesis of [3.3]-dithiaparacyclophane (21)³⁹

A solution of 1,4-phenylenedimethanethiol (3.0 g, 17.6 mmol) and 1,4-bis(chloromethyl)benzene (3.08 g, 17.6 mmol) in benzene (176 mL) was added dropwise to a refluxing solution of KOH (3.13g, 55.8 mmol) in EtOH (1.76 L) using a pressure equalizing funnel under magnetic stirring for 72 h. The solvents were removed *in vacuo*. Chloroform was added to dissolve the crude product, and the organic layer was washed with a saturated NaHCO₃ solution, a dilute HCl solution, and brine. The organic layer was then dried over anhydrous sodium sulfate and the

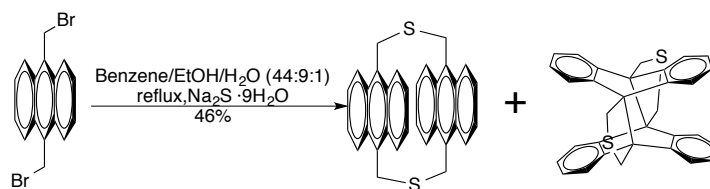
product was purified by flash column chromatography (SiO₂; hexanes: dichloromethane/60:40) to yield 3.7 g (74%) of **6** as a white solid: ¹H NMR (400 MHz, CDCl₃) δ 6.90-6.80 (s, 8 H), 3.83-3.78 (s, 8 H); LRMS (EI) m/z 272.1, 105.1.

¹H NMR of **21**

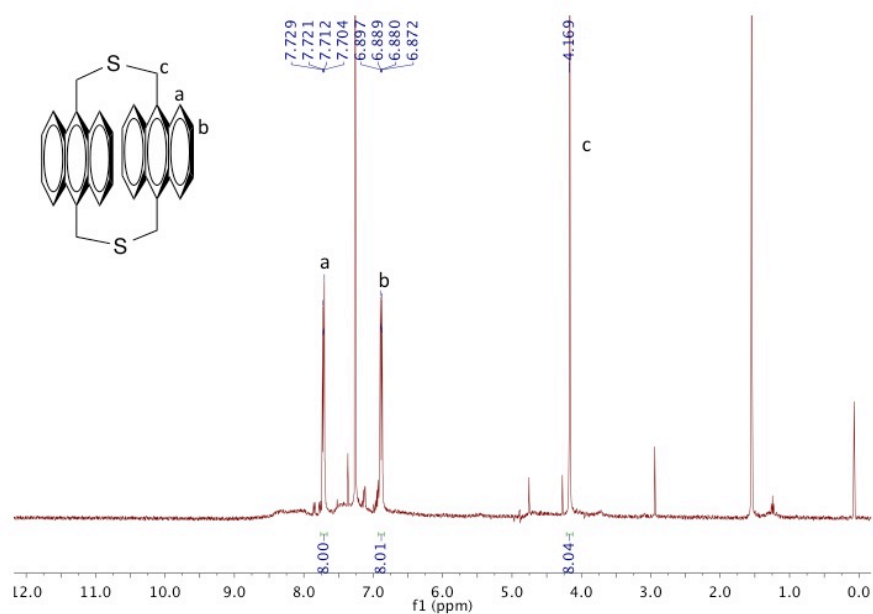


Synthesis of 3,7-dithia-1,5(9,10)-dianthracenacyclooctaphane (**22**).⁴⁰

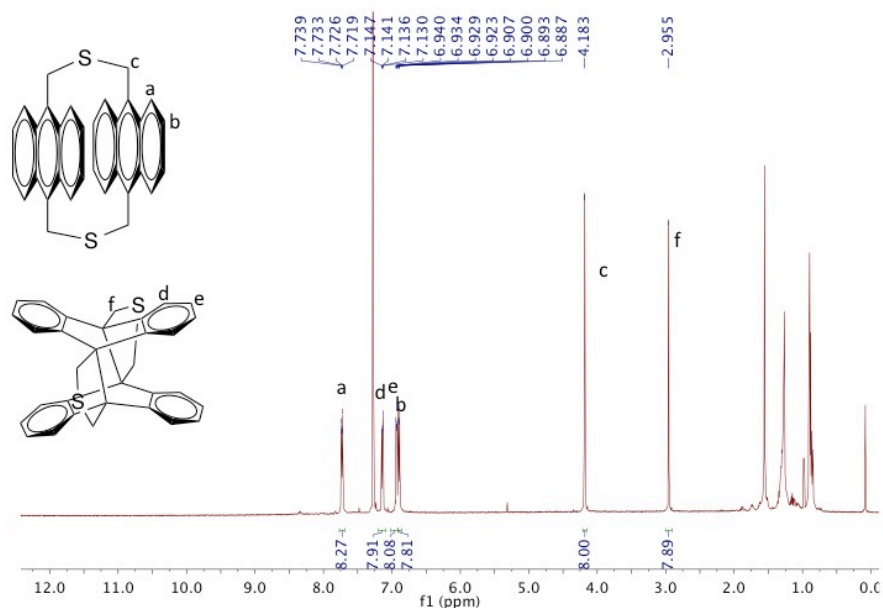
A mixture of 9,10-bis(bromomethyl)anthracene (5.0 g, 13.7 mmol) and Na₂S·9H₂O (6.6 g, 27.5 mmol) was dissolved in a solvent mixture composed of benzene (300 mL), EtOH (60 mL), and water (7 mL) under nitrogen. The reaction was stirred under reflux for 24 h. The solvents were removed *in vacuo*. The product was purified by flash column chromatography (SiO₂; hexanes: dichloromethane/50:50). Both cyclized product and non-cyclized product were present with overall 46% yield: ¹H NMR (500 MHz, (CD₃)₂SO)) δ 7.75-7.67 (dd, *J*= 2.5 Hz, 8H), 7.16-7.10 (dd, *J*= 2.5 Hz, 8H), 6.98-6.92 (dd, *J*= 2.5 Hz, 8H), 6.92-6.86 (dd, *J*= 2.5 Hz, 8H), 4.21-4.16 (s, 8H), 3.00-2.91 (s, 8H); LRMS (EI) m/z 205.1, 422.1. Crude product ¹H NMR (500 MHz, (CD₃)₂SO)) δ 7.75-7.67 (dd, *J*= 3.2 Hz and 6.6 Hz, 8H), 6.92-6.86 (dd, *J*= 3.2 Hz and 6.6 Hz, 8H), 4.21-4.16 (s, 8H).



^1H NMR of 22 (crude product)



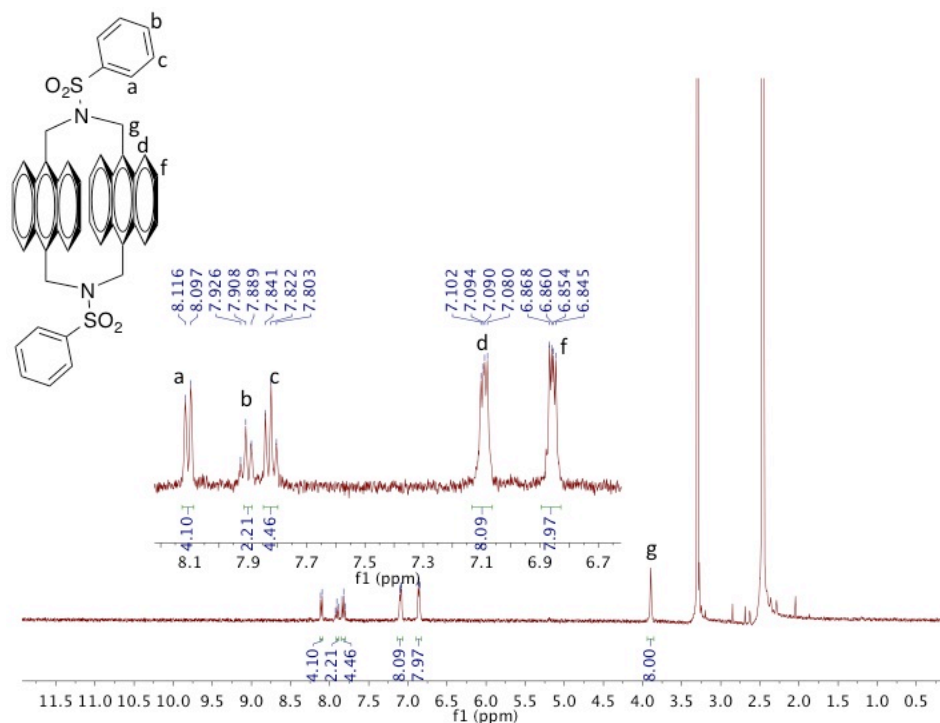
^1H NMR of 22 with cyclized product



Synthesis of benzenesulfonyl nitroanthracenophane (**23**)⁴¹

A mixture of benzenesulfonamide (1.58 g, 10 mmol) and 9,10-bis(chloromethyl)anthracene (3.0 g, 10 mmol) was added to a solution of NaH (0.93g, 20 mmol) in DMF (170mL) under nitrogen at 60 °C. The reaction was left in the dark for 6 h. The solution was cooled to room temperature before filtration. The solid was washed with dioxane, distilled water, and MeOH to yield 0.84g (11%) of pure product: ¹H NMR (400 MHz, (CD₃)₂SO) δ 8.09-8.13 (d, *J* = 7.4 Hz, 4H), 7.92-7.88 (t, *J* = 7.4 Hz, 2H), 7.85-7.80 (t, *J* = 7.4 Hz, 4H), 7.12-7.06 (dd, *J* = 5.6 Hz and 3.1 Hz, 8H), 6.88-6.83 (dd, *J* = 5.6 Hz and 3.1 Hz, 8H); LRMS (EI) *m/z* 77, 206.1, 718.0.

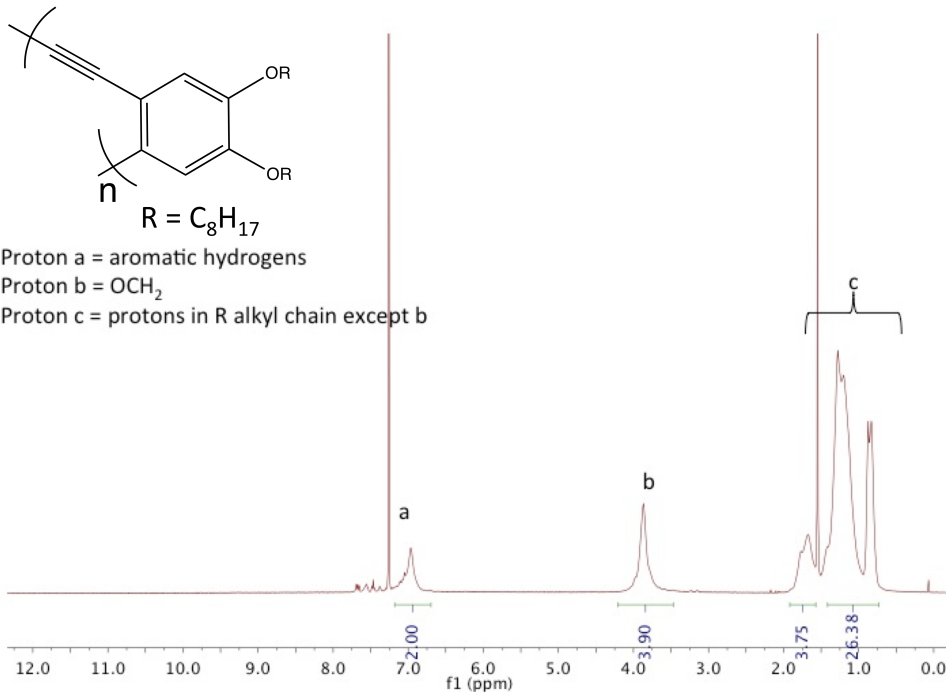
¹H NMR of **23**



Synthesis of poly[4-ethynyl-1,2-bis(octyloxy)benzene] (**P1**)

A mixture of 1,2-diethynyl-4,5-bis(octyloxy)benzene (0.1450g, 0.3790 mmol), 1,2-diiodo-4,5-bis(octyloxy)benzene (0.2334 g, 0.3980 mmol), Pd(PPh₃)₄ (0.0219 g, 0.0189 mmol), and CuI (0.0040 g, 0.0189 mmol) were dissolved in piperidine (2 mL) under N₂. The solution was heated to 50 °C, left to react for 3 days, and quenched with MeOH to yield 0.14 g (96%) of product: Mn=19759 Daltons, Mw=46829 Daltons, PDI = 2.37; ¹H NMR (500 MHz, CDCl₃) δ 7.20-6.70 (s, 2H), 4.2-3.5 (s, 4H), 1.9-1.6 (s, 4H), 1.4-0.7 (m, 26H).

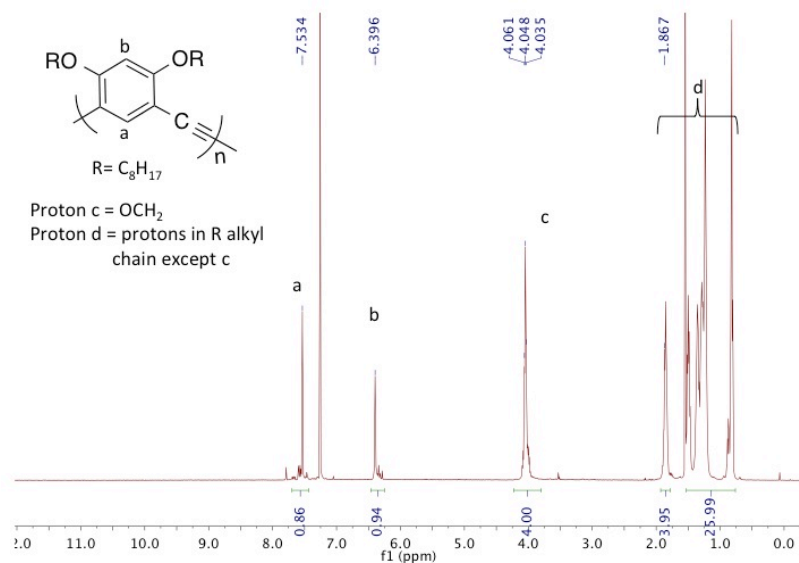
¹H NMR of P1



Synthesis of poly[4-ethynyl-1,3-bis(octyloxy)benzene] (P2)

A mixture of 1,5-diethynyl-2,4-bis(octyloxy)benzene (2.29 g, 6.0 mmol), 1,5-diiodo-2,4-bis(octyloxy)benzene (3.6873 g, 6.3 mmol), Pd(PPh₃)₄ (0.3461 g, 3.0 mmol), and CuI (0.057 g, 3.0 mmol) were dissolved in piperidine (50 mL) under N₂. The solution was heated to 55 °C, left to react for 1 week, and quenched with MeOH to yield 2.24 g (98%) of product: Mn = 7480 Daltons, Mw = 14061 Daltons, PDI = 1.88; ¹H NMR (500 MHz, CDCl₃) δ 7.70-7.45 (s, 1H), 6.45-6.25 (s, 1H), 4.22-3.82 (t, *J* = 6.4 Hz, 4H), 1.93-1.79 (m, 4H), 1.55-0.75 (m, 26H).

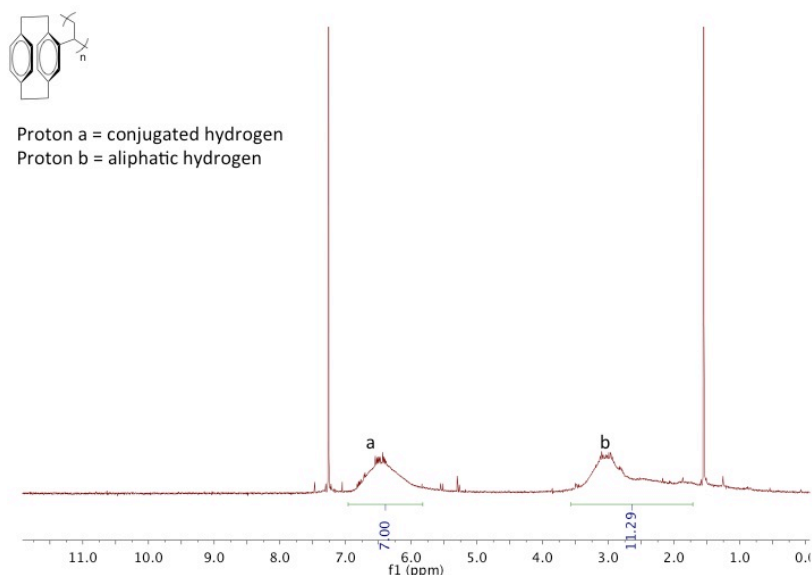
¹H NMR of P2



Synthesis of poly[(2,2)-paracyclophane] (P3)

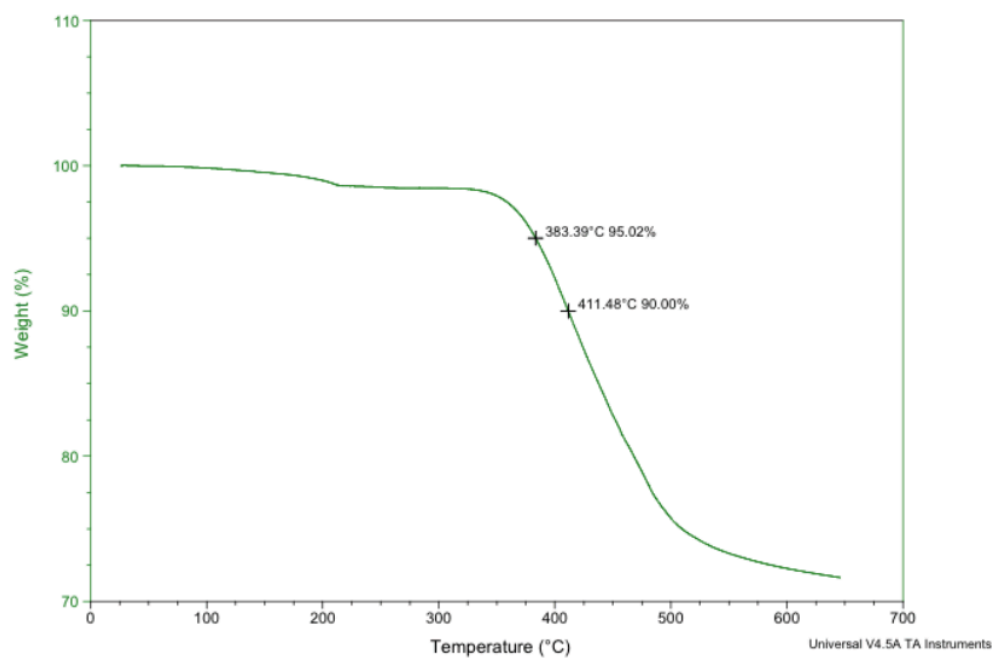
Bulk polymerization of 4-vinyl[2,2]paracyclophane (0.1000 g, 0.4267 mmol) with AIBN (5 mg, 0.0305 mmol) was carried out at 85 °C overnight. The resulting gel-like product was dissolved in chloroform (1 mL) and quenched with MeOH (25 mL) to give 0.0982 g (98%) of **11** as a white solid: Mn = 5,200 Daltons, Mw = 14,000 Daltons, PDI = 2.702; ¹H NMR (500 MHz, CDCl₃) δ 6.9-5.8 (s, 7H), 3.6-1.7 (s, 11H).

¹H NMR of P3

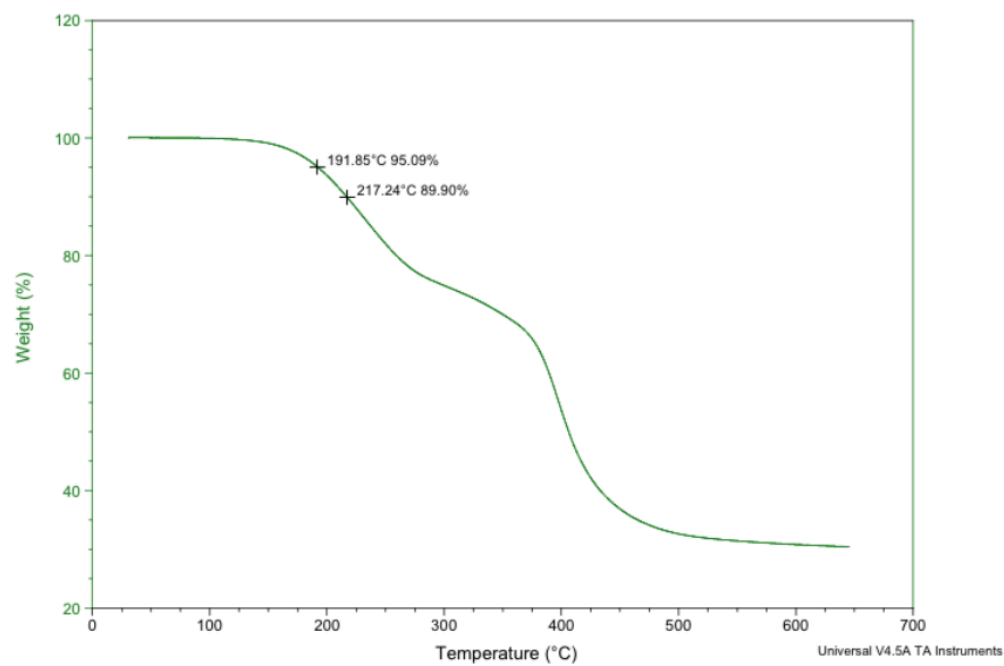


2.7.3 TGA Data of 1-3

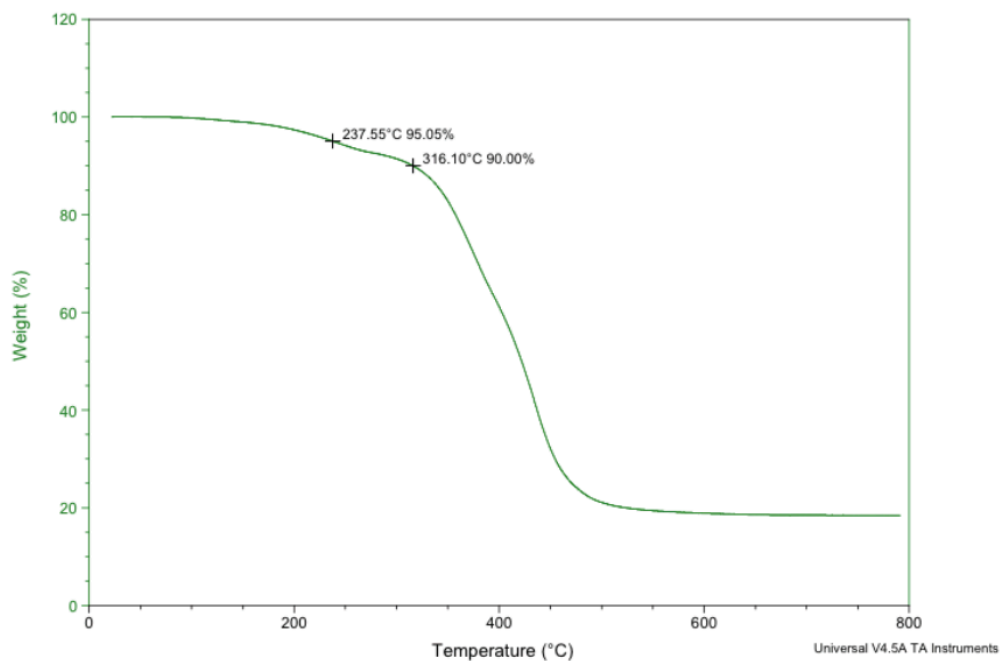
TGA of **1** ($T_d = 383\text{ }^\circ\text{C}$ at 5% weight loss, heating rate = $10\text{ }^\circ\text{C}/\text{min}$)



TGA of **2** ($T_d = 192\text{ }^\circ\text{C}$ at 5% weight loss, heating rate = $10\text{ }^\circ\text{C}/\text{min}$)



TGA of **3** ($T_d = 238\text{ }^\circ\text{C}$ at 5% weight loss, heating rate = $10\text{ }^\circ\text{C}/\text{min}$)



2.7.4 Absorption and Emission Spectra of **4** in Chloroform

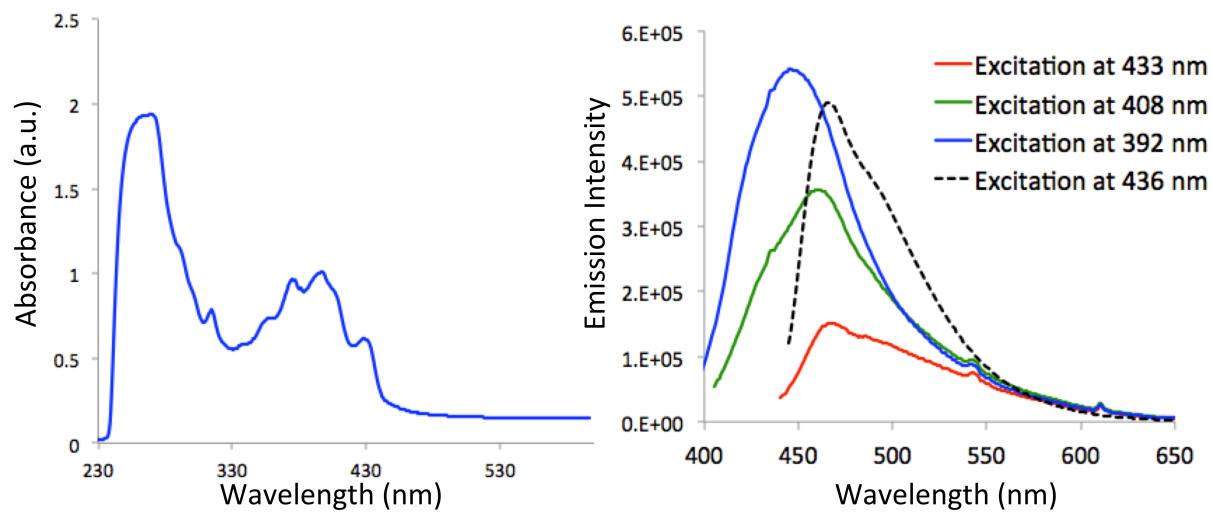


*Figure 2.7 Absorption and emission spectra of **4** in chloroform.*

2.7.5 Computational Methods

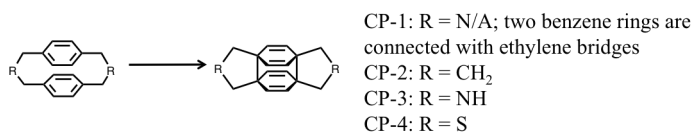
All calculations were carried out using Gaussian 09.⁴² For the cyclization reaction coordinates, geometry optimizations were performed with B3LYP/6-31G(d).^{1, 33} Calculations involving the closed-shell reactant arenediynes used restricted wave functions. Calculations on the open-shell transition states and diradical products used broken-symmetry unrestricted wave functions.² Vibrational frequencies were computed for each optimized structure to confirm that each geometry was a stationary point and to obtain free energies for all species.

Table 2.4 Activation energies for cyclization reactions of phenyl, trichlorophenyl, and naphthalene-1-yl substituted arenediynes.^a

molecule	ΔG^\ddagger C ¹ -C ⁵ (kcal/mol) ^b	ΔG^\ddagger C ¹ -C ⁶ (kcal/mol) ^c	$\Delta\Delta G^\ddagger(5-6)$ (kcal/mol) ^d
Phenyl	42.34	44.48	-2.14
Phenyl ^e	42.45	45.70	-3.25
Phenyl ^f	36.3	38.5	-2.2
Naphthalen-1-yl	42.10	45.28	-3.18
Naphthalen-1-yl ^e	41.11	46.04	-4.93
Trichlorophenyl	44.05	48.04	-3.99
Trichlorophenyl ^f	38.7	43.2	-4.5

^aCalculations are performed using B3LYP/6-31G(d) level of theory; ^bactivation energy for 5-membered ring cyclization; ^cactivation energy for 6-membered ring cyclization; ^ddifference in activation energies for 5-membered and 6-membered cyclization; ^{e&f}reported values from literature.¹⁻²

Table 2.5 Enthalpy and volume changes of cyclophane derivatives before and after cyclization reactions.



Substrate	% Volume change	ΔH (kcal/mol)
CP-1	-7.5%	78.28
CP-2	-8.9%	48.95
CP-3	-9.5%	47.48
CP-4	-9.9%	47.13

2.8 Notes and References

Notes:

Portions of this chapter have been published: Nagarjuna, G.; Ren, Y.; Moore, J. S. "Synthesis and reactivity of anthracenyl-substituted arenediynes." *Tetrahedron Lett.* **2015**, *56*, 3155–3159. They are reproduced/adapted with permission. Copyright 2015 Elsevier.

References:

1. Vavilala, C.; Byrne, N.; Kraml, C. M.; Ho, D. M.; Pascal, R. A., *J. Am. Chem. Soc.* **2008**, *130*, 13549.
2. Korovina, N. V.; Chang, M. L.; Nguyen, T. T.; Fernandez, R.; Walker, H. J.; Olmstead, M. M.; Gherman, B. F.; Spence, J. D., *Org. Lett.* **2011**, *13*, 3660.
3. Kar, M.; Basak, A., *Chem. Rev.* **2007**, *107*, 2861.
4. Kraka, E.; Cremer, D., *WIREs Comput. Mol. Sci.* **2014**, *4*, 285.
5. Gulevskaia, A. V.; Lazarevich, R. Y., *Chem. Heterocycl. Compd.* **2013**, *49*, 116.
6. Maretina, I. A., *Russ. J. Gen. Chem.* **2008**, *78*, 223.
7. Nath, M.; Pink, M.; Zaleski, J. M., *J. Am. Chem. Soc.* **2005**, *127*, 478.
8. Spence, J. D.; Hargrove, A. E.; Crampton, H. L.; Thomas, D. W., *Tetrahedron Lett.* **2007**, *48*, 725.
9. Lewis, K. D.; Matzger, A. J., *J. Am. Chem. Soc.* **2005**, *127*, 9968.
10. Kovalenko, S. V.; Peabody, S.; Manoharan, M.; Clark, R. J.; Alabugin, I. V., *Org. Lett.* **2004**, *6*, 2457.
11. Roy, S.; Anoop, A.; Biradha, K.; Basak, A., *Angew. Chem., Int. Ed.* **2011**, *50*, 8316.
12. Rainer, J.; Kennedy, A., *J. Org. Chem.* **2000**, *65*, 6213.
13. Scott, J.; Parkin, S.; Anthony, J., *Synlett* **2004**, 161.
14. Bowles, D.; Anthony, J., *Org. Lett.* **2000**, *2*, 85.
15. Xiao, Y.; Hu, A., *Macromol. Rapid Commun.* **2011**, *32*, 1688.
16. Dang, H.; Levitus, M.; Garcia-Garibay, M. A., *J. Am. Chem. Soc.* **2002**, *124*, 136.
17. Wang, C.; Dong, H.; Hu, W.; Liu, Y.; Zhu, D., *Chem. Rev.* **2012**, *112*, 2208.
18. Marsella, M. J.; Yoon, K.; Estassi, S.; Tham, F. S.; Borchardt, D. B.; Bui, B. H.; Schreiner, P. R., *J. Org. Chem.* **2005**, *70*, 1881.
19. Pickard, F. C.; Shepherd, R. L.; Gillis, A. E.; Dunn, M. E.; Feldgus, S.; Kirschner, K. N.; Shields, G. C.; Manoharan, M.; Alabugin, I. V., *J. Phys. Chem. A* **2006**, *110*, 2517.
20. Alabugin, I. V.; Manoharan, M.; Kovalenko, S. V., *Org. Lett.* **2002**, *4*, 1119.
21. Setaka, W.; Kanai, S.; Kabuto, C.; Kira, M., *Chem. Lett.* **2006**, *35*, 1364.
22. Roy, S.; Bag, S. S.; Basak, A., *Tetrahedron* **2012**, *68*, 8600.
23. Kraft, B. J.; Coalter, N. L.; Nath, M.; Clark, A. E.; Siedle, A. R.; Huffman, J. C.; Zaleski, J. M., *Inorg. Chem.* **2003**, *42*, 1663.
24. Hickenboth, C. R.; Rule, J. D.; Moore, J. S., *Tetrahedron* **2008**, *64*, 8435.
25. Basak, A.; Bag, S. S.; Das, A. K., *Eur. J. Org. Chem.* **2005**, 1239.
26. Kim, M.; Hohman, J. N.; Cao, Y.; Houk, K. N.; Ma, H.; Jen, A. K. Y.; Weiss, P. S., *Science* **2011**, *331*, 1312.
27. Becker, H. D.; Andersson, K., *J. Photochem.* **1984**, *26*, 75.

28. Yang, K.; Lee, J.; Sottos, N. R.; Moore, J. S., *J. Am. Chem. Soc.* **2015**, *137*, 16000.
29. Engelke, R.; Blais, N. C.; Sheffield, S. A.; Sander, R. K., *J. Phys. Chem. A* **2001**, *105*, 6955.
30. Warnes, R. H., *J. Chem. Phys.* **1970**, *53*, 1088.
31. Quenneville, J.; Germann, T. C., *J. Chem. Phys.* **2009**, *131*, 024313.
32. Lim, C.; Yasutake, M.; Shinmyozu, T., *Angew. Chem., Int. Ed.* **2000**, *39*, 578.
33. Okamoto, H.; Satake, K.; Ishida, H.; Kimura, M., *J. Am. Chem. Soc.* **2006**, *128*, 16508.
34. Shaw, W. L.; Ren, Y.; Moore, J. S.; Dlott, D. D., *AIP Confer. Proc.* **2017**, *1793*, 030026.
35. Grujicic, M.; Pandurangan, B.; Bell, W. C.; Cheeseman, B. A.; Yen, C. F.; Randow, C. L., *Mat. Sci. Eng. A* **2011**, *528*, 3799.
36. Li, W.; Sui, Z.; Liu, H.; Zhang, Z.; Liu, H., *J. Phys. Chem. C* **2014**, *118*, 16028.
37. Iwatsuki, S.; Itoh, T.; Kubo, M.; Okuno, H., *Polym. Bull.* **1994**, *32*, 27.
38. Golden, J. H., *J. Chem. Soc.* **1961**, 3741.
39. Montanari, M.; Bugana, A.; Sharma, A. K.; Pasini, D., *Org. Biomol. Chem.* **2011**, *9*, 5018.
40. Sakata, Y.; Toyoda, T.; Misumi, S.; Yamazaki, T.; Yamazaki, I., *Tetrahedron Lett.* **1992**, *33*, 5077.
41. Usui, M.; Shindo, Y.; Nishiwaki, T.; Anda, K.; Hida, M., *Chem. Lett.* **1990**, 419.
42. Frisch, M. J.; Trucks, G. W.; Schlegel, H. B.; Scuseria, G. E.; Robb, M. A.; Cheeseman, J. R.; Scalmani, G.; Barone, V.; Mennucci, B.; Petersson, G. A.; Nakatsuji, H.; Caricato, M.; Li, X.; Hratchian, H. P.; Izmaylov, A. F.; Bloino, J.; Zheng, G.; Sonnenberg, J. L.; Hada, M.; Ehara, M.; Toyota, K.; Fukuda, R.; Hasegawa, J.; Ishida, M.; Nakajima, T.; Honda, Y.; Kitao, O.; Nakai, H.; Vreven, T.; Montgomery Jr., J. A.; Peralta, J. E.; Ogliaro, F.; Bearpark, M. J.; Heyd, J.; Brothers, E. N.; Kudin, K. N.; Staroverov, V. N.; Kobayashi, R.; Normand, J.; Raghavachari, K.; Rendell, A. P.; Burant, J. C.; Iyengar, S. S.; Tomasi, J.; Cossi, M.; Rega, N.; Millam, N. J.; Klene, M.; Knox, J. E.; Cross, J. B.; Bakken, V.; Adamo, C.; Jaramillo, J.; Gomperts, R.; Stratmann, R. E.; Yazyev, O.; Austin, A. J.; Cammi, R.; Pomelli, C.; Ochterski, J. W.; Martin, R. L.; Morokuma, K.; Zakrzewski, V. G.; Voth, G. A.; Salvador, P.; Dannenberg, J. J.; Dapprich, S.; Daniels, A. D.; Farkas, Ö.; Foresman, J. B.; Ortiz, J. V.; Cioslowski, J.; Fox, D. J. *Gaussian 09*, Gaussian, Inc.: Wallingford, CT, USA, 2009.

Chapter 3: Development of Redox-Active Organic Materials for Force-Induced Volume Collapse

3.1 Abstract

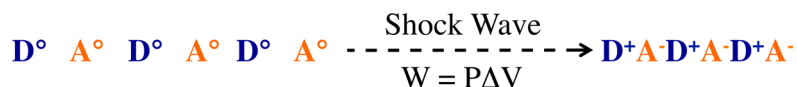
We describe the development of redox-active organic materials that undergo pressure-induced neutral-to-ionic transitions (PINITs) via ultrafast electron transfer reactions as potential candidates for shock wave energy dissipation (SWED). To combine the unique properties of polymers, such as processability and high functional group density, with the outstanding redox-properties of small molecules, we incorporate electron-donating tetrathiafulvalene (TTF) and electron-accepting 11,11,12,12-tetracyano-9,10-anthraquinodimethane (TCAQ) moieties as pendant groups into macromolecular backbones via post-polymerization modification and direct polymerization, respectively. We also demonstrate that an amorphous blend of molecular TTF and a polymer bearing TCAQ pendant motifs (1:2 molar ratio) is capable of undergoing pressure-induced electron transfer reactions. When the pressure applied to the amorphous blend is above 2.0 GPa at room temperature, new absorption bands appear between 500–800 nm, indicative of electron transfer. Upon removal of the applied pressure, the absorption and emission spectra return to their original form, suggesting the reversibility of the electron transfer process. This amorphous material is a valuable addition to the current repertoire of crystalline materials that exhibit PINITs and has potential applications as pressure responsive thin films.

3.2 Introduction

Since the volume of bulk materials depends on intermolecular distances, we sought to achieve shock-induced intermolecular volume collapse by enhancing non-covalent interactions. Compared to hydrogen-bonding and π - π interactions, an ionic interaction is generally isotropic, and its strength has relatively high tunability, which is ideal for building a reversible network with energy dissipation properties. Hydrostatic pressure has been utilized to trigger neutral-to-ionic transitions in both organic and inorganic co-crystals comprised of electron donors (D) and acceptors (A).¹⁻² Inspired by these works on the pressure-induced neutral-to-ionic transition (PINIT), we propose that a transient shock wave with nanosecond duration is also capable of

inducing electron transfer from an electron-rich donor to an electron-poor acceptor, thereby shortening intermolecular distances via ionic interactions to yield dense materials (Scheme 3.1). The amount of shock wave energy dissipated via the neutral-to-ionic transition (i.e. $W = P\Delta V$) depends on i) the activation energy required to achieve such a transition, which can be estimated using the transition pressure (P), and ii) the amount of volume that is reduced intermolecularly from neutral to ionic state (ΔV). These two parameters can be readily tuned by varying the electron acceptor or the electron donor in a charge-transfer complex (CTC) with desired electron affinity or ionization potential.¹

Scheme 3.1 SWED by intermolecular volume collapse via a neutral-to-ionic transition. *D* represents electron donor and *A* represents electron acceptor.



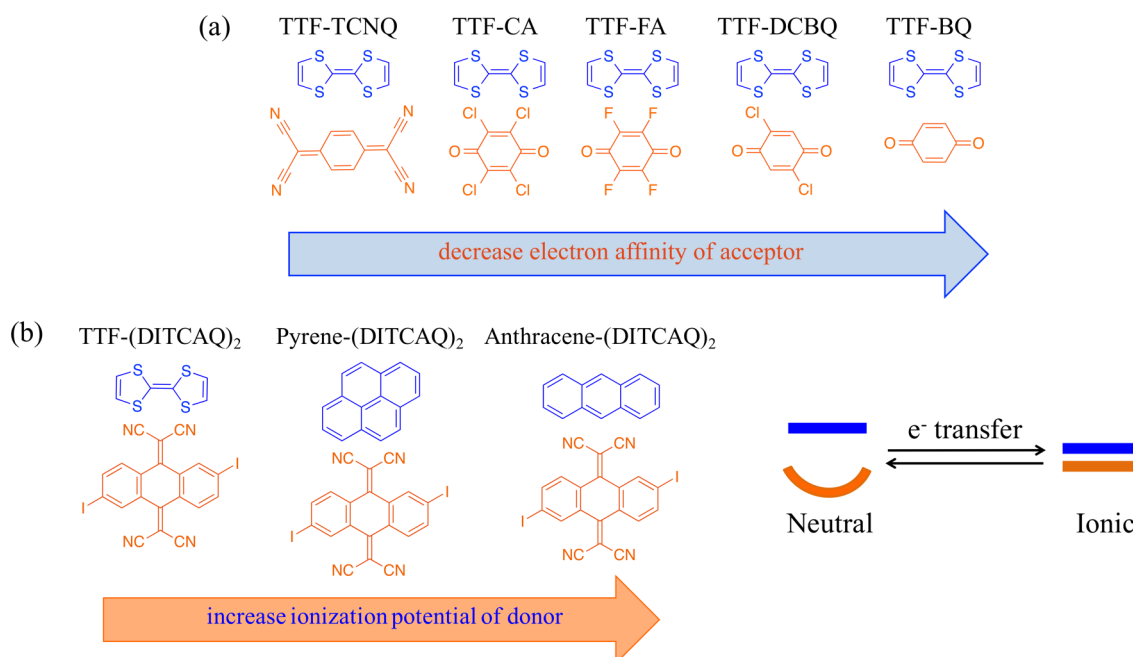
In this chapter, we describe our efforts to develop molecular and polymeric materials that undergo PINITs via electron transfer reactions. Section 3.3 discusses the development and preliminary energy-dissipative properties of molecular crystalline materials, whereas section 3.4 and section 3.5 focus on incorporating redox-active motifs, i.e. tetrathiafulvalene (TTF) and 11,11,12,12-tetracyano-9,10-anthraquinodimethane (TCAQ), into polymeric materials. The feasibility of PINIT in an amorphous material bearing TTF and TCAQ motifs is also discussed in section 3.5.

3.3 Development of Crystalline Charge-Transfer Complexes that Undergo a Pressure-Induced Neutral-to-Ionic Transition (PINIT)

A series of TTF-based co-crystals with varying electron affinities of the electron acceptors was synthesized following literature procedures¹ for SWED testing: TTF-tetracyanoquinodimethane (TTF-TCNQ), TTF-chloranil (TTF-CA), TTF-fluoranil (TTF-FA), TTF-dichlorobenzoquinone (TTF-DCBQ), and TTF-p-benzoquinone (TTF-BQ) (Scheme 3.2a). As the electron affinity of electron acceptor decreases, both the amount of energy required to ionize a donor-acceptor pair and the change in volume between the neutral and ionic states increase.¹ Thus, we hypothesized that the amount of shock wave energy dissipated via PINIT is

inversely correlated with the electron affinity of electron acceptor. Since TTF-TCNQ is the most ionic complex with a degree of charge transfer of 0.59 under ambient conditions,³ it is expected to dissipate the least amount of shock wave energy, whereas TTF-BQ is expected to dissipate the greatest amount of shock wave energy among the five co-crystals listed in Scheme 3.2a.

Scheme 3.2 (a) TTF-based co-crystals. (b) DITCAQ-based co-crystals. Upon accepting two electrons, DITCAQ transforms from a butterfly-shaped geometry to an aromatic planar-shaped geometry, which leads to more efficient molecular packing.



In addition to the TTF-based planar co-crystals, we developed a series of co-crystals using 2,2'-(2,6-diiodoanthracene-9,10-diylidene)dimalononitrile (DITCAQ) as the electron acceptor (Scheme 3.2b).⁴ DITCAQ was selected as the electron acceptor due to its i) high LUMO energy level, which ensures the neutral state of DITCAQ-based co-crystals under ambient conditions,⁵ ii) ability to transform from a butterfly-shaped geometry to an aromatic planar-shaped geometry upon accepting two electrons, which leads to larger volume collapse and enhanced SWED performance compared to the planar co-crystals,⁵ and iii) good solubility in common organic solvents, which promotes facile co-crystallization with various electron donors (Scheme 3.2b).⁴ A butterfly-shaped electron donor, 9,10-bis(1,3-dithiol-2-ylidene)-9,10-dihydroanthracene (TTFAQ), was also synthesized.⁶ However, attempts to grow co-crystals bearing TTFAQ and DITCAQ were unsuccessful. One major disadvantage of using TTFAQ as

the electron donor for PINIT is its high HOMO energy level, which promotes the ionic state of TTFAQ-based co-crystals under ambient conditions.

The processability of the crystalline materials shown in Scheme 3.2 remains poor even after blending with 10 wt% poly(vinyl alcohol) as the binding material. Up to this point, we were only able to assess the SWED properties of TTF-CA and TTF-TCAQ using the laser-driven flyer plates.⁷ The flyer plate is a thin aluminum foil that is launched by intense laser pulses aimed at the target samples. The impact speed is tunable from 0.2 km/s to 4.5 km/s, as determined by a Photon Doppler Velocimeter. The flyer plate velocity can be transduced to fluence, which represents shock wave energy.⁸ Materials with high shock-wave dissipating properties display low fluence upon shock wave impact. The fluence value after shock wave impact was determined for TTF-CA, TTF-TCNQ, and polyurea (Table 3.1). Compared to polyurea, a known energy dissipator, TTF-CA displayed superior performance on energy dissipation at all tested impact levels, whereas TTF-TCNQ exhibited inferior performance on energy dissipation as expected. The differences in the average fluence values between TTF-CA and polyurea are 0.2 kJ/m², 14.0 kJ/m², and 16.1 kJ/m² after flyer plate impact with velocities of 0.75 km/s, 1.3 km/s, and 1.6 km/s, respectively. Based on these preliminary SWED results, we expect to see larger differences on the fluence values between TTF-CA and polyurea at even higher impact levels.

Table 3.1 SWED properties of crystalline TTF-CA and TTF-TCNQ with polyurea as a reference assessed at various impact velocities with laser-driven flyer plates. 5 wt% of poly(vinyl alcohol) was used as the binding material. The film thickness is ca. 30 μm.

Entry	Fluence (kJ/m ²)		
	0.75 km/s	1.3 km/s	1.6 km/s
Glass (input)	16.5 ± 0.3	58.3 ± 0.5	106.7 ± 0.5
TTF-CA	10.5 ± 1.2	30.3 ± 1.5	69.3 ± 3.4
TTF-TCNQ	11.8 ± 1.1	63.6 ± 8.3	91.7 ± 9.5
polyurea	10.7 ± 0.4	44.3 ± 1.1	85.4 ± 7.9

Although TTF-CA showed promising SWED properties,⁸ the preliminary results should be interpreted with caution as i) no control studies were conducted (i.e. flyer plates experiments on the individual components of the co-crystals that are incapable of PINIT), ii) in-situ characterizations that support TTF-CA co-crystals undergo a shock-induced neutral-to-ionic transition were absent, and iii) more voids, which assist energy dissipation via volume collapse,

were present in crystalline samples compared with polyurea. Additional flyer plates experiments with improved accuracy and in-situ characterizations are required to address the first two issues. The problem associated with processability can be mitigated by incorporating both TTF and TCAQ motifs into polymeric materials, which are discussed in section 3.4 and 3.5 of this chapter.

3.4 Improved TTF Functionalization of Polymers for Two-Dimensional Charge-Transfer Network

3.4.1 Introduction

As a prototypical electron donor, TTF exhibits outstanding redox properties that are applicable for organic electronics, chemical sensors, molecular switches, and nonlinear optical materials.⁹ When combined with various π -electron acceptors, TTF moieties stack in the solid state to form highly electrically-conducting CTCs.¹⁰⁻¹³ The discovery of metallic behavior of CTCs composed of TTF and TCNQ¹² has generated numerous reports on the syntheses, properties and applications of TTF-based CTCs.¹³ Despite the inherent electronic advantages, most of the TTF-based CTCs exhibit quasi-one-dimensional electrical conductivity due to their highly ordered stacking. Higher dimensions in conductivity are achieved by increasing sulfur content or replacing sulfur with a different chalcogen (Se, Te) in TTF.¹⁴ However, CTCs with bis(ethylenedithio)tetrathiafulvalene, tetraselenafulvalenes, or tetratellurafulvalenes as the donor tend to be brittle and unprocessable.¹⁵ An alternative approach to achieve higher dimensionality in conducting compounds involves the incorporation of molecular CTCs into a polymeric scaffold.¹⁶⁻¹⁸ Integrating TTF into polymeric materials enhances processability and significantly influences solid-state organization.

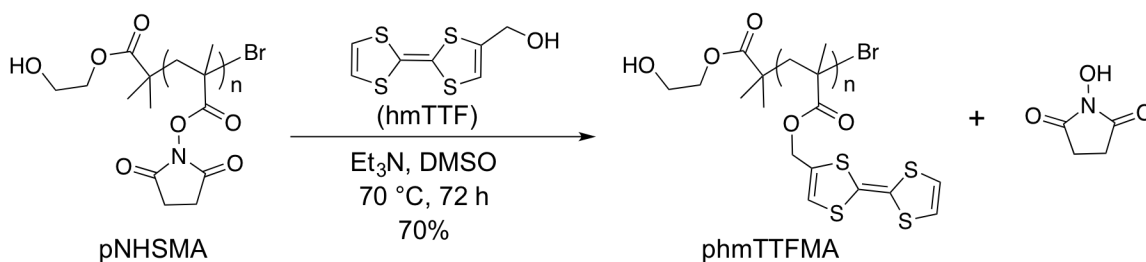
Many attempts have been made to prepare polymeric materials with TTF pendant groups. Direct polymerization of monomers with TTF motif remains a great challenge.¹⁹ Several reports have demonstrated that TTF is an inhibitor in anionic polymerization and free-radical polymerization.¹⁷⁻¹⁸ The TTF moiety also interferes with cationic polymerization.²⁰ Bulk polymerizations of monomers containing TTF motif have been reported, yet the products are poorly characterized due to limited solubility.¹⁴ Shimizu and Yamamoto successfully synthesized soluble poly(acetylene)s bearing TTF side chains using a rhodium catalyst through coordination

polymerization.²¹⁻²² However, their products exhibited low molecular weights with wide molecular weight distributions.

Compared to direct polymerization, post-polymerization modification (PPM) is a preferable approach for synthesizing polymers bearing pendant TTF units. The PPM approach begins with facile and highly controllable polymerizations to afford various precursor polymers bearing reactive pendant groups capable of highly efficient coupling with functionally-active units.²³⁻²⁴ Chujo and colleagues reported PPM of a polymethacrylate backbone by attaching TTF via azide-alkyne cycloaddition chemistry. This strategy was limited to a maximum of 59 mol% of TTF functionalization.²⁵ The incomplete degree of functionalization is proposed to result from steric hindrance between the neighboring triazole and/or TTF moieties.²⁵

To explore the electronic properties of polymers with higher TTF content, we herein report a facile PPM procedure using a substitution reaction between 4-(hydroxymethyl)TTF (hmTTF) and poly(*N*-hydroxylsuccinimide methacrylate) (pNHSMA), where NHS groups are replaced with TTF groups via nucleophilic acyl substitution (Scheme 3.3). With this method, we improved the TTF incorporation to *ca.* 70 mol% (76 wt%). The electrochemical and electric properties of the polymer have been studied and are shown to be analogous to those of molecular TTF. The conductivity and morphology of the obtained polymer are easily tuned by its electronic interactions with various electron acceptors.

Scheme 3.3 Synthesis of poly(hmTTF methacrylate) through PPM using an acyl substitution reaction with an active ester.



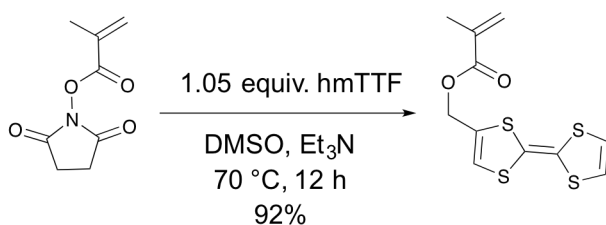
3.4.2 Incorporating TTF Motifs into Polymeric Materials

To synthesize polymers bearing pendant TTF motifs by PPM, we first synthesized the macromolecular precursor pNHSMA by atom-transfer radical polymerization (ATRP), which

was then functionalized via nucleophilic acyl substitution. Unlike Chujo's work employing azide-alkyne cycloaddition that yielded bulky pendant triazoles, we chose to use activated esters. We hypothesized that replacing sterically hindered NHS esters with TTF during PPM is a favorable process and allows for the improved extent of side-chain functionalization. Strong nucleophiles, such as primary amines, are frequently used in PPM due to their quantitative substitution with NHS esters. However, 4-(aminomethyl)TTF has very low stability and decomposes within a few hours at room temperature.²⁶ We also attempted the synthesis of amine-functionalized TTF analogs with an alkyl spacer to improve stability, but neither the substitution of protected amines nor the reduction of an azide were successful (Scheme 3.8).²⁷

In order to avoid the use of amine-functionalized TTF, we successfully synthesized hmTTF,²⁸ a TTF derivative with hydroxyl functional group that is stable up to 150 °C (Figure 3.12), and investigated its potential as the PPM nucleophile. Synthesis of hmTTF methacrylate via a nucleophilic acyl substitution reaction between hmTTF and NHSMA monomer was facile and proceeded in near-quantitative yield (Scheme 3.4). Subsequently, hmTTF was reacted with pNHSMA, resulting in the polymer phmTTFMA (Scheme 3.3). Optimized PPM conditions to maximize TTF loading required reactions in dimethylsulfoxide (DMSO) at 70 °C for 3 d with an excess amount of triethylamine. The triethylamine was needed to suppress side reactions such as succinimide ring opening.²³ TTF incorporation into the polymer backbone reached a plateau after 72 h of reaction time.

Scheme 3.4 Synthesis of hmTTF methacrylate through substitution reaction between hmTTF and NHSMA.



Direct polymerization of the TTF-functionalized monomer was compared to PPM by subjecting hmTTF methacrylate to both radical and anionic polymerization conditions. We attempted various polymerization methods, including free-radical polymerization and reversible addition-fragmentation chain transfer using azobisisobutyronitrile, ATRP and single-electron

transfer living radical polymerization using ethyl α -bromoisobutyrate, and anionic polymerization using *n*-butyllithium. However, no polymerization was observed for any of these methods, and a near-quantitative amount of starting material hmTTF methacrylate was recovered. Agreeing with previously published reports,¹⁷⁻¹⁸ these results support the claim that PPM is the preferred approach for incorporating the TTF motifs into polymers.

We determined the maximum TTF functionalization of a polymer by using various amount of hmTTF in the substitution reaction. As shown in Table 3.2a, the molar equivalent of hmTTF used in the substitution reaction corresponded to the percent TTF functionalization of the yielded polymer until 0.6 equivalent of hmTTF was reached. Based on the absorbance spectra, the maximum TTF functionalization into the pNHSMA was *ca.* 70 mol% (*ca.* 76 wt%) (Figure 3.7-3.9). Similar compositions were measured by ¹H NMR (Table 3.3 and 3.4) and sulfur or nitrogen elemental analysis (Table 3.5 and 3.6).

Table 3.2 (a) PPM results of pNHSMA ($M_n = 55.3$ kDa, PDI = 1.64) with varying amount of hmTTF used in the substitution reaction; (b) PPM results of pNHSMA with varying molecular weight. The molar equivalent of hmTTF is 1.2 with respect to the NHS repeating unit.

(a)	Mol. Equiv. of hmTTF ^a	Degree of TTF substitution (% of repeat units TTF) ^b	(b)	Molecular weight of pNHSMA (PDI)	Degree of TTF substitution (% of repeat units TTF)
	0.3	31 (P1)		18.2 kDa (1.32)	68 (P8)
	0.4	40 (P2)		30.2 kDa (1.57)	68 (P9)
	0.6	59 (P3)		55.3 kDa (1.64)	71 (P6)
	0.8	65 (P4)		81.8 kDa (1.42)	68 (P10)
	1.0	70 (P5)		125.7 kDa (1.52)	69 (P11)
	1.2	71 (P6)			
	4.0	70 (P7)			

^a Calculated relative to the NHS repeating unit.

^b Determined from UV-Vis data where the standard deviation is less than 0.02. Similar results were obtained by ¹H NMR and elemental analysis of S and N.

We attributed the observed incomplete conversion to the steric hindrance of neighboring TTF/NHS moieties and supported this hypothesis by synthesizing less compact precursor polymers.²⁹ We synthesized a random copolymer of p(NHS₄₀-co-MMA₆₀) where MMA is used as the comonomer. When p(NHS₄₀-co-MMA₆₀) was subjected to PPM with hmTTF, the conversion of NHS repeat units to TTF pendants was improved to over 80 mol% completion. We also synthesized poly(*N*-acryloxysuccinimide) (pNAS) where the less sterically congested acrylate monomer was used as the polymer backbone. When pNAS was subjected to the PPM conditions, the TTF incorporation was improved to 78 mol%. These results support our

hypothesis that bulky groups hinder the completion of PPM. In addition, we subjected phmTTFMA to a reaction with methanol. The infrared (IR) spectrum of the obtained polymer is similar to that of p(hmTTFMA₄₀-co-MMA₆₀) and the NHS peak intensities are significantly decreased, nearly to the limit of detection (Figure 3.10). The integral ratio (TTF peak area)/[(TTF peak area) + (NHS peak area)] from the ¹H NMR spectrum of the isolated polymer increased from 64% to 71% after reacting phmTTFMA with methanol. An additional resonance from the methoxy group appeared in the ¹H NMR spectrum as well. These results indicated that the remaining NHS group in the phmTTFMA remains active and is substituted by less sterically congested nucleophiles such as methoxy.

A series of pNHSMA polymers of different molecular weight were subjected to PPM conditions to probe whether the molecular weight of the polymer precursor affects the extent of TTF functionalization. As shown in Table 3.2b, when reacted with hmTTF using the conditions listed in Scheme 3.3, pNHSMA with molecular weight varying from 18 kDa to 126 kDa showed a consistent *ca.* 70 mol% of TTF functionalization. The obtained phmTTFMAs were soluble in DMSO and *N,N*-dimethylformamide (DMF) but insoluble in other common organic solvents. This result is an improvement from previous methacrylate-based polymers containing TTF pendants attached by a relatively short linker, with this reported polymer only soluble in strong acids.¹⁸

3.4.3 Characterization of Polymers Bearing TTF Motifs

To determine if TTF retains its electrochemical properties when incorporated into a polymer, we characterized the polymer's redox activity by cyclic voltammetry measurements. Although the anodic peaks of the polymer are broadened due to slow diffusion, they are detectable. Both TTF and phmTTFMA in DMF give rise to $E_{pa(1)}/E_{pa(2)}$ at similar positions, -0.04/0.25 V and -0.03/0.23 V, respectively (Figure 3.1). A silver wire was used as a quasi-reference electrode (QRE), and all potentials are reported versus the QRE. These results revealed that the TTF unit in the polymer exhibits analogous redox reactivity to the molecular counterpart.

Consistent with the TTF small molecule, phmTTFMA readily formed CTCs with TCNQ, and the CTCs were characterized by UV-Vis and IR spectroscopy. Dissolving phmTTFMA in

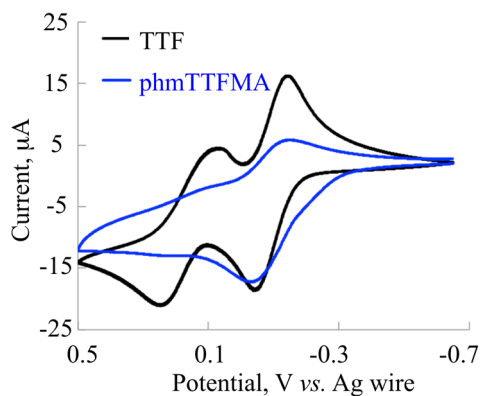


Figure 3.1 Cyclic voltammograms of *phmTTFMA* (10 mM) and *TTF* (5 mM) in DMF containing 0.1 M $[NBu_4]PF_6$ at 50 mV s^{-1} . A silver wire was used as a quasi-reference electrode.

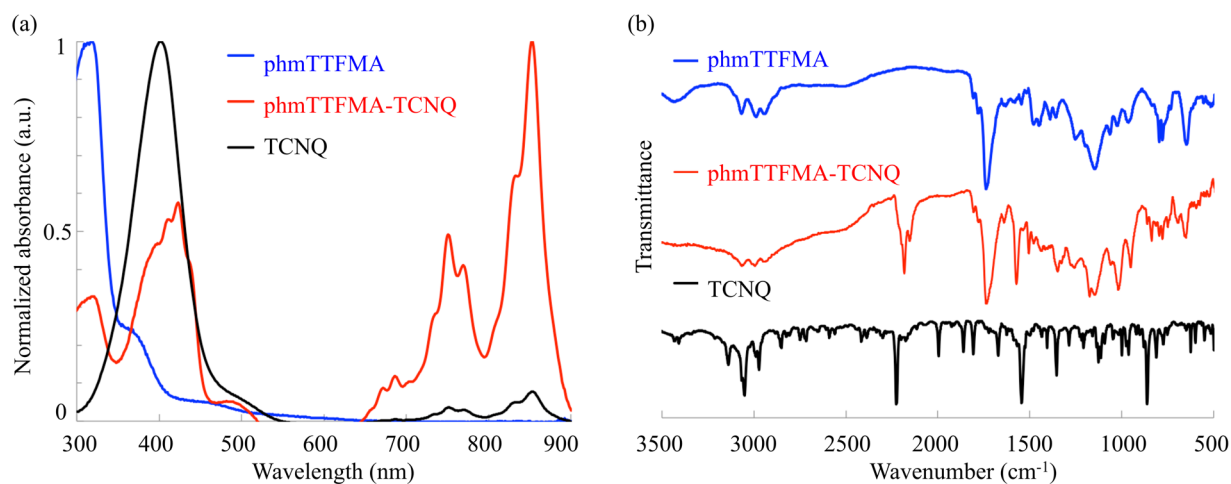


Figure 3.2 (a) UV-Vis spectra and (b) IR spectra of *phmTTFMA*, *TCNQ*, and *phmTTFMA-TCNQ*.

DMSO containing 1.0 equiv. of *TCNQ* with respect to *TTF* afforded a dark green solution. The absorption bands at 420 nm and between 650-900 nm are assigned to the radical anion of *TCNQ* (Figure 3.2a).³⁰ The IR spectrum of *phmTTFMA-TCNQ* exhibits a broad absorption band (2500-3500 cm^{-1}), suggesting the formation of CTC (Figure 3.2b).³¹ The degree of charge transfer for *phmTTFMA-TCNQ* sample is determined by the frequency of the nitrile-stretching band of *TCNQ*.³² The IR spectrum of *phmTTFMA-TCNQ* (1:1 molar ratio) shows a major band in the nitrile-stretching region at 2180 cm^{-1} and a minor band at 2149 cm^{-1} . With the addition of excess amount of *TCNQ* to the *phmTTFMA*, an uncomplexed nitrile-stretching band around 2222 cm^{-1} appeared in the IR spectrum while the bands at 2149 cm^{-1} and 2180 cm^{-1} persisted and were assigned to the anion radical of *TCNQ*, which is consistent with the UV-Vis absorption analysis.

The UV-Vis and IR spectra suggest that the TTF unit in phmTTFMA and TTF possess analogous chemical reactivity toward TCNQ.

We further compared the electrical conductivity and processability between phmTTFMA and TTF. Polymeric samples (phmTTFMA) form free-standing films with an electrical conductivity of 1.4×10^{-6} S/cm (Figure 3.14). We doped phmTTFMA with three different electron acceptors that possess varying electron affinity. When the film was oxidized by iodine and TCNQ, the electrical conductivities increased to 2.3×10^{-3} S/cm and 2.3×10^{-5} S/cm, respectively. The electrical conductivity of the phmTTFMA-TCNQ complex showed about one order of magnitude improvement, compared to that of phmTTFMA. This result was attributed to the inhomogeneous degree of CT in phmTTFMA-TCNQ samples as shown by its IR spectrum. Nevertheless, unlike TTF-TCNQ co-crystal whose electrical conductivity along the stacking direction is about three orders of magnitude higher than that in the perpendicular direction,¹⁴ phmTTFMA-TCNQ exhibits similar electrical conductivity in all directions. The conductivity of the film increased slightly to 1.5×10^{-6} S/cm when chloranil, a weaker electron acceptor, was used. This is expected since the small molecule analog is mostly neutral.³³ The conductivity studies revealed that phmTTFMA-based CTCs exhibit higher electrical conductivities when electron acceptors with higher electron affinities are employed.

Lastly, we investigated how the morphology of phmTTFMA-based CTCs impacts conductivity. Powder X-ray patterns of phmTTFMA showed only one broad peak around 16.6 degrees two-theta, suggesting that the inter-planar spacing of the TTF planes in the polymer is around 5.3 Å (Figure 3.3). The polymer remained amorphous after doping with iodine vapor. No crystalline peaks were observed when less than 0.3 equiv. of TCNQ/chloranil were added to the polymer system. However, when doping with 1 equiv. of TCNQ, sharp peaks at 6.7° and 10.7° appeared indicating an increase in crystallinity. Upon addition of chloranil to phmTTFMA, a sharp reflection appeared at 9.1° with higher-order reflections at 18.2, 27.3, 36.4, and 45.5°, indicating high crystallinity and lamella-like structures for the phmTTFMA-chloranil complex. Phase separation occurred when phmTTFMA with less TTF functionalization (**P1**) was used (Figure 3.13). The powder X-ray patterns of phmTTFMA and its CTCs indicated the materials morphologies depend on the specific electron acceptor.

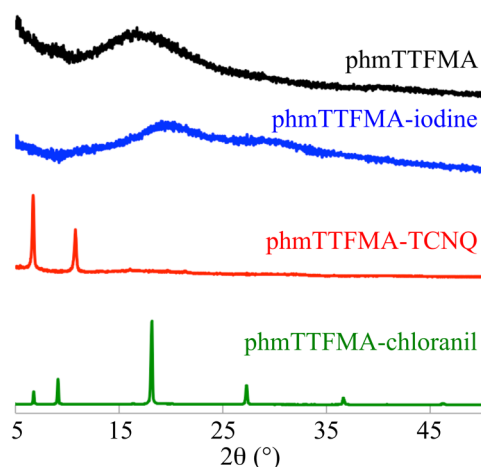


Figure 3.3 Powder X-ray patterns of the cast films of phmTTFMA and its CTCs with iodine, TCNQ, and chloranil from DMSO.

3.4.4 Conclusions

In summary, we developed an efficient method to graft TTF side chains to a polymethacrylate backbone using PPM via nucleophilic acyl substitution reaction. With this method, we achieved a degree of TTF functionalization to *ca.* 70 mol% (76 wt%) on polymers over a wide range of molecular weights ($18 \text{ kDa} \leq M_n \leq 126 \text{ kDa}$). The incomplete conversion is attributed to the steric hindrance of neighboring TTF/NHS moieties, especially when a congested polymer backbone was employed. The electrochemical and conductivity properties of the obtained polymer were measured and are analogous to that of molecular TTF. Unlike its brittle small-molecule analogs whose applications have been limited due to their one-dimensional conductivity, film-forming phmTTFMA-based CTCs with various electron acceptors including iodine, TCNQ, and chloranil showed an isotropic electrical conductivity. Compared to the uncomplexed phmTTFMA with a conductivity of $2.3 \times 10^{-5} \text{ S/cm}$, all of the polymeric CTCs showed enhanced electrical conductivity, which is primarily influenced by the electron affinity of the electron acceptors used in the CTCs. The morphology of the phmTTFMA also depends on its electronic interactions with different electron acceptors.

The energy-dissipative properties of phmTTFMA-based CTCs are currently under investigation via shock wave experiments. However, these CTCs may not be ideal candidates for SWED due to the incomplete functionalization of phmTTFMA. Instead of incorporating TTF

moieties to macromolecular backbones as discussed in this section, we decided to focus on the development of a polymethacrylate backbone with TCAQ as the pendant group using direct polymerization as shown in section 3.5.

3.5 PINIT in an Amorphous Organic Material Bearing TCAQ Motifs

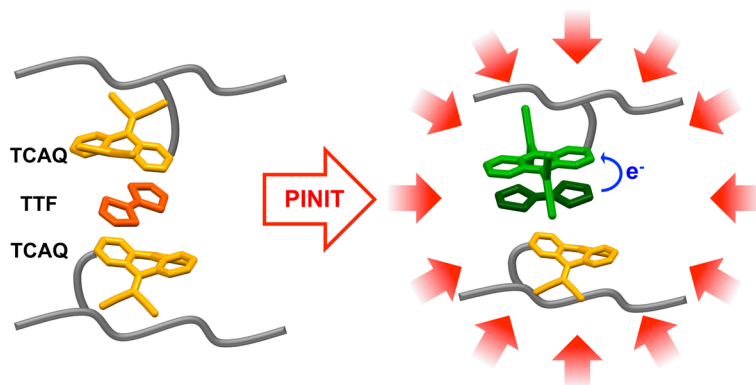
3.5.1 Introduction

PINIT is an intriguing phenomenon in which a material undergoes a change in its electrical, magnetic, and optical properties^{1, 34-36} as a result of electron transfer from an electron donor to an electron acceptor upon the application of external pressure. Since the pioneering work by Torrance et al. on PINIT using a TTF-CA complex,¹ many experimental and theoretical studies have been conducted to understand and control PINITs for both organic and inorganic crystalline materials.^{2, 35, 37-43} For example, the PINIT barrier is tunable by varying the ionization potential of the electron donor or the electron affinity of the electron acceptor in the donor-acceptor (DA) complexes.¹⁻² The composition of the crystalline material also affects the pressure barrier of the PINIT. Sano et al. reported that changing the molar ratio from 1:1 to 2:1 for an organic DA pair comprising TTF and iodanil increased the pressure required for the PINIT from 1.9 GPa to 3.1 GPa.³⁷⁻³⁸ To the best of our knowledge, PINIT has been limited to crystalline materials.^{1-2, 35, 37-43} The importance of the crystalline lattice in transmitting applied external force remains unclear. Herein, we demonstrate the feasibility of pressure-induced electron transfer behavior in amorphous and isotropic glassy solids that have potential use as pressure-responsive materials (Scheme 3.5).

From both fundamental and technological perspectives, there are advantages to studying pressure-induced electron transfer in amorphous solid polymers. First, the composition of donor acceptor co-crystal materials is not easily varied over a continuous range. In contrast, simply mixing varying proportions of donor and acceptor polymers allows for a range of compositions to be studied, provided that phase separation does not occur. Second, crystalline DA complexes tend to be brittle and are often unable to be processed. In contrast, their amorphous polymer analogs exhibit improved processability, which opens the way to uses in thin film forms that may

be of interest for applications as switchable materials in which external stimuli such as pressure, temperature, and magnetic/electric fields control the extent of charge transfer.^{1, 33-34}

Scheme 3.5 A schematic representation of PINIT in amorphous TTF-(pTCAQ)₂.

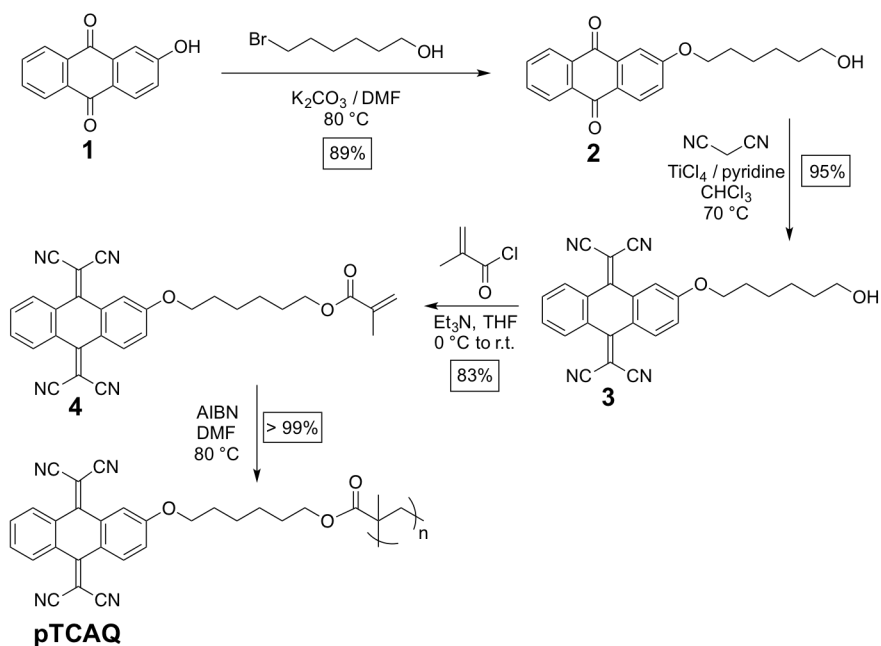


Herein, we incorporated electron-accepting 11,11,12,12-tetracyano-9,10-anthraquinodimethane (TCAQ) moieties covalently into a polymer backbone and added 0.5 molar equivalent of electron-donating TTF non-covalently to form DA pairs within the polymer matrix to produce an amorphous mixture of TTF-(pTCAQ)₂, and we investigated the feasibility and reversibility of pressure-induced electron transfer in such amorphous DA pairs using a diamond anvil cell (Scheme 3.5). TTF was chosen as the electron-donating motif due to its ability to form DA pairs with various electron acceptors capable of undergoing PINIT.¹ For the electron-accepting motif, TCAQ was chosen due to its high LUMO level and ability to transform from a butterfly-shaped geometry to an aromatic planar-shaped geometry upon accepting two electrons.⁵ We hypothesized that this butterfly-shaped to planar-shaped transformation of the TCAQ motif in TTF-(pTCAQ)₂ can be facilitated by pressure, similar to the reported anthracene cyclophane photodimer.⁴⁴ The energy difference between the HOMO of TTF and the LUMO of TCAQ was estimated to be 0.79 eV (Table 3.8), which indicates a neutral state as the value is greater than zero.⁴⁵ The DA pair composed of TTF and TCAQ was expected to undergo pressure-induced electron transfer around 2.4 GPa based on a comparison to related structures in Torrance's V-shaped diagram.¹

3.5.2 Synthesis and Characterization of PTCAQ and its Blends with Molecular TTF

In order to synthesize polymers bearing pendant TCAQ motifs, we prepared a methacrylate monomer containing a TCAQ moiety (Scheme 3.6). A hexyloxy group was added as a linker to ensure solubility in organic solvents and provide processability. Hydroxyhexyloxyanthraquinone **2** was synthesized by a substitution reaction between the 2-hydroxyanthraquinone **1** and 6-bromo-1-hexanol.⁴⁶ Knoevenagel condensation between compound **2** and malononitrile yielded hydroxyhexyloxy-TCAQ **3**.⁴⁶ Monomer **4** was synthesized by reacting methacryloyl chloride with **3**.⁴⁷ A soluble, TCAQ-bearing polymer, **pTCAQ**, with a number average molar mass $\langle M_n \rangle$ of 41.7 kDa (polydispersity, $D = 1.63$) was prepared by free-radical polymerization using 2,2'-azobis(2-methylpropionitrile) as the initiator.⁴⁸ We attempted to synthesize **pTCAQ** using various controlled polymerization techniques, including reversible addition-fragmentation chain transfer using 2,2'-azobis(2-methylpropionitrile) via atom transfer radical polymerization, and single-electron transfer living radical polymerization using ethyl α -bromoisobutyrate; however, the conversion was low and the resulting products were oligomers/polymers with low molecular weights.

Scheme 3.6 Synthesis of pTCAQ via free-radical polymerization.



Unlike the co-crystals of TTF-TCAQ which exhibit a fixed 1:2 molar ratio,⁴⁹ the ability to prepare continuously variable compositions of TTF-**pTCAQ** was easily demonstrated. We prepared a series of TTF and **pTCAQ** blends by mixing various amounts of TTF with **pTCAQ** in anhydrous dichloromethane (CH_2Cl_2). The solution was cast onto a glass slide, and the CH_2Cl_2 was removed via slow evaporation under nitrogen. The sample was further dried under vacuum at 40 °C overnight. The compositions of these blends were determined using elemental analysis (Table 3.7) and thermogravimetric analysis (Figure 3.20). All of the blends exhibited a single glass transition temperature (T_g), indicating TTF and **pTCAQ** are miscible within the tested window (Figure 3.19). The glass transition temperature decreased monotonically with TTF composition in the range of 105 °C to 65 °C. Despite the T_g s being above room temperature, the TTF-**pTCAQ** blends produced easily handled free-standing films (Figure 3.24).

The effect of TTF on the morphology of the blends was investigated. Powder X-ray patterns of the blends showed distinct, sharp peaks when the TTF concentration was above 17 wt%, the composition at which the molar ratio between TTF and **pTCAQ** is above 1:2 (Figure 3.4), suggesting the presence of ordered domains. Most of these peaks are consistent with the Powder X-ray diffraction patterns of crystalline TTF. However, due to preferred orientation, the relative intensity of each peak in the TTF-**pTCAQ** blends varied from that of molecular TTF prepared in the same fashion. The inhibitory effect of **pTCAQ** on TTF crystallization below the 1:2 molar ratio is potentially due to charge-transfer interactions,⁵⁰ which was corroborated by the IR spectra (Figure 3.18). The frequency of the nitrile stretching band of **pTCAQ** shifted slightly

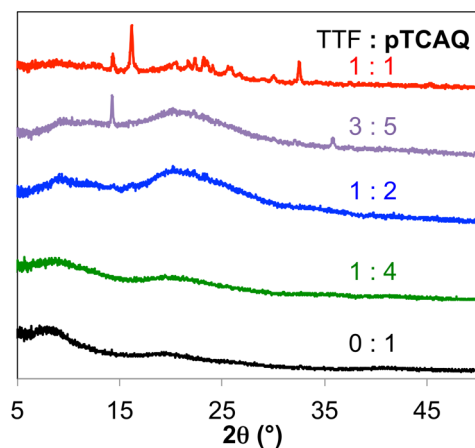


Figure 3.4 Powder X-ray patterns of the cast films of TTF-**pTCAQ** with varying molar ratios.

from 2226.0 cm^{-1} in pure **pTCAQ** to 2225.3 cm^{-1} in a 1:2 blend, indicating weak charge-transfer interactions between TTF and **pTCAQ** under ambient temperature and pressure.³ Plotting the frequency of the nitrile stretching band against TTF composition in the blend, we observed a nearly linear correlation up to 17 wt% TTF, at which point a smaller change was observed with further increases in TTF up to 40 wt% (Figure 3.18a). Additional data with higher TTF concentrations in the blends were collected to create a Job plot, which provided good evidence for 1:1 binding with peak found at $x = 0.55$ (cf. the theoretical values of 0.50 for 1:1 binding) (Figure 3.18b).

3.5.3 PINIT in TTF-(**pTCAQ**)₂

The TTF-(**pTCAQ**)₂ blend, whose molar ratio between molecular TTF and TCAQ motif in the polymer is 1:2, was chosen as the amorphous material for pressure-induced electron transfer experiments, given the similar composition to the small-molecule, co-crystal analog.⁴⁹ Pressure-induced electron transfer was evaluated using a diamond anvil cell where the fluorescence spectra of ruby chips were used to calibrate the pressure. As shown in Figure 3.5a, the absorption spectra of TTF-(**pTCAQ**)₂ exhibited new absorption bands in the region between 500 nm to 800 nm upon pressurization, suggesting the possibility of a pressure-induced electron transfer event.^{1, 49} The TTF-(**pTCAQ**)₂ blend remains amorphous under high pressure, as evidenced by its corresponding optical image under crossed polarized light (Figure 3.23). The absorption spectra of the control samples, i.e. TTF and **pTCAQ** as separate entities, only showed bathochromic shifts and broadened bands at high pressure, presumably due to increased van der Waals interactions (Figure 3.5b,c).⁵¹⁻⁵³

In order to demonstrate that the pressure-induced absorption bands for TTF-(**pTCAQ**)₂ are a result of charge-transfer interactions, we electrochemically reduced non-blended **pTCAQ** to **pTCAQ**²⁻ and oxidized molecular TTF to TTF⁺ and TTF²⁺ and investigated their absorption spectra (Figure 3.6 & 3.15). The absorption peak at 532 nm from TTF-(**pTCAQ**)₂ under 5.0 GPa is comparable to the absorption peak of **pTCAQ**²⁻ in anhydrous DMF solution at 522 nm (Figure 3.6). The wavelength of the 532 nm peak shifted to 527 nm when the applied pressure was 2.0 GPa (Figure 3.5a). The increased absorption wavelength of this peak from the solution state **pTCAQ**²⁻ to the solid state TTF-(**pTCAQ**)₂ under 2.0 and 5.0 GPa is likely due to decreased

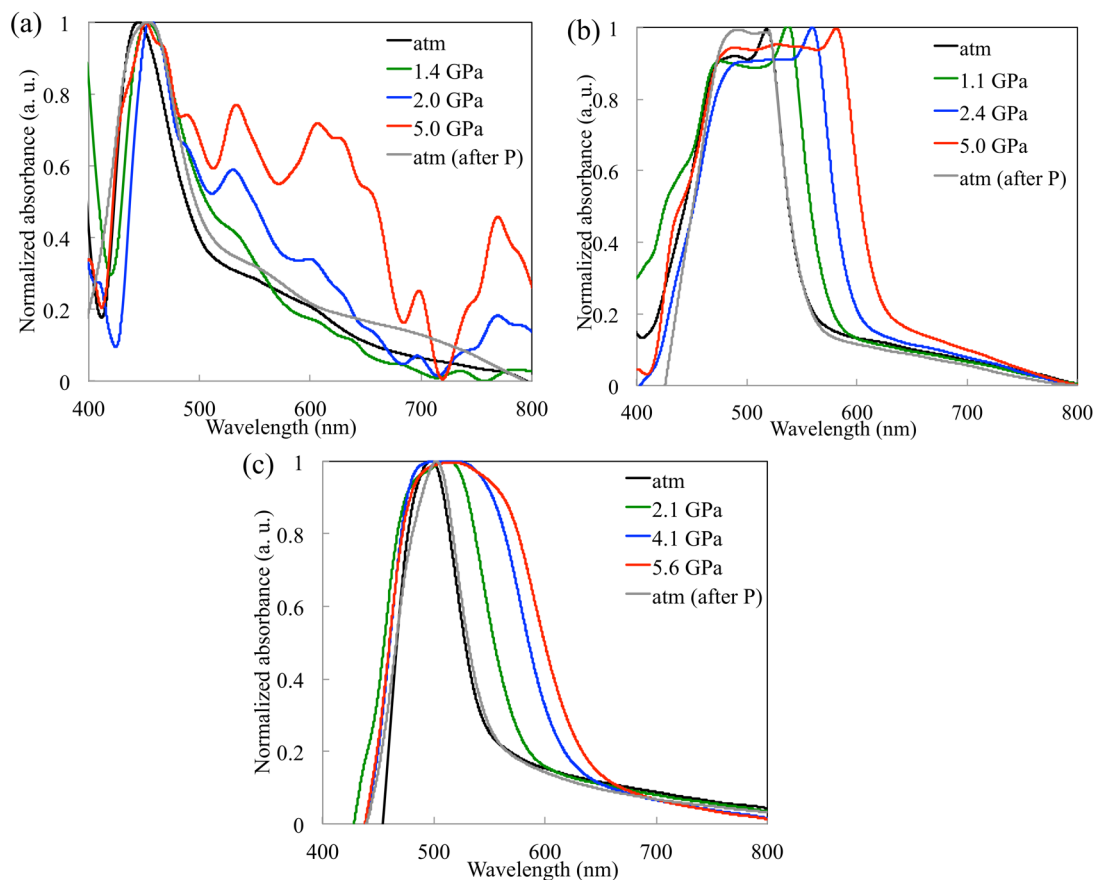


Figure 3.5 Solid-state absorption spectra of (a) TTF-(**pTCAQ**)₂, (b) TTF, and (c) **pTCAQ** under different pressures, where atm (after P) denotes the spectra collected after releasing pressure for 14 hours.

intermolecular distances.⁵¹⁻⁵³ We were not able to observe any spectroscopic evidence for the formation of the TCAQ⁻ radical anion within **pTCAQ**, which is in agreement with previously reported simultaneous two-electron reduction of TCAQ to TCAQ²⁻ (Figure 3.16).⁵ This led us to conclude that the anionic species in the blend is **pTCAQ**²⁻. Analogously, the absorption peak around 627 nm for the TTF-(**pTCAQ**)₂ blend under 5.0 GPa is comparable to the absorption peak of ionic TTF²⁺ in anhydrous DMF solution at 617 nm. Based on these results, we concluded amorphous TTF-(**pTCAQ**)₂ was capable of undergoing PINIT. As the pressure was increased from 2.0 GPa to 5.0 GPa, the absorption bands at 500–800 nm exhibited an increased intensity relative to the absorption peak around 450 nm, which represents the neutral species, suggesting an increase in the ionic species in the blend (Figure 3.5a). Based on the absorbance spectra of TTF-(**pTCAQ**)₂, the experimental transition pressure for electron transfer is ca. 2 GPa; that is, slightly lower than the extrapolated value of 2.4 GPa using Torrance’s model.¹ This difference

could be due to the composition variation from Torrance's model, where all the DA pairs have molar ratio of 1:1 instead of 1:2.

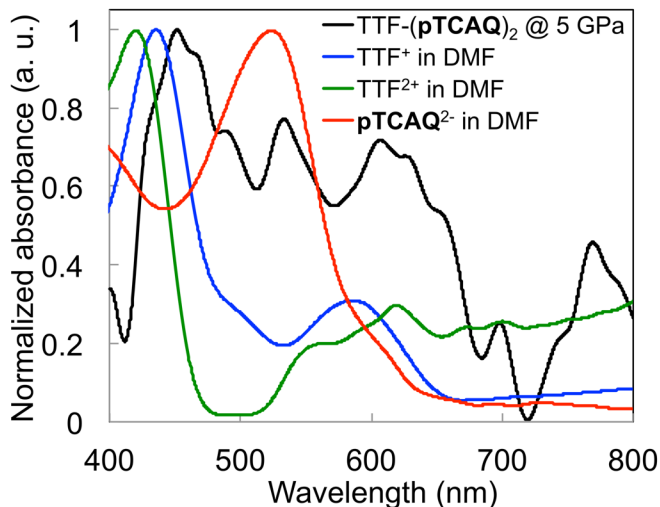


Figure 3.6 Absorbance spectra comparison of pressurized TTF-(pTCAQ)_2 (solid state) and electrochemically oxidized TTF^+ , TTF^{2+} and reduced pTCAQ^{2-} in anhydrous DMF containing 0.1 M $[\text{NBu}_4]\text{PF}_6$.

The reversibility of the pressure-induced electron transfer in the TTF-(pTCAQ)_2 material was subsequently probed. Upon releasing the pressure in the diamond anvil cell for 14 h, the absorbance (Figure 3.5a), IR (Figure 3.21a), fluorescence (Figure 3.21b) spectra, and powder X-ray diffraction patterns (Figure 3.22) of TTF-(pTCAQ)_2 were nearly identical to the spectra collected before pressurization. When the TTF-(pTCAQ)_2 sample was subjected to a second pressurization cycle, similar absorption peaks were observed at 500–800 nm, confirming this process is nearly reversible (Figure 3.21c). It is known that the driving force of neutral-to-ionic transition for crystalline materials is the increased Madelung energy of an ionic crystal lattice upon pressurization.³⁷ In contrast, for the amorphous TTF-(pTCAQ)_2 blend, we postulate the observed pressure sensitivity is caused by the destabilization of the neutral butterfly-shaped TCAQ motif relative to the ionic planar-shaped TCAQ^{2-} motif and the reduced activation barrier at high pressure due to the negative activation volume from TCAQ to TCAQ^{2-} , which is analogous to the previously reported system.^{44, 54}

3.5.4 Conclusions

In summary, we have demonstrated that neutral TTF-(**pTCAQ**)₂ forms charge-transferred species upon pressurization. Absorption and emission spectra of TTF-(**pTCAQ**)₂ collected under ambient temperature and pressure before and after pressurization provide direct evidence for the reversibility of electron transfer in TTF-(**pTCAQ**)₂. To the best of our knowledge, this is the first reported observation of such a transition in an amorphous material composed of a polymeric acceptor and a molecular donor. The improved processability and tunable composition of TTF-**pTCAQ**-based DA pairs broadens the available materials capable of pressure-induced electron transfer and can be potentially used as pressure switchable materials accompanied by changes in color, charge fluctuations, magnetism, and dielectric properties.

To build a comprehensive understanding of the PINIT in amorphous phase, more systematic studies are required, e.g. investigating the effects of blend compositions on the transition pressure of electron transfer by varying either the wt% of TTF in a series of TTF-**pTCAQ** blends or the electron donors with different ionization potentials in the **pTCAQ**-based amorphous blends. Shock-induced neutral-to-ionic transition and its role on SWED should also be studied for TTF-(**pTCAQ**)₂ and other **pTCAQ**-based blends.

3.6 Experimental Details

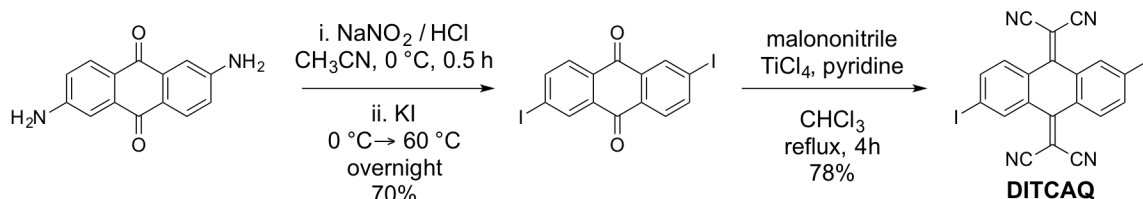
3.6.1 Experimental Details for Section 3.3

3.6.1.1 Materials and instrumentation measurements

All reagents and solvents were purchased from commercial sources and were used as received. ¹H and ¹³C NMR spectra were obtained using a Varian 500 MHz spectrometer in the VOICE NMR laboratory at the University of Illinois. All chemical shifts (ppm) were calibrated to the residual peak of the deuterated solvent. Mass spectra were obtained through the Mass Spectrometry Facility and elemental analysis data were obtained through the Microanalysis Laboratory, School of Chemical Sciences (SCS), University of Illinois at Urbana-Champaign.

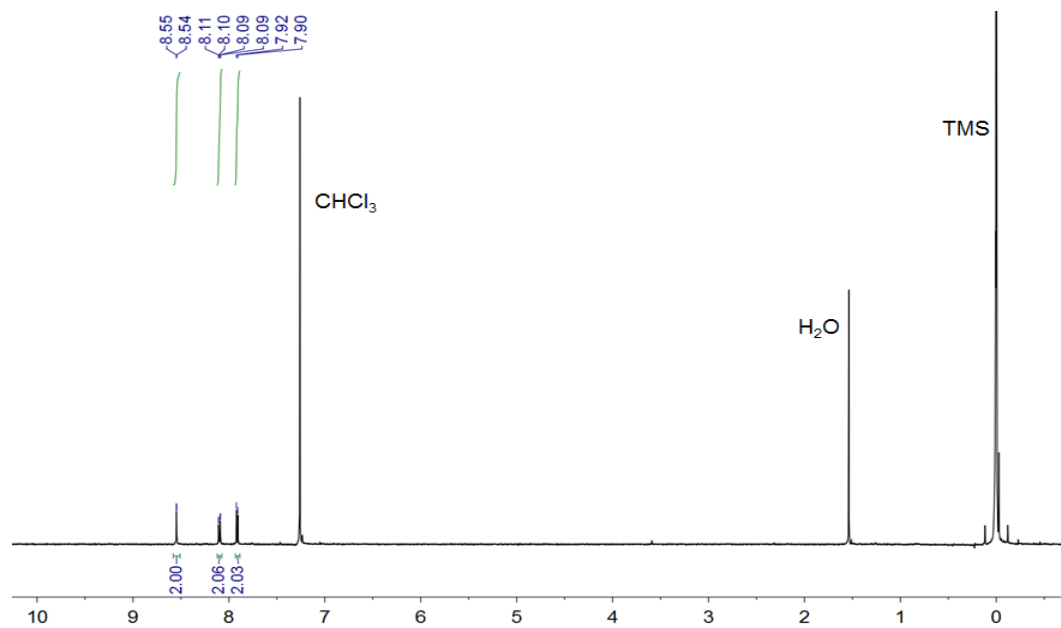
Synthesis of DITCAQ

Scheme 3.7 Synthesis of DITCAQ. The amino groups of commercially available 2,6-diaminoanthracene-9,10-dione were transformed into 2,6-diiodoanthracene-9,10-dione. The carbonyl functionalities of the intermediate were transformed to dicyanomethane groups under Knoevenagel conditions to yield DITCAQ.

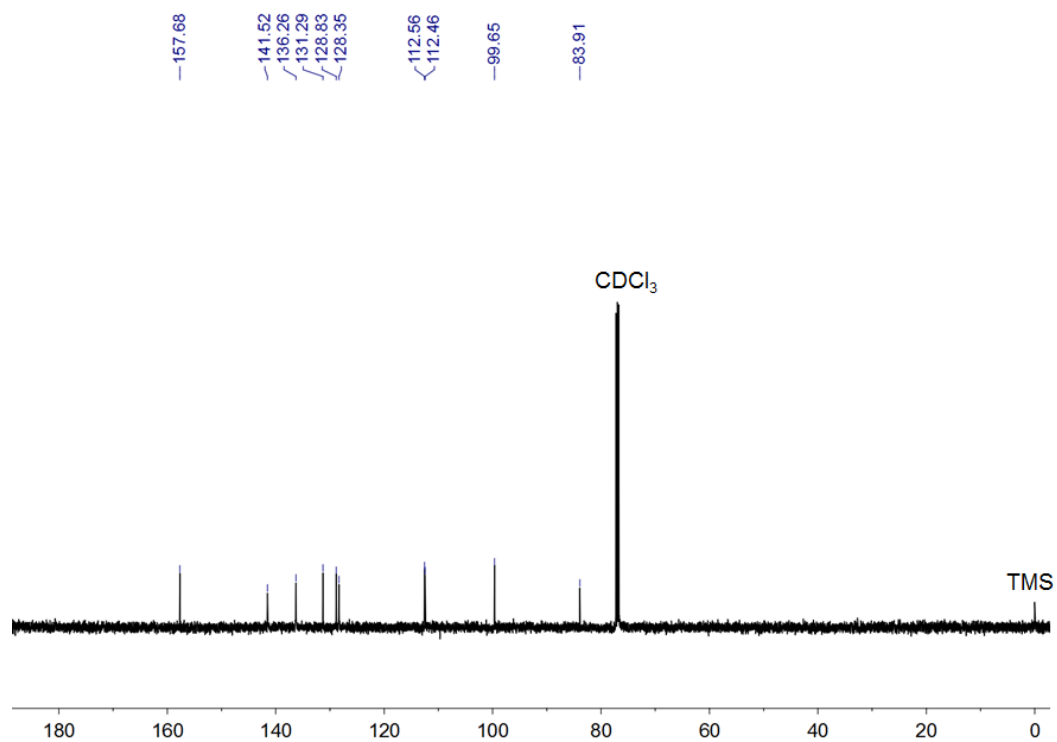


To a suspension of 2,6-diiodoanthracene-9,10-dione (5 g, 10.9 mmol) and malononitrile (2.9 g, 43.5 mmol) in chloroform (CHCl₃, 300 ml) was added dropwise titanium tetrachloride (TiCl₄, 4.8 ml, 43.5 mmol) at 0 °C. The ice bath was removed and pyridine (7 ml, 87 mmol) was added dropwise. The reaction mixture was stirred at reflux for 1 h. Additional TiCl₄ (4.8 mL, 43.5 mmol) and pyridine (7 ml, 87 mmol) were added to the reaction and the resulting solution refluxed for 4 h. The reaction mixture was cooled to room temperature, quenched with water (200 ml), and extracted with CHCl₃. The organic phase was dried with MgSO₄, and the solvents were removed under vacuum. The crude solid mixture was purified using column chromatography (silica gel) and eluted with CHCl₃ to give a yellow solid product (yield 4.7 g, 8.5 mmol, 78%). ¹H NMR (500 MHz, CDCl₃): δ 8.55 (*d*, *J* = 1.6 Hz, 2H), 8.10 (*dd*, *J* = 8.3, 1.6 Hz, 2H), 7.91 (*d*, *J* = 8.3 Hz, 2H). ¹³C NMR (125 MHz, CDCl₃): δ 157.7, 141.5, 136.3, 131.3, 128.8, 128.4, 112.6, 112.5, 99.7, 83.9. HRMS (ESI) calculated for C₂₀H₆I₂N₄ 555.8682, found 555.8680. Elemental analysis calculated for C₂₀H₆I₂N₄: C 43.20, H 1.09, N 10.08%; measured: C 43.47, H 0.85, N 9.95%.

^1H NMR of compound DITCAQ in CDCl_3



^{13}C NMR of compound DITCAQ in CDCl_3



3.6.1.2 Crystallization and sample fabrication details

Crystals of DITCAQ and anthracene-(DITCAQ)₂ were grown by slow diffusion of diethyl ether into CHCl₃ solutions. Crystals of pyrene-(DITCAQ)₂ and TTF-(DITCAQ)₂ were obtained by slow diffusion of methanol into CHCl₃ solutions. TTF-based co-crystals were grown by dissolving equimolar amounts in 60 °C acetonitrile and slowly cooling the solution to 0 °C. After washing with cold acetonitrile, the co-crystals were dried in vacuum for 24 h.

The flaky dark-green TTF-CA (or TTF-TCNQ) crystals were ground into a fine powder. The powder, which was insoluble in water, was suspended in an equal weight of a poly(vinyl alcohol) solution (5 wt% in water). Then 15 times extra mass of water was added to solution mixture. The suspension was shaken for one hour using a paint shaker and stirred for 24 hours to break up agglomerates. An adhesive-backed polyimide tape (Caplinq) was attached to a 50x50 mm² Pyrex window 6.35 mm thick (Chemglass). Circles 2 mm in diameter were cut into the tape using excimer laser ablation. The circle regions were cleaned by removing the leftover polymer disks and dissolving residual silicone adhesive with silicone remover (Motsenbocker). This yielded a 2" substrate with about sixty wells having well-defined depths ($\pm 1 \mu\text{m}$) determined by the purchased film thickness. Electron beam deposition was used to coat 150 nm of Au onto the window. The suspension from above was drop-coated over each Kapton well and allowed to dry to produce a composite for shock wave testings. Using a series of successively finer polishing papers, the excess TTF-CA (or TTF-TCNQ) material was removed until the sample was flush with the polyimide film. The sample layer thicknesses and thickness variations were confirmed with a Sloan Dektak³ ST stylus profilometer.

3.6.1.3 Laser-launched flyer plates apparatus

The apparatus for launching and monitoring laser driven flyer plates has been described in previous publications.⁵⁵⁻⁵⁶ The laser driven Al flyer plates were 700 μm in diameter and 75 μm thick. The flyer plates traveled 500 μm before impacting the sample, which was enough time to let reverberations inside the flyer plate caused by the short-duration launch laser pulses to damp out.⁵⁶ A Photon Doppler Velocimeter (PDV) was used to monitor the velocity histories of both the flyer plate and the ultrathin Au mirror. The PDV probed a region 60 μm in diameter at the center of the flyer plate.

3.6.2 Experimental Details for Section 3.4

3.6.2.1 Materials

Unless otherwise stated, all reagents and solvents were purchased from commercial sources and were used as received. *N*-hydroxysuccinimide methacrylate was recrystallized from a mixture of ethyl acetate and hexanes (*v:v* = 1:1) and dried under vacuum overnight before usage. Anhydrous DMSO, triethylamine, and methanol were obtained from an anhydrous solvent delivery system (SDS) equipped with activated alumina columns. Flash column chromatography was conducted with silica gel 60 (230-400 mesh) from Silicycle. All reactions were performed under an inert atmosphere (dry nitrogen gas) using standard Schlenk and vacuum line techniques. Poly(*N*-hydroxysuccinimide methacrylate) (pNHSMA), p(NHSMA₆₀-co-MMA₄₀), poly[*N*-(acryloyloxy)succinimide] (pNAS), and 4-(hydroxymethyl)TTF (hmTTF) were synthesized according to reported literature procedures.^{28, 57-58}

3.6.2.2 Instrumentation and measurements

¹H and ¹³C NMR spectra were obtained using either a Varian 400 MHz or 500 MHz spectrometer in the VOICE NMR laboratory at the University of Illinois at Urbana-Champaign. All chemical shifts (ppm) were calibrated to the residual proton peak of the deuterated solvent. Coupling constants (*J*) are expressed in Hertz (Hz). Splitting patterns are designated as s (singlet), d (doublet), dd (doublet of doublets), and m (multiplet). Mass spectra were obtained through the Mass Spectrometry Facility and elemental analysis data were obtained through the Microanalysis Laboratory, SCS, University of Illinois at Urbana-Champaign. UV-Vis spectra were recorded in DMSO using a Shimadzu UV-2401PC. Standard quartz cells with a path length of 2 mm from Starna Cells, Inc. were used. Infrared spectra were collected on a NEXUS 670 serial FTIR spectrophotometer. Thermal gravimetric analysis (TGA) was conducted using TA instrument Q50 at a ramping rate of 10 °C min⁻¹ under a dry nitrogen atmosphere.

Analytical Gel Permeation Chromatography (GPC) was performed on a system equipped with a Model 1200 isocratic pump (Agilent Technology, Santa Clara, CA, U.S.A.) in series with a Waters 717 autosampler, a DAWN HELEOS multiangle laser light scattering detector (MALLS) (Wyatt Technology, Santa Barbara, CA, U.S.A.), and an Optilab rEX refractive index detector (Wyatt Technology, Santa Barbara, CA, U.S.A.). Separations were performed using

serially connected size exclusion columns (10^2 Å, 10^3 Å, 10^4 Å, 10^5 Å, 10^6 Å Phenogel columns, 5 µm, 300×7.8 mm, Phenomenex, Torrance, CA, USA) at 60°C using *N,N*-dimethylformamide containing 0.1 mol/L LiBr as the mobile phase at a flow rate of 1 mL min⁻¹. Samples were filtered through a 0.45 µm PTFE filter before analysis. Absolute molecular weights of polymers were determined using ASTRA 6.1.1.17 software (Wyatt Technology, Santa Barbara, CA, U.S.A.) and calculated from dn/dc values assuming 100% mass recovery.

Electrochemical experiments were performed in an inert environment using a CHI1242b portable bipotentiostat (CH Instruments, Austin, TX). Solutions were prepared in an argon atmosphere glovebox. Cyclic voltammograms (CVs) were obtained using a silver wire as a quasi-reference electrode (QRE) and a platinum wire as a counter electrode. All potentials are reported versus the QRE. A Signatone Pro4-440N four-point-probe and a KLA-Tencor P-6 stylus surface profilometer were used to determine the electrical conductivity of casting films composed of phmTTFMA and phmTTFMA-based CTCs. The phmTTFMA-TCNQ and phmTTFMA-chloranil CTCs were prepared by mixing equimolar of phmTTFMA with TCNQ and chloranil, respectively, in DMSO. The solution was stirred at room temperature for 2 h before casting on a glass slide. A steady stream of dry nitrogen was used to evaporate DMSO overnight. The sample was further dried under vacuum at 40 °C for 24 h. Similar techniques were employed to produce phmTTFMA film for conductivity measurement. The phmTTFMA-iodine sample was prepared by exposing phmTTFMA film with iodine vapor for 2 h. For the conductivity measurement, three samples were used and each sample was measured at least five times. Powder X-ray diffraction patterns were recorded on a Rigaku MiniFlex at a scanning rate of 0.02°/s in two-theta ranging from 5° to 50°. Samples for the X-ray diffraction measurements were prepared by casting films on a zero diffraction plate purchased from MTI Corporation.

The degree of TTF functionalization for a PPM polymer was calculated from 1) absorbance spectra of the crude polymer in DMSO by using the Beer-Lambert law (see section 3.6.2.4); 2) ¹H NMR spectra of the as-obtained polymer in deuterated DMSO by using the integral ratio of (TTF peak area)/[(TTF peak area)+(NHS peak area)] (see section 3.6.2.5); and 3) weight percent of sulfur and nitrogen from elemental analysis data (see section 3.6.2.6).

3.6.2.3 Synthetic procedures

Synthesis of [2,2'-bi(1,3-dithiolylidene)]-4-ylmethyl methacrylate (hmTTF methacrylate)

To a Schlenk flask were added 4-(hydroxymethyl)TTF (0.65 g, 2.8 mmol) and *N*-succinimidyl methacrylate (0.48 g, 2.6 mmol). The solids were dissolved in anhydrous DMSO (6.5 mL) and triethylamine (3.3 mL) under nitrogen. The reaction mixture was left stirring at 70 °C for 12 h. Water (50 mL) was added and the aqueous layer was extracted with dichloromethane (4 × 50 mL). The combined organic phase was dried over MgSO₄. After filtration, the mixture was concentrated *in vacuo*. Purification of the residue by flash column (SiO₂, hexanes: ethyl acetate = 1:1 v/v) afforded the pure product as an orange solid. Yield: 0.73 g (92 %). ¹H NMR (500 MHz, CDCl₃): δ 6.34 (s, 1H), 6.31 (s, 2H), 6.20-6.18 (m, 1H), 5.68-5.64 (m, 1H), 4.93-4.91 (d, *J* = 1.0 Hz, 2H), 1.96 (dd, *J* = 1.0 Hz, 3H); ¹³C NMR (125 MHz, CDCl₃): δ 166.8, 135.7, 131.3, 126.8, 119.2, 119.1, 199.1, 111.7, 109.4, 61.2, 18.4; HRMS (ESI) calcd for C₁₁H₁₀O₂S₄ 301.9564, found 301.9557.

Typical procedure for PPM of pNHSMA

In a typical experiment, the polymer precursor pNHSMA (200 mg) and the desired amount of 4-(hydroxymethyl)TTF (Tables 2.2) were weighed into a Schlenk flask and dissolved in anhydrous DMSO (2.0 mL) and triethylamine (1.0 mL) under nitrogen. The reaction mixture was left stirring at 70 °C for 72 h and then brought to room temperature. The polymer was precipitated by pouring the reaction solution into acetone/ether (200 mL, 1:1 v/v) and was collected by filtration. The isolated polymer was further purified by re-dissolving into DMSO and re-precipitating the DMSO solution into an acetone/ether mixture. The collected re-precipitate was washed several times with acetone/ether and immediately dried under vacuum at 40 °C for 24 h. The yield of PPM ranged from 85% to 92%, whereas the TTF functionalization varied depending on reaction conditions (Tables 2.2).

Typical procedure for PPM of phmTTFMA with methanol

In a typical experiment, phmTTFMA (100 mg) and an excess amount of anhydrous methanol (0.4 mL) were added into a Schlenk flask and dissolved in anhydrous DMSO (1.0 mL) and triethylamine (1.0 mL) under nitrogen. The reaction mixture was left stirring at 70 °C for 24 h and then brought to room temperature. The polymer precipitated by pouring the reaction solution into acetone/ether (100 mL, 1:1 v/v) and was collected by filtration. The isolated polymer was further purified by re-dissolving into DMSO and re-precipitating the DMSO

solution into an acetone/ether mixture. The collected re-precipitate was washed several times with acetone/ether and immediately dried under vacuum at 40 °C for 24 h. The yield of the reaction is approximately 80%.

3.6.2.4 UV-Vis spectra and TTF functionalization calculation based on UV-Vis spectra

As shown in Figure 3.7, the maximum absorbance peak of TTF and phmTTFMA are identical (320 nm), whereas the much more concentrated pNHSMA shows little to none absorbance around that region. Thus, we can use Beer's law to determine how much TTF was incorporated into the polymer during the PPM process.

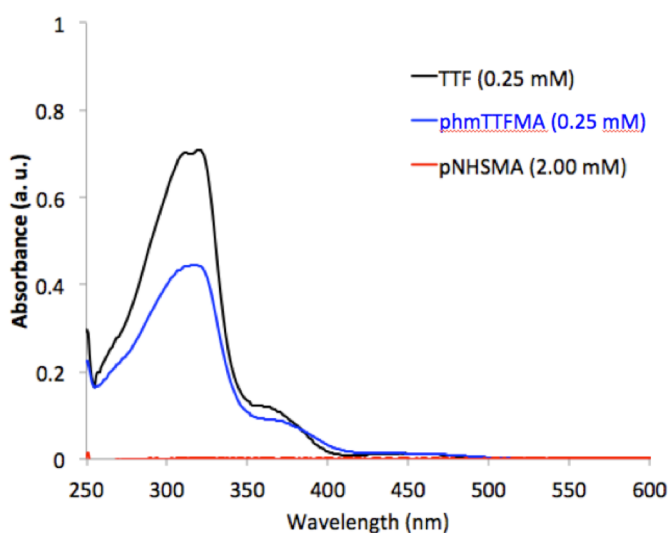


Figure 3.7 UV-Vis absorbance spectra of TTF (0.25 mM), phmTTFMA(0.25 mM), and pNHSMA (2.00 mM) in DMSO.

As shown in Figure 3.8, the concentrations of phmTTFMA in DMSO are calculated under the assumption that 100% conversion from NHS to TTF was achieved. However, based on the slope of the trendline for each series, we determined that the actual % conversion is lower than 100%. For example, for 100 mol. equiv. of **P1**, only $1.1094/2.6081 = 42.54$ mol was phmTTFMA. Since the molecular weight of hmTTFMA monomer (302.44 g/mol) differs from that of NHSMA monomer (183.16 g/mol), the mol. equiv. of unreacted pNHSMA is $(100 - 42.54) \times 302.44 / 183.16 = 94.93$ mol. Thus, the actual % TTF functionalization is $42.54 / (42.54 + 94.93) = 31\%$. Analogously, we can determine the % TTF functionalization for **P2-P11**.

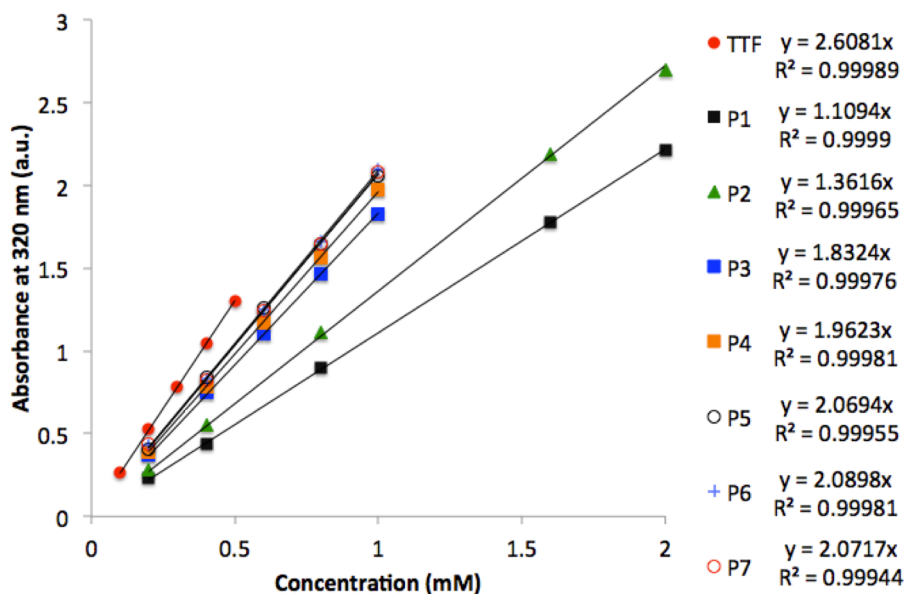


Figure 3.8 Calibration curve of TTF in DMSO and its comparisons with *phmTTFMA*, **P1** to **P7**, where 100% TTF substitution was assumed.

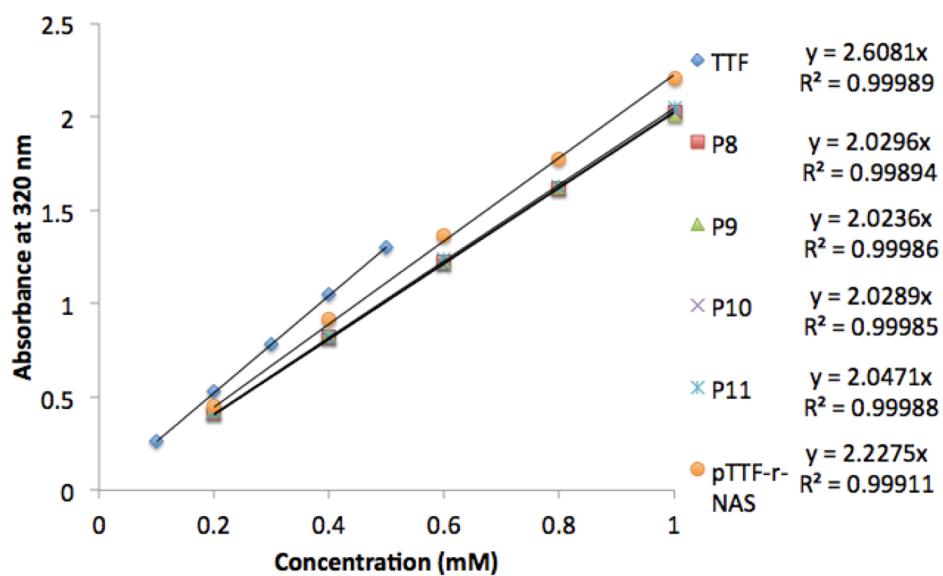
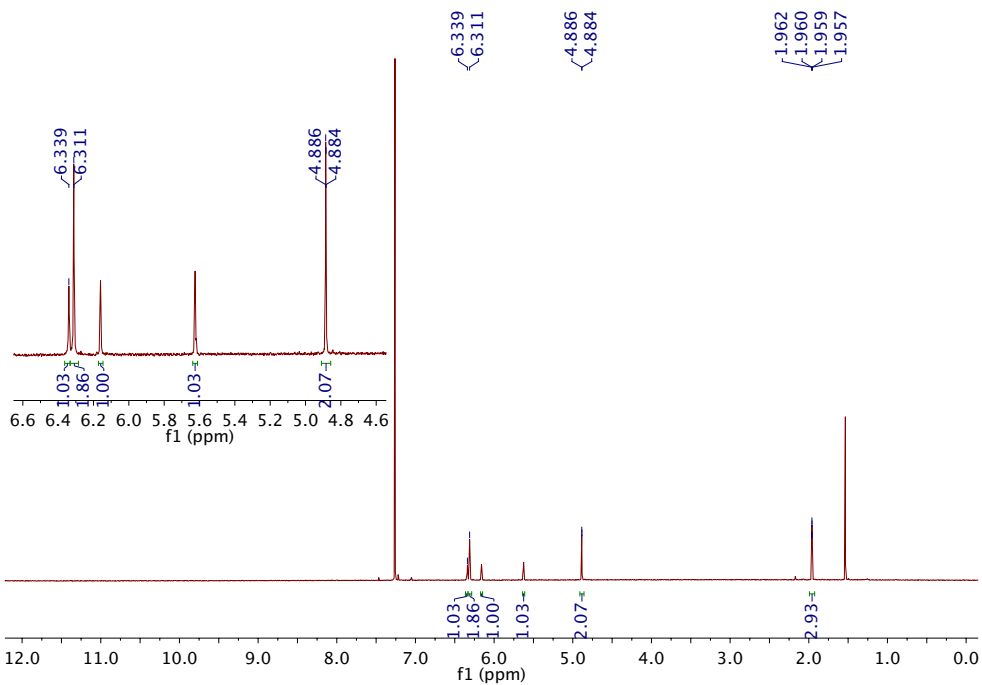


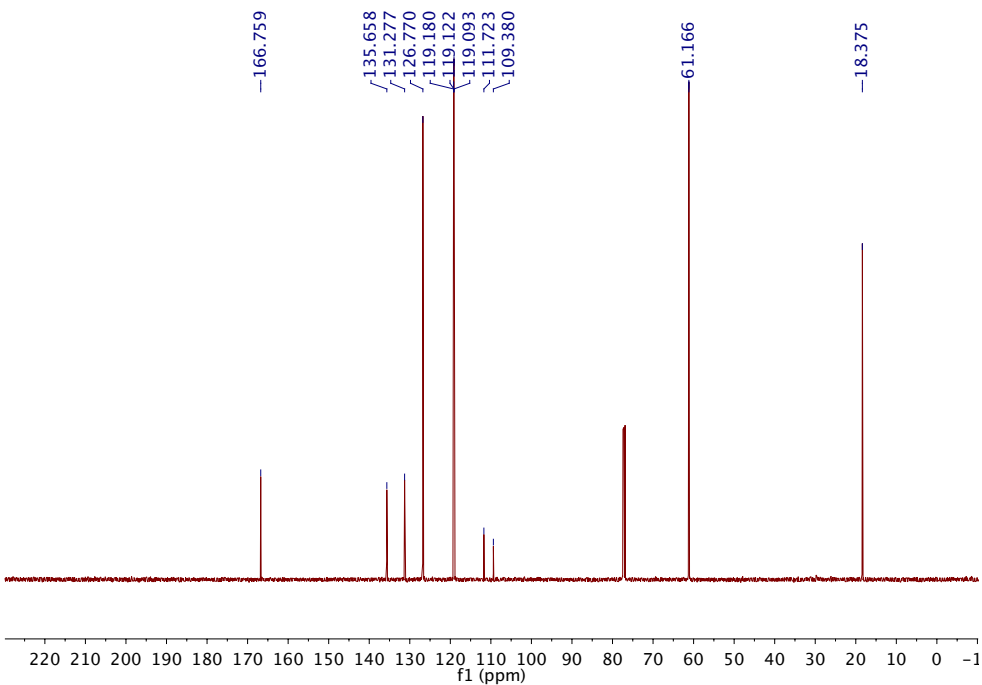
Figure 3.9 Calibration curve of TTF in DMSO and its comparisons with *phmTTFMA*, **P8** to **P11**, where 100% TTF substitution was assumed.

3.6.2.5 NMR spectra and TTF functionalization calculation based on ^1H NMR integration

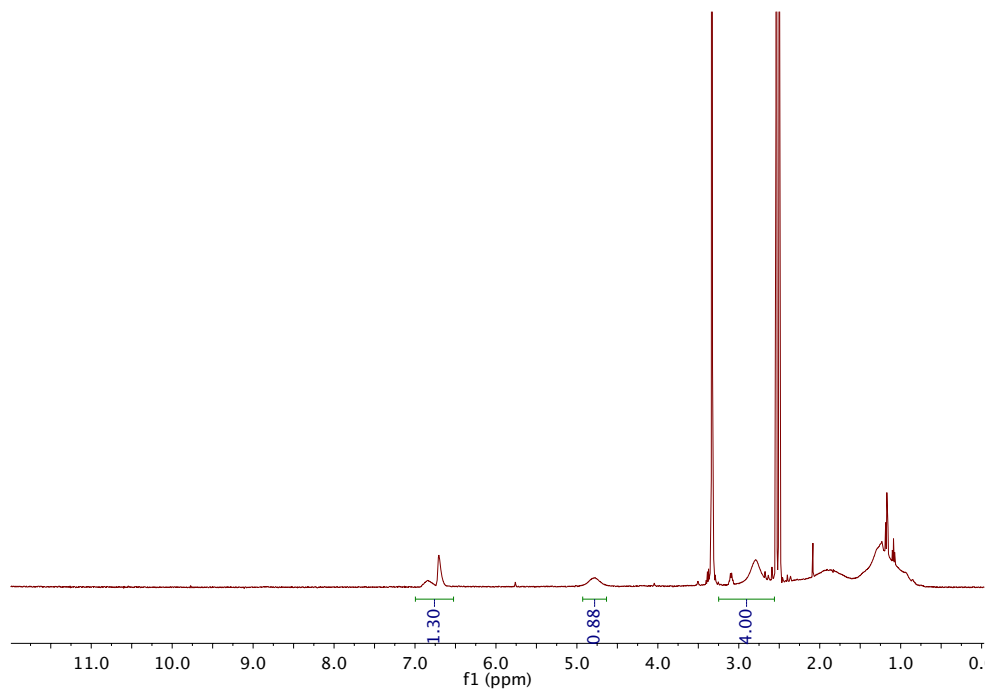
^1H NMR of compound hmTTF methacrylate in CDCl_3



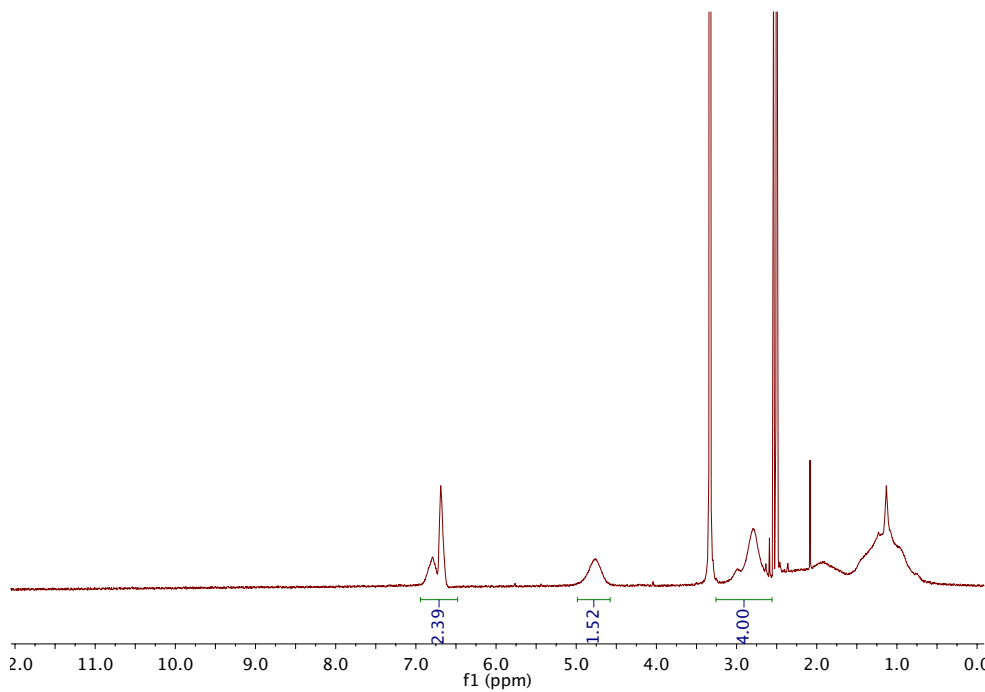
^{13}C NMR of compound hmTTF methacrylate in CDCl_3



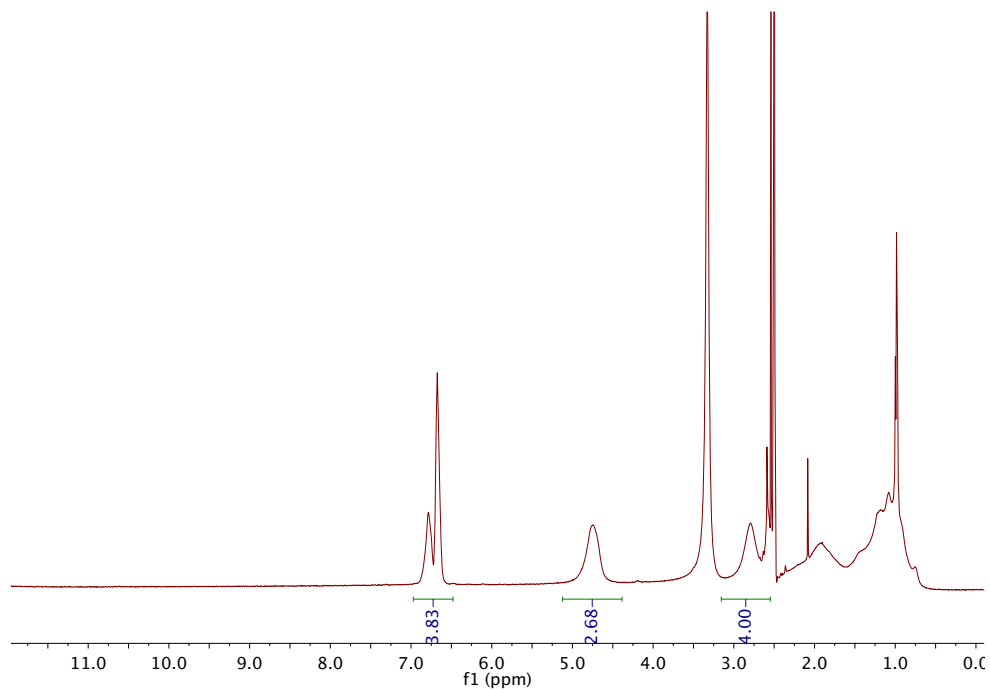
^1H NMR of P1 in $(\text{CD}_3)_2\text{SO}$



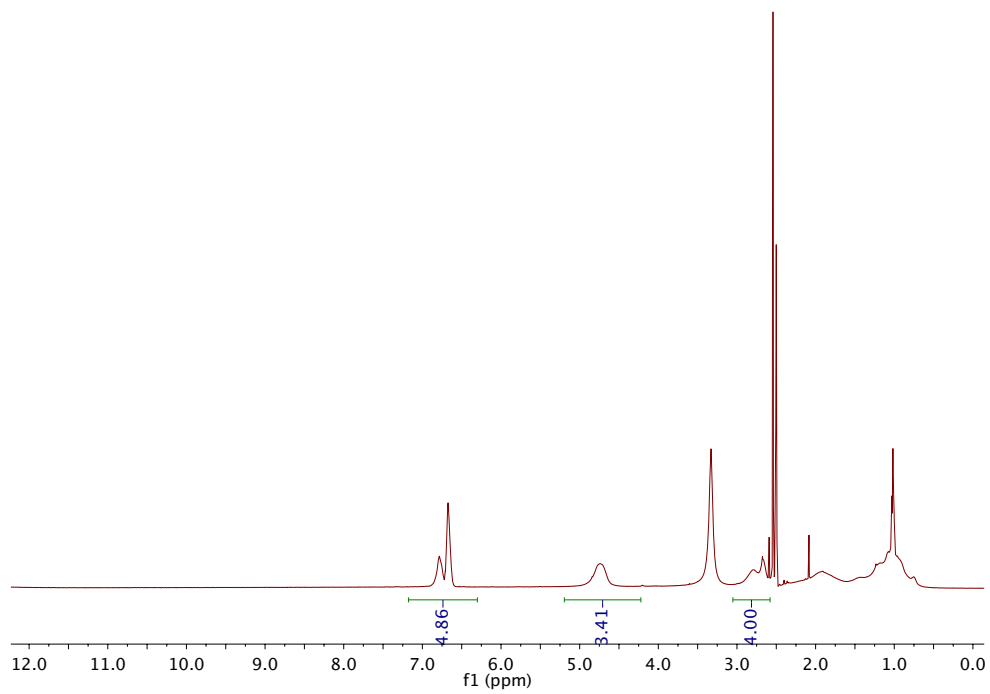
^1H NMR of P2 in $(\text{CD}_3)_2\text{SO}$



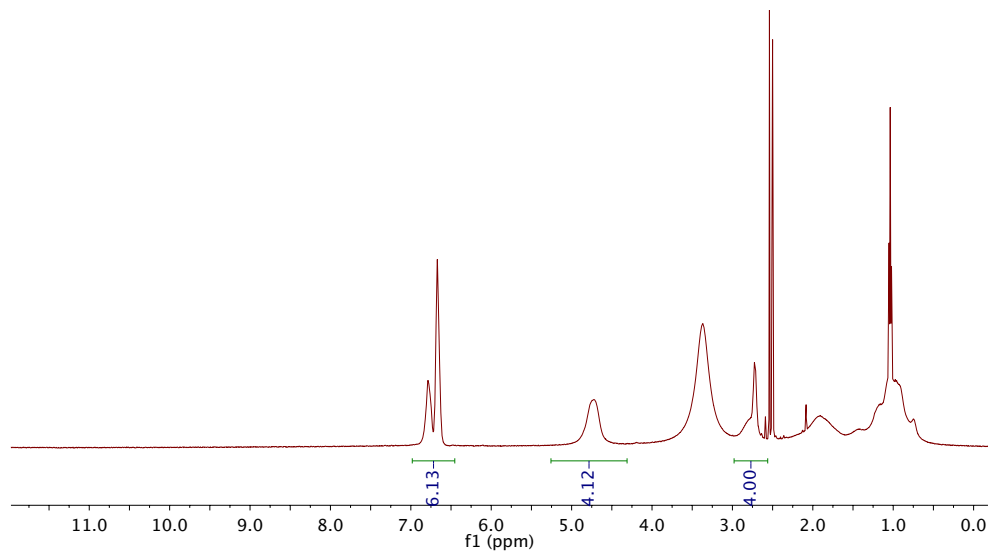
^1H NMR of P3 in $(\text{CD}_3)_2\text{SO}$



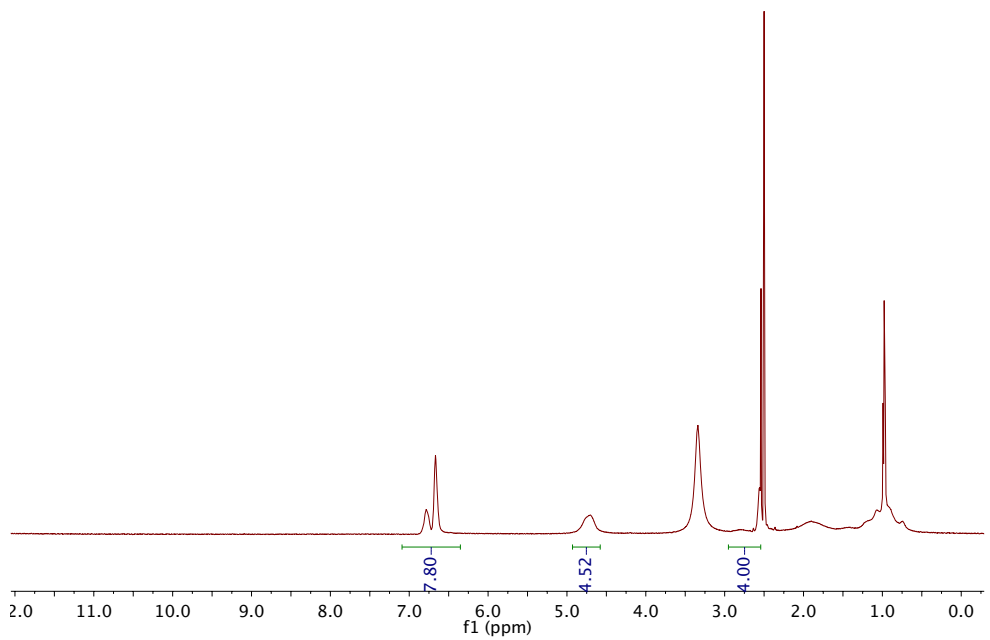
^1H NMR of P4 in $(\text{CD}_3)_2\text{SO}$



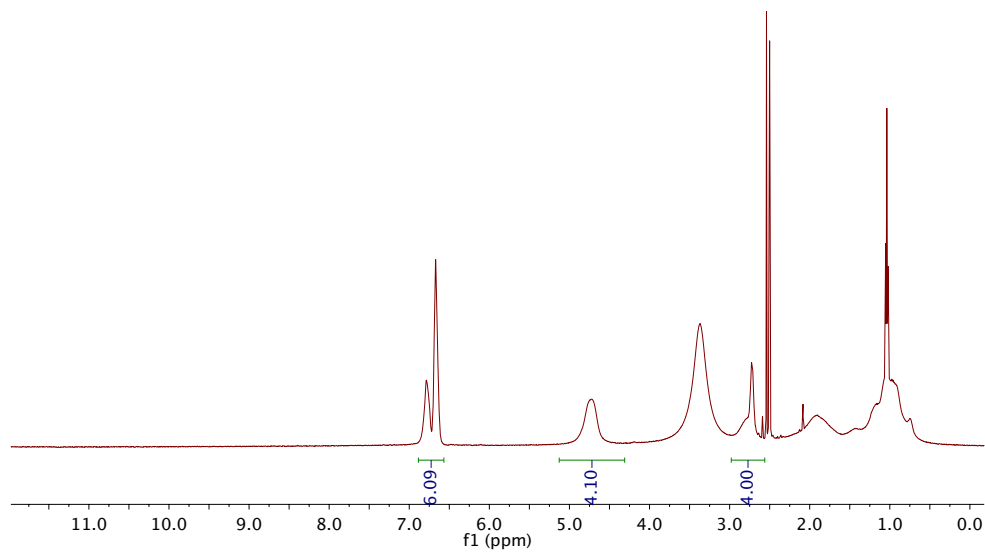
^1H NMR of P5 in $(\text{CD}_3)_2\text{SO}$



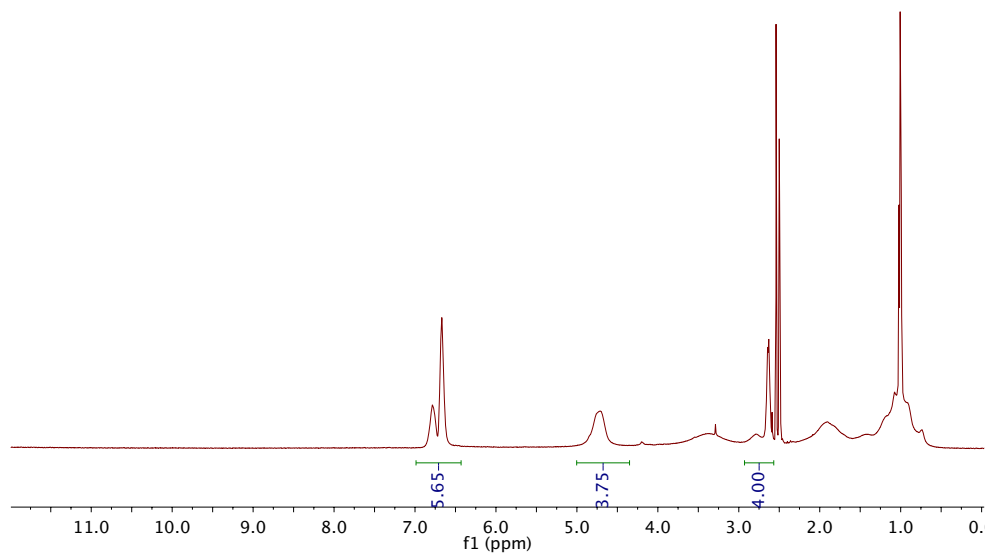
^1H NMR of P6 in $(\text{CD}_3)_2\text{SO}$



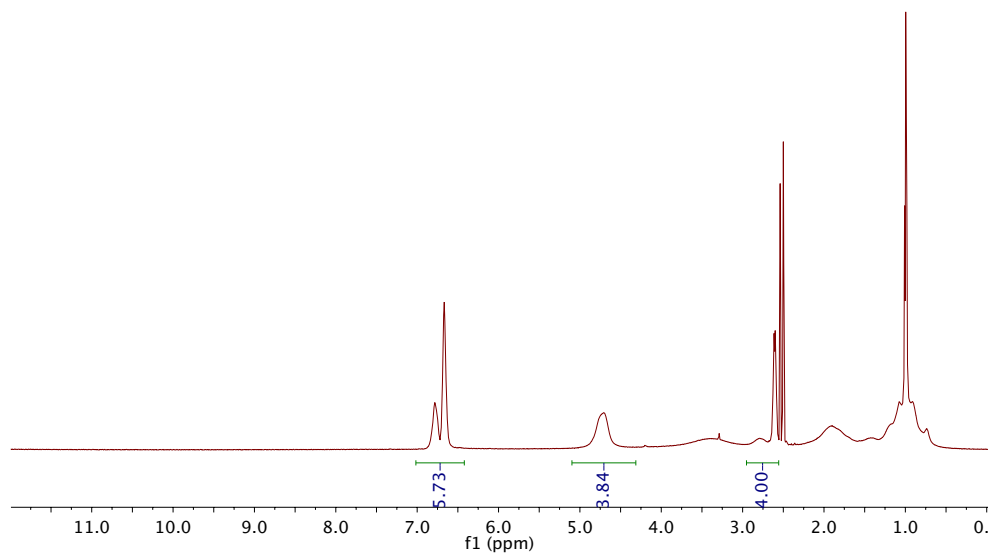
^1H NMR of P7 in $(\text{CD}_3)_2\text{SO}$



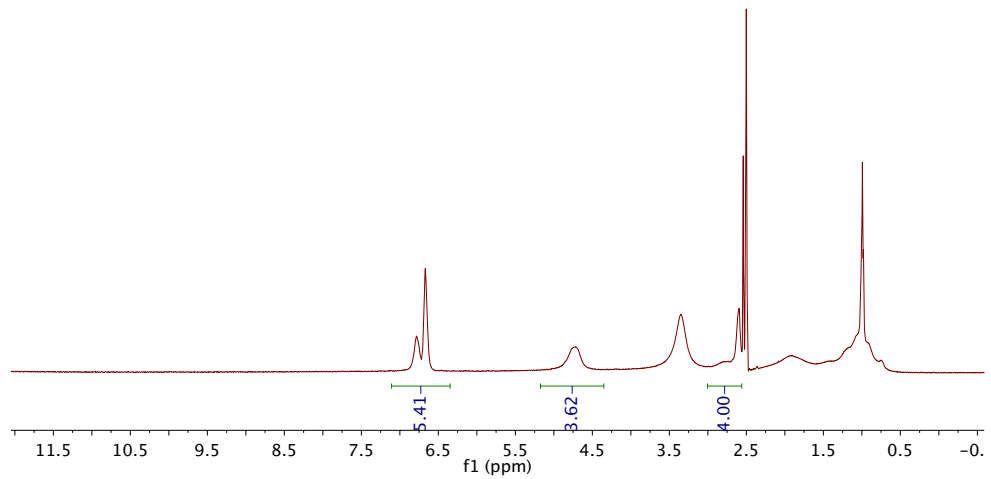
^1H NMR of P8 in $(\text{CD}_3)_2\text{SO}$



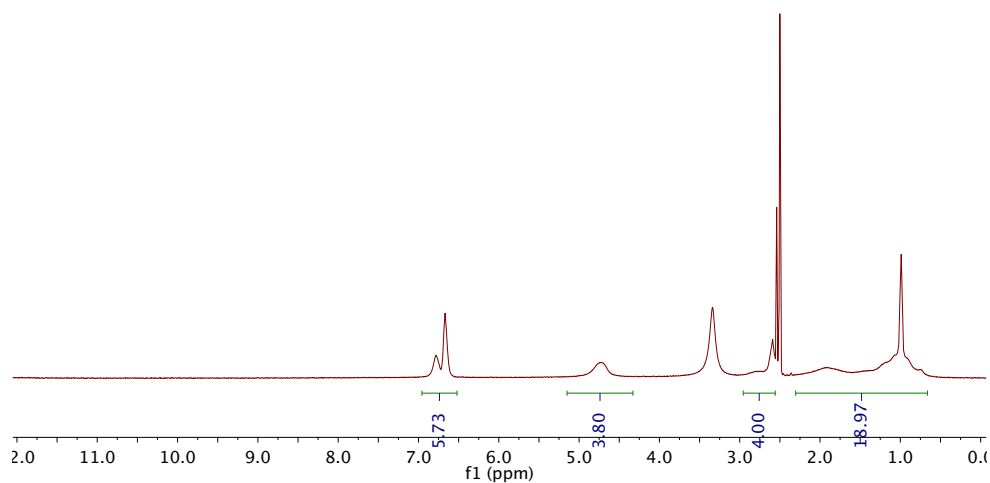
^1H NMR of P9 in $(\text{CD}_3)_2\text{SO}$



^1H NMR of P10 in $(\text{CD}_3)_2\text{SO}$



^1H NMR of P11 in $(\text{CD}_3)_2\text{SO}$



Sample calculation of %TTF functionalization of **P1** is listed below.

%TTF functionalization of **P1** based on TTF proton = $(1.3/3)/(1.3/3+4/4) \times 100\% = 30\%$.

%TTF functionalization of **P1** based on $-\text{OCH}_2-$ = $(0.88/2)/(0.88/2+4/4) \times 100\% = 31\%$

Table 3.3 Relative proton integration values of **P1** to **P11** from ^1H NMR spectra.

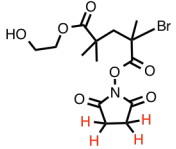
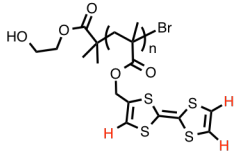
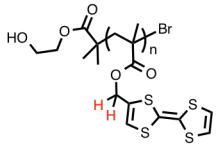
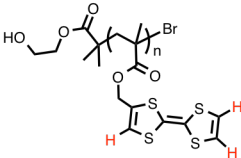
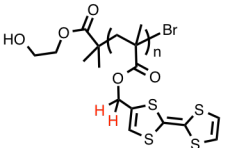
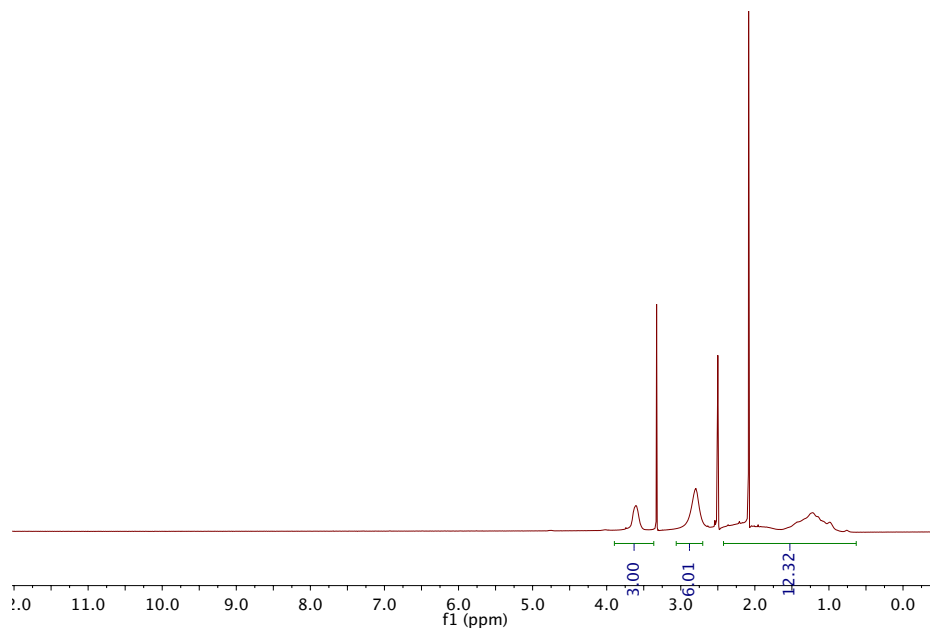
Relative proton integration value from ^1H NMR	P1	P2	P3	P4	P5	P6	P7	P8	P9	P10	P11
	4.00	4.00	4.00	4.00	4.00	4.00	4.00	4.00	4.00	4.00	4.00
	1.30	2.39	3.83	4.86	6.13	7.80	6.09	5.65	5.73	5.41	5.73
	0.88	1.52	2.68	3.41	4.12	4.52	4.10	3.75	3.84	3.62	3.80

Table 3.4 Percent TTF functionalization of the obtained polymer (**P1** to **P11**) after PPM based on relative proton integration values.

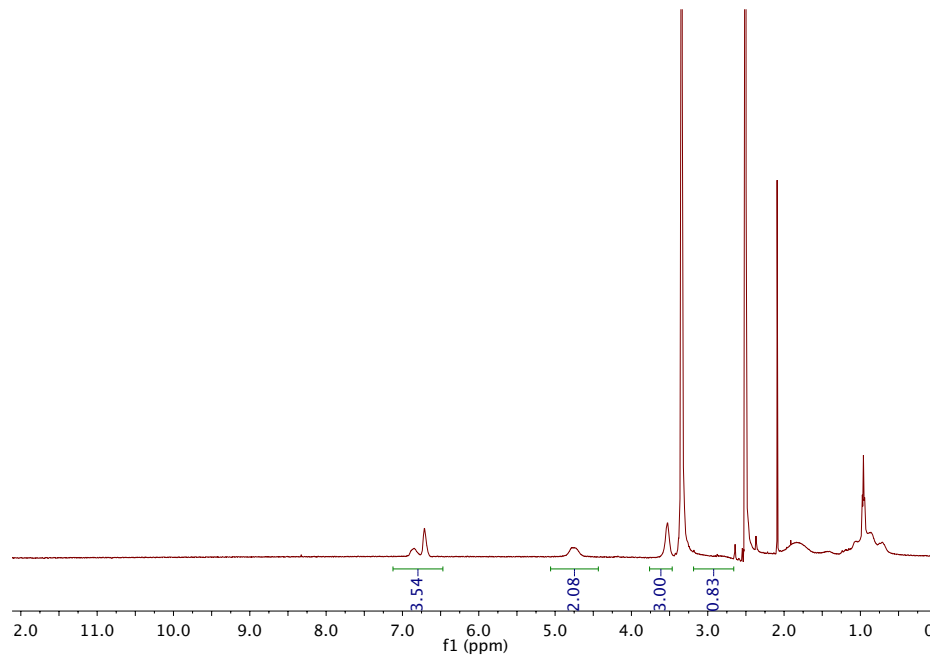
% TTF functionalization based on H integration	P1	P2	P3	P4	P5	P6	P7	P8	P9	P10	P11
	30	44	56	62	67	72	67	65	66	64	66
	31	43	57	63	67	69	67	65	66	65	66

^1H NMR of $\text{p}(\text{NHSMA}_{60}\text{-co-MMA}_{40})$ in $(\text{CD}_3)_2\text{SO}$



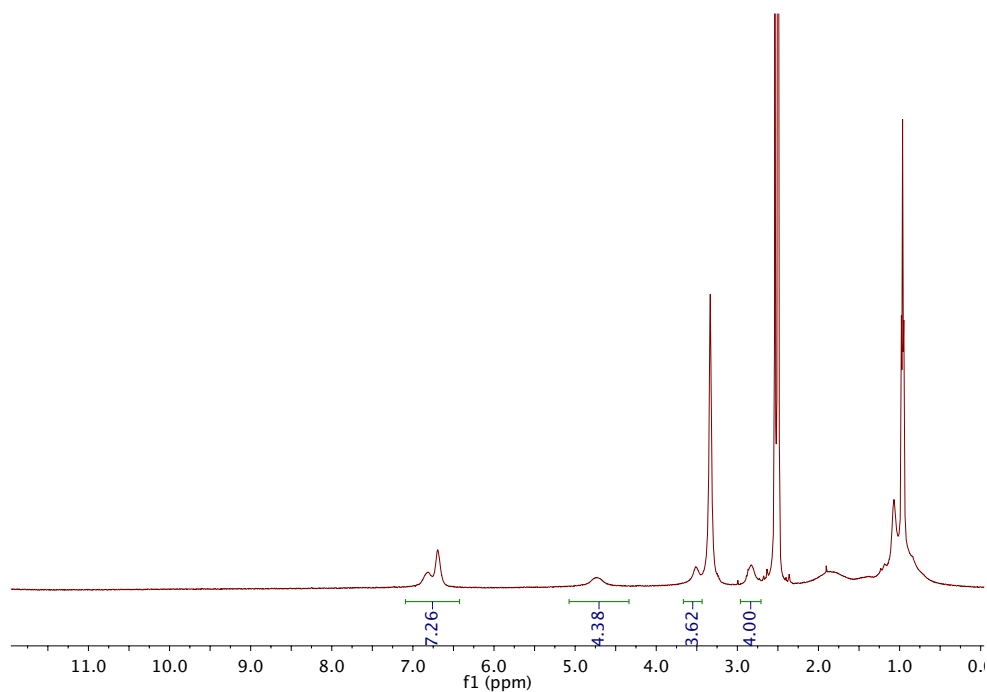
Based on the relative proton integration value, we can determine that the molar ratio between MMA and NHSMA in the copolymer is 2:3 (as calculated by $(3/3) : (6/4)$).

^1H NMR of $\text{p}(\text{hmTTFMA}_{60}\text{-co-MMA}_{40})$ in $(\text{CD}_3)_2\text{SO}$ (TTF functionalized polymer from $\text{p}(\text{NHSMA}_{60}\text{-co-MMA}_{40})$)



Analogous to the calculations for **P1** to **P11**, % TTF functionalization for phmTTFMA-co-MMA was determined to be 85 mol% (based on relative proton integration value on TTF) and 83 % (based on proton integration value on $-\text{OCH}_2-$).

^1H NMR of p(hmTTFMA-co-MMA) (Obtained polymer from p10 reacted with methanol) in $(\text{CD}_3)_2\text{SO}$



Based on the analysis of ^1H NMR spectra, proton TTF/(NHS+TTF) ratio increased from 64% to 71% after subjecting phmTTFMA (**P10**) with methanol. Additional methyl peak from MMA appeared which is consistent the ^1H NMR spectrum of phmTTFMA-co-MMA (TTF functionalized polymer from p(NHSMA₆₀-co-MMA₄₀). This indicated that the remaining NHS group in phmTTFMA(**P10**) remains active and is be replaced by methoxy, a less sterically congested group.

3.6.2.6 Elemental analysis data and TTF functionalization calculation based on weight percent of sulfur and nitrogen

Sample calculation of %TTF functionalization of **P1** is listed below.

%TTF functionalization of **P1** based on S:

$$\frac{4 * 32.06x}{302.44x + 183.16(1 - x)} 100\% = 18.06$$

Solve for x, where x = 31.

%TTF functionalization of **P1** based on N:

$$\frac{14.01y}{302.44(1 - y) + 183.16y} 100\% = 4.22$$

Solve for y, where y = 67. % TTF functionalization = 100-67 = 33.

Elemental analysis data of p(NHSMA₆₀-co-MMA₄₀) and phmTTFMA-co-MMA are [C(54.46); H(5.59); N (5.61)] and [S (30.24); C(47.50); H(4.40); N (0.73)], respectively. Analogous to the calculations for **P1** to **P11**, % TTF functionalization for phmTTFMA-co-MMA was determined to be 82 mol%. Elemental analysis data of p(NAS) and phmTTFA-r-NAS are [C(49.71); H(4.24); N (8.26)] and [S (37.98); C (43.01); H(3.03); N (1.12)], respectively. Analogous to the calculations for **P1** to **P11**, % TTF functionalization for phmTTFMA-co-MMA was determined to be 78 mol%.

Table 3.5 Elemental analysis results of sulfur and nitrogen for **P1** to **P11**.

Weight % from elemental analysis	P1	P2	P3	P4	P5	P6	P7	P8	P9	P10	P11
S analysis	18.06	20.88	30.57	32.66	34.32	34.35	34.00	33.66	33.63	33.33	33.30
N analysis	4.22	3.41	2.13	1.76	1.46	1.58	1.57	1.64	1.70	1.82	1.76

Table 3.6 Percent TTF functionalization of the obtained polymer (**P1** to **P11**) after PPM based on elemental analysis data.

% TTF functionalization based on elemental analysis	P1	P2	P3	P4	P5	P6	P7	P8	P9	P10	P11
S analysis	31	37	61	67	72	72	71	70	70	69	69
N analysis	33	43	61	67	72	70	70	69	68	66	67

3.6.2.7 IR of phmTTFMA and phmTTFMA-co-MMA from PPM using pNHSMA-co-MMA and phmTTFMA as polymer precursors

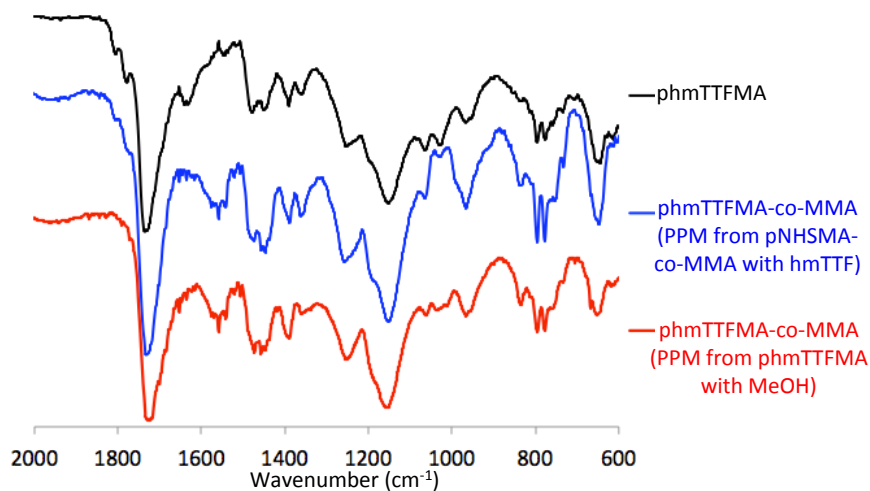


Figure 3.10 IR spectra of phmTTFMA and phmTTFMA-co-MMA from PPM using different polymer precursors.

3.6.2.8 GPC data

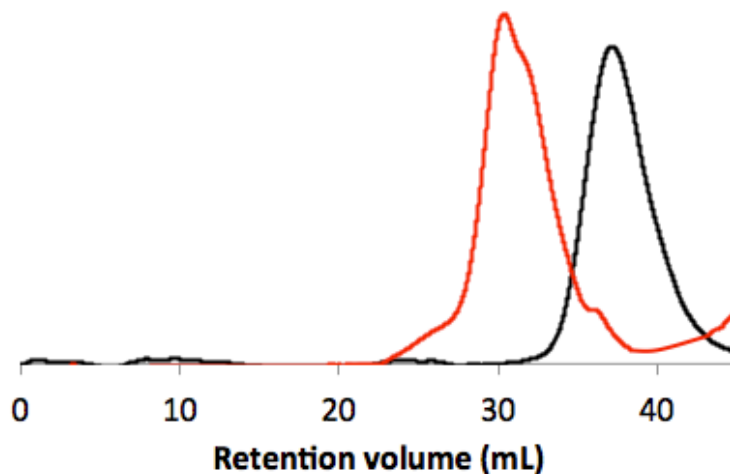


Figure 3.11 GPC curve of $p(\text{hmTTFMA}_{60}\text{-co-MMA}_{40})$ and $p\text{TTFMA-co-NAS}$. The black curve represents $p(\text{hmTTFMA}_{60}\text{-co-MMA}_{40})$, the TTF functionalized polymer from $p(\text{NHSMA}_{60}\text{-r-MMA}_{40})$, where its $M_n = 20.7$ kDa, $\mathcal{D} = 1.24$. The red curve represents $p\text{TTFMA-co-NAS}$, the TTF functionalized polymer from $p\text{NAS}$, where its $M_n = 44.5$ kDa, $\mathcal{D} = 1.67$.

3.6.2.9 TGA data of 4-(hydroxymethyl)TTF

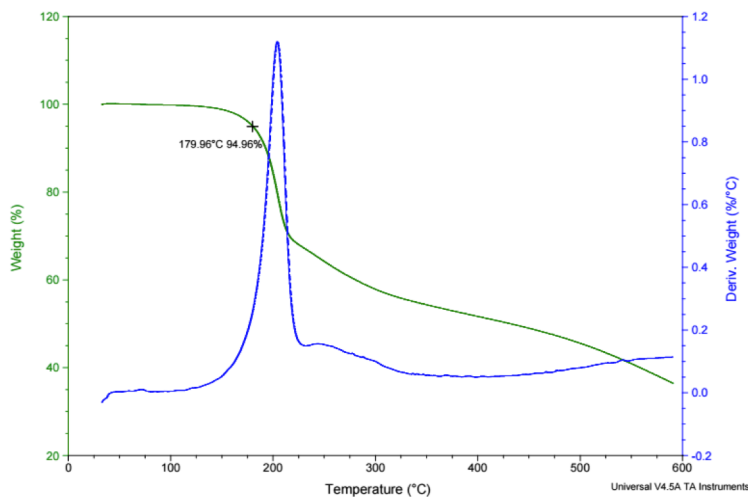


Figure 3.12 TGA curve of 4-(hydroxymethyl)TTF where $T_d = 179$ °C at 5 % weight loss with a heating rate of 10 °C min^{-1} .

3.6.2.10 Powder X-ray diffraction data

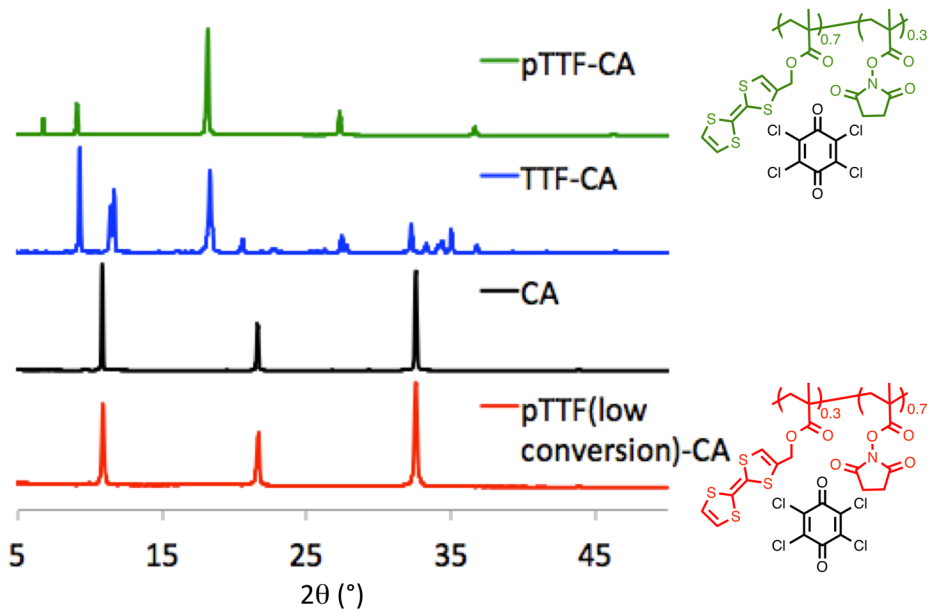


Figure 3.13 Powder X-ray patterns of the cast films of pTTF-CA (both low and high % TTF functionalization), TTF-CA, CA. When TTF incorporation to the polymer backbone is decreased, phase separation between pTTF and chloranil was observed.

3.6.2.11 Film-forming phmTTFMA

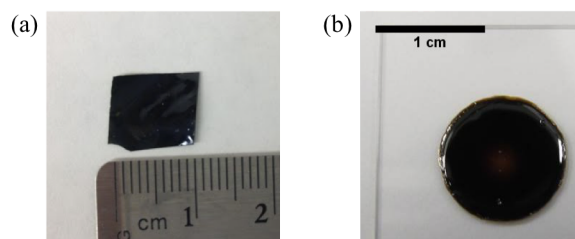
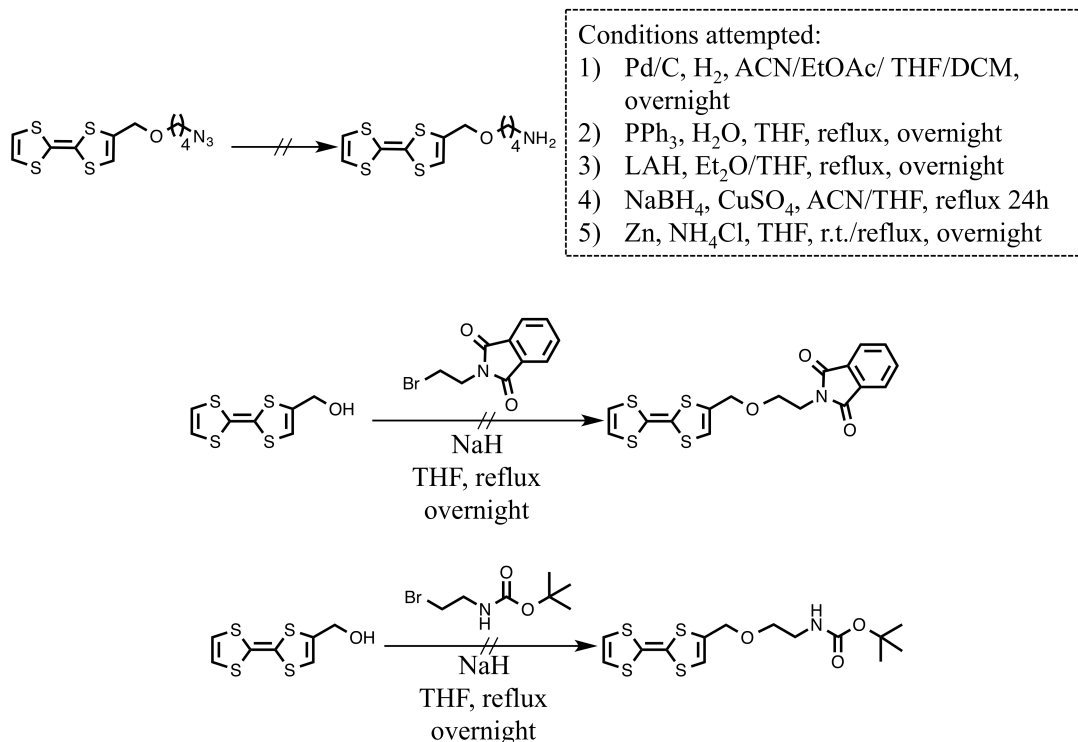


Figure 3.14 (a) Free-standing film of phmTTFMA; (b) phmTTFMA-chloranil film on glass substrate for electrical conductivity measurement.

3.6.2.12 Attempted syntheses of TTF-derivatives with primary amine

Scheme 3.8 Attempted syntheses of TTF-derivatives with primary amine, where the starting materials were synthesized following literature reports.^{25, 28}



3.6.3 Experimental Details for Section 3.5

3.6.3.1 General experimental details

All reagents were obtained from commercial suppliers and used as received unless otherwise noted. All anhydrous solvents were obtained from an anhydrous SDS equipped with activated alumina columns. All reactions were performed under an inert atmosphere (dry nitrogen gas) using standard Schlenk and vacuum line techniques. Column chromatography purifications were performed on Biotage Isolera using Silicycle Siliasep HP flash cartridges.

Nuclear magnetic resonance (NMR) spectra were recorded using either a Varian 400 MHz or 500 MHz spectrometer in the VOICE NMR laboratory at the University of Illinois at Urbana-Champaign. All chemical shifts (ppm) were calibrated to the residual proton peak of the deuterated solvent. Coupling constants (*J*) are expressed in Hertz (Hz). Mass spectra were

obtained through the Mass Spectrometry Facility, and elemental analysis data were obtained through the Microanalysis Laboratory, SCS, University of Illinois at Urbana-Champaign. Analytical gel permeation chromatography (GPC) was performed using a Waters 1515 Isocratic HPLC module equipped with a Waters (2998) Photodiode Array Detector, a Waters (2414) Refractive Index Detector, a Waters (2707) 96-well autosampler, and a series of 4 Waters HR Styragel columns (7.8 X 300 mm, HR1, HR3, HR4, and HR5) in THF at 30 °C and a flow rate of 1 mL/min. Molecular weights and molecular weight distributions were calculated relative to linear polystyrene standards. Unless otherwise noted, powder X-ray diffraction patterns were recorded on a Rigaku MiniFlex at a scanning rate of $0.02\text{ }^\circ\text{ s}^{-1}$ in two-theta ranging from 5° to 50° . Samples for the X-ray diffraction measurements were prepared by casting films on a zero diffraction plate purchased from MTI Corporation. The differential scanning calorimetry (DSC) measurement was performed using TA Instrument Q20. Hermetic zero aluminum pan and lids were used as sample testing containers. Typical DSC measurement procedure includes 3 cyclic scans with heating/cooling rate $10\text{ }^\circ\text{C/min}$. The glass transition temperature was determined at the inflection point of the step from the second heating scan. The thermogravimetric analysis (TGA) measurement was collected using TA Instrument Q50 with heating rate of $10\text{ }^\circ\text{C/min}$.

The diamond anvil cell (DAC) used was a Merrill-Bassett design with an opposing pair of 16-sided type IIa diamond anvils (3.5 mm thick with 0.80 mm culets). The gaskets were stainless steel with 500 μm diameter holes. The sample chips were loaded into the DAC along with 1-3 ruby chips surrounding the sample in order to obtain a precise measurement of the pressure and to monitor possible pressure gradients. The DAC was immersed in liquid Ar, and the screws were tightened to produce a seal. From 0 to 6 GPa, the maximum experimental errors and variances of the pressure within the cell, based on the fluorescence from individual ruby chips were less than 0.1 GPa. The absorbance spectra were obtained using an HL-2000-LL tungsten halogen light source and an USB4000-UV-Vis detector from Ocean Optics. The IR spectra were collected on either a Nicolet Magna 760 spectrometer (DAC experiment) or a Nicolet Nexus 670 spectrometer (non-DAC experiment). The optical images of TTF-(pTCAQ)₂ in the diamond anvil cell were collected under a LEICA M205C microscope, which was connected to a LEICA MC170 HD camera with Leica Application Suite Version 4.9.0. Due to the limited capacity of the diamond anvil cell (leading to limited amount of samples available after pressurization), the PXRD patterns of TTF-(pTCAQ)₂ before and after pressurization were

collected with a Bruker D8 Venture/Photon 100 diffractometer where the sample was loaded to a loop with minimum amount of parabar 10312 oil.

Electrochemical experiments were performed in an inert environment using a CHI1242b portable bipotentiostat from CH Instrument (Austin, TX). Solutions were prepared in an argon atmosphere glovebox. Cyclic voltammograms were obtained using a silver wire as a quasi-reference electrode (QRE) and a platinum wire as a counter electrode. All potentials are reported versus the QRE. All spectroelectrochemical measurements were obtained using a CH 601 E potentiostat from CH Instruments (Austin, TX). The working electrode was a thin Pt mesh that was used to electrochemically generate a specific oxidation state of the studied analytes. The counter electrode was a Pt wire. All potentials are listed versus a Ag/Ag^+ reference electrode which was fabricated using a Ag/Ag^+ non-aqueous reference electrode kit from CH Instruments (Austin, TX). The internal filling solution of the reference electrode consisted of anhydrous DMF (99% purity) with 0.1 M AgNO_3 dissolved therein, both chemicals were from Sigma-Aldrich. Spectroelectrochemical measurements in the UV-Vis wavelengths were performed using a SEC-2000 spectrometer from ALS Co. (Japan) inside of a nitrogen atmosphere glovebox from MBRAUN (Stratham, NH) to minimize any atmospheric presence of water and oxygen. The spectroelectrochemical cell was quartz and had a thin 1 mm path length to ensure that the working electrode could efficiently electrolyze all species within the small volume. UV-Vis spectra in the absorbance mode were collected after collecting a blank spectrum in a solution that contained only electrolyte. UV-Vis spectra were continuously collected while the working electrode was scanned at a slow scan rate of 2 mV/s between the set potential window to ensure that enough time was spent at each voltage to collect a representative UV-Vis spectrum of the analyte at the studied oxidation/reduction state.

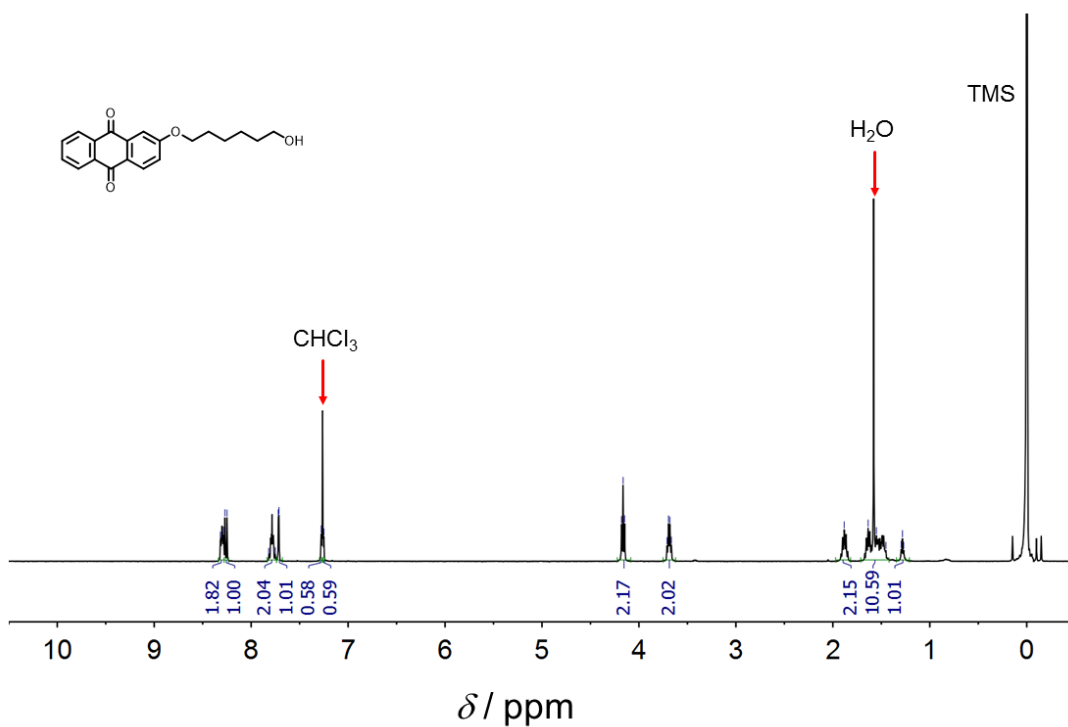
3.6.3.2 Synthesis, fabrication, and characterization of materials

Synthesis of 2-((6-Hydroxyhexyl)oxy)anthraquinone (2)

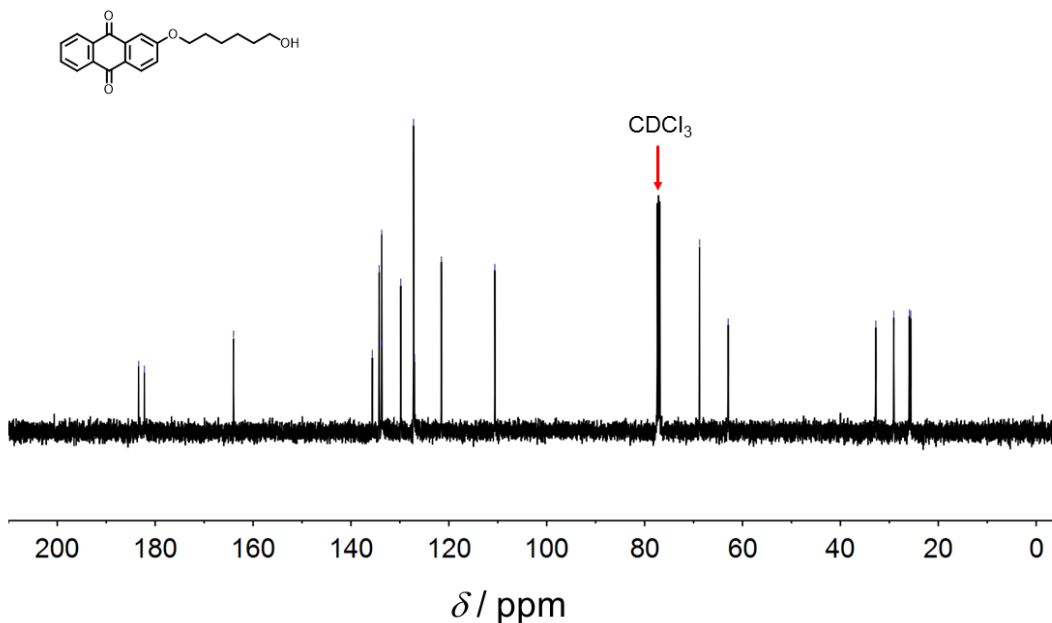
A mixture of 2-hydroxyanthraquinone (6.19 g, 27.6 mmol), 6-bromo-1-hexanol (5.00 g, 27.6 mmol), and K_2CO_3 (9.50 g, 69.0 mmol) in DMF (100 mL) was stirred at 80 °C overnight under N_2 atmosphere. The reaction mixture was cooled to room temperature, filtered through a pad of Celite, and washed with CH_2Cl_2 . Solvents were removed by azeotropic distillation using toluene. The crude mixture was purified using column chromatography on silica gel, eluted with a solvent

gradient from CH₂Cl₂ to EtOAc/CH₂Cl₂ 8:2. The product was obtained as a yellow solid (8.00 g, 24.7 mmol, 89% yield). ¹H NMR (400 MHz, CDCl₃): δ = 8.32–8.28 (m, 2H), 8.26 (d, *J* = 8.7 Hz, 1H), 7.82–7.75 (m, 2H), 7.72 (d, *J* = 2.6 Hz, 1H), 7.26 (dd, *J* = 8.5, 2.7 Hz, 1H), 4.16 (t, *J* = 6.5 Hz, 2H), 3.69 (q, *J* = 6.3 Hz, 2H), 1.88 (m, 2H), 1.64 (m, 2H), 1.55–1.45 (m, 4H), 1.28 (t, *J* = 5.2 Hz, 1H); ¹³C NMR (100 MHz, CDCl₃), δ = 183.38, 182.21, 163.99, 135.63, 134.23, 133.77, 133.71, 133.67, 129.82, 127.21, 127.00, 121.53, 110.61, 68.77, 62.93, 32.75, 29.09, 25.91, 25.63 (One aromatic carbon absent due to overlap); HRMS-ESI: C₂₀H₂₁O₄ [M+H]⁺, Calculated: 325.1440, Found 325.1432.

¹H NMR spectrum of 2 in CDCl₃



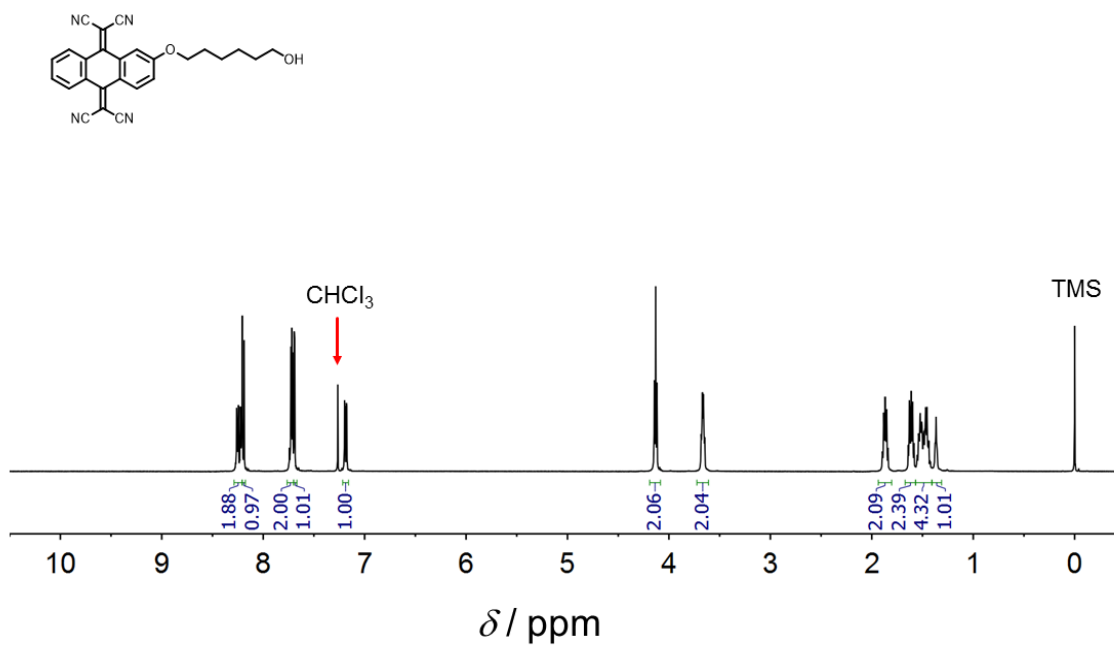
¹³C NMR spectrum of **2** in CDCl₃



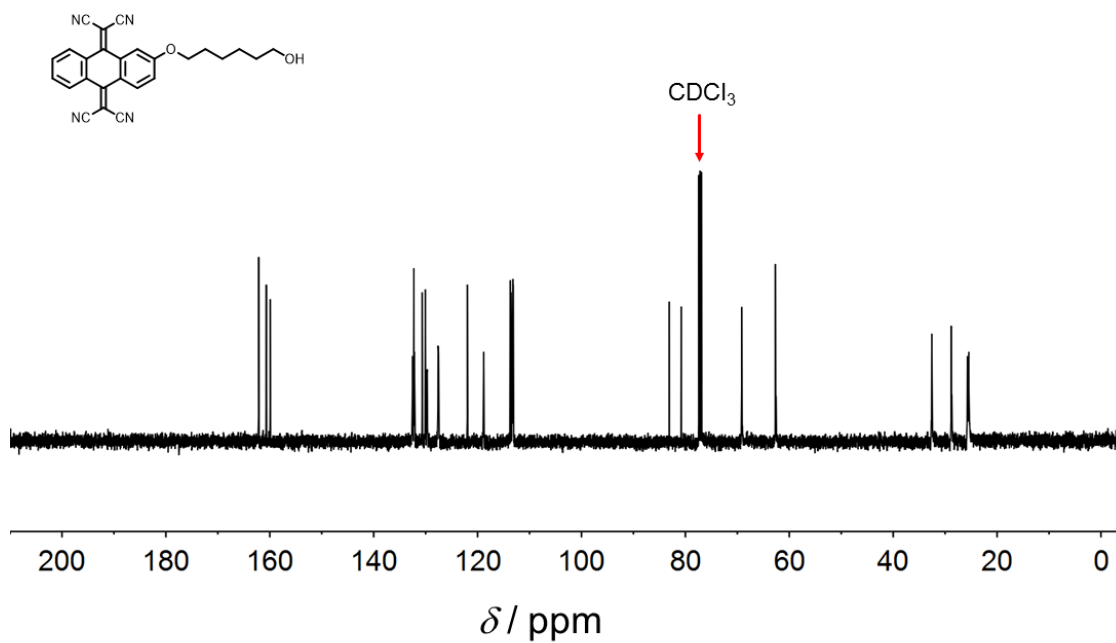
Synthesis of 2,2'-((6-Hydroxyhexyl)oxy)anthracene-9,10-diylidene)dimalononitrile (**3**)

To a solution of 2-((6-hydroxyhexyl)oxy)anthraquinone (2.00 g, 6.2 mmol), malononitrile (1.60 g, 24.7 mmol), and pyridine (4 mL, 49.4 mmol) in CHCl₃ (120 mL) was carefully dropwise added TiCl₄ (5.70 mL, 52 mmol) at room temperature. The reaction mixture was heated to 70 °C and stirred for 1 h, then cooled to room temperature, quenched with water and stirred for 10 min. The mixture was extracted with CH₂Cl₂ (×3) and the organic phase was dried with MgSO₄ and filtered. The solvents were removed under vacuum, and the crude mixture was purified using column chromatography on silica gel, eluted with a solvent gradient from CH₂Cl₂/hexanes 7:3 to CH₂Cl₂/hexanes/EtOAc 56:24:20. The product was obtained as a yellow solid (8.0 g, 24.7 mmol, 89% yield). ¹H NMR (400 MHz, CDCl₃), δ = 8.27–8.22 (m, 2H), 8.74 (d, *J* = 8.7 Hz, 1H), 7.75–7.71 (m, 2H), 7.69 (d, *J* = 2.3 Hz, 1H), 7.18 (dd, *J* = 8.8, 2.4 Hz, 1H), 4.13 (t, *J* = 6.4 Hz, 2H), 3.67 (q, *J* = 6.1 Hz, 2H), 1.87 (m, 2H), 1.61 (m, 2H), 1.54–1.43 (m, 4H), 1.29 (t, *J* = 5.0 Hz, 1H); ¹³C NMR (125 MHz, CDCl₃), δ = 162.14, 160.69, 159.93, 132.53, 132.27, 132.17, 130.67, 130.07, 129.76, 127.58, 127.53, 121.97, 118.86, 113.72, 113.62, 113.30, 113.21, 113.14, 83.13, 80.82, 69.15, 62.73, 32.59, 28.84, 25.74, 25.47; HRMS-ESI: C₂₆H₂₁N₄O₂ [M+H]⁺, Calculated: 421.1665, Found 421.1653.

^1H NMR spectrum of 3 in CDCl_3



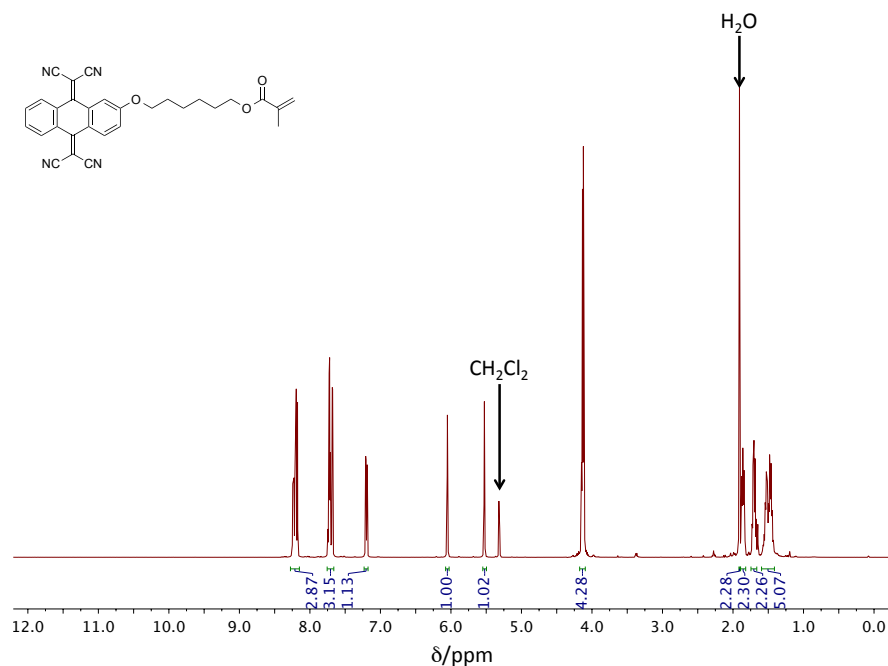
^{13}C NMR spectrum of 3 in CDCl_3



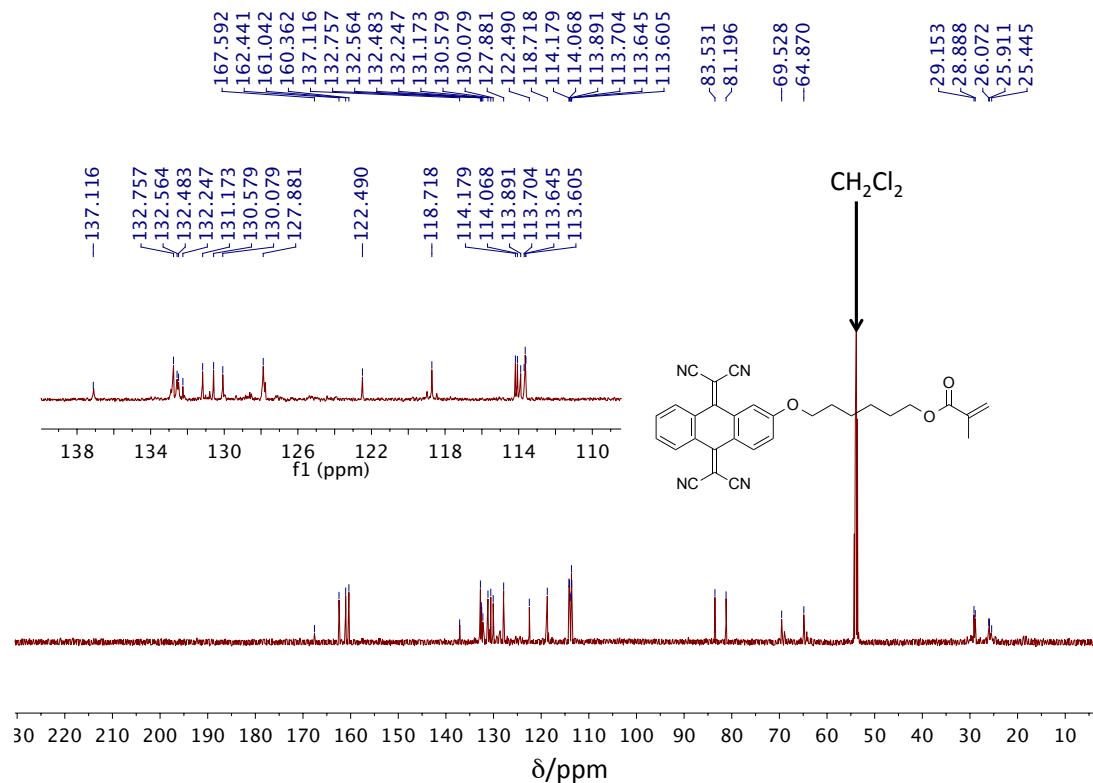
Synthesis of 6-((9,10-bis(dicyanomethylene)-9,10-dihydroanthracen-2-yl)oxy)hexyl methacrylate (4)

To a solution of 2,2'-(2-((6-hydroxyhexyl)oxy)anthracene-9,10-diylidene)dimalononitrile (4.00 g, 9.51 mmol) and triethylamine (1.60 mL, 11.41 mmol) in CH₂Cl₂ (100 mL) was carefully dropwise added a solution of methacryloyl chloride (1.11 mL, 11.41 mmol) in CH₂Cl₂ (10 mL) at 0 °C. The reaction mixture was slowly warmed to room temperature and left to stir overnight. 100 mL of water was added to the mixture and the aqueous layer was washed with CH₂Cl₂ (×2). The combined organic layer was washed with saturated NaHCO₃ solution (×2) and water (×2). The organic phase was dried with Na₂SO₄ and filtered. The solvents were removed under vacuum and the crude mixture was purified using column chromatography on silica gel, eluted with a solvent gradient from hexanes/EtOAc 9:1 to hexanes/EtOAc 5:5. The product was obtained as a yellow solid (3.85 g, 7.89 mmol, 83% yield). ¹H NMR (500 MHz, CD₂Cl₂), δ = 8.27–8.15 (m, 3H), 7.76–7.66 (m, 3H), 7.20 (dd, *J* = 8.5, 2.5 Hz, 1H), 6.08–6.03 (m, 1H), 5.55–5.50 (m, 1H), 4.16–4.10 (m, 4H), 1.92–1.90 (m, 2H), 1.89–1.82 (m, 2H), 1.74–1.66 (m, 2H), 1.60–1.40 (m, 5H); ¹³C NMR (125 MHz, CD₂Cl₂), δ = 167.59, 162.44, 161.04, 160.36, 137.12, 132.76, 132.56, 132.48, 132.25, 131.17, 130.58, 130.08, 127.88, 122.49, 118.72, 114.18, 114.07, 113.89, 113.70, 113.65, 113.61, 83.53, 81.20, 69.53, 64.87, 29.15, 28.89, 26.07, 25.91, 25.45; HRMS-ESI: C₃₀H₂₅N₄O₃ [M+H]⁺, Calculated: 489.1927, Found 489.1923.

¹H NMR spectrum of 4 in CD₂Cl₂



^{13}C NMR spectrum of **4** in CD_2Cl_2

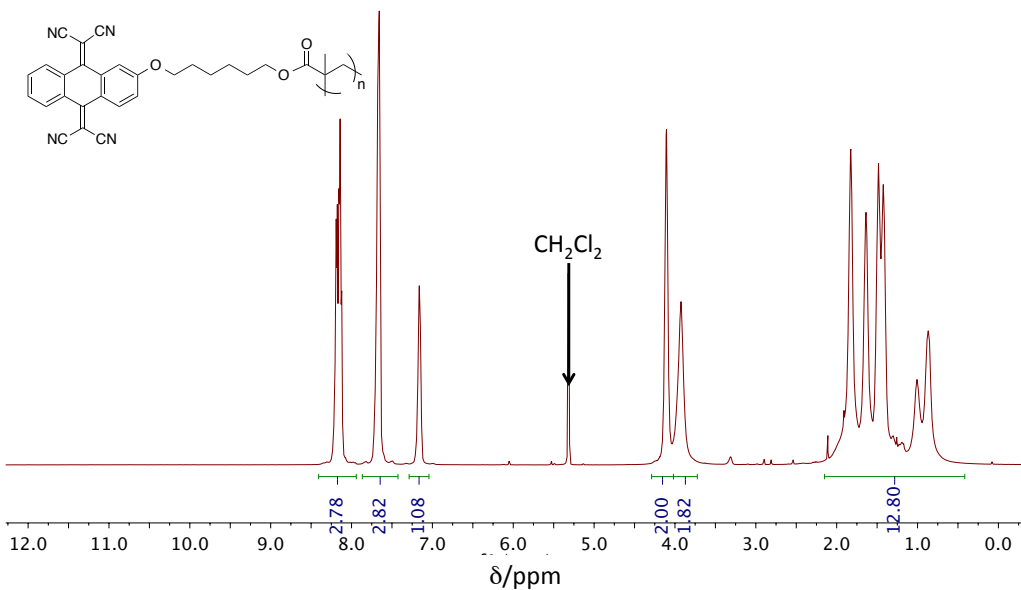


Synthesis of poly(6-((9,10-bis(dicyanomethylene)-9,10-dihydroanthracen-2-yl)oxy)hexyl methacrylate) (pTCAQ)

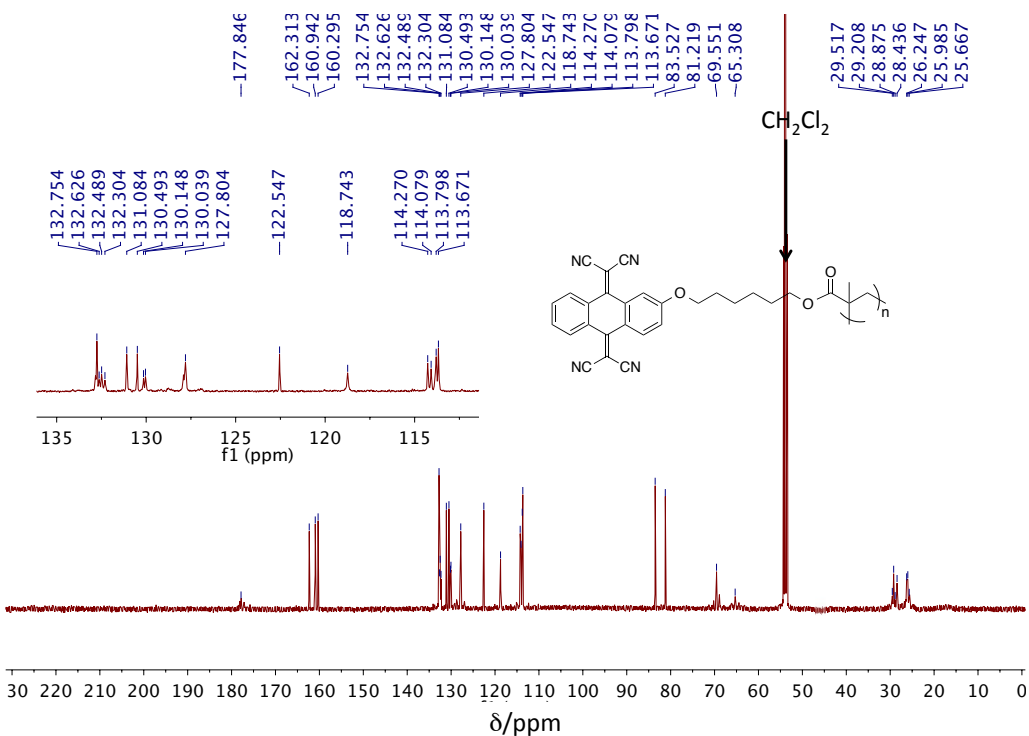
A mixture of monomer **1** (3.00g, 6.14 mmol) and initiator 2,2'-azobis(2-methylpropionitrile) (0.03 g, 0.18 mmol) was dissolved in anhydrous DMF (6.1 mL) under nitrogen in a 25-mL oven-dried Schlenk flask equipped with a stir bar. The solution was deoxygenated via four freeze-pump-thaw cycles, and after the final cycle, the flask was warmed to room temperature and backfilled with nitrogen. The reaction mixture was left stirring at 80 °C for 24 h and then brought to room temperature. The polymer precipitated by pouring the reaction solution into methanol and was collected by filtration. The isolated polymer was further purified by re-dissolving into CH_2Cl_2 and re-precipitating the CH_2Cl_2 solution into MeOH. The collected re-precipitate was washed several times with MeOH and immediately dried under vacuum at 40 °C for 24 h to provide 2.88 g of polymer as a yellow powder (96% yield, $M_n = 41\,700 \text{ g mol}^{-1}$, $D = 1.63$). ^1H NMR (500 MHz, CD_2Cl_2), $\delta = 8.41\text{--}7.94$ (m, 3H), 7.86–7.42 (m, 3H), 7.16 (b, 1H), 4.11 (b, 2H), 3.93 (b, 2H), 2.15–0.42 (m, 13H); ^{13}C NMR (125 MHz, CD_2Cl_2), $\delta = 177.85$, 162.31, 160.94, 160.30, 132.75, 132.63, 132.49, 132.30, 131.08, 130.49, 130.15, 130.04, 127.80,

122.55, 118.74, 114.27, 114.08, 113.80, 113.67, 83.53, 81.22, 69.55, 65.31, 29.52, 29.21, 28.88, 28.44, 26.25, 25.99, 25.67; elemental analysis: anal. calcd for C₃₀H₂₄N₄O₃: C, 73.76; H, 4.95; N, 11.47; found: C, 73.47; H, 4.98; N: 11:36.

¹H NMR spectrum of pTCAQ in CD₂Cl₂



¹³C NMR spectrum of pTCAQ in CD₂Cl₂



Preparation of CT complexes comprising TTF and pTCAQ

The TTF and polyTCAQ complexes with varying molecular ratio were prepared by mixing polyTCAQ with desired amount of TTF in anhydrous CH_2Cl_2 . The solution was stirred for 2 h at room temperature before casting on a glass slide. A steady stream of dry nitrogen was used to evaporate CH_2Cl_2 . The sample was further dried under vacuum at 40 °C overnight. The compositions of these blends were determined by TGA (Figure 3.20) and elemental analysis (Table 3.7).

Table 3.7 Characterizations of TTF-pTCAQ blends via CHN elemental analysis.

Compound	C wt%		H wt%		N wt%	
	Calcd	Found	Calcd	Found	Calcd	Found
pTCAQ (0 wt% TTF)	73.76	73.47	4.95	4.98	11.47	11.36
TTF-(pTCAQ) ₄ (10 wt% TTF)	70.11	69.95	4.67	4.42	10.38	10.02
TTF-(pTCAQ) ₂ (17 wt% TTF)	67.10	67.40	4.44	4.21	9.48	9.33
(TTF) ₃ -(pTCAQ) ₅ (20 wt% TTF)	66.03	65.90	4.35	4.18	9.17	8.90
TTF-pTCAQ (30 wt% TTF)	62.40	62.23	4.07	3.94	8.09	8.06

3.6.3.3 Cyclic voltammetry spectra and absorbance spectra

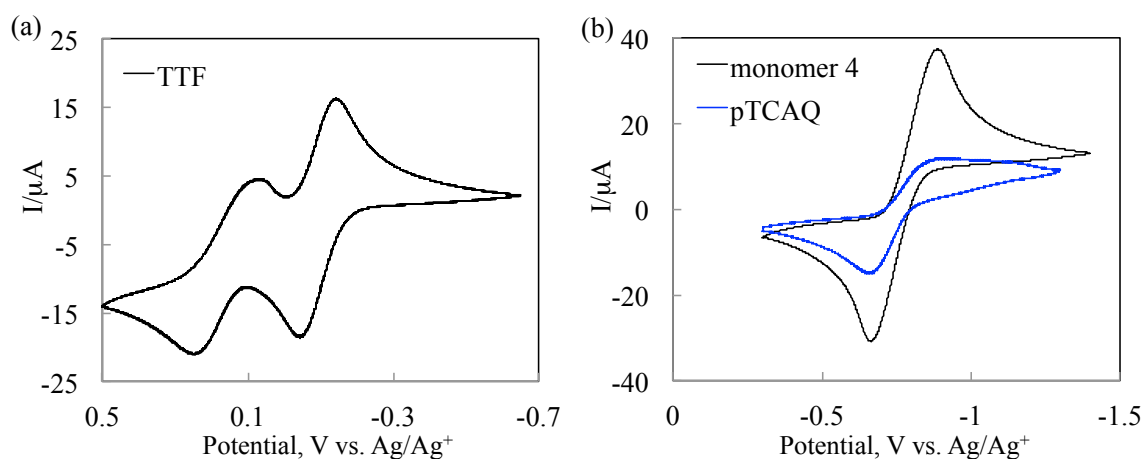


Figure 3.15 Cyclic voltammograms of (a) TTF (5 mM) and (b) monomer 4 (5 mM) and pTCAQ (10 mM) in DMF containing 0.1 M $[\text{NBu}_4]\text{PF}_6$ at 50 mV s^{-1} . A silver wire was used as a quasi-reference electrode.

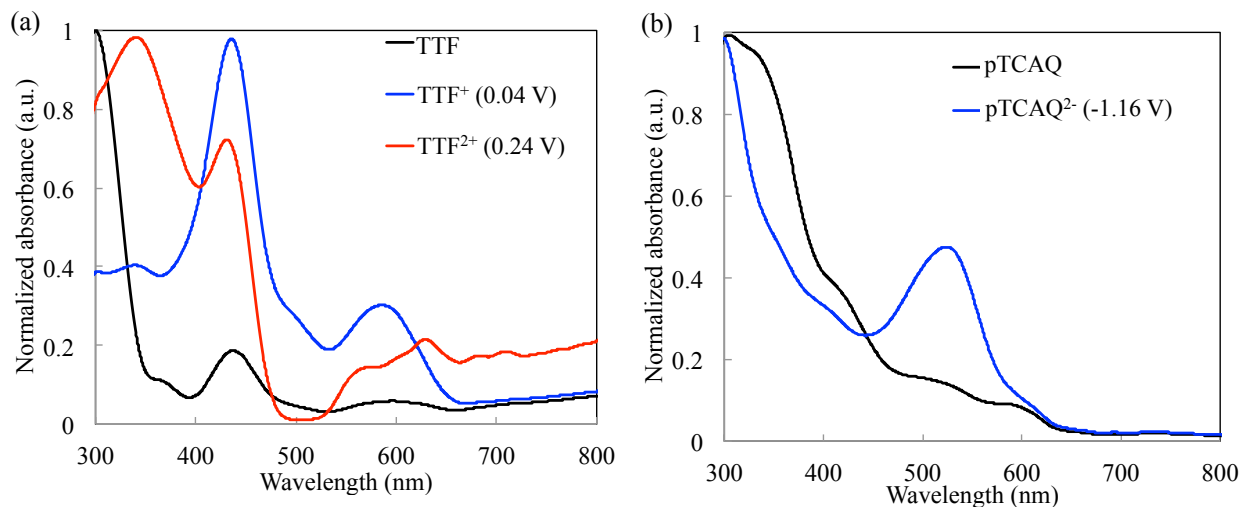


Figure 3.16 UV-Vis absorbance spectra of (a) TTF and (b) pTCAQ at different potentials in anhydrous DMF containing 0.1 M [NBu₄]PF₆.

3.6.3.4 Infrared spectra

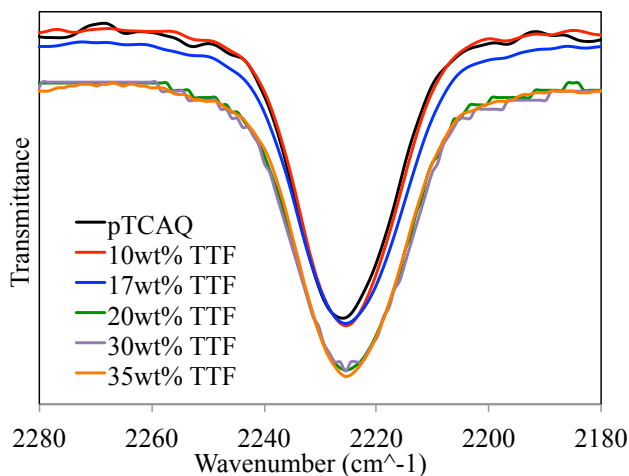


Figure 3.17 IR spectra of TTF-pTCAQ blends with varying compositions.

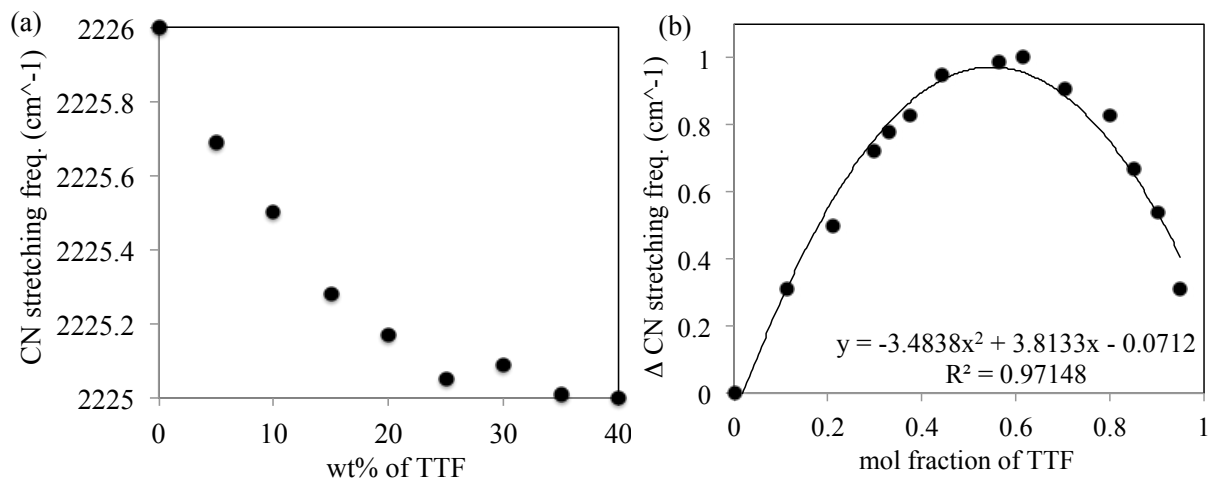


Figure 3.18 (a) Nitrile stretching frequency vs. wt% of TTF in TTF-pTCAQ blends; (b) a Job plot of TTF-pTCAQ blends based on the shift of nitrile stretching frequency from IR spectra.

3.6.3.5 DSC and TGA curves of TTF-pTCAQ blends

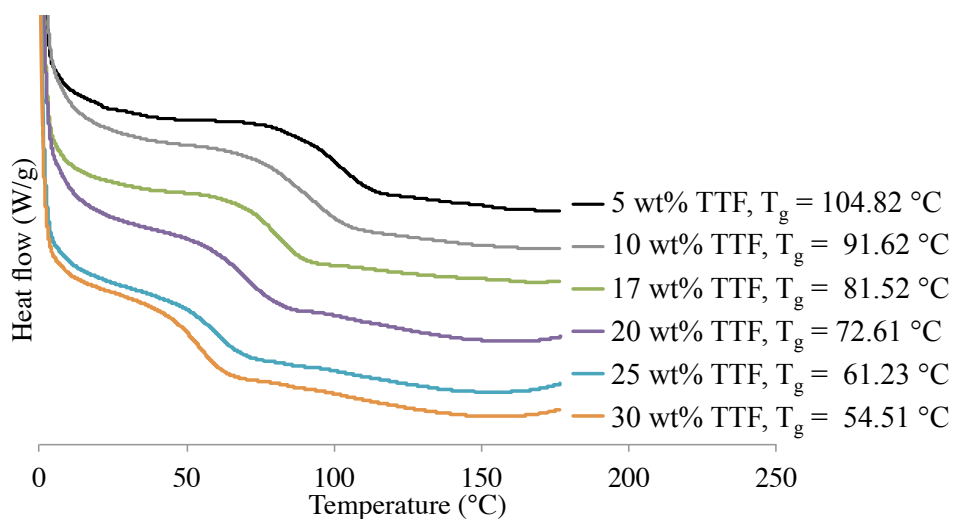


Figure 3.19 DSC curves of TTF-pTCAQ blends. Glass transition temperature (T_g) value is marked.

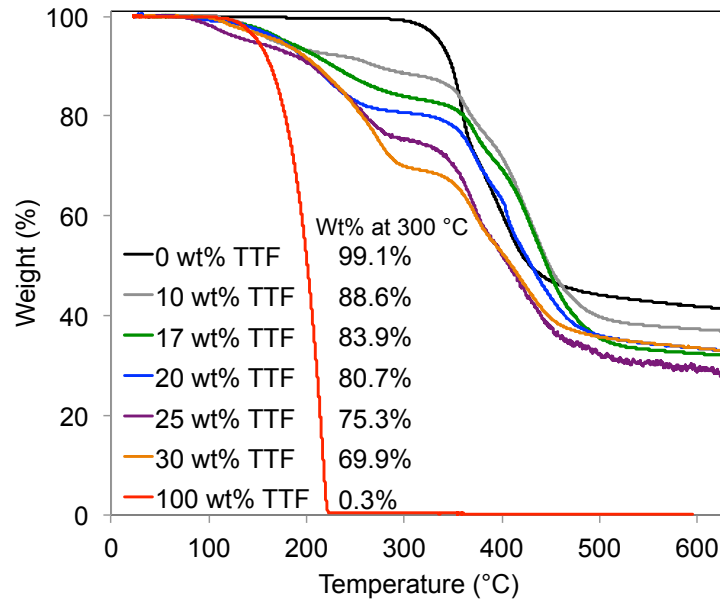


Figure 3.20 TGA curves of TTF-pTCAQ blends. At 300 °C, molecular TTF is completely degraded, whereas pTCAQ remains almost intact. The weight percent at 300°C of TTF-pTCAQ blends is marked to determine the compositions of TTF-pTCAQ blends, which are consistent to the results obtained from elemental analysis.

3.6.3.6 Spectroscopic support of the reversibility of PINIT in TTF-(pTCAQ)₂

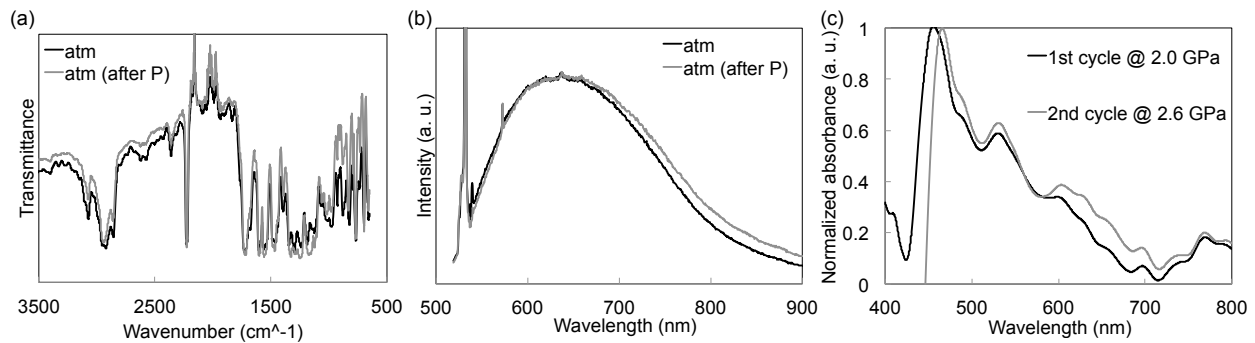


Figure 3.21 (a) IR and (b) fluorescence spectra of TTF-(pTCAQ)₂ under atmosphere pressure before and after pressurization; (c) comparison absorbance spectra of TTF-(pTCAQ)₂ between the 1st and the 2nd pressurization cycles.

3.6.3.7 Evidences of TTF-(pTCAQ)₂ remains amorphous before, during, and after pressurization

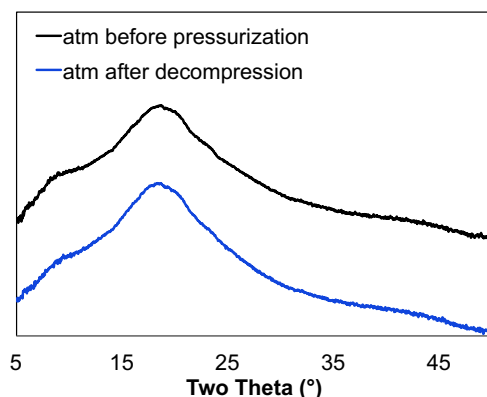


Figure 3.22 Powder X-ray patterns of TTF-(pTCAQ)₂ blend under atmosphere pressure before pressurization and after decompression. The sample was loaded to a loop with minimum amount of parabar 10312 oil, which caused the increased intensity from two theta = 15° to two theta = 25°. The absence of any sharp Bragg peak indicated that the sample remains amorphous upon decompression. We attempted to collect the X-ray patterns of the TTF-(pTCAQ)₂ blend under high pressure in a diamond anvil cell using in-house set-up. However, the X-ray intensity is not strong enough to provide reliable results.

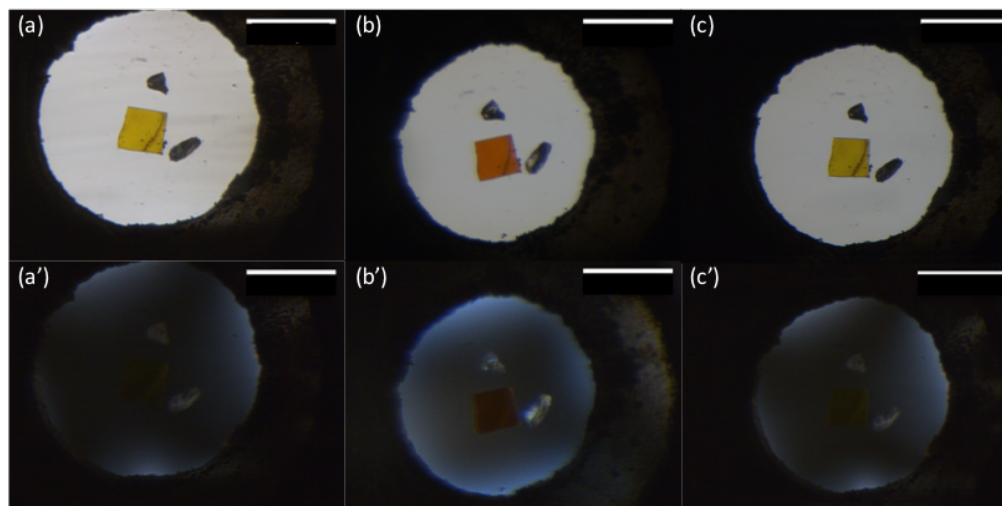


Figure 3.23 Optical images of the TTF-(pTCAQ)₂ blend with two ruby chips in a diamond anvil cell under different conditions where the scale bar is 200 μm : (a) atmosphere pressure before compression, air, plane polarized light; (a') atmosphere pressure before compression, air, crossed polarized light; (b) 5.0 GPa, Ar, plane polarized light; (b') 5.0 GPa, Ar, crossed polarized light; (c) atmosphere pressure after decompression, air, plane polarized light; (c') atmosphere pressure after decompression, air, crossed polarized light. Unlike the crystalline ruby chips, TTF-(pTCAQ)₂ sample is completely dark under the crossed polarized light before, during, and after pressurization suggesting that it remains amorphous and isotropic throughout the PINIT process.

3.6.3.8 Film-forming TTF-pTCAQ blends

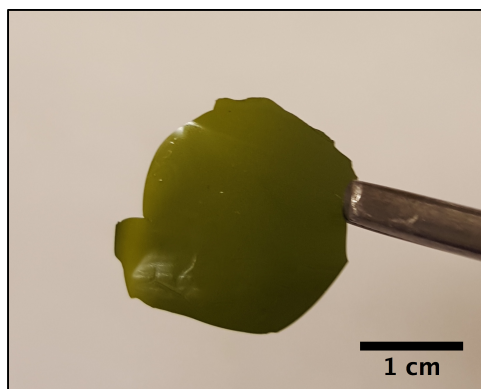
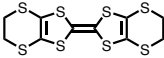
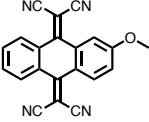
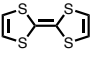
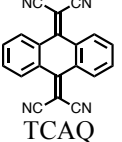
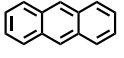
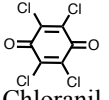
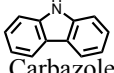
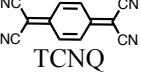


Figure 3.24 Free-standing film of TTF-(pTCAQ)₂.

3.6.3.9 Spartan calculation of orbital energies

Orbital energies of common electron donors and acceptors were estimated using DFT at the B3LYP 6-31G* level of theory with Spartan'14 (Wavefunction, Inc. Irvine, CA).

Table 3.8 HOMO energies of common electron donors and LUMO energies of common electron acceptors

Electron acceptors	HOMO (eV)	Electron donors	LUMO (eV)
 BEDT-TTF	-4.50	 TCAQ-OMe	-3.68
 TTF	-4.52	 TCAQ	-3.73
 Anthracene	-5.23	 Chloranil	-4.27
 Carbazole	-5.44	 TCNQ	-4.82

3.7 Notes and References

Notes: Portions of this chapter have been published: (a) Ren, Y.; Lee, S.; Christensen, J. M.; Plotnikov, N. V.; Burgess, M.; Martínez, T. J.; Dlott, D. D.; Moore, J. S. “Pressure-induced neutral-to-ionic transition in an amorphous organic material.” *Chem. Mater.* **2016**, *28*, 6446–6449; (b) Ren, Y.; Moore, J. S. “Improved TTF functionalization of polymers for two-dimensional charge-transfer networks.” *Polym. Chem.* **2015**, *6*, 8325–8330; (c) Ren, Y.; Lee, S.; Bertke, J. A.; Moore, J. S. “Crystal structure of 9,10-bis(1,3-dithiol-2-ylidene)-9,10-dihydroanthracene.” *Acta Cryst. E* **2015**, *71*, 1475–1479; (d) Ren, Y.; Lee, S.; Bertke, J. A.; Gray, D. L.; Moore, J. S. “Synthesis and structures of 2,6-diiodo-11,11,12,12-tetracyanoanthraquinodimethane and its cocrystals with various electron donors (2/1).” *Acta Cryst. C* **2016**, *72*, 923–931; (e) Shaw, W. L.; Ren, Y.; Moore, J. S.; Dlott, D. D. “Mechanochemistry for shock wave energy dissipation.” *AIP. Confer. Proc.* **2017**, *1793*, 030026. They are reproduced/adapted with permission. Copyright American Chemical Society, Royal Society of Chemistry, International Union of Crystallography, and American Institute of Physics.

References

1. Torrance, J. B.; Vazquez, J. E.; Mayerle, J. J.; Lee, V. Y. *Phys. Rev. Lett.* **1981**, *46*, 253.
2. Nakabayashi, K.; Nishio, M.; Miyasaka, H. *Inorg. Chem.* **2016**, *55*, 2473.
3. Chappell, J. S.; Bloch, A. N.; Bryden, W. A.; Maxfield, M.; Poehler, T. O.; Cowan, D. O. *J. Am. Chem. Soc.* **1981**, *103*, 2442.
4. Ren, Y.; Lee, S.; Bertke, J.; Gray, D. L.; Moore, J. S. *Acta Cryst. C* **2016**, *72*, 923.
5. Gomez, R.; Seoane, C.; Segura, J. L. *Chem. Soc. Rev.* **2007**, *36*, 1305.
6. Ren, Y.; Lee, S.; Bertke, J.; Moore, J. S. *Acta Cryst. E* **2015**, *71*, 1475.
7. Curtis, A. D.; Banishev, A. A.; Shaw, W. L.; Dlott, D. D. *Rev. Sci. Instrum.* **2014**, *85*, 043908.
8. Shaw, W. L.; Ren, Y.; Moore, J. S.; Dlott, D. D. **2017**, *1793*, 030026.
9. Segura, J. L.; Martin, N. *Angew. Chem., Int. Ed.* **2001**, *40*, 1372.
10. Baumer, V. N.; Starodub, V. A. *Synth. Met.* **1984**, *9*, 467.
11. Aumüller, A.; Hädicke, E.; Hünig, S.; Schätzle, A.; von Schütz, J. U. *Angew. Chem., Int. Ed.* **1984**, *23*, 449.
12. Ferraris, J.; Cowan, D. O.; Walatka, V.; Perlstein, J. H. *J. Am. Chem. Soc.* **1973**, *95*, 948.
13. Martin, N. *Chem. Commun.* **2013**, *49*, 7025.
14. Inagi, S.; Naka, K.; Chujo, Y. *J. Mater. Chem.* **2007**, *17*, 4122.
15. Graja, A.; Bułka, B. R.; Kajzar, F., *Molecular Low Dimensional and Nanostructured Materials for Advanced Applications*. Springer: Poznan, Poland, 2002; Vol. 59; p 67.
16. Kaplan, M. L.; Haddon, R. C.; Wudl, F. *J. Chem. Soc., Chem. Commun.* **1977**, 388.
17. Kaplan, M. L.; Haddon, R. C.; Wudl, F.; Feit, E. D. *J. Org. Chem.* **1978**, *43*, 4642.
18. Pittman, C. U.; Ueda, M.; Liang, Y. F. *J. Org. Chem.* **1979**, *44*, 3639.

19. Shirota, Y.; Kageyama, H. *Chem. Rev.* **2007**, *107*, 953.
20. Frenzel, S.; Arndt, S.; Gregorious, R. M.; Mullen, K. *J. Mater. Chem.* **1995**, *5*, 1529.
21. Shimizu, T.; Yamamoto, T. *Chem. Commun.* **1999**, 515.
22. Shimizu, T.; Yamamoto, T. *Inorg. Chim. Acta* **1999**, *296*, 278.
23. Guenay, K. A.; Theato, P.; Klok, H.-A. *J. Polym. Sci., Part A: Polym. Chem.* **2013**, *51*, 1.
24. Theato, P. *J. Polym. Sci., Part A: Polym. Chem.* **2008**, *46*, 6677.
25. Tanaka, K.; Matsumoto, T.; Chujo, Y. *Synth. Met.* **2013**, *163*, 13.
26. Fabre, J.-M.; Garín, J.; Uriel, S. *Tetrahedron* **1992**, *48*, 3983.
27. Binet, L.; Fabre, J. M. *Synthesis-Stuttgart* **1997**, 1179.
28. Garín, J.; Orduna, J.; Uriel, S.; Moore, A. J.; Bryce, M. R.; Wegener, S.; Yufit, D. S.; Howard, J. A. K. *Synthesis* **1994**, *1994*, 489.
29. Odian, G., *Principles of Polymerization*. 4 ed.; Wiley & Sons: New York, 2004.
30. Melby, L. R.; Mahler, W.; Mochel, W. E.; Harder, R. J.; Hertler, W. R.; Benson, R. E. *J. Am. Chem. Soc.* **1962**, *84*, 3374.
31. Choi, S. J.; Kuwabara, J.; Kanbara, T. *Chem. - Asian J.* **2010**, *5*, 2154.
32. Chappell, J. S.; Bloch, A. N.; Bryden, W. A.; Maxfield, M.; Poehler, T. O.; Cowan, D. O. *J. Am. Chem. Soc.* **1981**, *103*, 2442.
33. Garcia, P.; Dahaoui, S.; Katan, C.; Souhassou, M.; Lecomte, C. *Faraday Discuss.* **2007**, *135*, 217.
34. Sato, O.; Tao, J.; Zhang, Y. *Angew. Chem., Int. Ed.* **2007**, *46*, 2152.
35. Miyasaka, H.; Motokawa, N.; Chiyo, T.; Takemura, M.; Yamashita, M.; Sagayama, H.; Arima, T. *J. Am. Chem. Soc.* **2011**, *133*, 5338.
36. Mitani, T.; Kaneko, Y.; Tanuma, S.; Tokura, Y.; Koda, T.; Saito, G. *Phys. Rev. B* **1987**, *35*, 427.
37. Matsuzaki, S.; Hiejima, T.; Sano, M. *Bull. Chem. Soc. Jpn.* **1991**, *64*, 2052.
38. Matsuzaki, S.; Hiejima, T.; Sano, M. *Solid State Commun.* **1992**, *82*, 301.
39. Aoki, S.; Nakagama, T.; Miura, A. *Synth. Met.* **1995**, *70*, 1243.
40. Basaki, S.; Matsuzaki, S. *Synth. Met.* **1995**, *70*, 1239.
41. Hasegawa, T.; Akutagawa, T.; Nakamura, T.; Mochida, T.; Kondo, R.; Kagoshima, S.; Iwasa, Y. *Phys. Rev. B* **2001**, *64*, 085106.
42. Nakabayashi, K.; Miyasaka, H. *Chem. Eur. J.* **2014**, *20*, 5121.
43. Sadohara, R.; Matsuzaki, S. *Mol. Cryst. Liq. Cryst.* **1997**, *296*, 269.
44. Jezowski, S. R.; Zhu, L.; Wang, Y.; Rice, A. P.; Scott, G. W.; Bardeen, C. J.; Chronister, E. L. *J. Am. Chem. Soc.* **2012**, *134*, 7459.
45. Miyasaka, H. *Acc. Chem. Res.* **2013**, *46*, 248.
46. Bures, F.; Schweizer, W. B.; Boudon, C.; Gisselbrecht, J.-P.; Gross, M.; Diederich, F. *Eur. J. Org. Chem.* **2008**, 994.
47. Amemori, S.; Kokado, K.; Sada, K. *Angew. Chem., Int. Ed.* **2013**, *52*, 4174.
48. Haeupler, B.; Burges, R.; Janoschka, T.; Jaehnert, T.; Wild, A.; Schubert, U. S. *J. Mater. Chem. A* **2014**, *2*, 8999.
49. Mukai, T.; Suzuki, T.; Yamashita, Y. *Bull. Chem. Soc. Jpn.* **1985**, *58*, 2433.
50. Nair, R.; Nyamweya, N.; Gonen, S.; Martinez-Miranda, L. J.; Hoag, S. W. *Int. J. Pharm.* **2001**, *225*, 83.
51. Webster, S.; Batchelder, D. N. *Polymer* **1996**, *37*, 4961.
52. Wakita, J.; Ando, S. *J. Phys. Chem. B* **2009**, *113*, 8835.
53. Song, K.; Miller, R. D.; Wallraff, G. M.; Rabolt, J. F. *Macromolecules* **1991**, *24*, 4084.

54. Plotnikov, N. V.; Martinez, T. J. *J. Phys. Chem. C* **2016**, *120*, 17898.
55. Brown, K. E.; Shaw, W. L.; Zheng, X. X.; Dlott, D. D. *Rev. Sci. Instrum.* **2012**, *83*, 103901.
56. Curtis, A. D.; Banishev, A. A.; Shaw, W. L.; Dlott, D. D. *Rev. Sci. Instrum.* **2014**, *85*, 043908.
57. Godwin, A.; Hartenstein, M.; Müller, A. H. E.; Brocchini, S. *Angew. Chem., Int. Ed.* **2001**, *40*, 594.
58. Wang, J.-Q.; Chen, X.; Zhang, W.; Zacharek, S.; Chen, Y.; Wang, P. G. *J. Am. Chem. Soc.* **1999**, *121*, 8174.

Chapter 4: Ultrafast Proton Transfer in Polymer Blends Triggered by Shock Waves

4.1 Abstract

We describe ultrafast proton transfer in the ground electronic state triggered by using shock waves created by high-speed impacts. The emission of Nile Red (NR), a polarity sensing dye, was used to probe the effects of shock compression in a series of polymers, including polymer blends composed of Brønsted bases and organic acids. NR undergoes a shock-induced redshift due to an increase in both density and polymer polarity. In blends of poly(4-vinylpyridine) (PVP) and phenol, NR showed an excess shock-induced redshift with a distinct time dependence that was not present in control samples incapable of proton transfer. The excess redshift first appeared with $0.8 \text{ km}\cdot\text{s}^{-1}$ impacts. This NR redshift occurred in ca. 10 ns, and was caused by the formation of an ion pair created by shock-triggered proton transfer from phenol to PVP.

4.2 Introduction

Proton transfer plays a fundamental role in many chemical and biological processes,²⁻³ and extensive theoretical and experimental studies have been conducted to understand and control proton transfer in solutions and in solids.⁴⁻⁶ The most common method for rapidly triggering proton transfer uses optical excitation of a photoacid.⁷⁻⁹ Temperature jump¹⁰ and infrared (IR) vibrational excitation¹¹ have also been used to trigger proton transfer. Here, using a recently developed tabletop shock photoemission apparatus,¹² we demonstrate that proton transfer in ground electronic states is triggered on the nanosecond time scale by shock compression.

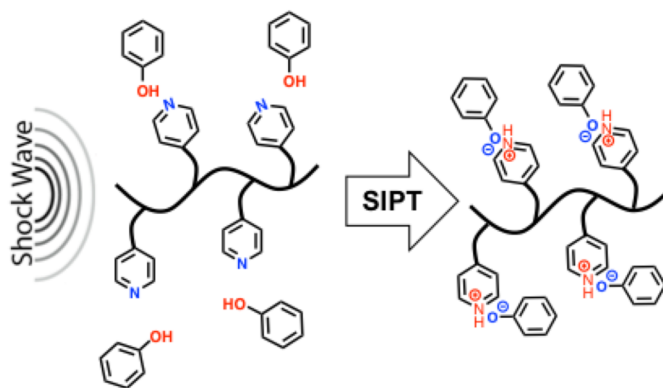
Shock compression generally favors ion pairs over neutrals, due to the typically smaller volumes of ion pairs.^{7, 13} A shock-induced polarity increase could also trigger proton transfer, since ground-state proton transfer is enabled by solvent fluctuations that increase local polarity.¹⁴⁻¹⁵ Shock-triggered proton transfer would create an ion pair that would further increase the medium's polarity. The polarity increase in shocked water¹⁶ is due to shock-induced

dissociation of water into ion pairs.¹⁷⁻¹⁸ In fact, Hamann and Linton proposed that the ionization of water to H_3O^+ and OH^- can proceed nearly to completion with sufficiently strong shocks.¹⁷⁻¹⁹ Shock-induced proton transfer has also been invoked as one of the key initial steps in shock initiation of high explosives. An early step in nitromethane initiation is believed to be formation of the aci ion CH_2NO_2^- ,²⁰⁻²¹ and an early step in the initiation of nitramine explosives such as RDX²² and HMX²³ ($[\text{CH}_2\text{-NNO}_2]_n$, $n = 3$ or 4) is believed to be the formation of HONO.

4.3 Shock-Induced Polarity Increase Probed with Nile Red

Inspired by the shock-promoted ionization of water,¹⁷⁻¹⁹ we hypothesized that polarization and proton transfer in solid-state polymeric materials is favored by shock waves produced by high-speed impacts, as illustrated in Scheme 4.1. We utilized emission from Nile Red (NR), a well-known polarity-sensing dye,²⁴⁻²⁶ to investigate shock-induced polarity increases and proton transfer in polymers. The polarity-sensing ability of NR derives from the ability of polar media to lower the energy of its charge-transfer excited state.²⁴⁻²⁶ In more polar media, the NR absorption and emission redshift.

Scheme 4.1 Depiction of shock-induced proton transfer (SIPT) in a polymeric blend comprised of poly(4-vinylpyridine) and phenol in 1:1 molar ratio.

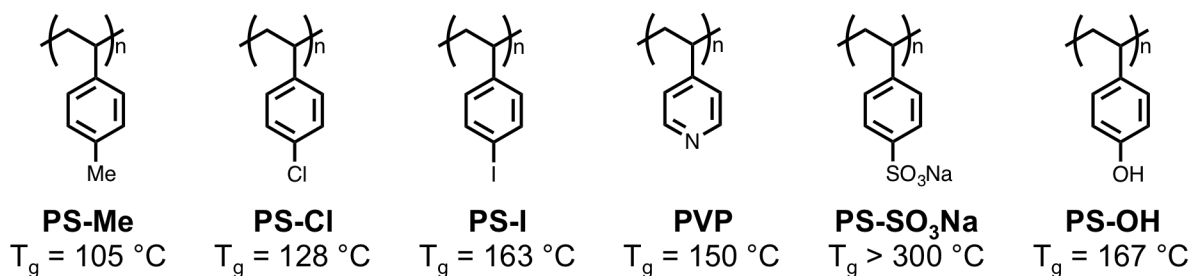


In a shocked polymer, there will be three sources of shock-induced redshift. First, there is density-induced level shifting,²⁷ which occurs because increased density causes the excited singlet S_1 state to shift in energy by a different amount than the ground S_0 state; most commonly, the transition energy redshifts. Second, there can be a density-induced increase in polarity due to

compression, which causes the density of existing dipoles to increase and provides additional stabilization for the creation of new dipoles. The third process, the focus of this study, is the proposed additional redshift caused by ion pairs created by shock-induced proton transfer. The first two processes have no threshold, so over a small range of impact velocity those redshifts will be approximately linear in impact velocity.^{12,28} Shock-induced proton transfer would create an excess redshift and will exhibit an impact velocity threshold.

A first step was to identify polymers that undergo significant shock-induced polarity increases. We selected a series of commercially available polymers having the same backbone but different side-chains (Scheme 4.2). These polymers have relatively high glass transition temperature (T_g) values, which minimize the likelihood that shock-induced polymer softening or melting might influence NR emission (Scheme 4.2 and Table 4.2).²⁹ To avoid NR aggregates,³⁰ the NR concentration was kept at only 0.1 mol% per monomer unit of the polymer.

Scheme 4.2 Chemical structures of the polymers used in this study and their corresponding glass transition temperature (T_g) as determined by differential scanning calorimetry (DSC) with heating/cooling rate = 10 °C/min.



The shock spectroscopy apparatus has been described previously,^{12,31} and a schematic is shown in Figure 4.4. The shock waves were generated by laser-launched Al flyer plates (75 μm thick), which produced a steady shock drive lasting 11 ns.³² The velocity could be varied up to 2.3 $\text{km}\cdot\text{s}^{-1}$. A number of initial measurements were performed at 1.1 $\text{km}\cdot\text{s}^{-1}$. The samples were polymer films $15 \pm 2\ \mu\text{m}$ thick on glass substrates, and the shock transit time across a film was 3-4 ns.²⁸ The shock pressure and temperature at 1.1 $\text{km}\cdot\text{s}^{-1}$ depends on the properties of the polymer, but these polymers were reasonably similar mechanically and the shocks were generally about 3.4 GPa with a peak temperature of about 170 °C.^{28,33} The impact velocities were measured using photon Doppler velocimetry,³² and the photoemission spectra were

measured by irradiating the NR molecules during the shock with 250 ns green laser pulses (527 nm), and acquiring one spectrum every 0.5 ns with a streak camera and spectrograph.^{12, 28, 31}

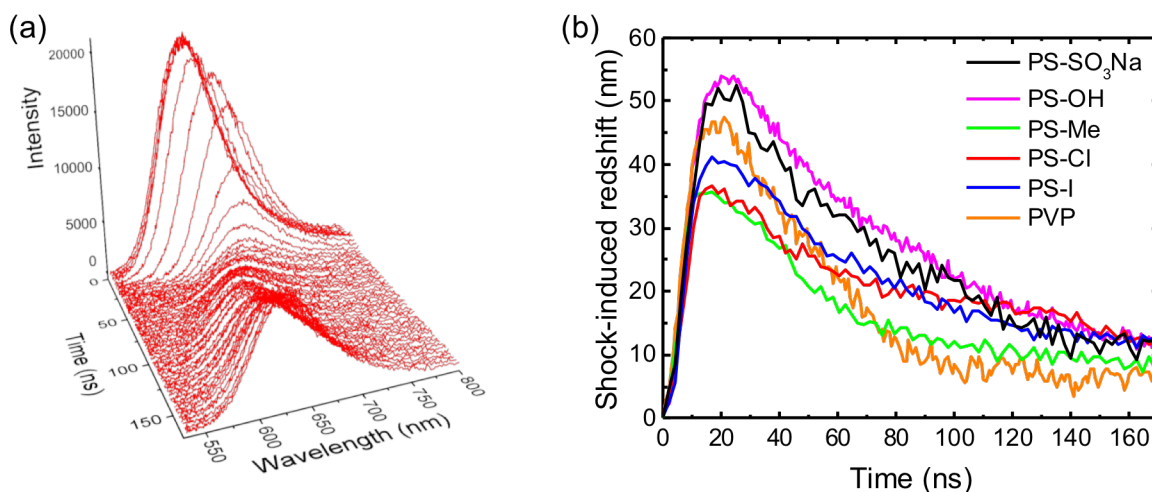


Figure 4.1 (a) Time-resolved dye photoemission from NR in poly(4-vinylpyridine) (PVP) after impact with a 75 μm thick flyer at $1.1 \text{ km}\cdot\text{s}^{-1}$. When the shock front arrived, NR emission lost intensity, redshifted, and broadened slightly. After the shock wave passes, the redshift is partially recovered. (b) Redshift transients from NR in different polymers with $1.1 \text{ km}\cdot\text{s}^{-1}$ impacts.

According to the discussion above, more polar polymer media should show larger shock-induced NR redshifts. Results showing NR used to probe shock-induced polarity increases in polymers are presented in Figure 4.1 & 4.2. Figure 4.1a shows a time stream of emission spectra from NR in poly(4-vinylpyridine) (PVP) with a $1.1 \text{ km}\cdot\text{s}^{-1}$ impact. When the shock arrived, the emission redshifted, and the maximum value of the redshift was 47 nm. The NR emission also lost intensity and broadened slightly. In studies of the polarity-independent dye Rhodamine 6G (R6G) in PMMA,²⁸ the redshift at the same impact velocity was 30 nm and the intensity loss was caused by shock-enhanced intersystem crossing into dark triplet states.³¹ Figure 4.1b shows time-dependent NR redshift transients for the six polymers in Scheme 4.2. In PS-Me and PS-Cl, the redshift built up during the 11 ns shock and then decayed on the 100 ns time scale. In the other polymers, due to sluggish polymer response the redshift continued to build up until it reached a maximum around 20 ns, followed by ~ 100 ns decay. Figure 4.2 shows the maximum redshift versus a measure of polymer polarity, namely the ambient (unshocked) NR emission maximum. The smallest shock-induced redshift was 35 nm for PS-Me, already greater than R6G in PMMA. The largest was 55 nm for PS-OH. A linear relationship exists between the polymer's

polarity, as determined from the ambient NR redshift, and the shock-induced redshift. The high degree of correlation between polymer polarity and NR shock redshift was interpreted as the shock-induced polarity increase was greatest for the most polar polymers.

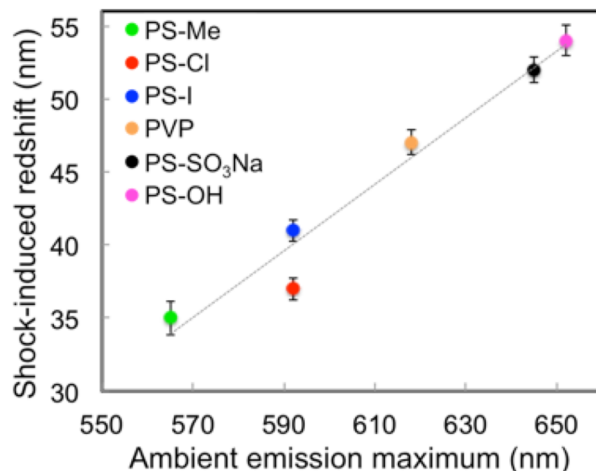


Figure 4.2 Correlation between polymer polarity, determined from the ambient-pressure NR redshift, and the shock-induced polarity increase at $1.1 \text{ km}\cdot\text{s}^{-1}$, interpreted by the shock-induced redshift.

4.4 Shock-Induced Proton Transfer in Poly(4-Vinylpyridine)-Based Blends

We then investigated the ability of NR to detect shock-induced proton transfer in polymer blends. Since temperature- and pressure-induced proton transfer had previously been observed in pyridine-based co-crystals with organic proton donors,^{13, 34-36} we selected PVP as the polymer base. We screened a series of small proton donors with a range of pK_a values (Table 4.4), and mixed them in a 1:1 molar ratio with the NR-doped PVP. All the blends exhibited a single glass transition temperature, indicating that PVP was miscible with the proton donors (Figure 4.7). The donors only slightly affected the ambient NR emission (Table 4.1). For this reason, we believe that little, if any, proton transfer from the molecular proton donor to PVP occurred under ambient conditions. In addition, the NR redshifts with proton donors were always at least 20 nm less than in $\text{PS-SO}_3\text{Na}^+$ (Table 4.3), a polymer salt where an ion pair is present at ambient conditions. The lack of proton transfer in the donor-acceptor polymer blends was also confirmed by the absence of the pyridinium ring stretch in the IR spectra (Figure 4.6).

Table 4.1 Emission maximum and shock-induced redshift for NR in PVP polymer with various proton donors (1:1 molar ratio).

Proton donor	Emission _{max} (nm) ^a	Shock-induced redshift (nm)
3,5-Dinitrobenzoic acid	617	37
Benzoic acid	622	44
Aniline	612	49
4-Methoxyphenol	625	51
Phenol	618	57
4-Bromophenol	617	57
4-Isopropylphenol	622	58
None	618	47

^a Spectra collected under ambient temperature and pressure.

We subjected all the PVP-based blends to flyer plate impacts at 1.1 km·s⁻¹, while monitoring the maximum NR redshift (Table 4.1). Our expectation was that the most acidic proton donors with the smallest pK_a values would most readily undergo shock-induced proton transfer.³⁷ The blends with phenol, 4-bromophenol, or 4-isopropylphenol as proton donors had the largest shock-induced redshifts. The redshifts for 4-methoxyphenol and aniline, which have higher pK_a's than phenol, were significantly smaller. With 3,5-dinitrobenzoic acid (DNBA), which had the most acidic proton donor, the redshift was the smallest. We attribute this result to DNBA dimerization, which competes with proton transfer to the polymer.

We turned our focus to PVP-phenol, since the 1.1 km·s⁻¹ results with such a large NR redshift suggested it was a likely candidate for shock-triggered proton transfer. We studied the NR redshift as a function of impact velocity. We also looked at PVP-phenol-d₁ to investigate the possibility of an isotope effect, and we used pure PVP and PVP-anisole, where proton transfer is blocked by the methyl ether, as controls. Figure 4.3a shows the peak NR redshifts as a function of impact velocity from 0.3 to 2.3 km·s⁻¹. As expected, the NR redshifts in PVP and PVP-anisole, where no proton transfer is possible, were linear in impact velocity, which is consistent with a NR redshift caused mainly by density-induced NR level shifting and density-induced polarity increase of PVP. The results for PVP-phenols were dramatically different. At a threshold of ca. 0.8 km·s⁻¹, the NR redshifts grew beyond what could be attributed to density increase alone. This excess redshift is strongly suggestive of the polarity increase caused by proton transfer. The PVP-phenol-d₁ results were the same, indicating no significant kinetic isotope effect.

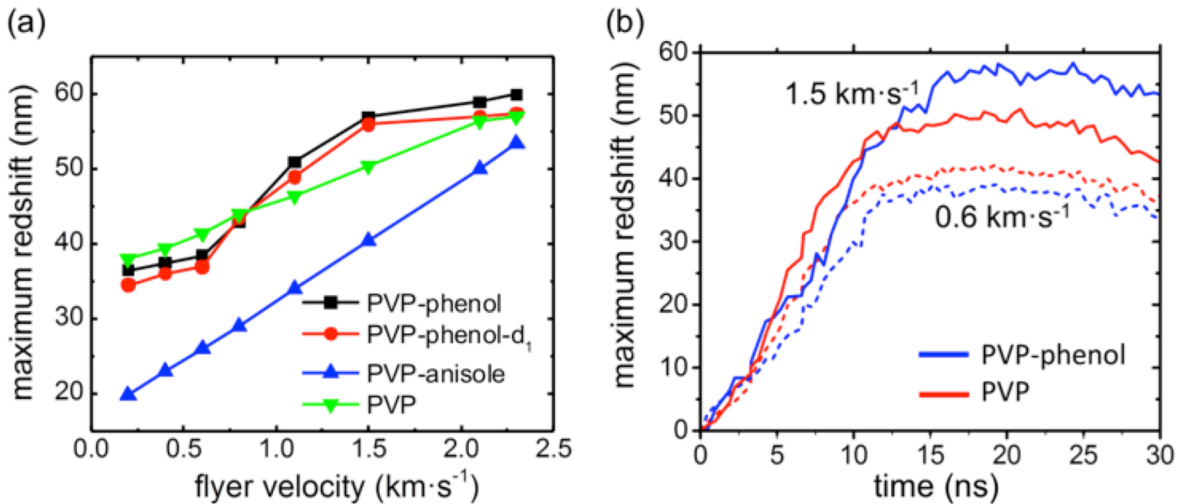


Figure 4.3 (a) Maximum emission redshift of NR in different polymers versus flyer plate velocity. PVP and PVP-anisole showed the usual redshift linearity, in flyer velocity, but PVP-phenol and PVP-phenol-d₁ had an excess redshift with a threshold in the 0.6-0.7 km·s⁻¹ range. (b) Time-dependent redshifts for PVP and PVP-phenol at 0.6 km·s⁻¹ (below threshold) and at 1.5 km·s⁻¹ (above threshold). The excess NR redshift associated with proton transfer in PVP-phenol started at the end of the steady shock drive at 11 ns and was a maximum near 20 ns.

The NR redshift transients in Figure 4.3b compare PVP and PVP-phenol below (0.6 km·s⁻¹) and above (1.5 km·s⁻¹) the threshold velocity. Below the threshold, both have approximately the same redshift dynamics. Above the threshold, however, the PVP-phenol has an additional redshift increase that starts at the end of the steadily-driven shock and becomes a maximum at about 20 ns. Because of the sluggish response of the polymer to shock,^{28, 38} it was difficult to precisely assign a time constant for the shock-induced proton transfer. Based on the data in Figure 4.3b, a reasonable estimate would be about 10 ns.

4.5 Conclusions

In summary, we have demonstrated shock-induced proton transfer in blends having a proton donor and acceptor (PVP-phenol). The polarity-sensing dye NR showed a shock-induced redshift that surpassed the NR redshifts in the PVP or PVP-anisole controls, which are incapable of proton transfer. Unlike the usual shock redshifts of dyes caused by the effects of the density increase on the dye energy levels or the increase in the polymer polarity, this excess redshift shows a shock threshold and appeared at a threshold velocity in the 0.6-0.7 km·s⁻¹ range. The

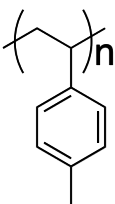
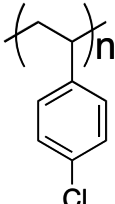
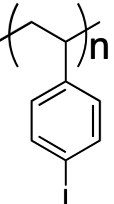
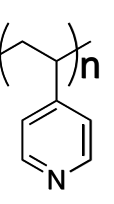
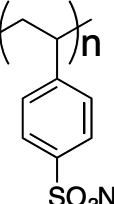
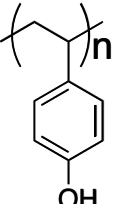
excess redshift appeared with a time constant of roughly 10 ns. Based on the detailed characterization performed and the extensive controls studied, we can confidently attribute this time-delayed polarity increase to the appearance of ion pairs created by shock-triggered proton transfer. The energy-dissipative properties of PVP, PVP-anisole, and PVP-phenol are currently under investigation to probe the role of proton transfer in shock wave energy dissipation.

4.6 Experimental Details

4.6.1 Materials and Sample Preparation Details

All materials were obtained from commercial suppliers (Sigma-Aldrich and Scientific Polymer Products) and were used as received. The names, abbreviations, molecular structures, and specifications of the polymers used in this study are given in Table 4.2. A $15 \pm 2 \mu\text{m}$ thick

Table 4.2 Specifications of polymers used in this study.

Name	Poly(4-methylstyrene)	Poly(4-chlorostyrene)	Poly(4-iodostyrene)	Poly(4-vinylpyridine)	Poly(sodium 4-styrenesulfonate)	Poly(4-hydroxystyrene)
Acronym	PS-Me	PS-Cl	PS-I	PVP	PS-SO ₃ Na	PS-OH
Structure						
Molecular Weight (kDa)	100	75	60	60	70	25
Glass Transition Temperature (°C)	105	128	163	150	>300	167
Solvent used	DMF	DMF	DMF	EtOH	H ₂ O	EtOH

thin film sample was spin-coated on top of a 50x50x6.35 mm³ borosilicate glass substrate (McMaster Carr) and further dried under vacuum for 48 hours at 40 °C. The thin film sample was either a Nile Red (NR)-doped polymer or a NR-doped mixture containing poly(4-vinylpyridine) and a molecular proton donor in 1:1 molar ratio. The dye-doped sample was prepared by mixing the NR solution (2.5 mM in ethanol) with the pre-dissolved polymer or polymer mixture solution (5 wt% in ethanol, DMF, or water), where the NR dye concentration in the polymer matrix was 0.1 mol% per monomer unit of the polymer. The thickness and flatness of the polymer layers were determined using a Sloan Dektak 3 profilometer.

4.6.2 Laser-Launched Flyer Plates Apparatus

A schematic illustration of the shock-compression experimental setup is shown in Figure 4.4, with details described previously.^{12, 28, 31} A Photon Doppler Velocimeter was used to monitor the flyer plate velocity history, while a streak-camera was simultaneously used to record time-resolved fluorescence spectra from the laser-excited dye. The flyer plates were launched from an assembly consisting of a 6.35 mm thick glass substrate and a 75 μm thick aluminum foil (5 × 5 cm², Alufoil) which were connected using low-viscosity Eccobond 24 water-clear epoxy (Henkel Loctite). A spatially homogenized Q-switched Nd:YAG laser (Quanta-Ray Pro-350) was used to

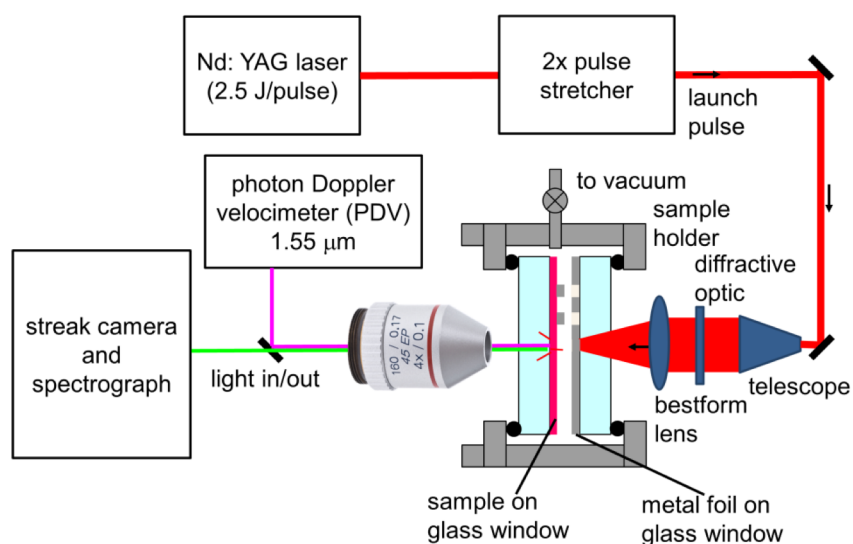


Figure 4.4 A schematic depiction of studying Nile Red emission in different polymers shocked by laser-launched flyer plates.

launch the flyer, producing shock pulses of 11 ns in duration following impact on the sample. The flyer plate velocities were controlled by varying the launch pulse energy up to a maximum of 2.5 J/pulse. The laser launch beam has a uniform central 500 μm diameter region and duration of ca. 11 ns (full width at half maximum, FWHM). The dye fluorescence was excited by 250 ns FWHM pulses from a Q-switched 527 nm Nd:YLF laser (Quantronix 527 DP) and recorded with 0.5 ns effective time per CCD pixel using a streak camera.

4.6.3 Absorption and Emission Results of Nile Red Embedded in Different Polymeric Matrices

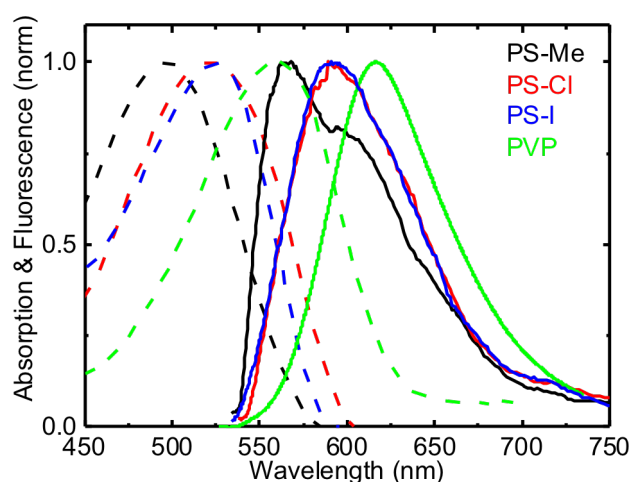


Figure 4.5 Absorption (dotted line) and emission (solid line) spectra of Nile Red embedded in different polymers under ambient (steady-state) conditions.

Table 4.3 Spectroscopic data of NR embedded in different polymers under ambient (steady-state)^a and shock^b conditions.

Polymer	PS-Me	PS-Cl	PS-I	PVP	PS-SO ₃ Na	PS-OH
Shock-induced redshift (nm) ^b	35	37	41	47	52	54
Absorbance _{max} (nm) ^a	497	524	526	560	587	599
Fluorescence _{max} (nm) ^a	565	592	592	618	645	652

Table 4.4 Spectroscopic data of NR in a binary system composed of PVP and different proton donors (1:1 molar ratio) under steady-state^a and shock^b conditions.

PVP with different proton donors	pKa of proton donor* (in DMSO**)	Shock-induced redshift (nm) ^b	Emission _{max} (nm) ^a	Absorbancemax (nm) ^a
3,5-Dinitrobenzoic acid	2.86 (N/A, but pKa of 4-Nitrobenzoic acid is 9.1)	37	617	564
Benzoic acid	4.08 (11.1)	44	622	568
Aniline	25.0 (30.6)	49	612	560
4-Methoxyphenol	9.9 (19.1)	51	625	584
Phenol	10.0 (18.0)	57	618	567
4-Bromophenol	9.09 (N/A, but pKa of 4-Chlorophenol is 16.7)	57	617	569
4-isopropylphenol	10.3 (N/A, but pKa of 4-Methylphenol is 18.9)	58	622	573
N/A	N/A (N/A)	47	618	560

*pK_a values are calculated using MarvinSketch 15.9.28. **pK_a values in DMSO are obtained from Bordwell pK_a Table (<http://www.chem.wisc.edu/areas/reich/pkatable/index.htm> accessed on Jan. 9, 2017).

4.6.4 Infrared Spectra of PVP and its Blends with Various Proton Donors under Ambient Conditions

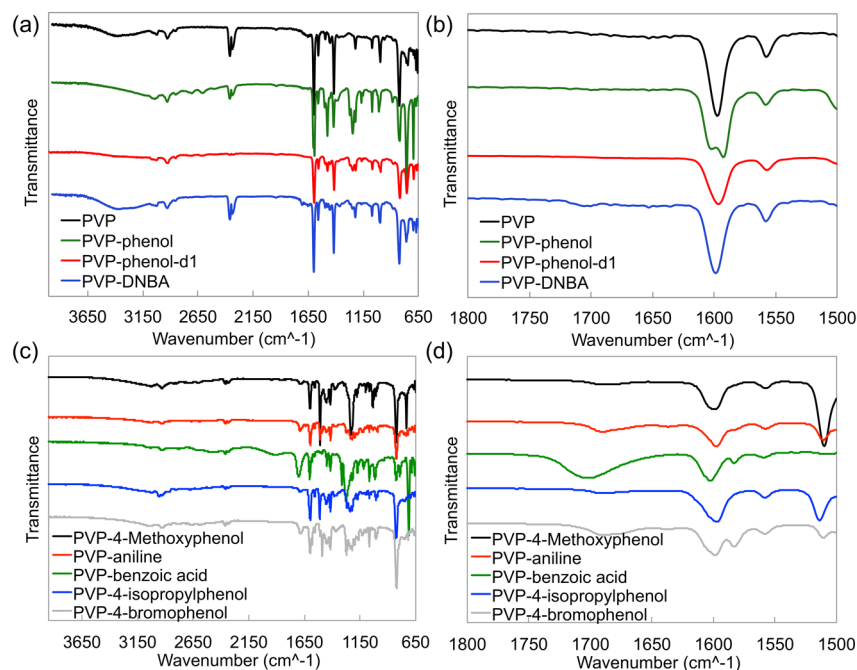


Figure 4.6 (a) FTIR spectra of PVP and its blends with phenol, phenol-d₁, and DNBA. (c) FTIR spectra of PVP blends with 4-methoxyphenol, aniline, benzoic acid, 4-isopropylphenol, and 4-bromophenol. (b) and (d) are the zoomed-in spectra ranging from 1500 to 1800 cm⁻¹. The absence of a pyridinium ring stretch around 1630 cm⁻¹ suggests that little, if any, proton transfer from the molecular proton to PVP has occurred.¹ These spectra were collected on a NEXUS 670 serial FTIR spectrophotometer.

4.6.5 Differential Scanning Calorimetry Curves of PVP and its Blends with Various Proton Donors

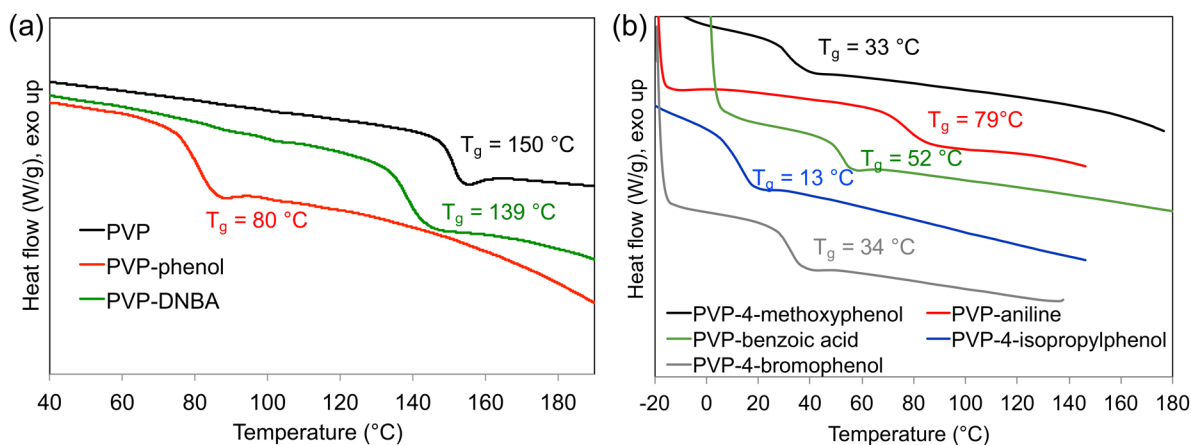


Figure 4.7 DSC curves of (a) PVP and its blends with phenol and DNBA. (b) PVP blends with 4-methoxyphenol, aniline, benzoic acid, 4-isopropylphenol, and 4-bromophenol. The DSC measurements were performed using TA Instrument Q20 with heating/cooling rate of 10 °C/min. Hermetic zero aluminum pans and lids were used as sample testing containers.

4.6.6 Results of the Varying Flyer Plate Velocity Experiments

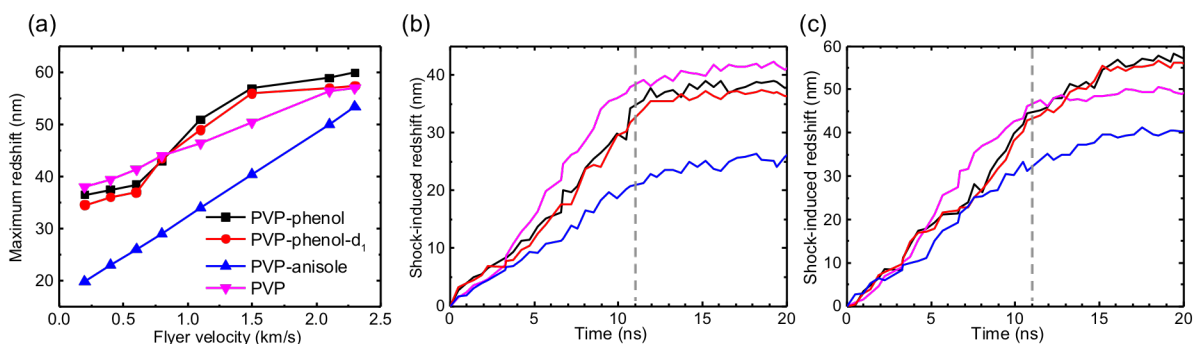


Figure 4.8 (a) Maximum emission redshift of NR in different polymers versus flyer plate velocity. PVP and PVP-anisole showed the usual redshift increase that was approximately linear in flyer velocity, but PVP-phenol and PVP-phenol- d_1 showed an excess redshift with a threshold in the 0.6-0.7 km·s⁻¹ range. (b) Time-dependent redshifts at 0.6 km·s⁻¹, below the threshold. (c) Time-dependent redshifts at 1.5 km·s⁻¹, above the threshold, show the excess redshift appeared within about 15 ns of the end of the steady shock drive at 11 ns (indicated by the vertical dashed line).

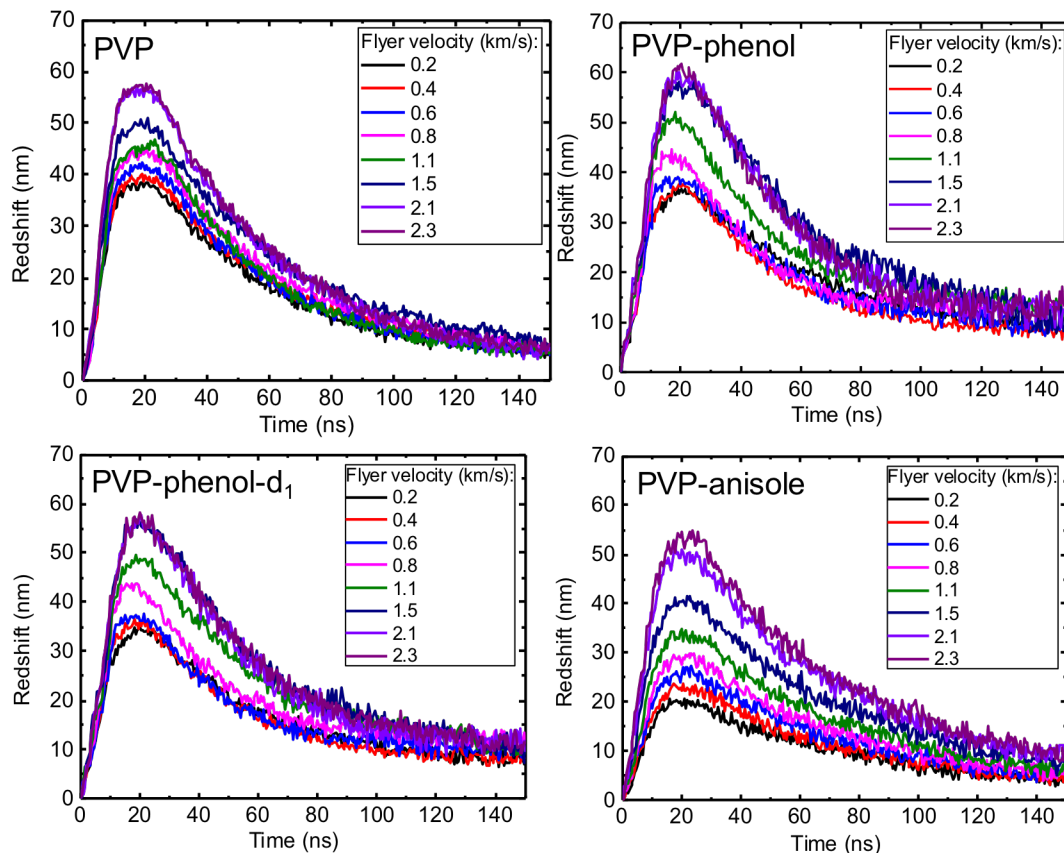


Figure 4.9 Redshift transients from the emission of the embedded NR in PVP and PVP-based blends impacted by a 75 μm thick flyer plate moving at various velocities.

4.7 Notes and References

Notes:

Portions of this chapter have been published: Ren, Y.; Banishev, A. A.; Suslick, K. S.; Moore, J. S.; Dlott, D. D. “Ultrafast Proton Transfer in Polymer Blends Triggered by Shock Waves.” *J. Am. Chem. Soc.* **2017**, *139*, 3974–3977. They are reproduced/adapted with permission. Copyright 2017 American Chemical Society.

References:

1. Zhou, X.; Goh, S. H.; Lee, S. Y.; Tan, K. L. *Polymer* **1998**, *39*, 3631.
2. Scheiner, S. *Acc. Chem. Res.* **1985**, *18*, 174.
3. Okamura, M. Y.; Feher, G. *Annu. Rev. Biochem.* **1992**, *61*, 861.
4. Caldin, E. F. *Chem. Rev.* **1969**, *69*, 135.
5. Hammes-Schiffer, S.; Tully, J. C. *J. Chem. Phys.* **1994**, *101*, 4657.
6. Steiner, T. *Angew. Chem., Int. Ed.* **2002**, *41*, 48.

7. Scherl, M.; Haarer, D.; Fischer, J.; DeCian, A.; Lehn, J. M.; Eichen, Y. *J. Phys. Chem.* **1996**, *100*, 16175.
8. Wang, Y.; Yin, H.; Shi, Y.; Jin, M.; Ding, D. *New J. Chem.* **2014**, *38*, 4458.
9. Schwartz, B. J.; Peteanu, L. A.; Harris, C. B. *J. Phys. Chem.* **1992**, *96*, 3591.
10. Eigen, M. *Angew. Chem., Int. Ed.* **1964**, *3*, 1.
11. Liu, L.; Bakker, H. J. *Phys. Rev. Lett.* **2014**, *112*, 258301.
12. Brown, K. E.; Fu, Y. X.; Shaw, W. L.; Dlott, D. D. *J. Appl. Phys.* **2012**, *112*, 103508.
13. Martins, D. M. S.; Middlemiss, D. S.; Pulham, C. R.; Wilson, C. C.; Weller, M. T.; Henry, P. F.; Shankland, N.; Shankland, K.; Marshall, W. G.; Ibberson, R. M.; Knight, K.; Moggach, S.; Brunelli, M.; Morrison, C. A. *J. Am. Chem. Soc.* **2009**, *131*, 3884.
14. Borgis, D. C.; Lee, S. Y.; Hynes, J. T. *Chem. Phys. Lett.* **1989**, *162*, 19.
15. Borgis, D.; Hynes, J. T. *J. Chem. Phys.* **1991**, *94*, 3619.
16. Holzapfel, W. B. *J. Chem. Phys.* **1969**, *50*, 4424.
17. David, H. G.; Hamann, S. D. *Trans. Faraday Soc.* **1959**, *55*, 72.
18. Hamann, S. D.; Linton, M. *Trans. Faraday Soc.* **1966**, *62*, 2234.
19. Hamann, S. D.; Linton, M. *Trans. Faraday Soc.* **1969**, *65*, 2186.
20. Gruzdkov, Y. A.; Gupta, Y. M. *J. Phys. Chem. A* **1998**, *102*, 2322.
21. Han, S. P.; van Duin, A. C. T.; Goddard, W. A.; Strachan, A. *J. Phys. Chem. B* **2011**, *115*, 6534.
22. Strachan, A.; van Duin, A.; Chakraborty, D.; Dasgupta, S.; Goddard III, W. A. *Phys. Rev. Lett.* **2003**, *91*, 098301.
23. Chakraborty, D.; Muller, R. P.; Dasgupta, S.; Goddard III, W. A. *J. Phys. Chem. A* **2001**, *105*, 1302.
24. Dutta, A. K.; Kamada, K.; Ohta, K. *J. Photochem. Photobiol. A* **1996**, *93*, 57.
25. Sarkar, N.; Das, K.; Nath, D. N.; Bhattacharyya, K. *Langmuir* **1994**, *10*, 326.
26. Reichardt, C.; Welton, T., *Solvents and Solvent Effects in Organic Chemistry*. 4th ed.; Wiley-VCH: Weinheim, 2011.
27. Drickamer, H. G. *Annu. Rev. Phys. Chem.* **1982**, *33*, 25.
28. Banishev, A. A.; Shaw, W. L.; Curtis, A. D.; Dlott, D. D. *Appl. Phys. Lett.* **2014**, *104*, 101914.
29. Jee, A. Y.; Park, S.; Kwon, H.; Lee, M. *Chem. Phys. Lett.* **2009**, *477*, 112.
30. Dreger, Z. A.; Lang, J. M.; Drickamer, H. G. *Chem. Phys.* **1992**, *166*, 193.
31. Banishev, A. A.; Dlott, D. D. *J. Appl. Phys.* **2014**, *115*, 203515.
32. Curtis, A. D.; Banishev, A. A.; Shaw, W. L.; Dlott, D. D. *Rev. Sci. Instrum.* **2014**, *85*, 043908.
33. Zheng, X.; Curtis, A. D.; Shaw, W. L.; Dlott, D. D. *J. Phys. Chem. C* **2013**, *117*, 4866.
34. Johnson, S. L.; Rumon, K. A. *J. Phys. Chem.* **1965**, *69*, 74.
35. Huang, K. S.; Britton, D.; Etter, M. C.; Byrn, S. R. *J. Mater. Chem.* **1997**, *7*, 713.
36. Bhogala, B. R.; Nangia, A. *Cryst. Growth Des.* **2003**, *3*, 547.
37. Bhogala, B. R.; Basavoju, S.; Nangia, A. *CrystEngComm* **2005**, *7*, 551.
38. Gupta, Y. M. *J. Appl. Phys.* **1980**, *51*, 5352.

Chapter 5: Crystal Structure, Thermal Properties, and Shock-Wave-Induced Nucleation of 1,2-Bis(phenylethynyl)benzene

5.1 Abstract

We report the single crystal structure and thermal properties of 1,2-bis(phenylethynyl)benzene (**PEB**), revealing that **PEB** forms a metastable liquid at rt, ca. 35 °C below its melting point. Accelerated nucleation of **PEB** from its supercooled state was induced with high reproducibility by a shock wave with ca. 15 ns duration and 1.2 GPa peak pressure. By conducting shock wave experiments with varying peak pressures, we observed a correlation between the frequency of accelerated nucleation and shock intensity. The generality of shock-induced nucleation for supercooled liquids was probed with other organic supercooled liquids bearing phenyl rings. However, accelerated nucleation after shock-wave impact was only observed for **PEB**, possibly due to the low rotational energy barrier of the terminal phenyl rings. Based on preliminary energy-dissipative results, supercooled **PEB** dissipates more energy than supercooled salol and diphenyl phthalate when subjected to low-intensity shock waves. However, upon high-intensity shock impacts, salol dissipates more energy than **PEB** suggesting that the viscosity of these phenyl-bearing supercooled liquids is crucial for energy dissipation.

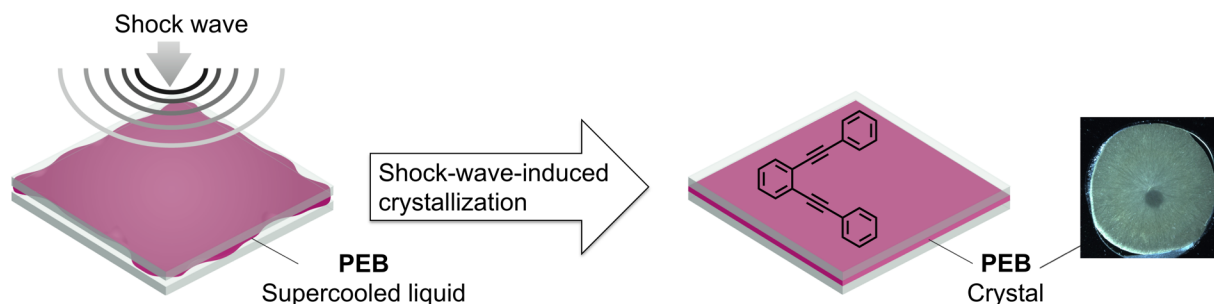
5.2 Introduction

Controlling crystallization of organic molecules is of great interest for the development of pharmaceuticals,¹⁻² organic electronics,³ and gas-storage materials.⁴ Upon cooling, some molten crystalline materials are capable of forming thermodynamically unstable supercooled liquids. The effect of pressure in the form of compression on crystal nucleation and growth in supercooled liquids has been explored;⁵⁻⁷ however, contradictory examples of pressure-promoted or inhibited crystallization are found in literature.^{5, 8-9} Other external forces such as ultrasonication,¹⁰ mechanical grinding,¹¹ and shear¹² are often utilized to assist in crystallization, but the complex mechanisms of crystallization, especially in the presence of such external triggers, still lacks a thorough understanding. Recently, our group demonstrated that a shock wave is capable of inducing structural ordering in an amorphous ionic liquid.¹³ A shock wave

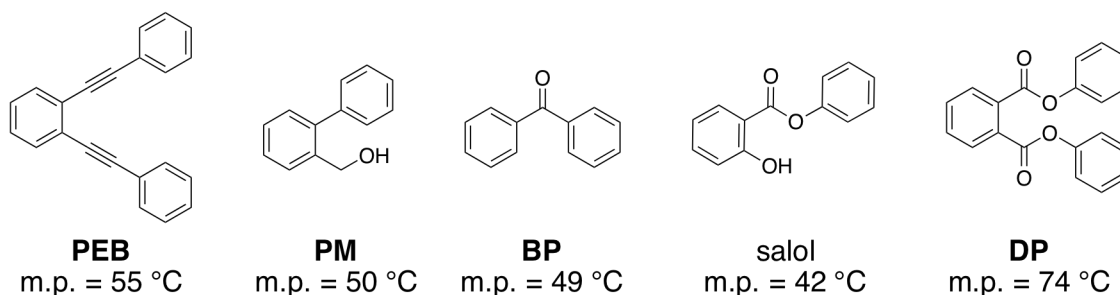
imparts a transient pressure jump of ns duration, potentially long enough for nuclei to form¹⁴ and may serve as a useful probe for crystal nucleation in supercooled liquids. Additionally, volume reduction during the transformation from an amorphous phase to a crystalline phase is potentially useful for shock wave energy dissipation (SWED).

While studying the reactivity of aryl-substituted arenediynes,¹⁵ we discovered that 1,2-bis(phenylethynyl)benzene (**PEB**) forms a stable supercooled liquid at room temperature. Although **PEB** has been extensively studied to probe the Bergman cyclization reaction and to investigate its optical properties,^{10, 16-18} to the best of our knowledge, its crystal structure is not reported. Herein, we present the single crystal structure and thermal properties of **PEB**, along with crystallization of the supercooled liquid. We demonstrate that a shock wave with 1.2 GPa peak pressure and 15 ns duration accelerates nucleation of supercooled **PEB** (Scheme 5.1). Systematic studies of shock wave peak pressures were conducted to correlate pressure effects and frequency of nucleation. The generality of shock-induced nucleation was probed with other supercooled liquids including diphenyl phthalate (**DP**), benzophenone (**BP**), salol, and 2-

Scheme 5.1 Depiction of shock-wave-induced crystallization of supercooled **PEB**.



Scheme 5.2 Chemical structures of supercooled liquids used in this study and their corresponding melting points (*m.p.*) as determined by differential scanning calorimetry (DSC).



biphenylmethanol (**PM**) (Scheme 5.2). However, accelerated nucleation after shock wave impact was only observed for **PEB**. Several hypotheses are discussed to provide insight into the mechanism of shock-accelerated crystal nucleation of supercooled liquids bearing phenyl rings.

5.3 Synthesis and Characterization of 1,2-Bis(Phenylethynyl)Benzene (**PEB**)

PEB was synthesized via a Sonogashira coupling reaction following a literature procedure (Figure 5.5).¹⁹ Nonplanar molecules with limited conformational flexibility often lead to the formation of amorphous materials,²⁰ and **PEB** falls into this category based on simulations with the B3LYP/6-31G(d) basis set (Figure 5.11).^{15, 21} Solution grown, diffraction quality crystals of **PEB** were attempted using common organic solvents such as cyclohexane, benzene, tetrahydrofuran, and chloroform at different temperatures (see Table 5.1). In spite of extensive experimentation with typical crystallization conditions, **PEB** generally remained in solution or oiled-out after solvent evaporation. We were able to successfully obtain single crystals of **PEB**

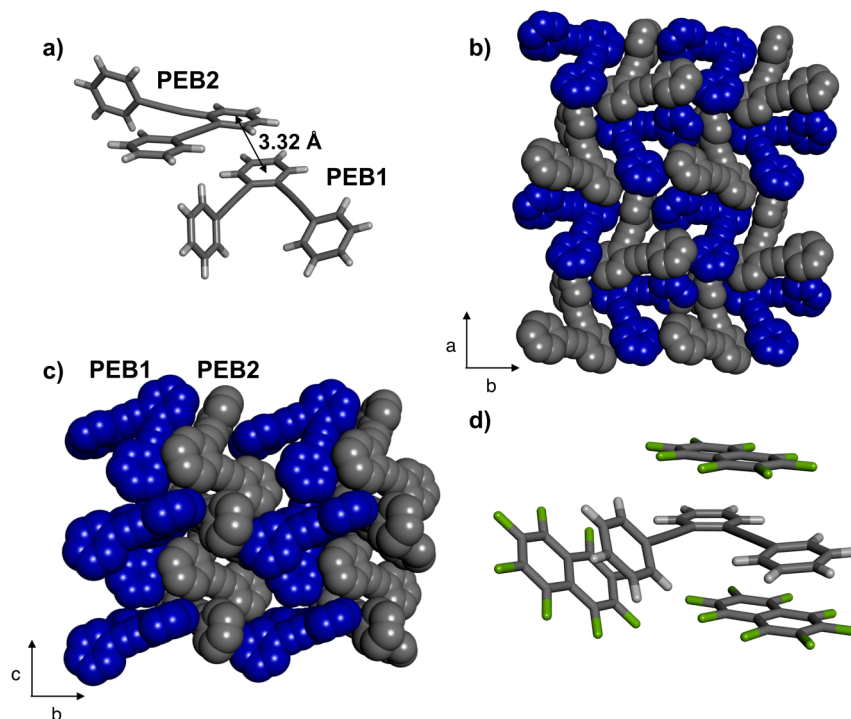


Figure 5.1 Single-crystal X-ray structures involving **PEB**: (a) **PEB1** and **PEB2** rotamers, (b) alternating packing along *a*-axis, (c) column packing, and (d) cocrystal with **OFN** highlighting phenyl-perfluorophenyl interactions.

suitable for X-ray analysis through slow evaporation of a saturated hexanes solution at -20 °C. A single-crystal X-ray analysis revealed that **PEB** crystallizes in the acentric space group $Pca2_1$, with two crystallographically unique molecular conformations (**PEB1** and **PEB2**) in the asymmetric unit (Figure 5.1a). The terminal phenyl rings of **PEB1** lie twisted from the plane of the central benzene ring at dihedral angles of 28.6° and 74.2°. In **PEB2**, however, one terminal phenyl ring lies nearly coplanar with the central benzene ring (4.4° twist), while the second terminal phenyl ring is twisted significantly from the plane of the central benzene at 71.0°. The dihedral angle between the two terminal phenyl rings is 87.9° for **PEB1** and 73.0° for **PEB2**, confirming that **PEB** crystallizes in a nonplanar geometry. The two **PEB** rotamers pack in an alternating **PEB1** | **PEB2** pattern along the *a*-axis (Figure 5.1b), and neighboring central benzene rings engage in π -facial interactions (3.32 Å separation). Conformers **PEB1** and **PEB2** pack into alternating columns²² that extend along the *b*-axis (Figure 5.1c), sustained by edge-to-face C-H $\cdots\pi$ interactions (ca. 3.5 Å separation).

Although we obtained a single crystal of **PEB**, we sought to further investigate its solid-state structure to test whether it adopts planar conformations, or whether twisted conformations are typical. One approach to facilitate the crystallization of **PEB** involves forming stabilized electrostatic interactions via cocrystallization with perfluorinated analogues.^{20, 23-25} In fact, cocrystals comprised of octafluoronaphthalene (**OFN**) and **PEB** were readily obtained using various conditions (see section 5.8.6). A single-crystal X-ray analysis revealed that **OFN** and **PEB** crystallize in a 3:2 molar ratio in the space group $P\bar{1}$. One terminal phenyl ring of **PEB** lies nearly coplanar with the central benzene ring of **PEB** (6.9° twist), while the second terminal phenyl ring is twisted significantly from the plane of the central benzene (52.8° twist). The coplanar rings engage in phenyl-perflorophenyl interactions with one crystallographically unique **OFN** (centroid-centroid distance: 3.60 Å (central benzene-**OFN**) and 3.73 Å (phenyl-**OFN**)), while the twisted phenyl ring engages in phenyl-perflorophenyl interactions with the second crystallographically unique **OFN** (centroid-centroid distance: 3.71 Å) (Figure 5.1d). The dihedral angle between the two terminal phenyl rings of **PEB** is 55.3°, further demonstrating propensity for **PEB** to crystallize in nonplanar geometries.

While crystalline **PEB** melts at 55 °C as seen in the DSC trace (Figure 5.6), subsequent cooling of the molten **PEB** results in a supercooled liquid phase that is stable down to ca. 0 °C.

The supercooled liquid phase persists during the second heating cycle without showing any crystallization peaks, indicating it forms a supercooled liquid with good thermal stability.¹² Using the Hoffman equation,¹² the Gibbs free energy difference (ΔG) between supercooled and crystalline **PEB** at 25 °C was estimated as -1.84 kJ/mol (Figure 5.9). This value is comparable to the ΔG between tolfenamic acid polymorphs and is over one order of magnitude smaller than the ΔG between *cis*- and *trans*-azobenzene.²⁶⁻²⁷ The relatively small ΔG of **PEB** suggests that **PEB** has a relatively large critical radius of nucleation (r^*), the minimum nucleus size that can grow spontaneously.¹² Thus, the large r^* of **PEB** suppresses nucleation, which potentially explains the formation of supercooled **PEB**.

5.4 Shock-Induced Nucleation of Supercooled PEB

Since external forces often trigger the crystallization of amorphous materials and crystal nucleation in liquids occurs in nanoseconds,¹³⁻¹⁴ we investigated the possibility of using a laser-induced shock wave with GPa peak pressure and ns duration to induce the nucleation of supercooled **PEB**.¹³ The shock waves were generated by impingement of a high-energy Nd:YAG pulsed laser on a 400 nm thick aluminum energy-absorbing layer (see section 5.8.3).¹³ The transferred laser power drives rapid expansion of the aluminum producing, a high-amplitude stress wave (i.e. a shock wave) that propagates through the specimen and impacts the supercooled liquid. The peak pressure of the shock wave was controlled by systematically varying the laser fluence (see section 5.8.4). Interestingly, a nucleation site within the **PEB** liquid was immediately observed with optical imaging after shock wave exposure (Figure 5.2), whereas no nucleation site was observed after one week for liquid **PEB** without impact.

The powder X-ray diffraction (PXRD) patterns of solidified **PEB** after shock wave impact are consistent with the predicted pattern from the single crystal X-ray data (Figure 5.3a). No chemical change in the **PEB** sample was observed by NMR, UV-Vis, or IR following shock wave impact (Figure 5.10). These findings suggest that the nucleation rate of supercooled **PEB** is significantly increased upon shock wave impact. Using the relationship $[\frac{\partial(\ln K)}{\partial P}]_T = \frac{\Delta V^0}{RT}$, the change in natural log of the equilibrium constant (K) is proportional to the change in pressure (P), since ΔV^0 is fixed for the transformation from supercooled liquid to crystal. Thus, crystallization

of **PEB** is preferred under high pressure (large ΔP). Shock-wave-induced nucleation experiments with varying peak pressure were conducted (Figure 5.9). As the peak pressure of the shock wave increased, the frequency of shock-induced nucleation also increased (Figure 5.3b). Since $r^* \propto -\frac{1}{\Delta G}$ and $\Delta G = V\Delta P - S\Delta T$,^{5, 12} it follows that r^* decreases as ΔP increases. At higher pressure, the shock-accelerated nucleation of **PEB** is therefore promoted by a reduction in r^* .⁵⁻⁶

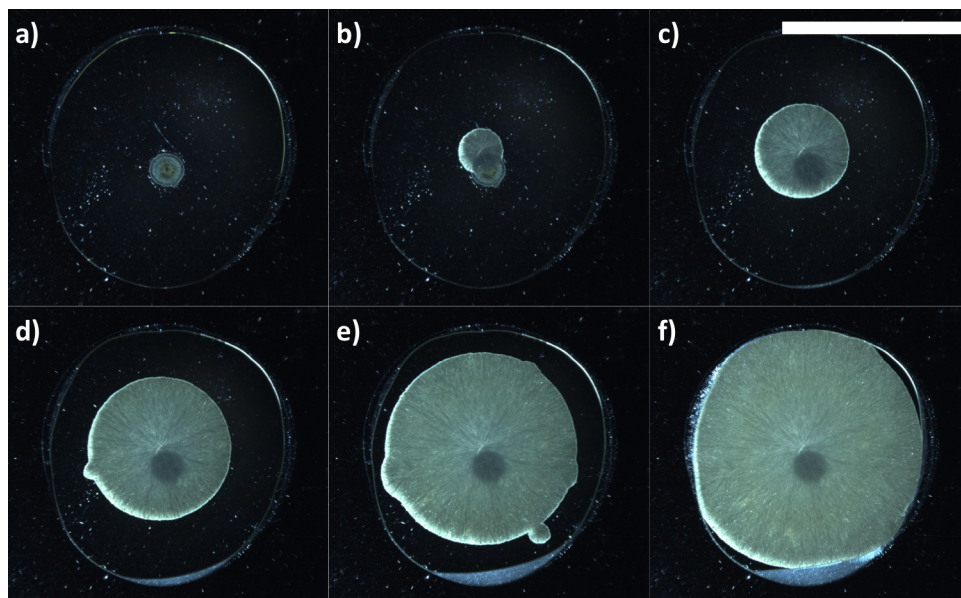


Figure 5.2 Shock induced crystallization of supercooled **PEB** after a) 0 hr; b) 7 hrs; c) 14 hrs; d) 22 hrs; e) 29 hrs; f) 36 hrs. Scale bar = 1 cm.

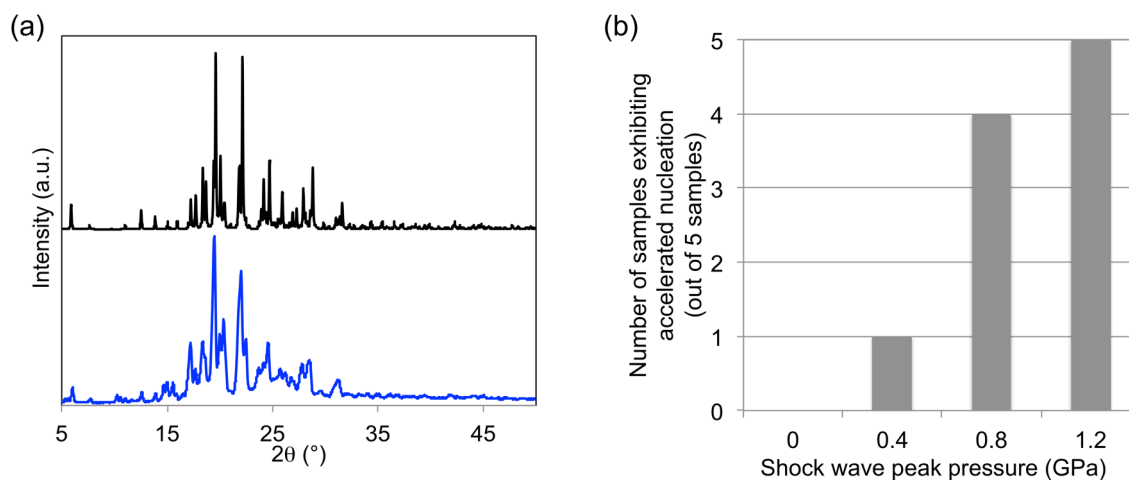


Figure 5.3 (a) PXRD pattern of crystallized **PEB** after shock wave impact (blue) and simulated pattern from single crystal of **PEB** (black); (b) Investigation of shock wave peak pressure on accelerated nucleation of **PEB**.

5.5 Scope and Generality of Shock-Induced Crystallization of Supercooled Liquids Bearing Phenyl Rings

To explore the scope and generality of shock-induced nucleation of supercooled liquids, we performed similar experiments on **DP**, **BP**, salol, and **PM** (Scheme 5.1b), which are also capable of forming stable supercooled liquids at room temperature (Figure 5.6).²⁸⁻³⁰ No accelerated nucleation rate was observed with any of these four substances upon shocking their supercooled liquids under 1.2 GPa pressure. Although it is known that the effect of pressure on crystallization of supercooled liquids is not universal,^{5, 7, 9, 31-32} we propose several hypotheses to explain our observations. We originally assumed that compounds with high crystal packing efficiencies crystallize more readily upon shock wave impact due to shock-induced densification. However, crystal packing efficiencies among these five tested compounds are similar, lying in the normal range of 65-68% (Table 5.3). We then hypothesized that shock-induced nucleation is more successful for compounds possessing smaller r^* values. The free energy of crystallization at 25 °C was calculated for each tested compound using the Hoffman equation (Figure 5.6).¹² Based on the ΔG values, r^* of **PEB** is smaller than that of **BP**, **PM**, salol, but larger than that of **DP**.

We also determined the viscosity and glass transition temperature of each compound to test the hypothesis that nucleation is transport limited. However, these properties of **PEB** do not stand out from that of salol, **BP**, **PM**, and **DP** (Table 5.4). Since the kinetics of nucleation also depend on rotational energy barrier,³³ *i.e.* the energy required for molecules to go through an intermediate arrangement and achieve structural alignment, we calculated the energy profile of each molecule as its terminal phenyl ring rotates 360° using the optimized structure as the starting geometry (Figure 5.11 and Table 5.5). Among all the compounds tested, the only unique characteristic of **PEB** is that its rotational barrier is at least one order of magnitude lower than the other molecules. Whether this is a coincidental finding or has consequences for shock-induced crystallization remains unresolved at this time.

5.6 Energy-Dissipative Properties of Supercooled Liquids Bearing Phenyl Rings

Since the transformation from an amorphous phase to a crystalline phase leads to volume collapse, supercooled **PEB** has been proposed as a promising candidate for SWED. We have

determined the energy-dissipative properties of supercooled **PEB**, salol, and **DP** under shock wave impact with various intensities (Figure 5.4). Compared to materials with high peak pressure values, materials with low peak pressure values are more efficient at dissipating shock wave energy.¹³ As shown in Figure 5.4, supercooled **PEB** possesses the lowest peak pressure when the laser fluence is below 45 mJ/mm². However, as the laser fluence increases, the peak pressure of **PEB** falls between that of salol and **DP**. As shown in Table 5.4, the viscosity of **PEB** is higher than that of salol, but lower than that of **DP**. These preliminary results suggest that viscosity of these phenyl-bearing supercooled liquids plays a crucial role in energy dissipation, especially for high-intensity shock wave impacts. Of course, a systematic series of shock experiments is required to make a definitive conclusion.

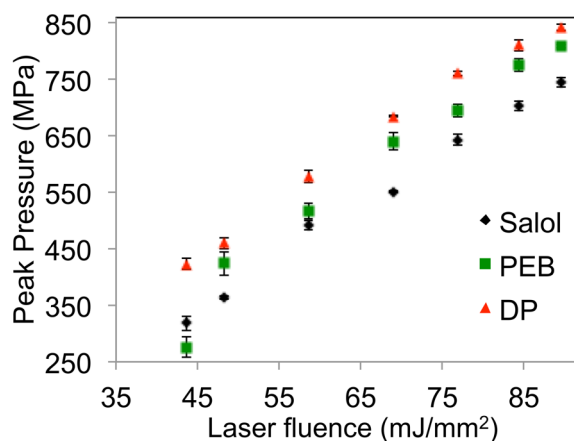


Figure 5.4 SWED properties of **PEB**, salol, and **DP** under various impact levels.

5.7 Conclusions

In summary, we successfully obtained the single crystal structure of **PEB**, as well as a co-crystal, to demonstrate its propensity to pack in nonplanar arrangements. The DSC curve of **PEB** indicated that it has a relatively low ΔG , which leads to the formation of a stable supercooled liquid at room temperature. A shock wave with ns duration induced nucleation of supercooled **PEB**, confirming that nucleation in liquids can occur within a very short time frame. The nucleation behavior of additional supercooled liquids was studied using shock wave impact; however, the facilitated crystallization was observed only for **PEB**. The low rotational energy barrier of the terminal phenyl rings potentially explains the unique behavior of **PEB**. However,

more systematic shock studies on a larger library of supercooled liquids are required to make a definitive conclusion. Questions remain to be solved include: how short of a shock duration is required for nucleation to ensue if the peak pressure of a shock wave is fixed? Can the shape of a shock profile control the nucleus structure? What is the role of shear waves on nuclei formation?

In addition to building an understanding of the shock-induced nucleation, the SWED properties of the phenyl-bearing supercooled liquids are also under investigation. Preliminary results suggest that viscosity plays a vital role in SWED, especially at high shock-wave impact levels. One future direction involves the development of amorphous imidazolium-based ionic liquids with high viscosity, as the shock-induced ordering in an ammonium-based ionic liquid was observed to achieve promising SWED results.¹³

5.8 Experimental Details

5.8.1 General Experimental Details

All chemicals were purchased from commercial suppliers and used as received unless otherwise noted. All anhydrous solvents were obtained from an anhydrous solvent delivery system equipped with activated alumina columns. All reactions were performed under an inert atmosphere (dry nitrogen gas) using standard Schlenk and vacuum line techniques. Column chromatography purifications were performed on Biotage Isolera using Silicycle Siliasep HP flash cartridges. Nuclear magnetic resonance (NMR) spectra were recorded using a Varian 400 MHz spectrometer in the VOICE NMR laboratory at the University of Illinois at Urbana-Champaign. All chemical shifts (ppm) were calibrated to the residual proton peak of the deuterated solvent. The mass spectrum was obtained through the SCS Mass Spectrometry Facility at the University of Illinois at Urbana-Champaign. Powder XRD patterns were recorded on a Rigaku MiniFlex at a scanning rate of $0.02^\circ \text{ s}^{-1}$ in 2θ ranging from 5° to 50° using a zero diffraction holder purchased from MTI Corporation. Crystal structures of **PEB** and **(OFN)₃-(PEB)₂** were obtained by Dr. Danielle Gray through the George L. Clark X-Ray Facility at the University of Illinois, Urbana-Champaign. UV-Vis spectra were recorded in chloroform using a Shimadzu UV-2401PC. Standard quartz cells with a path length of 2 mm from Starna Cells, Inc. were used. Infrared spectra were collected on a NEXUS 670 serial FTIR spectrophotometer. The

differential scanning calorimetry (DSC) measurements were performed using a TA Instrument Q20. Hermetic zero aluminum pans and lids were used as sample testing containers. A typical DSC measurement has a heating/cooling rate of 10 °C/min. The rheological measurement was performed using TA Instruments AR-G2 Rheometer. The geometry used was 8 mm aluminum plates and the testing method was frequency sweep in flow mode.

5.8.2 Synthesis and Characterization of PEB

PEB was synthesized via a Sonogashira coupling reaction following a literature procedure.¹⁹ The ¹H NMR spectrum (Figure 5.5) and HRMS are in good agreement with the published report. HRMS-ESI: C₂₂H₁₄, Calculated: 278.1096, Found 278.1096.

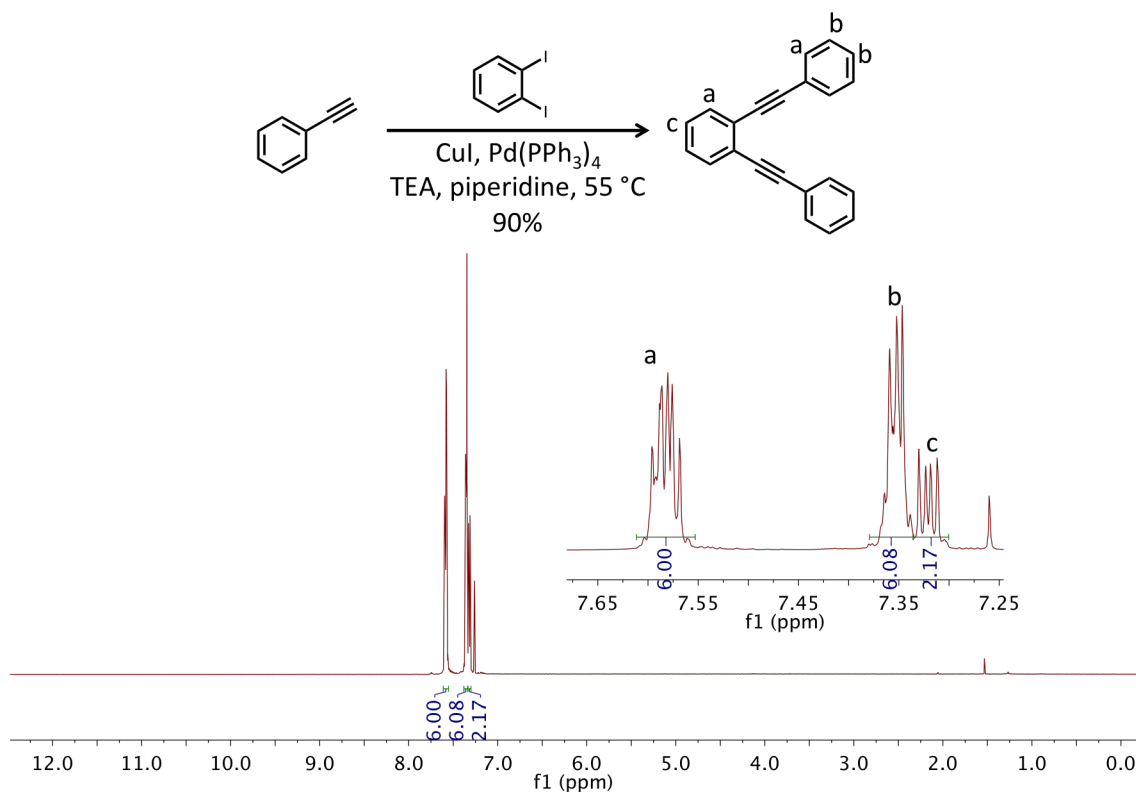


Figure 5.5 Synthesis and ¹H NMR spectrum of **PEB**.

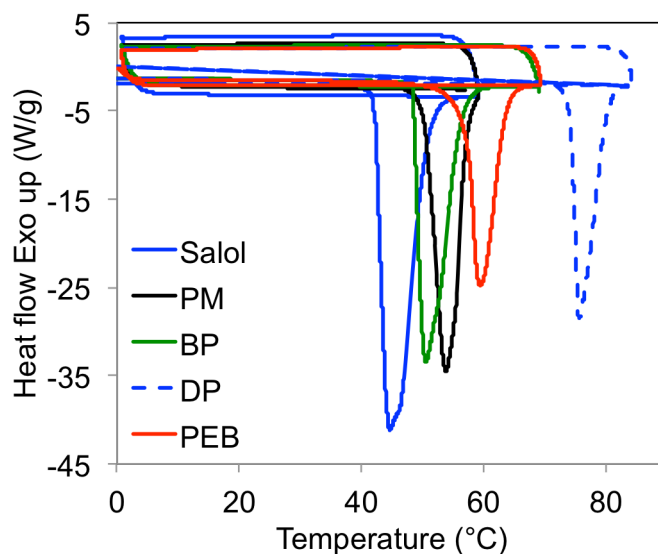


Figure 5.6 DSC curves of supercooled **PEB**, **DP**, **PM**, **BP**, and salol. Upon cooling at 10 °C/min, no recrystallization was observed after melting. The melting point of **PEB**, **DP**, **PM**, **BP**, and salol from the first heating cycle was 55.23 °C, 73.97 °C, 50.39 °C, 48.81 °C, and 42.10 °C, respectively. The heat of fusion of **PEB**, **DP**, **PM**, **BP**, and salol was 22.05 kJ/mol, 30.83 kJ/mol, 19.20 kJ/mol, 17.75 kJ/mol, and 19.44 kJ/mol, respectively. The Gibbs free energy difference (ΔG) between supercooled liquid and crystalline solid can be calculated using the Hoffmann equation, $\Delta G = \Delta H_f(T_m - T) * T * T_m^{-2}$.¹² The ΔG of **PEB**, **DP**, **PM**, **BP**, and salol at 25 °C (298.15 K) was -1.84 kJ/mol, -3.74 kJ/mol, -1.39 kJ/mol, -1.22 kJ/mol, and -1.00 kJ/mol, respectively.

5.8.3 Specimen Preparation for Shock-Wave-Induced Nucleation

The specimen configuration for observing shock-wave-induced nucleation is shown schematically in Figure 5.7. Supercooled liquids were sandwiched between two glass substrates. The glass substrates (1 mm thick, 1" x 1" square) were cleaned with a piranha solution (a mixture of sulfuric acid and hydrogen peroxide). A 50 μm thick polyimide film as a spacer was applied on the glass substrate. A 2 cm diameter circle was laser-cut and removed to allow space for the supercooled liquids between the two glass substrates. Each powder sample of **PEB**, **DP**, **BP**, salol, and **PM** (15 mg per sample) was placed in the circle where the polyimide was removed. The sample was then heated above its melting temperature on a hot plate for 5 min and subsequently cooled to room temperature to form a supercooled liquid. A 400 nm thick Al film was deposited by electron beam deposition on the other glass substrate. A 6 μm thick transparent water-glass confining layer was deposited on the Al film by spin-coating of a sodium silicate

solution. This glass substrate was then placed on top of the supercooled specimen with a pressure of 55 kPa such that the water glass layer was on the outer surface.

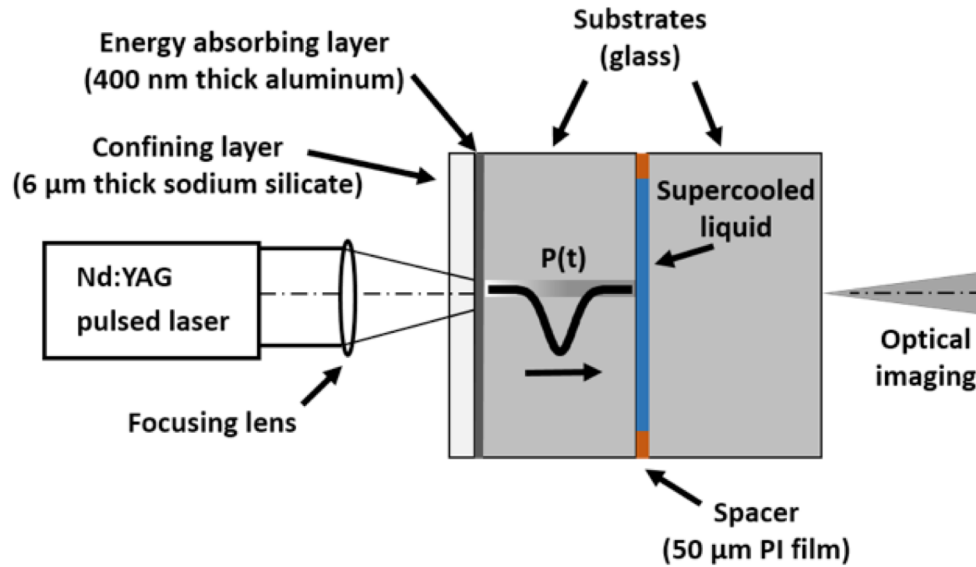


Figure 5.7 Schematic of specimen configuration for shock-wave-induced nucleation.

5.8.4 Experimental Procedures for Measurement of Shock Wave Pressure

Impingement of a high power Nd:YAG pulsed laser on the 400nm thick Al film initiates laser-induced shock waves.³⁴⁻³⁶ The sodium silicate layer confines the rapid expansion of the Al film, launching a high-amplitude compressive shock wave through the specimen. The amplitude and duration of the stress pulse were controlled by varying the YAG laser fluence. The input pressures were characterized in a series of calibration experiments shown schematically in Figure 5.8. The specimen for the calibration experiment consisted of a single glass substrate with a 400 nm Al film and 6 μm water glass layer as described above, but with an additional 100 nm Al film deposited on the opposite surface to provide a reflective surface for interferometric measurements. A Michelson interferometer with a 532 nm continuous laser was used to monitor the out-of-plane displacement of the free surface. The temporal interference signal as a voltage trace was recorded by using a photodetector connected to a 40 GHz oscilloscope. The interference signal was converted to displacement history, leading to the pressure calculation as described previously by Yang et al.¹³ Figure 5.9 shows the resulting pressure profiles as a function of laser fluence used to induce crystallization in the supercooled liquids. After the

supercooled liquid specimens were subjected to shock wave loading, time-lapse images of nucleation and crystal growth were recorded using a QImaging micropublisher 3.3 with AF Micro-Nikkor 60mm f/2.8D lens.

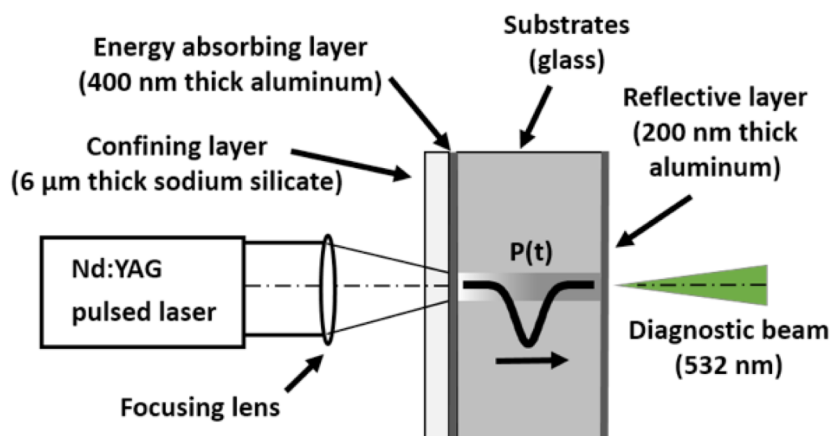


Figure 5.8 Schematic of calibration experimental setup for measurement of shock wave pressure.

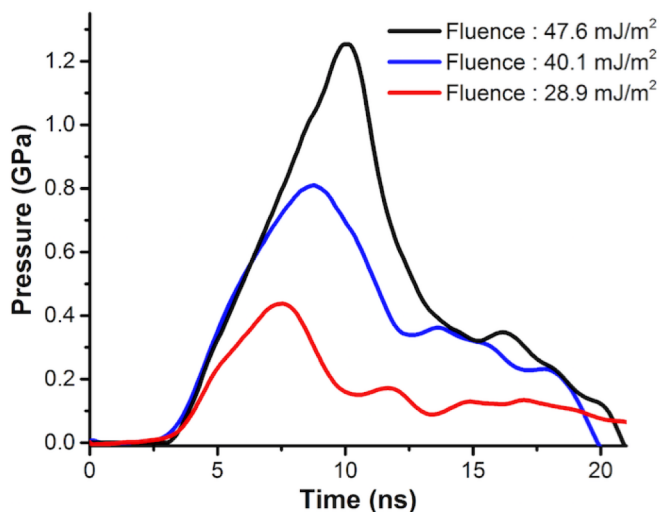


Figure 5.9 Shock wave pressure profiles at 28.9, 40.1, and 47.6 mJ/m^2 laser fluence with peak pressure at 0.4, 0.8, and 1.2 GPa, respectively.

5.8.5 Characterization of PEB Before and After Shock Wave Impact

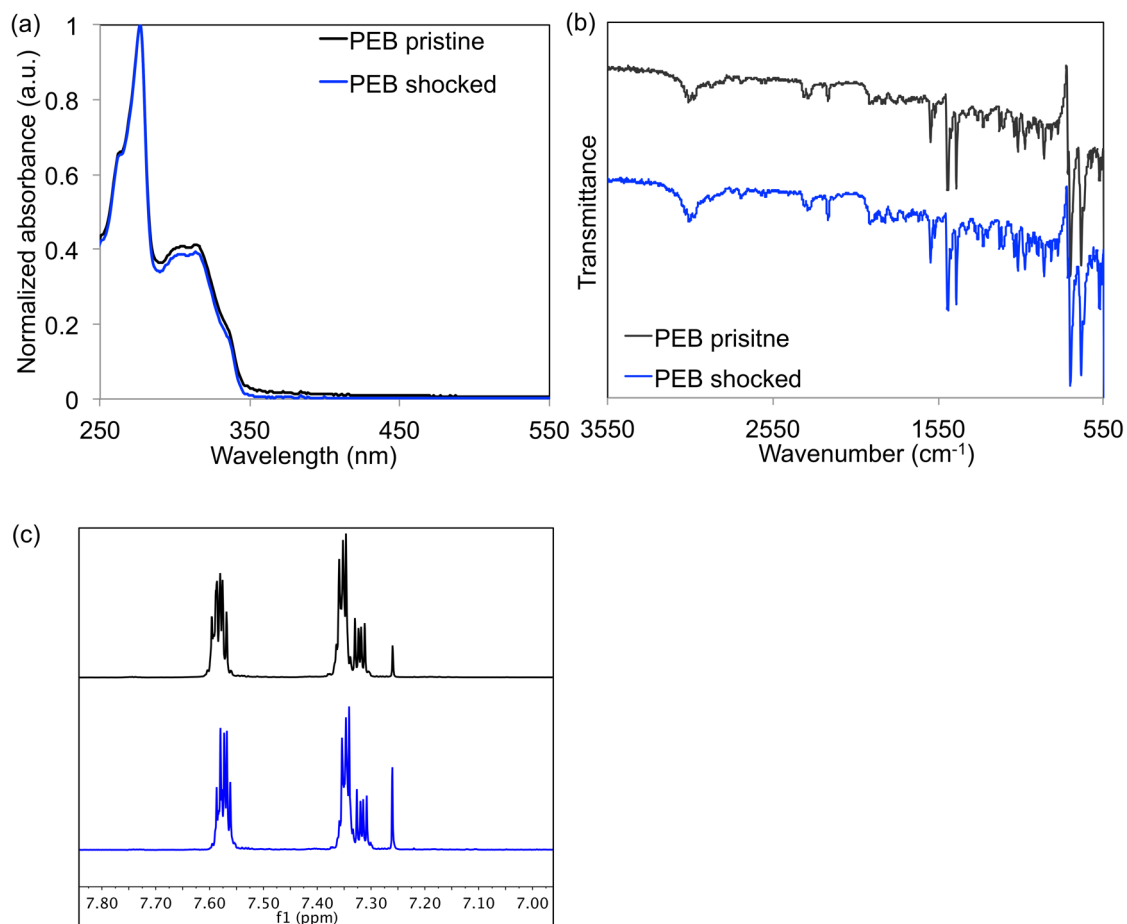


Figure 5.10 (a) UV-Vis; (b) IR; and (c) ¹H NMR spectra of **PEB** before and after shock wave impact.

5.8.6 Crystallization Experiments

A number of saturated solutions were screened for ability to grow single crystals of **PEB** (Table 5.1). A suitable single crystal of **PEB** was obtained by slowly evaporating a saturated hexanes solution at -20 °C. The crystals were kept in an ice bath until mounting for X-ray diffraction experiments. A suitable single crystal of (OFN)₃-(PEB)₂ was obtained by dissolving a 1:1 molar ratio of **OFN**:**PEB** in cyclohexane and allowing the solution to evaporate slowly. Similar crystals could also be obtained using chloroform, benzene, toluene, and dichloromethane as the solvent.

Table 5.1 Summary of crystallization attempts for **PEB**.

Solvent for crystallization	Temperature (°C)	Result
acetone	25, -20	PEB remains as an oil after solvent evaporation.
acetonitrile		
benzene		
chloroform		
cyclohexane		
dichloromethane		
ethyl acetate		
tetrahydrofuran		
toluene		
water	25	PEB precipitates immediately upon cooling as a crystalline powder.
dichloromethane: hexane (1:1)	-20	PEB remains as an oil after solvent evaporation.
ethanol: hexane (v:v = 1:1 and 1:9)	-20	Crystals were formed at -20°C. However, PEB dissolved back in the solution within 2 minutes at room temperature. PEB remained as oil after solvent removal at room temperature.
methanol: hexane (v:v = 1:1 and 1:9)		
hexane	-20	Single crystals were formed. However, twin crystals coexist.
pentane		
hexane	25	Crystalline solids were obtained, but they were not single crystals.
pentane		
ethanol	25, -20	
methanol		
diethyl ether		

5.8.7 Single Crystal X-Ray Diffraction Measurements³⁷⁻⁴⁰

Single crystal XRD for **PEB** and **(OFN)₃-(PEB)₂** were measured on a Bruker APEX-II CCD single-crystal X-ray diffractometer using Cu radiation ($\lambda=1.5418 \text{ \AA}$) and Mo radiation ($\lambda=0.71073 \text{ \AA}$), respectively. Structure solution and refinement were accomplished using SHELXS and SHELXL, respectively. All non-hydrogen atoms were refined anisotropically. All hydrogen atoms were refined in geometrically constrained positions. The structures were solved and refined using the same programs above within the Olex2 graphical user interface.

Table 5.2 Crystallographic parameters for **PEB** and **(OFN)₃-(PEB)₂** at 100 K.

compound name	PEB	(OFN)₃-(PEB)₂
chemical formula	C ₂₂ H ₁₄	C ₃₇ H ₁₄ F ₁₂
formula mass	278.33	686.48
crystal system	Orthorhombic	Triclinic
space group	<i>Pca2₁</i>	<i>P-1</i>
T/K	100(2)	100(2)
a/Å	18.2729(9)	7.0779(3)
b/Å	14.9975(7)	11.1665(5)
c/Å	11.1065(5)	18.3261(8)
$\alpha/^\circ$	90.00	91.2370(18)
$\beta/^\circ$	90.00	94.1192(17)
$\gamma/^\circ$	90.00	98.4474(18)
V/Å ³	3043.7(2)	1428.24(11)
$\rho_{\text{calc}}/\text{g cm}^{-3}$	1.215	1.596
Z	8	2
radiation type	Cu K $_{\alpha}$ ($\lambda=1.54178 \text{ \AA}$)	Mo K $_{\alpha}$ ($\lambda=0.71073 \text{ \AA}$)
μ/mm^{-1}	0.522	0.147
no. of reflections measured	36804	89693
no. of independent reflections	5323	7125
No. of reflection ($I > 2\sigma(I)$)	5046	6415
R _{int}	0.0379	0.0326

Table 5.2 (cont.)

compound name	PEB	(OFN)₃-(PEB)₂
R ₁ (I > 2σ(I))	0.0274	0.0344
wR(F ²) (I > 2σ(I))	0.0663	0.0908
R ₁ (all data)	0.0303	0.0384
wR ₂ (all data)	0.0680	0.0940
CCDC deposition number	1479187	1479188

5.8.8 Other Properties of *PEB*, *Salol*, *BP*, *DP*, and *PM*

Table 5.3 Crystal packing efficiencies of *PEB*, *salol*, *BP*, *DP*, and *PM*.

Compounds	Number of molecules in a unit cell	Molecular volume (Å ³)	Unit cell Volume (Å ³)	Packing Efficiency (%)
PEB	8	252.8	3043.7	66.4
salol	4	178.1	1051.9	67.7
BP	4	165.7	992.3	66.8
DP	4	261.5	1604.3	65.2
PM	8	165.3	2035.2	65.0

Table 5.4 Viscosities and glass transition temperatures (*T_g*) of *PEB*, *salol*, *BP*, *DP*, and *PM*.

Compounds	Viscosity at 25 °C (Pa·s) ^a	<i>T_g</i> (K) ^b
PEB	0.2	247
salol	0.019	224
BP	0.013	214
DP	13.7	257
PM	N/A*	242

**PM* crystallized upon cooling from 80 °C to 25 °C using the rheometer's parallel plate geometry;^a the viscosity of each tested compound was determined as a function of frequency (1 to 1000 s⁻¹) at 25°C using a rheometer; ^b the glass transition temperatures were determined at the inflection point of the step from the second heating scan with heating/cooling/heating rate of 10 °C/min using DSC.

5.8.9 Theoretical Calculation of Tested Supercooled Liquids

All calculations were performed with the B3LYP/6-31G(d) basis set. Geometry optimizations were carried out using Gaussian 09.⁴¹ Vibrational frequencies were computed for each optimized structure to confirm that each geometry was a stationary point. Calculations on rotational energy of the terminal phenyl ring were carried out using Spartan 10.⁴² Both the optimized structures and crystal structures were used as the starting structures and all atoms except the terminal phenyl ring were frozen. The relative energy profile was generated for each molecule as the unfrozen terminal phenyl ring rotated 360° with a step size of 5°.

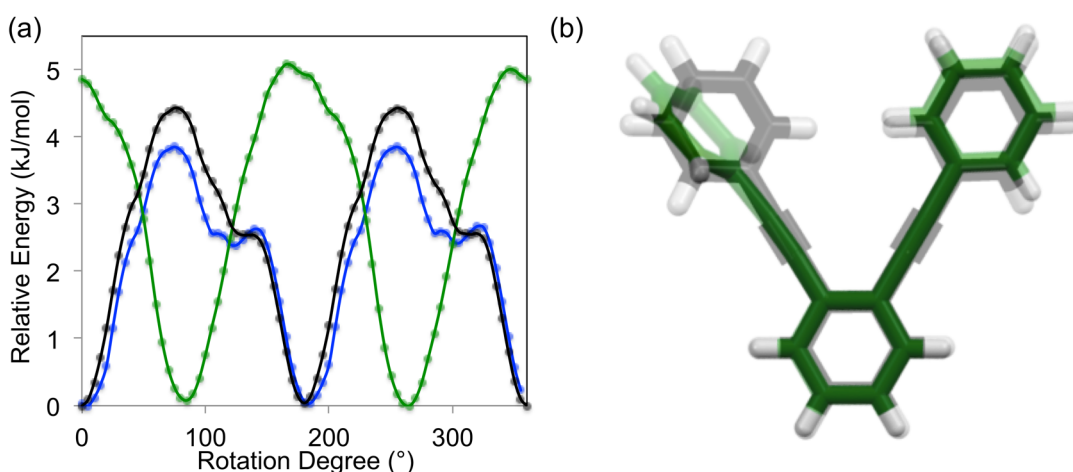


Figure 5.11 (a) Energy profiles of supercooled **PEB** as the terminal phenyl ring rotates 360° while other atoms are frozen using optimized geometry in vacuum (black), optimized geometry in dichloromethane (blue), crystal structure in vacuum (green) as the starting geometry. (b) Optimized **PEB** geometry (black) vs. crystal (green) **PEB** geometry. The difference in geometry likely explains the difference in relative energy.

Table 5.5 Rotational energy barriers of supercooled liquids under different conditions.

Compounds	In vacuum (kJ/mol) (optimized geometry)	In CH ₂ Cl ₂ (kJ/mol) (optimized geometry)	In vacuum (kJ/mol) (crystal geometry)
PEB	4.4	3.9	5.1
salol	78.8	80.5	12.3
BP	137.9	135.3	158.2
DP	67.7	71.5	57.5
PM	172.1	155.0	165.6

5.9 Notes and References

Notes:

Portions of this chapter have been published: Ren, Y.; Lee, J.; Hutchins, K. M.; Sottos, N. R.; Moore, J. S. “Crystal structure, thermal properties and shock-wave-induced nucleation of 1,2-bis(phenylethynyl)benzene.” *Cryst. Growth Des.* **2016**, *16*, 6148–6151. They are reproduced/adapted with permission. Copyright 2016 American Chemical Society.

References:

1. Almarsson, O.; Zaworotko, M. J. *Chem. Comm.* **2004**, 1889.
2. Vippagunta, S. R.; Brittain, H. G.; Grant, D. J. W. *Adv. Drug Deliv. Rev.* **2001**, *48*, 3.
3. Chung, H.; Diao, Y. *J. Mater. Chem. C* **2016**, *4*, 3915.
4. Furukawa, H.; Cordova, K. E.; O’Keeffe, M.; Yaghi, O. M. *Science* **2013**, *341*.
5. Adrjanowicz, K.; Grzybowski, A.; Grzybowska, K.; Pionteck, J.; Paluch, M. *Cryst. Growth Des.* **2013**, *13*, 4648.
6. Adrjanowicz, K.; Kaminski, K.; Paluch, M.; Niss, K. *Cryst. Growth Des.* **2015**, *15*, 3257.
7. Adrjanowicz, K.; Grzybowski, A.; Grzybowska, K.; Pionteck, J.; Paluch, M. *Cryst. Growth Des.* **2014**, *14*, 4226.
8. Mierzwa, M.; Paluch, M.; Rzoska, S. J.; Ziolo, J. *J. Phys. Chem. B* **2008**, *112*, 10383.
9. Adrjanowicz, K.; Kaminski, K.; Wojnarowska, Z.; Dulski, M.; Hawelek, L.; Pawlus, S.; Paluch, M.; Sawicki, W. *J. Phys. Chem. B* **2010**, *114*, 6579.
10. Evenzahav, A.; Turro, N. J. *J. Am. Chem. Soc.* **1998**, *120*, 1835.
11. James, S. L.; Adams, C. J.; Bolm, C.; Braga, D.; Collier, P.; Friscic, T.; Grepioni, F.; Harris, K. D. M.; Hyett, G.; Jones, W.; Krebs, A.; Mack, J.; Maini, L.; Orpen, A. G.; Parkin, I. P.; Shearouse, W. C.; Steed, J. W.; Waddell, D. C. *Chem. Soc. Rev.* **2012**, *41*, 413.
12. Chung, K.; Kwon, M. S.; Leung, B. M.; Wong-Foy, A. G.; Kim, M. S.; Kim, J.; Takayama, S.; Gierschner, J.; Matzger, A. J.; Kim, J. *ACS Cent. Sci.* **2015**, *1*, 94.
13. Yang, K.; Lee, J.; Sottos, N. R.; Moore, J. S. *J. Am. Chem. Soc.* **2015**, *137*, 16000.
14. Sosso, G. C.; Chen, J.; Cox, S. J.; Fitzner, M.; Pedevilla, P.; Zen, A.; Michaelides, A. *Chem. Rev.* **2016**, *116*, 7078.
15. Nagarjuna, G.; Ren, Y.; Moore, J. S. *Tetrahedron Lett.* **2015**, *56*, 3155.
16. Jana, S.; Anoop, A. *Phys. Chem. Chem. Phys.* **2015**, *17*, 29793.
17. Melinger, J. S.; Pan, Y.; Kleiman, V. D.; Peng, Z.; Davis, B. L.; McMorro, D.; Lu, M. *J. Am. Chem. Soc.* **2002**, *124*, 12002.
18. Zhang, W.; Huang, P. C. *Mater. Chem. Phys.* **2006**, *96*, 283.
19. Kovalenko, S. V.; Peabody, S.; Manoharan, M.; Clark, R. J.; Alabugin, I. V. *Org. Lett.* **2004**, *6*, 2457.
20. Shirota, Y.; Kageyama, H. *Chem. Rev.* **2007**, *107*, 953.
21. Korovina, N. V.; Chang, M. L.; Nguyen, T. T.; Fernandez, R.; Walker, H. J.; Olmstead, M. M.; Gherman, B. F.; Spence, J. D. *Org. Lett.* **2011**, *13*, 3660.
22. Zhu, N.; Hu, W.; Han, S.; Wang, O.; Zhao, D. *Org. Lett.* **2008**, *10*, 4283.
23. West, A. P.; Mecozzi, S.; Dougherty, D. A. *J. Phys. Org. Chem.* **1997**, *10*, 347.

24. Prosser, C. R. P. G. S. *Nature* **1960**, *187*, 1021.
25. Coates, G. W.; Dunn, A. R.; Henling, L. M.; Ziller, J. W.; Lobkovsky, E. B.; Grubbs, R. H. *J. Am. Chem. Soc.* **1998**, *120*, 3641.
26. Lopez-Mejias, V.; Kampf, J. W.; Matzger, A. J. *J. Am. Chem. Soc.* **2009**, *131*, 4554.
27. Cembran, A.; Bernardi, F.; Garavelli, M.; Gagliardi, L.; Orlandi, G. *J. Am. Chem. Soc.* **2004**, *126*, 3234.
28. Graham, D. J.; Magdolinos, P.; Tosi, M. *J. Phys. Chem.* **1995**, *99*, 4757.
29. Hatase, M.; Hanaya, M.; Oguni, M. *J. Non-Cryst. Solids* **2004**, *333*, 129.
30. Diogo, H. P.; Pinto, S. S.; Ramos, J. J. M. *J. Therm. Anal. Calorim.* **2006**, *83*, 361.
31. Polsky, C. H.; Martinez, L. M.; Leinenweber, K.; VerHelst, M. A.; Angell, C. A.; Wolf, G. H. *Phys. Rev. B* **2000**, *61*, 5934.
32. Yoshino, T.; Maruyama, K.; Kagi, H.; Nara, M.; Kim, J. C. *Cryst. Growth Des.* **2012**, *12*, 3357.
33. Shah, N.; Sandhu, H.; Choi, D. S.; Chokshi, H.; Malick, A. W., *Amorphous Solid Dispersions : Theory and Practice*. Springer: New York, NY, 2014.
34. Grady, M. E.; Geubelle, P. H.; Braun, P. V.; Sottos, N. R. *Langmuir* **2014**, *30*, 11096.
35. Gupta, V.; Argon, A. S.; Parks, D. M.; Cornie, J. A. *J. Mech. Phys. Solids* **1992**, *40*, 141.
36. Wang, J. L.; Weaver, R. L.; Sottos, N. R. *Exp. Mech.* **2002**, *42*, 74.
37. *APEX2, SAINT, XCIF, XPREP and SADABS. Bruker AXS Inc., Madison, Wisconsin, USA.* **2014**.
38. Dolomanov, O. V. B., L. J.; Gildea, R. J.; Howard, J. A. K.; Puschmann, H. *J. Appl. Cryst.* **2009**, *42*, 339.
39. Shledrick, G. M. *Acta Cryst A* **2008**, *64*, 112.
40. Shledrick, G. M. *Acta Cryst. C* **2015**, *71*, 3.
41. Frisch, M. J. T., G. W.; Schlegel, H. B.; Scuseria, G. E.; Robb, M. A.; Cheeseman, J. R.; Scalmani, G.; Barone, V.; Mennucci, B.; Petersson, G. A.; Nakatsuji, H.; Caricato, M.; Li, X.; Hratchian, H. P.; Izmaylov, A. F.; Bloino, J.; Zheng, G.; Sonnenberg, J. L.; Hada, M.; Ehara, M.; Toyota, K.; Fukuda, R.; Hasegawa, J.; Ishida, M.; Nakajima, T.; Honda, Y.; Kitao, O.; Nakai, H.; Vreven, T.; Montgomery Jr., J. A.; Peralta, J. E.; Ogliaro, F.; Bearpark, M. J.; Heyd, J.; Brothers, E. N.; Kudin, K. N.; Staroverov, V. N.; Kobayashi, R.; Normand, J.; Raghavachari, K.; Rendell, A. P.; Burant, J. C.; Iyengar, S. S.; Tomasi, J.; Cossi, M.; Rega, N.; Millam, N. J.; Klene, M.; Knox, J. E.; Cross, J. B.; Bakken, V.; Adamo, C.; Jaramillo, J.; Gomperts, R.; Stratmann, R. E.; Yazyev, O.; Austin, A. J.; Cammi, R.; Pomelli, C.; Ochterski, J. W.; Martin, R. L.; Morokuma, K.; Zakrzewski, V. G.; Voth, G. A.; Salvador, P.; Dannenberg, J. J.; Dapprich, S.; Daniels, A. D.; Farkas, Ö.; Foresman, J. B.; Ortiz, J. V.; Cioslowski, J.; Fox, D. J.; Gaussian, Inc.: Wallingford, CT, USA **2009**.
42. *Spartan 10*, Wavefunction Inc.: Irvine, CA, USA.